RÉPUBLIQUE FRANÇAISE
Liberté Égalité Fraternité

Université de Toulouse

Doctorat de l'Université de Toulouse

préparé à Toulouse INP

Soudage laser par transmission de thermoplastique semi-cristallin PEKK : prédiction de la cristallinité du joint de soudure et de la résistance mécanique des assemblages

---

Thèse présentée et soutenue, le 16 décembre 2024 par

Marcela MATUS AGUIRRE

École doctorale
SDM - SCIENCES DE LA MATIERE - Toulouse

Spécialité
Sciences et Génie des Matériaux

Unité de recherche
LGP - Laboratoire Génie de Production

Thèse dirigée par
France CHABERT et Benoît COSSON

Composition du jury
Mme Nadine ALLANIC, Présidente, Nantes Université
Mme Yun-Mei LUO, Rapporteuse, Université Gustave Eiffel
M. Eric DANTRAS, Examinateur, Université Toulouse III - Paul Sabatier
M. Bart BUFFEL, Examinateur, KU Leuven
M. André Chateau AKUE ASSEKO, Examinateur, IMT Nord Europe
Mme France CHABERT, Directrice de thèse, UTTOP
M. Benoît COSSON, Co-directeur de thèse, UTTOP

Membres invités
M. Rémi GILBLAS , IMT Mines Albi
M. Christian GARNIER, Université de Technologie Tarbes Occitanie Pyrénées

There's always a way.
When the odds are impossible... do the impossible.

— SUPERMAN

It's never as bad as it seems.
You're much stronger than you think you are.

— SUPERMAN All-Star

Laser transmission welding (LTW) of semi-crystalline thermoplastic PEKK: prediction of the weld joint crystallinity and mechanical strength of assemblies

---

Soudage laser par transmission de thermoplastique semicristallin PEKK : prédiction de la cristallinité du joint de soudure et de la résistance mécanique des assemblages

---

Soldadura láser por transmisión del polímero termoplástico semicristalino PEKK: predicción de la cristalinidad de la zona de soldadura y de la resistencia mecánica de los ensamblajes

— Marcela MATUS AGUIRRE —

Vulgarized abstract — Welding thermoplastic materials is gaining popularity in the aerospace industry as a result of the need for lightweight and strong structures. Laser transmission welding (LTW) is an effective technique for joining these materials, providing precision and high-quality welds. This thesis investigates the LTW process of PEKK, with a focus on the effect of material properties and welding parameters (laser power and thickness of the upper part) on the weld joint morphology and strength. Heat treatment (annealing) was applied to welds to improve their quality. The weld joints were analyzed and compared by mechanical tests and microscopy. The laser welding process was also modeled using numerical simulations to predict the weld joint crystallinity. The work expands on the LTW process of PEKK composites with carbon fibers. The results of this thesis provide insights into optimizing LTW for strong and lightweight materials in aerospace applications.

Résumé vulgarisé — Le soudage de matériaux thermoplastiques est de plus en plus répandu dans l'industrie aérospatiale, en réponse au besoin de structures à la fois légères et résistantes. Le soudage laser par transmission (LTW en anglais) est une technique efficace pour assembler ces matériaux, en produisant des soudures de précision et de haute qualité. Cette thèse étudie le procédé de soudage laser par transmission de pièces en PEKK, en mettant l'accent sur l'effet des propriétés des matériaux et des paramètres de soudage (puissance du laser et épaisseur de la pièce semi-transparente) sur la morphologie et la résistance du joint de soudure. Un traitement thermique de recuit a été appliqué à certaines soudures pour améliorer leur qualité. Les joints soudés ont été analysés et comparés par des essais mécaniques et de la microscopie. Le procédé de soudage laser a également été modélisé à l'aide de simulations numériques afin de prédire la cristallinité des joints de soudure. L'étude s'étend également aux composites PEKK renforcés de fibres de carbone. Les résultats de cette thèse fournissent des outils pour l'optimisation du soudage laser par transmission pour des matériaux solides et légers dans les applications aérospatiales.

Resumen vulgarizado — La soldadura de materiales termoplásticos está ganando popularidad en la industria aeroespacial como resultado de la necesidad de estructuras ligeras y resistentes. La soldadura láser por transmisión (LTW por sus siglas en inglés) es una técnica eficaz para unir estos materiales, proporcionando soldaduras de precisión y alta calidad. Esta tesis doctoral investiga el proceso LTW de PEKK, centrándose en el efecto de las propiedades del material y los parámetros de soldadura (potencia del láser y espesor de la parte superior) sobre la morfología y resistencia de la unión soldada. Un tratamiento térmico de recocido se aplicó a las soldaduras para mejorar su calidad. Las uniones soldadas se analizaron y compararon mediante ensayos mecánicos y microscopía. También se modelizó el proceso de soldadura láser mediante simulaciones numéricas para predecir la cristalinidad de la unión soldada. El trabajo se extiende en el proceso LTW de compuestos PEKK con fibras de carbono. Los resultados de esta tesis aportan ideas para optimizar la soldadura LTW de materiales resistentes y ligeros en aplicaciones aeroespaciales.

Abstract — Thermoplastic materials are gaining popularity in the aerospace industry as alternatives to metals and thermosets, providing benefits such as fast manufacturing, repairability, and recyclability. Their ability to soften and melt allows them to be welded without needing to incorporate external components. Additionally, high-performance thermoplastics exhibit resistance to harsh environments, such as high temperatures and various chemicals, making them ideal for high-demanding applications. These features make thermoplastics suitable for applications in which weight reduction, performance, and durability are essential.

Laser transmission welding (LTW) has emerged as an effective technique for welding thermoplastics due to its simplicity, precision, and ability to produce high-quality joints. In LTW, a laser beam passes through a semi-transparent upper part and is absorbed by a lower absorbent sample, generating heat at the interface to assemble the parts. The LTW process relies on the thermo-chemical and optical properties of the materials to be welded. Careful consideration is needed when laser welding semi-crystalline thermoplastics, like polyaryletherketones (PAEK). Polyetherketoneketone (PEKK) has received less attention than PEEK in laser welding. However, PEKK is a more promising material for LTW due to its unique crystallization properties compared to PEEK. The crystallization kinetics of PEKK can be modified, which provides better control of its crystallinity by manipulating processing parameters.

This PhD thesis investigates the laser transmission welding process of PEKK, focusing on the influence of material properties and process parameters on the weld joint morphology and mechanical properties. The overlapping configuration consists of a quasi-amorphous semi-transparent PEKK sample over a highly crystallized opaque PEKK one (PEKK-A/SC). Thermo-physical and optical properties of the PEKK samples are characterized to ensure their suitability for LTW. Then, process parameters for LTW, such as laser power and thickness of the upper part, are systematically studied to understand their impact on weld joint properties. After welding, some assemblies are annealed at the cold crystallization temperature of PEKK to enhance joint quality. The quality of the weld joints is assessed by mechanical tests and microscopic observations. Single lap-shear tests are employed to identify the failure type and mechanical strength of assemblies. Microscopy is used to analyze failure zones and the weld joint morphology on the cross-section along the welding path.

A numerical simulation of the LTW process of PEKK parts was developed in MatLab using the finite differences method, incorporating heat transfer and the crystallization kinetics of PEKK. This model provided insights into the thermal history of the samples during welding and predicted the evolution of weld joint crystallinity as a function of welding parameters. The developed simulations offer insights into the complex thermal and crystallization behaviors observed during LTW of PEKK.

Furthermore, after studying and validating the LTW process for PEKK polymer, this thesis extends the LTW study to PEKK composites reinforced with short carbon fibers (PEKK-CF). To enable LTW of PEKK-CF samples, the quasi-amorphous PEKK is used as the upper part for the overlapping configuration. That represents a novel area of research, with no prior studies found on LTW of PEKK-CF composites. The welding of PEKK-CF samples is optimized through new experimental trials, and the weld joint quality is evaluated under varying laser intensities and the thickness of the upper part.

The findings from this thesis contribute to a deeper understanding of the LTW process for PEKK and its composites, providing valuable guidelines for optimizing welding parameters and improving joint strength in industrial applications.

Keywords: laser welding, polymer welding, crystallization, composites, numerical simulation, polyetherketoneketone.

Résumé — Les matériaux thermoplastiques gagnent en popularité dans l'industrie aérospatiale en tant qu'alternatives aux métaux et aux thermodurcissables, offrant des avantages tels que la rapidité de fabrication, la réparabilité et la recyclabilité. Leur capacité à ramollir et à fondre sous l'effet de la chaleur leur permet d'être soudés sans avoir besoin d'incorporer de composants. De plus, certains thermoplastiques présentent une résistance aux environnements extrêmes, tels que des températures élevées et divers produits chimiques, ce qui les rend idéaux pour des applications exigeantes. Ces caractéristiques font des thermoplastiques des matériaux adaptés aux applications où la réduction du poids, les performances et la durabilité sont des critères essentiels.

Dans ce contexte, le soudage par transmission laser (LTW) se révèle être une technique efficace pour le soudage des thermoplastiques en raison de sa simplicité, de sa précision et de sa capacité à produire des joints de haute qualité. Dans cette technique, un faisceau laser traverse une partie supérieure semi-transparente et est absorbé par une pièce inférieure absorbante, ce qui génère de la chaleur à l'interface pour faire fondre et fusionner les pièces. Le procédé LTW repose sur les propriétés thermochimiques et optiques des matériaux à souder. Le soudage laser de thermoplastiques semi-cristallins, tels que les polyaryléthercétone (PAEK), nécessite une attention particulière. Le polyéthercétonecétone (PEKK) a reçu moins d'attention que le PEEK en soudage laser. Cependant, le PEKK est un matériau encore plus prometteur pour le soudage laser par transmission en raison de sa cinétique de cristallisation modifiable par rapport au PEEK.

Cette thèse doctorale étudie le procédé de soudage laser par transmission du PEKK, en se concentrant sur l'influence des propriétés du matériau et des paramètres de soudage sur la morphologie et les propriétés mécaniques du joint de soudure. La configuration d'assemblage consiste en un échantillon de PEKK quasi-amorphe sur une pièce de PEKK fortement cristallisée (PEKK-A/SC). Les propriétés thermophysiques et optiques des matériaux sont caractérisées afin de s'assurer qu'ils sont adaptés au LTW. Ensuite, les paramètres du procédé, tels que la puissance du laser et l'épaisseur de la pièce semi-transparente, sont systématiquement étudiés pour comprendre leur impact sur les propriétés du joint. Certains assemblages sont recuits à la température de cristallisation à froid du PEKK pour améliorer la qualité des joints soudés. La qualité des assemblages soudés et recuits est évaluée à l'aide d'essais mécaniques de cisaillement à simple recouvrement et de la microscopie.

Le procédé LTW est modélisé à l'aide de la méthode des différences finies sous environnement MatLab, en incorporant le transfert de chaleur et la cinétique de cristallisation du PEKK. Cette modélisation a permis de comprendre l'histoire thermique des échantillons pendant le soudage et de prédire l'évolution de la cristallinité du joint de soudure en fonction des paramètres de soudage.

Après avoir étudié et validé le procédé LTW pour le PEKK, la thèse étend l'étude LTW aux composites PEKK renforcés par des fibres courtes de carbone (PEKK-CF). Pour permettre le LTW des échantillons PEKK-CF, le PEKK quasi-amorphe est utilisé comme pièce supérieure pour l'assemblage. Cela représente un nouveau domaine de recherche, car aucune étude antérieure n'a été trouvée sur le soudage laser par transmission des composites PEKK-CF. Le soudage des échantillons de PEKK-CF est optimisé par des nouveau essais expérimentaux, et la qualité du joint de soudure est évaluée en faisant varier l'intensité de laser.

Les résultats de cette thèse contribuent à une meilleure compréhension du procédé de soudage laser par transmission du PEKK et de ses composites, et fournissent des lignes directrices pour optimiser les paramètres de soudage et améliorer la résistance des joints dans les applications industrielles.

Mots clés : soudage laser, soudage de polymères, cristallisation, composites, simulation numérique, polyéthercétonecétone.

Resumen — Los materiales termoplásticos están ganando popularidad en la industria aeroespacial como alternativas a los metales y termoestables, ya que ofrecen ventajas como la rapidez de fabricación, la posibilidad de reparación y la reciclabilidad. Su capacidad para ablandarse y fundirse permite soldarlos sin necesidad de incorporar componentes externos. Además, los termoplásticos de alto rendimiento presentan resistencia a entornos agresivos, como altas temperaturas y diversos productos químicos, lo que los hace ideales para aplicaciones de alta exigencia. Estas características hacen que los materiales termoplásticos sean adecuados para aplicaciones en las que la reducción de peso, el rendimiento y la durabilidad son esenciales.

En este contexto, la soldadura láser por transmisión (LTW) está revelándose como una técnica eficaz para soldar termoplásticos debido a su sencillez, precisión y capacidad para producir uniones de alta calidad. En esta técnica, un rayo láser atraviesa una pieza superior semitransparente y es absorbido por una pieza inferior absorbente, generando calor en la interfaz para fundir y fusionar las piezas. El proceso LTW depende de las propiedades termoquímicas y ópticas de los materiales a soldar. La soldadura por láser de termoplásticos semicristalinos, como las poliarilcetonas (PAEK), requiere una atención especial. El poliétercetonacetona (PEKK) ha recibido menos atención que el poliéterétercetona (PEEK) en la soldadura láser. Sin embargo, el PEKK es un material aún más prometedor para la soldadura láser por transmisión debido a su cinética de cristalización modificable en comparación con el PEEK.

Esta tesis doctoral investiga el proceso de soldadura láser por transmisión de PEKK, centrándose en la influencia de las propiedades del material y los parámetros del proceso sobre la morfología de la unión soldada y sus propiedades mecánicas. La configuración del ensamblaje consiste en una muestra de PEKK cuasiamorfo sobre una pieza de PEKK altamente cristalizado (PEKK-A/SC). Las propiedades termofísicas y ópticas de las muestras de PEKK se caracterizan para garantizar su adecuación para LTW. A continuación, se estudian sistemáticamente los parámetros del proceso de LTW, como la potencia del láser y el grosor de la parte superior, para comprender su impacto en las propiedades de la unión soldada. Algunos ensamblajes se recuecen a la temperatura de cristalización en frío del PEKK para mejorar la calidad de las uniones soldadas. La calidad de las uniones soldadas y recocidas se evalúa mediante ensayos mecánicos de cizalladura simple y microscopía.

Una simulación numérica del proceso LTW de piezas PEKK se desarrolló en MatLab utilizando el método de diferencias finitas, incorporando la transferencia de calor y la cinética de cristalización del PEKK. Esta modelización permitió comprender la historia térmica de las muestras durante la soldadura y predecir la evolución de la cristalinidad de la unión soldada en función de los parámetros de soldadura.

Además, tras estudiar y validar el proceso LTW para el polímero PEKK, la tesis amplía el estudio LTW a los compuestos PEKK reforzados con fibras cortas de carbono (PEKK-CF). Para permitir el LTW de las muestras PEKK-CF, se utiliza el PEKK cuasiamorfo como pieza superior para el ensamblaje (PEKK-A/CF). Esto representa un área de investigación novedosa, ya que no se han encontrado estudios previos sobre LTW de composites PEKK-CF. La soldadura de las muestras de PEKK-CF se optimiza mediante nuevos ensayos experimentales, y la calidad de la unión soldada se evalúa bajo diferentes intensidades de láser y el espesor de la parte superior.

Los resultados de esta tesis contribuyen a una comprensión más profunda del proceso LTW para PEKK y sus compuestos, proporcionando valiosas directrices para optimizar los parámetros de soldadura y mejorar la resistencia de la unión en aplicaciones industriales.

Palabras clave: soldadura láser, soldadura de polímeros, cristalización, materiales compuestos, simulación numérica, poliétercetonacetona.

Acknowledgements

This PhD work was carried out in three different laboratories: the LGP of UTTOP, the ICA of IMT Mines Albi, and the CERI MP of IMT Nord Europe Douai. I want to express my gratitude to these institutions for their welcome and for providing the necessary resources to accomplish this research.

The completion of this PhD thesis has been a challenging yet enriching journey, and I am deeply grateful to those who have supported and guided me throughout these years.

I want to start by sincerely thanking the jury members. Thank you, Nadine Allanic and Yun-Mei Luo, for agreeing to review my thesis and for your thorough evaluation. And thanks Eric Dantras and Bart Buffel for your participation and insightful questions. Thank you all for your interest in my work and for the valuable exchanges during my defense.

Then, I want to thank my five supervisors for their contributions.

First, to those who welcomed me at the LGP in Tarbes. To my thesis director, France Chabert, without her initiative and leadership, this project would not have existed. And to my supervisor, Christian Garnier, who guided me in the welding and mechanical tests. Thanks for your involvement in my doctoral research, your expertise and insights have contributed to shaping this work.

Then, I would like to acknowledge André Akué and Benoît Cosson for warmly welcoming me into the CERI MP at Douai and for their help with the numerical simulations.

A special thanks to Benoît, for his continuous support, kindness, and encouragement. His patience, guidance, and ability to always offer thoughtful advice have been invaluable. Beyond the academic aspect, I am grateful for his music recommendations and for reminding me of the importance of balance during these years.

Another special thanks to Fabrice Schmidt, who was not only an essential support in my experimental tests and travels to Albi but also a great source of moral and emotional support. His kindness and availability have made a real difference throughout my PhD journey.

I would also like to extend a special thanks to Rémi Gilblas for his help with the optical characterization of the material, a crucial part of my research. His good humor, advice, and willingness to speak español mexicano with me always made me feel at home at Albi.

A heartfelt thank you to my intern, Damien Thierry, who worked tirelessly to assist me with the final experimental campaigns. Together, we achieved great results, and I truly appreciate his dedication and effort.

Additionally, I want to express my gratitude to the technicians, research engineers, researchers, and administrative personnel who assisted me daily in the three laboratories I worked in. Furthermore, I thanks the other PhD students who were always there through the good and the bad times. Their presence, support, discussions, and shared moments have been invaluable in making this experience more enjoyable.

I greatly thanks my friends — my old friends in Mexico, those from Albi, from Toulouse, and the new people I met during my PhD journey. Thank you all for being there, following this journey with a different perspective, always believing in me, and wishing me the best.

Mi mayor agradecimiento va dirigido a mi familia, en particular a mi hermana, mi mamá, mi papá y a mis tíos, Susy e Isac. Gracias por su apoyo inquebrantable, sus consejos, su paciencia y su amor, que fueron mi mayor fuente de fuerza y motivación a lo largo de este proyecto. Y gracias por haber venido a Francia desde México para acompañarme y echarme porras durante mi ponencia.

Enfin, ma plus profonde gratitude va à Gaspard, qui a toujours été présent dans les hauts et les bas, écoutant mes frustrations et célébrant mes réussites. Ses encouragements inébranlables et sa foi en moi m'ont rappelé que j'étais assez forte pour réussir. Merci pour tout ce soutien.

To all those who, in one way or another, have been part of this adventure ...

— Thank you! Gracias! Merci !

Marcela Matus Aguirre

Contents

Table of Contents **xvi**

List of Figures **xxi**

List of Tables **xxix**

General introduction **1**

1 State of art on laser transmission welding of thermoplastic parts **5**

1.1 Laser transmission welding (LTW) of polymers 6

1.1.1 Fundamentals of laser transmission welding 10

1.1.2 Laser technologies 12

1.1.3 LTW techniques 13

1.1.4 Material properties influencing LTW 16

1.1.5 Laser welding parameters and their influence on weld quality 19

1.2 Physical phenomena involved during LTW 23

1.2.1 Light-Matter interaction 23

1.2.2 Laser intensity and heat generation 26

1.2.3 Heat transfer at the interface 26

1.3 LTW of semi-crystalline thermoplastics and composites 27

1.3.1 Characteristics of semi-crystalline thermoplastics 27

1.3.2 Crystalline structure and its impact on LTW 29

1.3.3 Laser irradiation impact on the crystalline structure 30

1.4 LTW on poly(aryletherketone)s (PAEKs) 31

1.4.1 Crystallization mechanisms of PEKK thermoplastic 33

1.4.2 PEKK crystallization kinetics models 35

1.5 Synthesis 52

2 Material of study: PEKK samples and properties for LTW 53

2.1 Introduction 54

2.2 Overview of the welded material 54

2.2.1 The poly-ether ketone ketone 54

2.2.2 PEKK grade 70/30 60

2.3 Samples manufacturing for welding 60

2.3.1 Drying process for PEKK pellets 61

2.3.2 Injection molding process and parameters 63

2.3.3 Crystallization phenomena from the melt state 65

2.4 Plates characterization for LTW 68

2.4.1 Thermal transitions and degree of crystallinity by DSC 69

2.4.2 Heat capacity and thermal conductivity 72

2.4.3 Optical properties for laser welding 72

2.5 Synthesis 85

3 Laser transmission welding of PEKK parts 87

3.1 Introduction 88

3.2 LTW setup and parameters 88

3.2.1 Laser welding machine device 89

3.2.2 Diode laser power source 93

3.2.3 Laser-material interaction tests for PEKK 7002 94

3.2.4 Process parameters for LTW of PEKK 7002 106

3.3 Crystallizing the welded assemblies by annealing 109

3.3.1 Preliminary annealing tests 109

3.3.2 Annealing parameters and process description 112

3.4 Weld joint characterization methods . . . 112
3.4.1 Mechanical tests by single lap shear . . . 112
3.4.2 Weld joint observation by microscopy . . . 114
3.5 PEKK-A/SC assembly weld joint properties . . . 114
3.5.1 Morphological properties . . . 114
3.5.2 Mechanical properties . . . 120
3.6 Synthesis . . . 126

4 Modeling the laser transmission welding process for PEKK parts 127

4.1 Introduction . . . 128
4.2 Models and equations for the LTW of PEKK . . . 129
4.2.1 Thermo-optical model . . . 129
4.2.2 Laser energy absorption in the semi-transparent part . . . 131
4.2.3 Crystallization model for PEKK . . . 132
4.2.4 Model assumptions . . . 133
4.3 Finite difference method and discretizations for the modeling . . . 134
4.3.1 Geometry definition and discretization . . . 134
4.3.2 Discretization of the time domain . . . 135
4.3.3 Heat equation discretization by FDM . . . 136
4.3.4 Crystallization model discretization by FDM . . . 137
4.4 Modeling the LTW of an overlapped configuration . . . 138
4.4.1 Study on the laser irradiation, temperature field and melted zone . . . 141
4.4.2 Study on the crystallinity evolution of the weld joint . . . 144
4.4.3 Predicting the weld joint morphology of PEKK-A2/SC assemblies . . . 147
4.5 Synthesis . . . 153

5 Welding PEKK composite by LTW 155

5.1 Introduction 156
5.2 The PEKK composite material 157
5.2.1 PEKK grade 80/20 157
5.2.2 PEKK-carbon fibers samples 157
5.2.3 Material properties 157
5.3 Welding set-up for PEKK composite 159
5.3.1 Laser-material interaction tests 159
5.3.2 Welding parameters for LTW of PEKK-A/CF 160
5.4 PEKK-A/CF weld joint properties 163
5.4.1 Morphological properties 163
5.4.2 Mechanical properties 169
5.5 Synthesis 171

General conclusion & perspectives **173**

List of publications **181**

Dissemination **183**

French abstract **185**

Appendix A Drying protocol for PEKK 7002 pellets **211**

Appendix B Mass lost tracking when drying PEKK 7002 pellets samples **213**

Bibliography **215**

List of Figures

1.1 Main classification of the welding techniques for thermoplastics [Costa et al., 2012]. 6

1.2 Laser welding types: a) butt-joint and b) laser transmission welding [Mingareev et al., 2012]. 7

1.3 Laser transmission welding (a) principle and (b) basic steps of the process. . 11

1.4 Laser systems identified inside the electromagnetic spectrum by their working wavelengths [Gonçalves et al., 2021]. 13

1.5 LTW techniques: a) simultaneous, b) quasi-simultaneous, c) mask and d) contour welding [Gonçalves et al., 2021]. 14

1.6 Gaussian and top-hat laser beam profiles [Acherjee, 2020]. 20

1.7 Diagram of relative intensity (I/I_o) representing the Light-Matter interaction. Insert indicates the intensity path as function of the absorption ranges on the material depth (reproduced from [Bachmann and Russek, 2002]). 23

1.8 Light scattering on a) amorphous and b) semi-crystalline thermoplastics [Bachmann and Russek, 2002]. 26

1.9 Schematic representation of the formation of a spherulite [Pérez-Martín et al., 2022]. 28

1.10 Schematic representation of the thermal transitions on semi-crystalline thermoplatics [Klein, 2012]. 29

1.11 Chemical structure of (a) PEEK and (b) PEKK. 31

1.12 DSC scans of PEKK (70/30) specimens annealed at different temperatures [Gardner et al., 1992]. 33

1.13 PEKKs crystallization peak time vs temperature [Gardner et al., 1992]. . . . 34

1.14 DSC heating scans after crystallization from melt at 10 $°C.min^{-1}$ of PEKK 8002, 7002 and 6002 [Choupin, 2017]. 35

1.15 Isothermal DSC scans of crystallized PEKK 60/40 from the melt. Isothermal crystallization at 230 °C (solid line) and 210 °C (dashed line) [Choupin et al., 2017]. 39

1.16 DSC thermograms of neat PEKK 7002 crystallized from the melt at 250°C with the fitting of the derivative Hillier model (solid line) and the primary (dash curves) and secondary crystallization (dash-dot curves) modeling [Choupin, 2017]. 42

1.17 Logarithmic plot of the primary (a) and the secondary crystallization (b) rate constants vs temperature for neat PEKK 6002 and 7002 isothermal crystallization from the melt with the Hoffman and Lauritzen model fitting [Choupin, 2017]. 43

1.18 Weight factor of the primary crystallization vs temperature for PEKK 6002 and 7002 isothermal crystallization from the melt with the linear model fitting [Choupin, 2017]. 44

1.19 TTT diagram of the relative crystallinity for the overall crystallization for PEKK 7002 crystallized from the melt [Choupin, 2017]. 45

1.20 Diagram of the decomposition of a non-isothermal crystallization cycle by small isotherms [Choupin, 2017]. 45

1.21 Relative crystallinity X_R against temperature for PEKK 7002 crystallized from the melt at different cooling rates with the modified non-isothermal crystallization kinetics modeling [Choupin, 2017]. 49

1.22 Variation of the crystallization relative content (w_1 and w_2) with cooling rate for non-isothermal crystallization kinetics of PEKK 70/30 [Pérez-Martín et al., 2022]. 50

1.23 Dual Nakamura Model fist to the X_R evolution for non-isothermal crystallization of PEKK 70/30 for different cooling rates [Pérez-Martín et al., 2022]. . . 51

2.1 Variation of the melting and glass transition temperature of PAEK varieties as function of ether/ketone ratio (V) [Friedrich et al., 1995]. 55

2.2 PEEK, PEK and PEKK (T/I = 100) (a) X-ray powder diffraction patterns and (b) unit-cell parameters vs. ketone content [Gardner et al., 1992]. 56

2.3 PEKK chemical structure when combining DPE with (a) terephthalic (T) acid or with (b) isophthalic (I) acid [Hsiao et al., 1994]. 56

2.4 Relationship between the terephthalate content (% T) and the equilibrium melting temperature, as well as the glass transition temperatures [Gardner et al., 1992]. 57

2.5 Crystal unit cells of PEKK 7002: form 1 and form 2 [Gardner et al., 1992]. . 58

2.6 X-ray diffraction patterns of different grades of PEKK when (a) melt crystallized and (b) solvent crystallized [Gardner et al., 1992]. 59

2.7 Phase diagram of PEKK [Gardner et al., 1994]. 59

2.8 PEKK 7002 injected plates of $95 \times 95\ mm^2$: (a) quasi-amorphous (4 and 2 mm thick) and (b) semi-crystalline (2 mm thick). (c) General representation of the injected plate cutting pattern to obtain the samples for welding. 61

2.9 Drying process study on PEKK 7002 pellets. (a) Mass lost evolution over time for three different samples; (b) moisture content evolution in the samples over time (average values). 62

2.10 Injection molding machine. 63

2.11 Mold footprint with the shape of a square plate and thermocouples locations. 67

2.12 Mold temperature evolution during the injection cycle of PEKK-SC plates for a) the 3 monitoring points (TM1, TM2 and TM3), and b) four measurements of TM1 point. Cooling and solidification step indicated between the vertical dashed lines. 67

2.13 DSC 1 Stare System Mettler Toledo. 69

2.14 Typical DSC thermogram of PEKK 7002 a) pellets, b) semi-crystalline plates, c) amorphous plates 2 mm thick and d) amorphous plates 4 mm thick. Exothermic reaction direction goes upwards. 71

2.15 Cold crystallization peaks of PEKK injected samples. 71

2.16 FTIR spectrophotometer Bruker Vertex 70 used for optical characterization of the PEKK injected plates at IMT Mines Albi. 74

2.17 Schematic representation of (a) specular reflection on the surface of a sample and (b) characterization of the diffuse (hemispherical) reflection of a sample with the integration sphere. 75

2.18 Bidirectional and hemispherical reflection spectra of PEKK-A2 (top), PEKK-A4 (middle) and PEKK-SC (bottom) injected plates. 76

2.19 Hemispherical reflection spectra of PEKK 7002 injected plates. 77

2.20 Schematic representation of (a) bidirectional transmission properties characterization and (b) hemispherical transmission on a diffusant material. 78

2.21 Schematic representation of the hemispherical transmission properties characterization with the integration sphere. 78

2.22 Bidirectional and hemispherical transmission spectra of PEKK-A2 (top), PEKK-A4 (middle) and PEKK-SC (bottom) injected plates. 79

2.23 Hemispherical transmission spectra of PEKK 7002 injected plates. 80

2.24 Bidirectional transmission spectra of PEKK-A2 sample. Comparison between a dried and a humid sample. 82

2.25 Same amorphous 2 mm thick circular sample oriented at three different angles. The green arrow indicates the injection direction. 83

2.26 Circular samples extraction from a PEKK-A2 injected plate and their correspondent bidirectional transmission factor characterized. 84

2.27 Qualitative characterization of the laser beam scattering after going through the PEKK-A2 injected plate. 85

3.1 Welding machine ES Weld 200 at LGP-ENIT, exterior visualization with the components indicated by the numbers (1) power supply switch, (2) compressed air pump, (3) laser activation keys panel, (4) screen, (5) control panel, (6) protection door and (7) observation glass. 89

3.2 Working space at the interior of the welding machine ES Weld 200. Components indicated by the numbers (1) laser source, (2) laser focus lens and output, (3) X-Y displacement systems, (4) working platform and (5) clamping glass. . 90

3.3 Schematic representation of the workspace inside the welding machine, showing an assembly between the working platform and the semi-transparent clamping glass: (a) before and (b) after applying the clamping pressure. 92

92figure.caption.85

3.5 Gaussian intensity profile of the laser beam from the welding machine ES Weld 200 characterized experimentally. 93

3.6 LMI tests static conditions on PEKK-SC sample. Different laser powers tested for an irradiation time of (a) 4 s and (b) 2 s. 98

3.7 Irradiated zones from LMI tests in static condition on PEKK-SC sample. Irradiation time = 2s. $P_{\%}$ between 16 and 24 %. 99

3.8 Irradiated zones from LMI tests in static condition on PEKK-A2/SC configuration. Irradiation time = 2 s. $P_{\%}$ between 22 and 29 %. 100

3.9 Irradiated zones from LMI tests in static condition on PEKK-A4/SC configuration. Irradiation time = 2 s. $P_{\%}$ between 22 and 37 %. 100

3.10 LMI tests in dynamic condition with a beam diameter of 2 mm. Tests made on PEKK-SC samples for different scanning speed and $P_{\%} = 20$ %. 101

3.11 LMI tests in dynamic condition with a beam diameter of 2 mm. Tests made for a scanning speed of 1 mm·s^{-1} and different power values on (a) PEKK-SC samples and (b) PEKK-A2/SC overlapped configuration. 102

3.12 LMI tests dynamic conditions on PEKK-A2/SC assembly configuration. Laser powers tested from (a) 52 to 68 % and (b) 69 to 73 %. 104

3.13 LMI tests dynamic conditions on PEKK-A2/SC assembly configuration for the lower laser powers between 53 and 56 %. 104

3.14 Micrographs of the irradiated zones from LMI tests for the pre-welding conditions on PEKK-SC sample. Scanning speed = 60 mm·min^{-1}. $P_{\%}$ = 20 %. Arrow indicates injection direction. 105

3.15 Schematic representation of lap-joint configuration used for welding PEKK-A/PEKK-SC. 107

3.16 Schematic diagram of the melted zone's shape created at the interface when irradiating with (A) dynamic procedure, (B) static and dynamic procedure. . 108

3.17 Typical DSC thermogram of PEKK-A (amorphous) samples. Cold crystallization temperature (T_{cc}) values are indicated in the plot. Heating and cooling ramps at 10 °C·min^{-1}. 110

3.18 Preliminary annealing tests: PEKK-A/SC trial (a) welded assemblies and (b) after annealing. 110

3.19 Mold fabricated for the annealing tests (a) opened and (b) closed. 111

3.20 Single lap shear test on PEKK-A/SC welded assemblies. 113

3.21 Representative micrographs of the weld joints cross-sections along the weld path of the PEKK-A/SC assemblies. 115

3.22 Representative micrograph of the weld joint cross-section with a schematic representation of the different zones inside the weld joint HAZ. The interface location prior to weld is identified by the horizontal dotted line. 115

3.23 Weld joint HAZ layers depths inside the thickness of each bulk sample for each PEKK-A/SC assembly combination. 117

3.24 Weld joint HAZ length plotted against laser power used for welding. 118

3.25 PEKK-A/SC weld joint cross section a) before welding, b) after welding and c) after annealing process. 119

3.26 Weld joints cross-section along the weld path of the crystallized assemblies (PEKK-Ac/SC). 119

120figure.caption.121

121figure.caption.122

3.29 Representative micrographs of the failed weld joint of assemblies failed with CI type for each assembly combination. Visualizations are made at the overlapped zone of the PEKK-SC sample. 122

122figure.caption.124

123figure.caption.125

124figure.caption.126

125figure.caption.127

4.1 Plot of $\alpha(X_c)$ for PEKK injected plates for the study. 132

4.2 Temperature field and melted zone simulated for a high value of spatial discretization ($\Delta x, \Delta y, \Delta z = 0.001$ m) for (a) $\Delta t = 0.2$ s and (b) $\Delta t = 0.002$ s when LTW modeling of PEKK parts. $P_{top} = 100$ W. 135

4.3 (a) Temperature field and (b) melted zone simulated for a high value of $\Delta t = 0.2$ s and a good spatial discretization (Δx and $\Delta y = 0.0002$ m, $\Delta z = 0.0001$ m) when LTW modeling of PEKK parts. $P_{top} = 100$ W. 136

4.4 Schematic representation of the model geometry: (a) overlapped parts and laser beam orientations and (b) boundary conditions at time t = 0s. Dimensions are in millimeters. 139

4.5 Simulated temperature field at the weld joint cross-section perpendicular to the weld path (a) before and (b) after implementing the condition for α. Laser power $P_{top} = 100$ W and irradiation time t = 10 s. 143

4.6 Simulated melted zone at the weld joint cross-section along the weld path obtained after irradiation (t = 20 s) for a laser power P_{top} = (a) 100 W and (b) 20 W. 144

4.7 Simulated crystallinity field at the weld joint cross-section along the weld path obtained after irradiation and cooling (t = 140 s) (a) before and (b) after adding the condition from Equation 4.27 (for $P_{top} = 20$ W). 146

4.8 Simulated crystallinity field at the weld joint cross-section along the weld path obtained after irradiation and cooling (t = 140 s) when using the crystallization model of (a) Choupin, (b) Perez-Martin and (c) Choupin with Perez-Martin parameters. ($P_{top} = 20$ W). 146

4.9 Simulations results: Temperature field on the weld joint at (a) 1s and (b) 20s of irradiation. 149

4.10 Simulations results: (a) weld joint HAZ isovalues of the crystallinity after welding process, along the welding path and at the interface plans, and (b) plots of the temperature and the crystallinity degree over time. 150

4.11 PEKK-A2/SC weld joint morphology at its cross-section along the weld path. Comparison between experimental micrographs and simulated crystallinity fields. 151

4.12 Simulated distribution of the X_c in the thickness of the PEKK-A2/SC assemblies for different laser powers. 152

5.1 Typical DSC thermogram of PEKK-CF injected plates. 158

5.2 Process window for welding PEKK-A/CF by LTW. 160

5.3 Assembly configuration for welding PEKK-A/PEKK-CF. Schematic representation not to scale. 161

5.4 Transmission spectra of PEKK 7002 amorphous injected plates. Vertical line indicates the wavelength of interest at 975 nm. 162

5.5 Laser welding set-up with power transmission. Schematic representation not to scale. 162

5.6 Representation of the weld joint HAZ dimensions on PEKK-A/CF-P1 post-welding assembly. Observation made at the interface through the PEKK-A sample. 163

5.7 Optical micrographs of PEKK-A/CF assemblies welded with P1. 164

5.8 Optical micrographs of of PEKK-A/CF assemblies welded with P2. 164

5.9 Optical micrographs of of PEKK-A/CF assemblies welded with P3. 165

5.10 Optical micrographs of representatives weld-joints HAZ of post-welding assemblies for each weld combination. Observations were made at the weld interface through the PEKK-A sample. Images were treated differently to allow a better visualization of the HAZ. 165

166figure.caption.159

167figure.caption.160

5.13 Weld joint cross-section along the weld path of PEKK-A2/CF-P1 assembly. Observations made with (a) the accurate colors of the samples, (b) at gray scale. 167

5.14 Weld joint cross-section and details of PEKK-A4/CF-P2 assembly. (a) Whole cross-section along the weld path. Details at the borders: (b1) left border, end of the weld; (b2) right border, weld starting point. Details at center: (c1.1) focusing on the cross-section surface, (c1.2) focusing on the cross-section depth. 168

5.15 Micrograph of the weld joint interface line observed in the depth. 169

170figure.caption.164

171figure.caption.165

1 Soudage laser par transmission (a) principe and (b) mécanisme d'interdiffusion macromoléculaire. 186

2 Machine de moulage par injection utilisée pour l'injection de plaques PEKK. 187

3 Temps et température de refroidissement utilisés pour la solidification de la matière PEKK dans le moule. 188

4 (a) Thermogramme typique DSC des plaques injectées en PEKK 7002, (b) pics de cristallisation froide. 189

5 Spectophotomètre utilisé pour la caractérisation optique des échantillons PEKK. 190

6 Spectres de transmission, réflexion et absorption hemisphériques des plaques injectées en PEKK 7002. 191

7 Machine à soudage laser ES Weld 200, visualisation extérieure avec les composants indiqués par les numéros (1) sectionneur général, (2) pompe à air comprimé, (3) panneau de clés d'activation du laser, (4) écran, (5) pupitre commande numérique, (6) porte de protection et (7) vitre d'observation. . . . 193

8 Représentation graphique de la configuration du joint de recouvrement utilisé pour le soudage en LTW du PEKK-A/SC (pas à l'échelle). 194

9 Configuration de soudage à l'intérieur de la machine (représentation graphique, pas à l'échelle). 195

10 Représentation graphique et banc expérimental de l'essai mécanique de cisaillement à recouvrement simple. 195

11 Valeurs de résistance au cisaillement par recouvrement (LSS) obtenues pour les assemblages soudés PEKK-A/SC qui se sont rompus à l'interface et à l'intérieur du joint. 196

12 Coupe transversale du joint de soudure le long du chemin de soudage de l'assemblage PEKK-A4/SC A) avant et B) après le soudage. 197

13 Dimensions de la ZAT du joint de soudure en corrélation avec la puissance du laser utilisé pour effectuer le soudage: (a) longueur et (b) hauteur. 197

14 Moule fabriqué pour le recuit des assemblages soudés : a) fermé et b) ouvert avec les assemblages recuits. 198

15 Coupe transversale du joint de soudure le long du chemin de soudage de l'assemblage PEKK-A4/SC A) avant, B) après le soudage et C) après recuit post-soudage. 199

16 Résistance au cisaillement (LSS) des assemblages PEKK recuits (PEKK-Ac/SC) comparés aux assemblages PEKK non recuits (PEKK-A/SC). 200

17 Représentation schématique de (a) la géométrie du modèle et (b) ses conditions limites. 202

18 Champ de température pendant l'irradiation du laser. 203

19 Champ de cristallinité obtenu après soudage. 204

20 Évolution de la température (T) et de la cristallinité (Xc) du joint pendant le soudage. 204

21 Morphologie du joint soudé. Résultats expérimentaux et numériques. 205

22 Schéma représentant la configuration d'assemblage PEKK-A/CF. 206

23 Fenêtre de soudabilité des pièces PEKK-A/CF. 207

24 Micrographies des joints de soudure des assemblages PEKK-A/CF. 208

25 (a) Longueur et (b) largeur des ZAT des joints de soudure des assemblages PEKK-A/CF. 208

26 Resistance mécanique (LSS) des assemblages PEKK-A/CF. 209

List of Tables

1.1 Laser systems characteristics. *CW = continuous wavelength. 12

1.2 Sample's properties and factors influencing LTW. 17

1.3 Important material properties for LTW. 17

1.4 Differences between PEEK and PEKK copolymers [Maloo et al., 2022]. . . . 31

1.5 Crystallinity Xc (%) for each cooling rate used to crystallize PEKK from melt [Choupin, 2017]. 35

1.6 Avrami's exponent values [Avenet, 2021] 37

1.7 Avrami's crystallinity rate constant values [Avenet, 2021]. 37

1.8 Parameters of the kinetic models for the crystallization rate constants (K_1 and K_2) and the weight factor (w_1) for PEKK 6002 and 7002 crystallized from the melt [Choupin, 2017]. 44

1.9 Crystallization kinetic parameters modified for PEKK 7002 crystallized from the melt [Choupin, 2017]. 48

1.10 Parameters of the non-isothermal crystallization kinetic model for PEKK 7002. (r accounts for the cooling rate in the calculation of w_1) [Pérez-Martín et al., 2022]. U^* from [Choupin et al., 2017]. 51

2.1 Some members of the PAEK family with their chemical structure and ketone contents [Gardner et al., 1992]. 55

2.2 PEKK grades T/I ratios and their diads distribution. 56

2.3 Injection molding machine characteristics. 63

2.4 Screw temperature settings defined for the injection process of PEKK 7002. . 64

2.5 Injection process parameters defined to fabricate the PEKK-A2 plates. 65

2.6 Injection process parameters defined to fabricate the PEKK-A4 plates. 65

2.7 Injection process parameters defined to fabricate the PEKK-SC plates. 65

2.8 Mold temperature and cooling times defined for material solidification after injection. 66

2.9 Maximum and minimum temperatures registered for each point of measurement in the mold at the injection process of PEKK-SC plates. 68

2.10 PEKK injected plates thermal transitions, crystallinity, coloration and thickness. 72

2.11 Thermal properties of PEKK samples. 72

2.12 Optical properties of PEKK samples at the laser wavelength of interest (975nm). 74

2.13 Reflection factors of PEKK injected plates at the wavelength of interest of 975 nm. 76

2.14 Transmission factors of PEKK injected plates at the wavelength of interest of 975 nm. 79

2.15 Absorption factors of PEKK injected plates at the wavelength of interest of 975 nm. 81

2.16 Absorption coefficient α calculated for each sample. 82

2.17 Bidirectional transmission factors obtained for different sample orientation of PEKK-A2 samples. 83

3.1 Output laser power values in watts for some laser power percentages indicated in the G-code of the welding machine. 94

3.2 Welding parameters values and limits imposed by the laser and welding machine used for the study. 94

3.3 Initial operation points for LMI tests on PEKK-SC. 97

3.4 Process window for a suitable LMI on PEKK-SC for an irradiation time of 2 s and a beam diameter of 2 mm. 98

3.5 Process window for a suitable LMI on PEKK-A/SC overlapped configuration for an irradiation time of 2 s and a beam diameter of 2 mm. 101

3.6 Process window for a suitable LMI on PEKK-SC samples and PEKK-A2/SC overlapped configuration for a scanning speed of 1 mm·s^{-1} and a beam diameter of 2 mm. 102

3.7 Process window for a suitable LMI on PEKK-SC samples and PEKK-A2/SC overlapped configuration for a scanning speed of 1 mm·s^{-1} and a beam diameter of 6 mm. 104

3.8 Pre-welding conditions of the samples explored on the LMI tests. 106

3.9 Operation points to achieve LTW of PEKK-A/SC parts with a diode laser of 975 nm. 106

3.10 Assembly combinations for the study 107

3.11 Laser power values used for LTW of PEKK-A/SC 108

3.12 Welding parameters used to LTW PEKK-A/SC injected plates. 109

3.13 Failure types definitions for LTW assemblies tested by SLS. 113

4.1 Summary of the PEKK 7002 injected plates properties. 140

4.2 Welding parameters for LTW modeling. 140

4.3 Parameters of the non-isothermal crystallization kinetic model for PEKK 7002. (r accounts for the cooling rate in the calculation of w_1). 145

4.4 Parameters for the crystallization kinetic model. 147

4.5 Weld joint HAZ depths obtained for 4 laser powers. Comparison between experimental and numerical results. 152

5.1 KEPSTAN®PEKK 8010C30 properties from technical data sheet [Arkema, 2023]. 157

5.2 PEKK injected plates thermal transitions characterized. 158

5.3 Power range (in Watts) that allows material melting at the irradiated zone for a fixed welding speed ($mm{\cdot}s^{-1}$). 160

5.4 Laser power used for LTW. 163

1 Transitions thermiques et degrés de cristallinité des plaques injectées en PEKK 7002 190

2 Facteurs de transmission, réflexion et absorption des plaques injectées en PEKK 7002 192

3 Propriétés thermiques des plaques injectées en PEKK 7002 192

4 Modèles employés pour simuler le soudage laser par transmission des pièces PEKK-A/SC 203

5 Mass of the PEKK pellets samples (in grams and in percentage) for each time monitored. 213

6 Mass lost and moisture content lost in % per drying time. Average values. . . 214

General introduction

Thermoplastic materials are becoming increasingly common in various high-tech industries, such as medical, electronics, automotive and aerospace. Their capacity to be easily reshaped and reformed by heat gives them a high versatility for production and repair. In addition, some thermoplastics have high capabilities, the one called "high-performance thermoplastics". This type of thermoplastics can resist harsh environments, being able to withstand high temperatures without chemical degradation, resist various chemicals, and offer good fracture toughness and abrasion resistance. Moreover, when those thermoplastics are combined with fibers (like carbon or glass), their strength/weight ratio become very interesting. For applications where lightweight with high durability, reliability and safety are essential, high-performance thermoplastics and composites play an important role.

As an example, in the aerospace industry some of the main studied high-performance thermoplastics are the polyetheretherketone (PEEK), since the years 1990 [Brandt et al., 1993], and more recently the polyetherketoneketone (PEKK) [Parlevliet and Weimer, 2011]. These materials have shown withstanding characteristics compatible with the needs of aerospace structures, like high viscosity, high processing temperatures (up to 390°C), excellent mechanical and thermal properties, high chemical resistance, among others. All the last mentioned features make thermoplastics materials (polymers and composites) an attractive choice for parts that require both lightweight properties and high durability.

Another great advantage of thermoplastics is that they can be welded. The fact that their thermo-mechanical properties allow them to soften and melt when heated, make it possible to be joined by fusion. Fusion bonding, or welding, allows to assemble two parts without the use of external components, just by fusion and consolidation of their interface. Assembling parts without the need for mechanical fasteners or adhesives offer major benefits in terms of weight, material, and cost savings when incorporating them into other structures. Different welding techniques exist for fusion bonding thermoplastic materials depending on the technology used to heat the aimed section to be welded. Among all the welding methods, laser transmission welding (LTW) is distinguished by its simplicity, precision, and capacity to create high joint quality. The laser transmission welding (LTW) process uses a near-infrared (NIR) laser to join two overlapping thermoplastic parts. The upper part must be as transparent as possible to the laser irradiation, while the lower part must absorb the laser. The laser beam irradiates and melts the interface of the assembly after passing through the upper part. On cooling, molecular interdiffusion of the polymer chains creates a welded joint.

The effectiveness of the LTW process relay on the thermal and optical properties of the materials to be welded. In one hand, the transparency and absorption properties of the parts to the laser radiation condition the feasibility of the process. In the other hand, the thermal properties of the materials influence their heating and thermal transitions, conditioning the weld joint formation. Additionally, the quality of the LTW assemblies is impacted by the welding parameters. These parameters are conditioned by the laser source technology and by

the welding technique employed to assemble the parts.

Despite its advantages, few works have studied the welding process of high-performance thermoplastic materials by LTW. Especially when it comes to the polyaryletherketone (PAEK) family, which includes the PEEK and PEKK materials. These semi-crystalline polymers require additional care during processing, due to their tendency to crystallize when heated, adding complexity to the laser welding process. Most research on laser transmission welding of PAEK thermoplastics has been conducted on PEEK material. PEKK has gotten less attention due to its novelty in the market. However, compared to PEEK, PEKK shows greater potential for the LTW process due to unique crystallization properties. The crystallization kinetics of PEKK can be modified, which provides for better control of its crystallinity by manipulating the processing parameters.

This project was launched thanks to a collaboration between three french laboratories: the Laboratoire Génie de Production (LGP) (EA1905) at École Nationale d'Ingénieurs de Tarbes (ENIT-INPT), the Centre d'Enseignement de Recherche et d'Innovation Matériaux et Procédés (CERI-MP) at IMT Nord Europe engineering school, and the Institut Clement Ader (ICA) (CNRS UMR 5312) at IMT Mines Albi engineering school, France. The project received funding from the Occitanie Region, France and from IMT Nord Europe. The research work of this project was carried out in the three laboratories mentioned above. Different methods and resources were provided by each laboratory to carry out the thesis work in the best conditions. Arkema company, France, supplied the PEKK polymer bulk material and the PEKK composite samples for the study.

This PhD thesis focuses on studying the laser transmission welding (LTW) process of PEKK material. The main objective of this project is to predict the weld joint properties according to material properties, welding parameters, and thermal history during welding, for PEKK parts joined by laser transmission welding. Several objectives are also breakdown to accomplish the main objective:

- To validate the suitability of PEKK grade 7002 material for LTW.
- To define the optimal welding parameters for PEKK parts (polymer and composite).
- To establish the relationship between material properties and welding parameters with the weld joint morphology and mechanical properties.
- To improve the weld joint quality by post-welding heat treatments (annealing).
- To predict the weld joint morphology with numerical simulations.

To achieve the thesis scopes, experimental and numerical approaches are employed. The experimental work will investigate the influence of welding parameters and material properties on weld joint morphology and strength. The numerical simulations approach will focus on simulating the welding process to predict the weld joint development. For that, numerical models will be validated with the experimental results. The thesis is organized as follows:

Chapter 1: establishes a context on the laser transmission welding (LTW) process as a key technique for joining thermoplastic parts. The chapter begins with an introduction on

LTW of thermoplastics, presenting its advantages, disadvantages and existent applications. Then, the fundamentals of LTW are explained, including the working principle, laser technologies, and process variants. The material properties influencing the welding process, and the welding parameters influence on the weld joint quality are also detailed. Furthermore, the physical phenomena that take part on LTW due to material properties and process parameters are presented and explained. This allows to introduce the relevant laws and equations governing the welding process. Special attention is put on the LTW process for semi-crystalline thermoplastics. Explaining how the crystalline structure impacts the welding process, and how the welding process can affect this structure. Finally, the chapter focuses on LTW of polyaryletherketone (PAEK) polymers, highlighting research made on PEEK and PEKK. Emphasis is put on the unique crystallization mechanisms and kinetics of PEKK, which are essential to understand its behavior during LTW.

Chapter 2: focuses on the material of study, the PEKK thermoplastic material. First, an overview of the welded material is presented, describing the generalities and characteristics of PEKK. Then, the manufacturing process of the PEKK samples is detailed with its methods and parameters. The parameters defined to obtain the two different crystalline states on the PEKK samples (quasi-amorphous and semi-crystalline), are explained. Afterwards, the properties of the samples relevant for LTW process are characterized. These properties include the samples degree of crystallinity, thermal transitions, heat conductivity, heat capacity, and transmission, reflection and absorption properties. The methods and protocols used for the characterization are presented, and the resulting properties are described and analyzed. Most of the obtained properties are correlated with the crystalline state of the PEKK samples.

Chapter 3: presents the laser transmission welding experimental tests made on PEKK samples. The laser welding machine used for the project is presented, with its components, characteristics and capabilities. The main component of the machine, the laser power source, is presented in detail, with its characteristics and capabilities. Then, the studies made on the PEKK samples laser-material interaction are described and detailed, and the process window for achieving welding on PEKK amorphous/semi-crystalline configuration is defined. Subsequently, the process parameters employed and studied for the welding of PEKK parts are revealed. The annealing thermal treatment that some welded assemblies undergone post-welding is described with the parameters and protocol. The methods for assessing the weld joint quality are described: single-lap shear tests and weld joint observations by microscopy. At the end, the results obtained on welded joint mechanical and morphological properties are presented and analyzed. The weld joint properties are correlated with the welding parameters. Additionally, the properties of the just-welded and post-annealed joints are compared, this to validate the improvement on the joint quality when annealed after welding.

Chapter 4: describes the procedure for modelling the LTW process of PEKK parts in MatLab. Initially, the equations and models used to simulate the LTW process of PEKK parts are presented and narrowed for the studied material. The assumptions made for the modelling are included and explained. Then, the finite differences method used to solve the equations is presented, including the discretization made for the studied model on the geometry and time, and for the heat transfer and crystallization equations. Subsequently, the

first simulations developed to study the laser irradiation, temperature field, melted zone and crystallinity evolution of the weld joint, are presented. The modifications and adaptations included to the simulations along the modelling are also explained on each study. At the end, the final model obtained and the results on predicting the weld joint morphology of PEKK-A2/SC assembly are presented and analyzed. Those results are also compared with the experimental ones.

Chapter 5: the last chapter outlines the laser transmission welding study made on PEKK composite parts reinforced with short carbon fibers. An introduction of the PEKK matrix used on the composite, as well as for the PEKK composite samples, including their characteristics and basic properties, is made. Then, the process window obtained from the laser-material interaction tests made on PEKK amorphous/composite parts is detailed. Process parameters chosen for welding and for studying are presented. Finally, the results obtained on weld joint morphology and mechanical properties are shown and analyzed.

Chapter 1

State of art on laser transmission welding of thermoplastic parts

Contents

1.1 Laser transmission welding (LTW) of polymers 6
1.1.1 Fundamentals of laser transmission welding 10
1.1.2 Laser technologies 12
1.1.3 LTW techniques 13
1.1.4 Material properties influencing LTW 16
1.1.5 Laser welding parameters and their influence on weld quality 19
1.2 Physical phenomena involved during LTW 23
1.2.1 Light-Matter interaction 23
1.2.2 Laser intensity and heat generation 26
1.2.3 Heat transfer at the interface 26
1.3 LTW of semi-crystalline thermoplastics and composites 27
1.3.1 Characteristics of semi-crystalline thermoplastics 27
1.3.2 Crystalline structure and its impact on LTW 29
1.3.3 Laser irradiation impact on the crystalline structure 30
1.4 LTW on poly(aryletherketone)s (PAEKs) 31
1.4.1 Crystallization mechanisms of PEKK thermoplastic 33
1.4.2 PEKK crystallization kinetics models 35
1.5 Synthesis 52

1.1 Laser transmission welding (LTW) of polymers

Nowadays, polymers play a crucial role in society because of their many uses and versatility. They are widely used in various daily life items and are essential for a wide range of applications in many fields of industry, research, and technology [Namazi, 2017]. In the industrial field, polymers have become important industrial materials used mostly for packaging, but also in electronics, automotive, and aerospace. For example, in the aerospace industry, high-performance polymers have enabled the production of robust, lightweight components that can withstand harsh environments, increasing performance and fuel efficiency. Because of their integration into those fields, polymers significantly contribute to the advancement of material science and technology.

In this context, thermoplastic polymers (and their composites) have gained recognition over thermosets and elastomers. The ability of thermoplastics to be molded and remolded makes them ideal for creating a wide array of everyday objects, as well as for the industry. Because of that, their use is increasing considerably in our society, leading to the development of new joining techniques to improve the final product. Welding is one of these new joining techniques that is acquiring relevance on the industry, particularly for the emerging structural application of these materials [Stokes, 1989].

Welding, also known as fusion bonding, is the process of assembling two polymer parts by fusion and consolidation of their interface [Avenet, 2021]. It involves surface preparation (if necessary), heating and melting the polymers on the joint surface (interface) of the parts; physically causing polymer chains to inter-diffuse (by pressing the surfaces together), and cooling for the polymers to solidify and consolidate. During welding, the polymer chains blend across the assembly interface which generates the disappearance of the joint surfaces, developing the ability to transfer loads through the welded zone. Using welding as joining technique for assembling thermoplastics and their composites can reduce overall manufacturing costs and is expected to replace traditional joining and assembly methods such as adhesive bonding and mechanical fastening [Yousefpour et al., 2004].

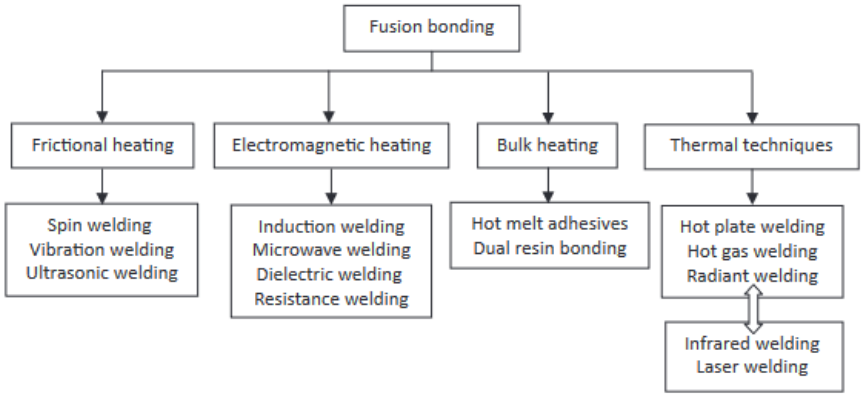

Figure 1.1: Main classification of the welding techniques for thermoplastics [Costa et al., 2012].

Many welding techniques exist for fusion joining thermoplastic polymers and their composites, as shown in the diagram of Figure 1.1. These techniques are commonly classified according to the technology used to heat the interface. *Ageorges et al., 2001* [Ageorges et al., 2001] established a broad classification of the welding techniques into four classes: bulk heating, frictional heating, elecromagnetic heating and two-stage techniques, also called thermal techniques by *Costa et al., 2012* [Costa et al., 2012]. Inside the thermal techniques, we can find the "radiant welding" where the "laser welding" is positioned. Some thermal welding techniques are considered as "two-stage" techniques because of the two phases needed to achieve joining: 1) an external heating stage where an external heating source applies heat directly at the surfaces of the bonding parts to melt the polymer; 2) a forging stage, where the heat source is removed to put in contact the bonding surfaces under forging pressure [Yousefpour et al., 2004]. Nevertheless, in laser welding, both stages can happen simultaneously, thanks to the used technology.

Laser welding consist in using the laser beam radiation (in the infrared (IR) or near-infrared (NIR) spectra), and transform this electro-magnetic energy into heat energy to melt the materials at the joining area (joint interface). All of which occurs spatially and on a timely basis defined within the joining area [Russek et al., 2003]. Two varieties of laser welding exist, as shown in Figure 1.2: butt joint [Atanasov, 1995, Potente and Becker, 1999] and laser transmission welding (LTW) [Nakamata, 1987, Potente et al., 1999]. Butt joint allows the welding of two parts arranged side by side, by focusing the beam on the external surfaces and irradiating their interconnection line. Laser transmission welding consist on welding the parts in an overlapped configuration, where the upper part is semi-transparent to the laser beam, so the interface of the joining parts can be irradiated.

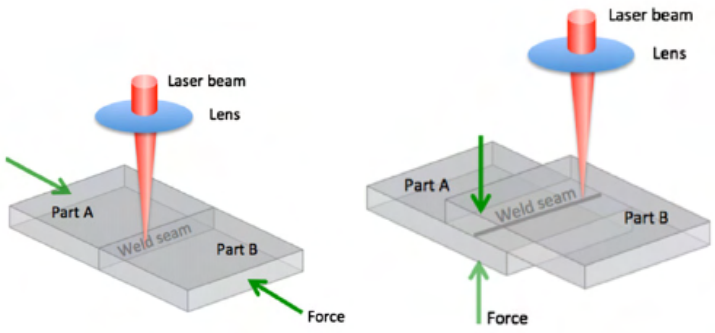

(a) (b)

Figure 1.2: Laser welding types: a) butt-joint and b) laser transmission welding [Mingareev et al., 2012].

In laser butt joining (Figure 1.2a) the polymer parts are placed side by side, assuring that the surfaces to be welded are in contact. The laser beam is focused on the external surfaces at their interconnection line and irradiates the whole joint interface. Then, both polymer parts melt at the entire butt joint area, and are pushed towards each other to ensure welding. The plastified or melted volume generated and the joining energy necessary for welding are higher

than for LTW. As a result, precise positioning of the parts to be welded becomes increasingly important. Butt welding is typically used to weld polymer pipes and shafts.

Butt welding is more popular for laser welding applications on metal than on polymers. This is due to the unique properties of polymers compared to metals, which poses significant challenges. Despite various experimental demonstrations under specific material configurations and laser wavelengths [Balkan et al., 2008, Casalino and Ghorbel, 2008, Mingareev et al., 2012, Nakhaei et al., 2013], butt welding is found to be unsatisfactory for laser polymer welding. *Casalino et Ghorbel* [Casalino and Ghorbel, 2008] concluded that this laser welding variety is not the ideal configuration for joining thermoplastics. Whereas *Amanat et al.* [Amanat et al., 2010] indicated that this technique is more suitable for highly heat-resistant thermoplastics.

Extensive research by several groups involved in laser polymer welding has consistently favored the overlap weld configuration (Figure 1.2b), the one called the laser transmission welding variety (LTW). Unlike butt welding, LTW provides grated manageability, control and a broader range of configurations and applications [Bachmann and Russek, 2002]. Properly executed and respecting materials compatibility and suitability for laser welding, LTW can yields to a robust and aesthetically pleasing seam that is nearly imperceptible, with minimal thermal impact on the product. Laser transmission welding technique was patented by Hideo Nakamata in 1987. *Nakamata* [Nakamata, 1987] described this welding technique as "a process for joining different kinds of synthetic resins to each other [...] using the heat of a laser beam [...] in which the second kind of synthetic resin transmits the laser beam to the first kind of synthetic resin, which stores up heat of the laser beam".

Advantages of LTW:

- Non-contact process [Russek et al., 2003]: "the joining energy is fed into the joining area without being in direct contact with this area . This avoids mechanical stress and thermal load on the joining partners."
- Clean, non-contaminant, and non destructive [Russek et al., 2003]: "during the welding process no vibration, no thermal stress, no particle release takes place."
- Reliable: The energy supply can be very well defined, by means of the interaction time and the irradiated zone.
- Locally restricted energy input: the energy input is well restricted to the interface, to the desired zone of welding between the parts.
- Fast [Coelho et al., 2000]: welding can be achieved by using high speeds of several meters per second (depending on the material to be welded). This can make the process competitive for industrial applications.
- Flexible: different process strategies are available and can be selected of adapted according to the product shape and weld needs.

- Easy to control and automated [Russek, 2001]: welding technology shows excellent integration abilities and automation potentials.
- High quality weld seams can be obtained: hermetic sealing and good optical appearance.
- Low workplace pollution: compared to other welding technologies, the pollution generated in the workplace is minimal.
- High reproducibility is possible to achieve.
- Possibility to weld different kind of thermoplastics: amorphous, crystalline and dissimilar polymers and thermoplastic elastomers are weldable [Russek, 2001].
- Suited for joining 3D weld contours.
- Process stability.

Disadvantages or limitations of LTW [Acherjee, 2020, Acherjee, 2021b]:

- High intensity of laser beam, that can lead to material burning (decomposition).
- Limited constraints on the geometry and size of the components to be weld.
- Requires a high initial investment for laser equipment.
- The process is reliant on the optical properties of the polymers.
- A close and good contact between the mating parts is required, because the process relies on the conduction between these parts.
- Part thickness limitation for semi-crystalline thermoplastics.

Existent applications of LTW

- *Bachmann et al.* indicated that "one of the very first industrial applications of the diode laser for polymer welding is the hermetic seal of the electronic car key" [Bachmann et al., 2000].
- Laser welding of thermoplastics has been applied in the automotive industry since 2000 [Gillner et al., 2000].
- *Coelho et al.* specified the high use and applications of laser welding of plastics on the packaging industry [Coelho et al., 2000].
- In 2001 *Adeb et al.* talked about the already existing applications of this technology. Used already for industrial series production in different industries. Giving as example the automobile and the packaging sector [Abed et al., 2001].
- Others fields are mentioned by *Russek et al.*: information and communication technologies, packaging technologies, automotive industry, electrical and electronic industries, medical technologies, micro technologies and chemistry, house hold goods [Russek, 2001].

1.1.1 Fundamentals of laser transmission welding

The first description of the laser transmission welding process steps are defined in the patent made by *Hideo Nakamata* [Nakamata, 1987]. In his patent he indicates the following:

1. Two synthetic resins are needed for the process:
   - A first kind that will be able to store up the heat from the laser beam, placed at the lower position.
   - A second kind that will be able to transmit the laser beam, placed over the first one, at the upper position.
2. The second contact surface of the second kind of synthetic resin is set on the first contact surface of the first kind of synthetic resin.
3. The outer surface of the upper-synthetic resin is exposed to the laser beam.
4. The upper-synthetic resin transmits the laser beam to the lower-synthetic resin.
5. The lower-synthetic resin stores up the heat of the laser beam.
6. By means of heat conduction, the contact surface of the upper-synthetic resin is heated.
7. The surfaces of the synthetic resins that were put in contact are melted by the heat of the laser beam.
8. A plurality of projections and a plurality of recesses are formed on both contact surfaces.
9. A plurality of projections of the lower-synthetic resin engage with a plurality of the recesses of the upper-synthetic resin.
10. A downward compressive force is applied to the outsides of the synthetic resins to press them together while being exposed to the laser beam irradiation.
11. The assembly is also cooled while being in contact, or after exposure, leaving the plurality of the projections of the lower-synthetic resin contact surface to engage securely with the plurality of recesses of the upper-synthetic resin contact surface, and vice-versa.
12. Therefore, one kind of synthetic resin is securely joined to the other kind of synthetic resin.

As thus indicated by *Hideo Nakamata*, LTW process operates with an overlap configuration of the thermoplastic parts to be welded. The principle of the laser transmission welding process is schematized in Figure 1a. For LTW to work, the upper-part must be semi-transparent to the laser beam wavelength, so the laser can go through it and irradiate the assembly's interface. Then, the bottom-one must be absorbent, whether in the surface or in volume, so the laser energy can be absorbed at the interface. Also, both parts must be in close contact at their interfaces so that the polymer chains can inter-diffuse between

them and achieve welding. This close contact must also be maintained until cooling and re-solidification.

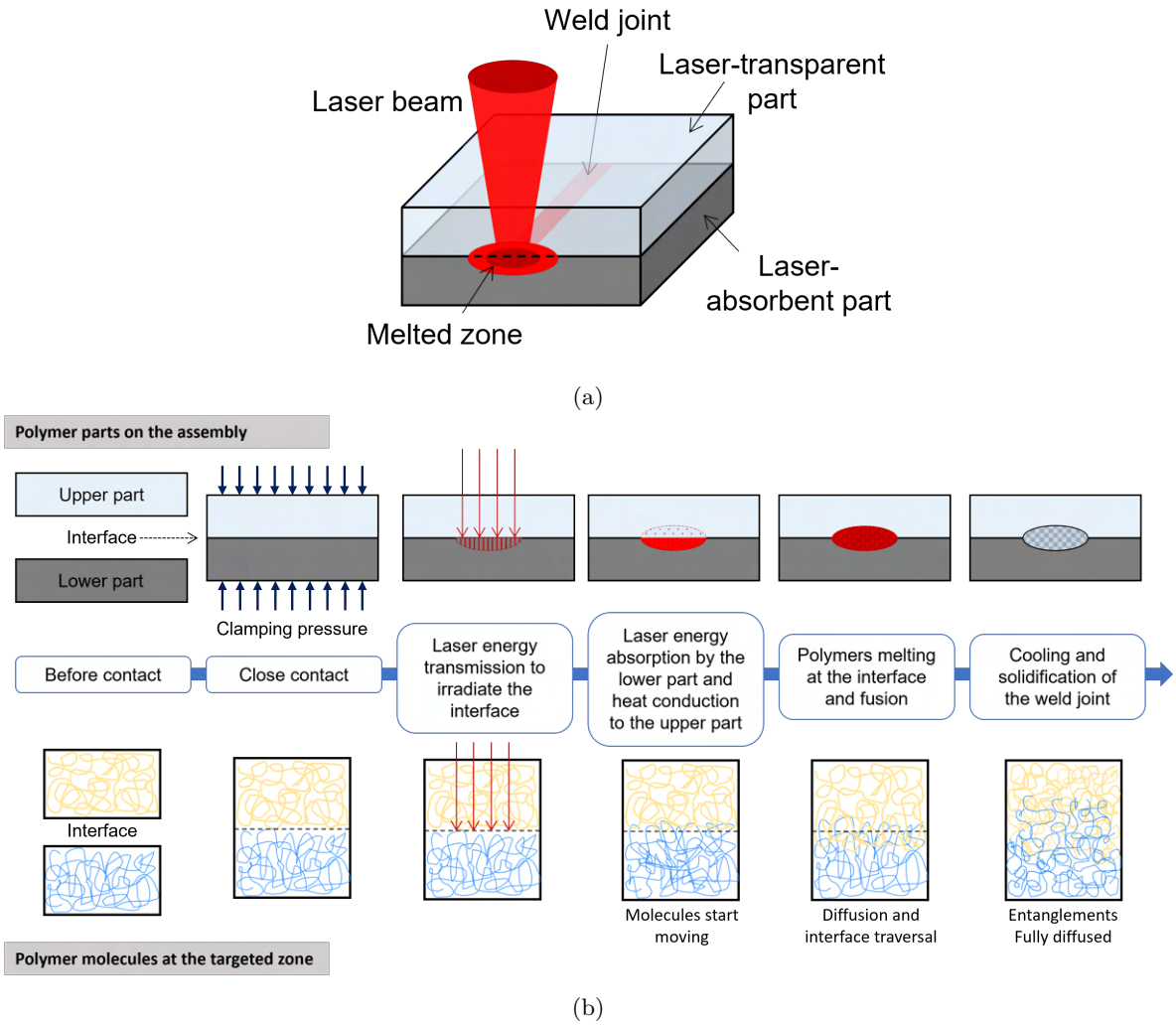

Figure 1.3: Laser transmission welding (a) principle and (b) basic steps of the process.

Figure 1.3b describes the basic steps of the LTW process with the parts of the assembly, and the interaction of the macromolecules in the target zone for welding. To begin the welding process the parts are superposed to each other, and their contact surfaces create what is called the "interface" of the assembly. Then, clamping force is applied to maintain adequate contact pressure between the parts at the interface. The laser beam is thus projected on the top surface of the upper part, normal to the interface. The laser energy will enter the upper part and go through it to stroke and irradiate the interface of the assembly. At the interface, the energy of the laser is absorbed by the bottom-part and is transformed into heat. This heat propagates at the interface from the bottom to the upper part by means of heat condition. Therefore, a portion of the absorbed energy is transferred to the semi-transparent part. Both

parts will start heating at the interface, then softening and melting as their temperature reaches their respective glass-transition temperature (T_g) for amorphous thermoplastics, or melting temperature (T_m) for semi-crystalline ones. While heating the molecular chains of polymers in the contact region will start moving. Then, molecular diffusion and interface traversal take place at the molten interface. Hence, with both polymers softened or melted at the interface, the welding between the two polymer parts is produced by material fusion. The molten polymer at the joint interface solidifies when cooling, allowing the formation of the weld joint.

1.1.2 Laser technologies

Different type of laser technologies, or systems, are used for welding thermoplastic materials: Co_2, fiber, Nd:YAG and diode lasers. The laser type differs in type of laser used, active medium, wavelength, maximum output power, efficiency and beam quality. These characteristics material weldability, welding process parameters and joint quality for the LTW process. The choose of laser type is thus of importance on LTW to obtain a reliable weld joint. Table 1.1 presents a comparison of these laser systems. Also, the type of laser system can be identified in the electromagnetic spectrum by their different ranges of working wavelengths, as shown in Figure 1.4.

Laser system	**Co_2**	**Nd:YAG**	**Fiber**	**Diode**
Type of laser	Gas	Solid-state	Solid-state	Semiconductor
Active medium	Mixture of CO_2, N_2 and He	Yttrium Aluminium Garnet	Silica fiber doped with rare-earth elements	P-N junction diode
Wavelength (nm)	10 600	1 064	1 000 - 2 100	405 - 1 940
Max. CW* out put power (kW)	50	5	100	45
Efficiency (%)	5 - 10	3 - 5	20 - 50	30 - 60
Beam quality	High	High	High	Low

Table 1.1: Laser systems characteristics. *CW = continuous wavelength.

The Co_2 laser was the first laser used for welding polymers for the first time in 1970 [Silvus Jr and Wachtell, 1970]. These type of laser system works in a wavelength of 10 600 nm. At this wavelength, most polymers absorb the irradiation within a small depth of the material [Acherjee, 2020]. Thus, the parts thickness are limited to less than 0.5 mm when welding thermoplastics with CO_2 lasers. Nevertheless, these lasers are typically used for welding flexible polymer thin films, such as in the packaging industries.

Nd:YAG are solid state lasers operating at 1 064 nm wavelength. They can pass through uncolored thermoplastics over several millimeters thickness, allowing the LTW process. These lasers are mostly used for high precision welding, thanks to their superior beam quality which enables to produce very small spot sizes. However, they are now rarely used for LTW.

Fiber lasers are regarded as an alternative to Nd:YAG lasers: they have an equal beam quality with superior electro-optical efficiency, and they operate in the same wavelength withing a wider range (between 1 000 and 2 100 nm). These type of lasers are mainly used for precision welding, and for welding films, sheets, molded parts and fabrics. For wavelengths higher than 1 400 nm, fiber lasers are used for LTW without additives, taking advantage of the natural absorption properties of some polymers at these high wavelengths.

The last laser type is the diode laser. Operating in wavelengths from 405 to 1 940 nm, diode lasers have the higher efficiency for the irradiation process generation. Also, the power of the diode laser can be controlled very accurately, compared to the pulsed Nd:YAG [Bachmann et al., 2000]. They are also compact, efficient, flexible, and inexpensive, make them a good concurrent for the other laser types and very convenient for industrial applications. On the other hand, they have poor beam quality compared to Nd:YAG and fiber lasers, resulting in larger laser spot sizes, increasing the difficulty to obtain sharply precision welding.

Diode lasers are mostly used in the near-infrared (NIR) spectral region, with different wavelengths between 808 and 980 nm [Gonçalves et al., 2021]. This ability to be available in a variety of radiation wavelengths make them ideal for welding a variety of thermoplastics. These type of lasers are the most used for LTW, with high quantity of studies found within the different wavelengths and laser powers [Gonçalves et al., 2021].

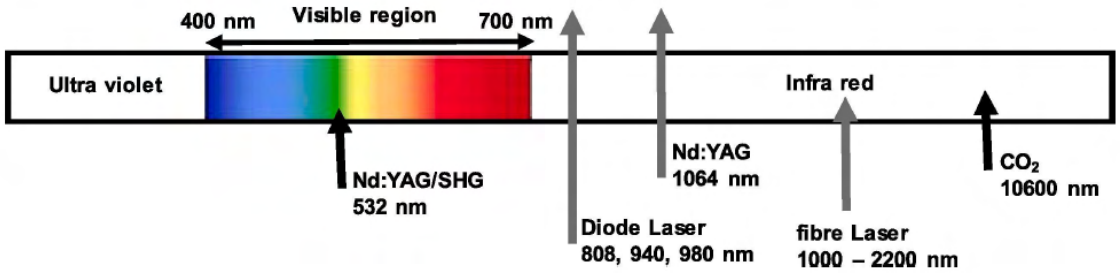

Figure 1.4: Laser systems identified inside the electromagnetic spectrum by their working wavelengths [Gonçalves et al., 2021].

1.1.3 LTW techniques

LTW has different process variants, or techniques, that differ on the irradiation strategies, the cycle times and the process flexibility. Each technique is chosen depending on the assembly requirements and specifications: the size and complexity of the parts and zones to irradiate, as well as the volume of production. These LTW techniques are simultaneous, quasi-simultaneous, mask and contour welding (Figure 1.5).

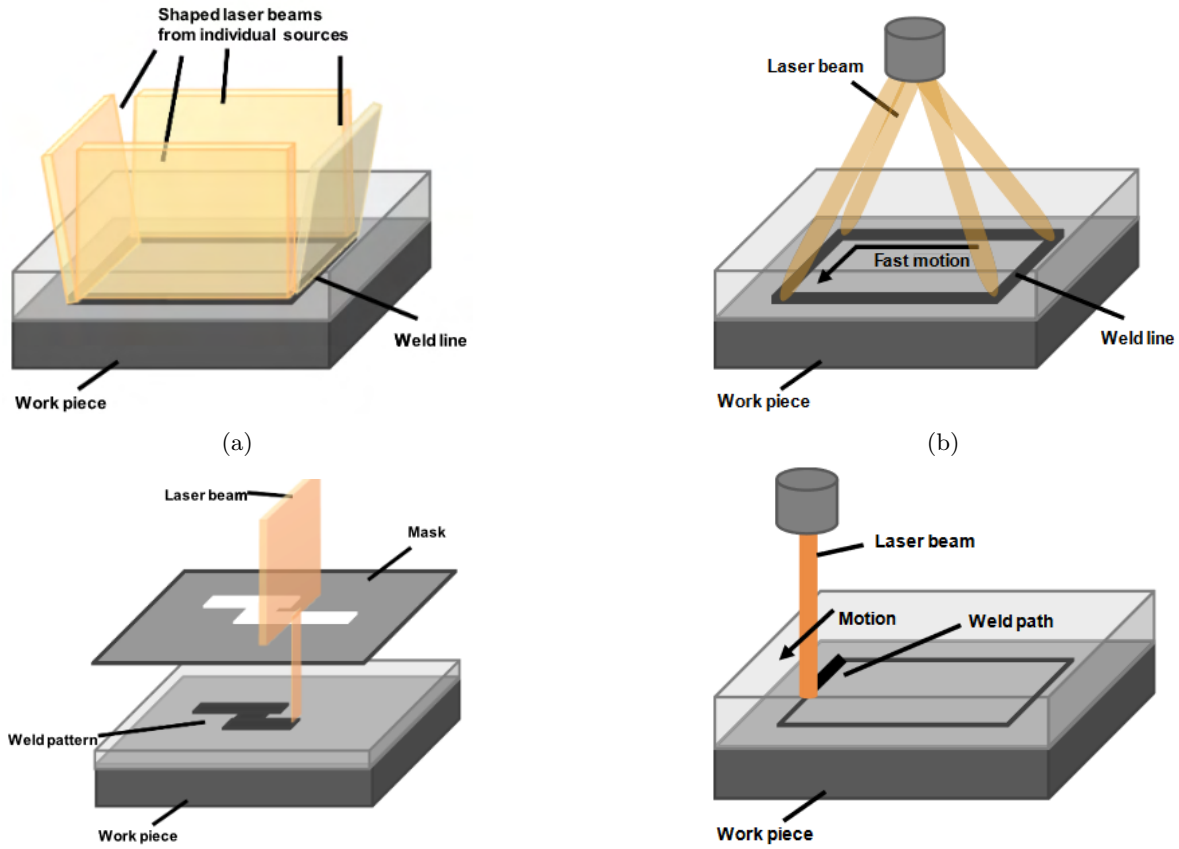

Figure 1.5: LTW techniques: a) simultaneous, b) quasi-simultaneous, c) mask and d) contour welding [Gonçalves et al., 2021].

Simultaneous welding

Laser simultaneous welding is a technique that uses an arrangement of a series of high-power diode lasers to irradiate the whole weld seam contour in a single, brief exposure. This configuration, detailed by Bachmann [Bachmann and Russek, 2002] and Russek et al. [Russek et al., 2003], enables the entire contour to be irradiated and welded at once, which decreases the process times and provides a larger process window. The diode lasers are positioned compactly and modularly to ensure homogeneous irradiation, which is critical for maintaining constant welding quality. This technology avoids the need for dynamic motion systems because the workpiece remains stationary when welding [Acherjee, 2020].

One of the primary challenges in laser simultaneous welding is obtaining a homogenous intensity distribution to minimize overlapping beam areas and non-irradiated zones, which can result in uneven melting or incomplete welds [Acherjee, 2021b]. Proper beam formation and guiding are required to ensure that the entire weld zone is evenly heated. This process is noted for its speed and ability to handle higher tolerances because the temperature rise is homogeneous across the whole weld contour, resulting in constant melting and bonding under

applied pressure. However, it is more complex and expensive than contour welding, with less adaptability to various weld geometries.

Quasi-simultaneous welding

Laser quasi-simultaneous welding uses high-speed laser scanning and galvo mirrors to produce a homogeneous weld comparable to simultaneous welding. A concentrated laser beam scans the weld seam many times using a preset path [Bachmann and Russek, 2002]. The *trick* is to employ adequate laser power and fast scanning speeds to preserve the heat created, preventing re-solidification and keeping the entire weld seam softened.

According to *Russek et al.* [Russek et al., 2003], this method involves repeatedly passing the laser beam over the weld contour within a narrow scanning field, gradually rising the temperature of the weld interface. Due to poor thermal conductivity of polymers (typically in the range of 0.1 to 1 $W{\cdot}m^{-1}K^{-1}$, which is 3 to 4 orders of magnitude lower than the values observed in metals e.g. for Cu $\lambda \approx 10^3$ $W{\cdot}m^{-1}K^{-1}$ [Bachmann and Russek, 2002]), heat increases progressively and uniformly, causing the entire weld seam to melt practically simultaneously [Acherjee, 2020]. The high scanning speed is critical for avoiding heat loss and guaranteeing constant melting, preventing the polymer from re-solidifying throughout the welding process [Acherjee, 2021b]. This approach is particularly successful for producing high-quality welds while maintaining exact control over the welding conditions.

Laser mask welding

Laser mask welding is a precise technique in which a mask that fits the intended weld pattern is placed between the laser source and the workpiece. This mask shields areas that should not be exposed to laser radiation, only enabling specific zones to be irradiated [Bachmann and Russek, 2002]. This approach is very useful for producing small seams of roughly 100 microns and complicated seam designs, making it perfect for usage in microtechnology, biology, and life sciences [Russek et al., 2003].

The mask, which generally consists of sheet metal, is placed between the laser output lens and the target specimens to ensure that the laser beam only hits the exposed surfaces. This selective exposure can be accomplished using either line irradiation or simultaneous scanning [Acherjee, 2020]. While the mask effectively modifies the laser beam to adapt to complex weld patterns, it also blocks some laser irradiation, reducing overall welding efficiency [Acherjee, 2021b]. Despite this, laser mask welding remains a highly controlled and precise welding technique for specialized applications.

Contour welding

Laser contour welding, also known as vector welding, is a popular and adaptable way to join thermoplastics. In this process, a laser beam passes across the interface of the materials to be welded at a set pace, often controlled by an XY-handling system or a robot [Bachmann and Russek, 2002]. The pieces remain motionless throughout the welding operation. Diode or Nd:YAG lasers are commonly utilized, with power levels of 10 to 100 W and welding rates of 2 to 5 m/min [Russek et al., 2003]. However, speeds can sometimes reach up to 25 m/min.

Laser contour welding is very useful for long and complex 3D seam geometries because the laser can cover the weld seam geometry in a precise sequence [Acherjee, 2020]. Its versatility and ease of use make it a popular choice for a variety of applications that require high-quality welds with minimal thermal damage to the surrounding materials. This process is simple, adaptable, and inexpensive, making it one of the most popular laser welding procedures in both research and industry. The laser beam focuses on the joining area, causing localized heating and melting that results in a strong weld. Achieving optimal weld strength requires careful calibration of welding parameters such as laser power, welding speed, beam diameter, and clamp pressure [Acherjee, 2021b].

1.1.4 Material properties influencing LTW

Laser transmission welding involves different mechanisms related to the light-matter interaction. Those mechanisms include: light transmission and absorption, heat conduction, polymer softening, melting, blending and re-solidification. Therefore, this welding process relies strongly on the thermo-optical relationship between the laser beam and the target material. The composition, thermal and optical properties of the polymers used are one of the most significant variables influencing the LTW process [Acherjee, 2021b]. It is important to properly assess the optical and physical properties of the materials for the functionality of LTW. Special care must also be consecrated to the composition and condition of the parts to be welded, because they determine the material properties. Table 1.2 summarizes the properties and pre-welding conditions of the parts to be welded that are required to known and master for effective design and manufacture of laser transmission welded polymer parts. The material properties are further breakdown in Table 1.3.

The composition and type of micro-structure of the thermoplastic parts is one of the principal factors to take into account for LTW. This factor can be a determinant of all the other material properties. A thermoplastic part in its natural state have intrinsic material properties that can be modified if some kind of additives is included in it. Additives like colorants, fibers, reinforcements, mineral fillers, etc. Also, a semi-crystalline thermoplastic can acquire different material properties depending on its degree of crystallinity (point that will be better explained and developed in Section 1.3.1).

The optical properties of the polymers to be welded highly affect the laser transmission welding process. The materials should ensure laser transmission and absorption. For that, the polymers parts must have different optical properties: the upper-part should be semi-transparent, while the lower-one must be absorbent, this to the wavelength of the laser beam used. Reflection and scattering properties are also important for the welding process. Reflection properties are more related to the light reflection at the surface of the sample. This can cause energy loss before the laser beam enters the material. Then, scattering effects take place at the interior of the material, on the sample's thickness. Scattering induces the deflection of the incoming laser irradiation while going through the material, which generates a distribution of the laser power. If the semi-transparent part scatters the light, the laser spot diameter may increase at the joining interface [Bachmann and Russek, 2002], compared to

the initial spot size that irradiates the upper surface of the upper-part. If the lower absorbent part scatters the light, lower absorption of the laser beam energy can be generated.

Material properties	**Pre-welding conditions**
Type of microstructure and composition	Part thickness
Optical	Surface quality/conditions
Thermo-physical	Moisture content
Mechanical	Part gaps

Table 1.2: Sample's properties and factors influencing LTW.

Type of microstructure and/or composition	**Optical**	**Thermo-physical**	**Mechanical**
1. Degree of crystallinity	1. Transmissivity	1. Thermal transitions	1. Yield strength
2. Additives	2. Absorptivity	- Glass transition temperature (for amorphous polymers)	2. Ultimate strength
- Type and weight	3. Reflectivity	- Melting point or range (for semi-crystalline polymers)	
- Shape and size	4. Scattering	- Melt and cold crystallization temperatures	
		- Degradation temperature	
		2. Thermal conductivity	
		3. Specific heat	
		4. Diffusivity	
		5. Thermal expansion	
		6. Density	

Table 1.3: Important material properties for LTW.

The samples thermo-physical properties influence the weld formation. After the laser energy is transmitted by the upper part and absorbed by the lower one, it will be converted into heat to allow polymer softening and melting at the interface. This can only be achieved with the proper thermal properties. The materials must be sufficiently conductive to allow the heat to be conducted from the absorbent to the semi-transparent part and heat the interface. Then, the thermal transitions condition the temperatures to achieve and maintain at the

interface. During welding, the interface must reach the softening or melting temperature, and avoid to reach the degradation temperature. Thus, both polymers must share their melting and degradation ranges. When welding semi-crystalline thermoplastics, if crystallinity is intended to be achieved at the weld joint, the temperatures must stay at the crystallization range for a period of time determined by the crystallization kinetics of the material. Thus, to achieve weld joint formation, the materials to be joined must be chemically compatible, and they should not differ significantly in their melting ranges.

Mechanical properties of the base materials are important for LTW to have an estimation of the weld joint mechanical resistance. Good mechanical properties on the bulk materials expect to produce strong assemblies. The pre-welding conditions of the samples are also important for LTW. Moisture content, surface quality, part thickness and part gaps are some pre-welding conditions of relevance. These conditions have an influence on the physical properties of the samples, as well as on the performance of the final weld joint.

The thickness of the polymer parts affects their optical properties (especially for semi-crystalline ones). The thickness of the semi-transparent part has great effect on the energy density and laser beam width that reaches the joint interface [Gonçalves et al., 2021]. To evaluate the effect of the part thickness on the LTW process, measurements of laser transmission and absorption through the part are often made at the wavelength of the used laser beam. For amorphous thermoplastics, the part thickness does not highly affect the laser transmission, as demonstrated on PC by *Rhew et al. in 2003* [Rhew et al., 2003]. In semi-crystalline thermoplastics, the transmission of the laser beam can be greatly influenced by the part thickness. This transmissivity decreases with increasing part thickness, as already demonstrated for PA6, PE and PP. Part thickness also influence the welding parameters necessary to allow successful welding, mostly by decreasing the range of values [Gonçalves et al., 2021]. When increasing the part thickness, the amount of material to be melted also increases, which increase the amount of energy necessary for welding. If more energy is required, longer welding times are also necessary, particularly because of the low heat conductivity of thermoplastics. On the other hand, it is also important to avoid thermal damaging, which results in a decrement of the laser power necessary for welding.

The sample surface finish has a big influence on the light reflection and scattering. From different studies it has been found that smooth samples mainly reflect light specularly, while the rough samples tend to have a reflection much more diffuse. This can be transposed to the fact that the smoother surfaces reflect less percentage of the incident laser beam than those with a rougher surface finish [Wang et al., 2010], [Acherjee, 2020]. "The intensity of specular reflection reduces as the roughness increases while the diffuse reflection increases with surface roughness [Acherjee, 2020]".

The moisture content of the bulk parts has a bigger effect on the resulted weld joint quality, than on the process feasibility. Until now, there is no evidence that the presence of moisture in the semi-transparent polymer part affects the light transmission capacities. On the other hand, the weld joint quality and performances can be highly affected. If moisture is present in the polymer parts at the moment of irradiation this moisture can evaporate because of the generated heat and generate cavities in the weld joint. This can decrease the

weld quality and mechanical performances.

When welding two parts by LTW, parts are superposed and an interface is generated at their contact surfaces. When put in contact, a gap could be generated between the parts. If that occurs, and if the gap is too large, the heat generated in the absorbent part will risk not being fully transferred by heat conduction to the semi-transparent part. To avoid that, specific restrictions on the geometry design of the parts are considered. Another way to decrease the gap between the parts is by using a clamping tool design to press the parts together. Using the clamping system is actually very common and almost indispensable for LTW, from where a process parameter is obtained: the clamping pressure (further detailed in Section 1.1.5). To avoid the first, a surface treatment can be performed to improve the surface properties. For the last one, it is important to apply enough pressure for clamping. That is a significant process parameter for LTW.

1.1.5 Laser welding parameters and their influence on weld quality

The laser technology and the LTW technique used for welding condition the welding parameters possible to use and control on the process. Then, the values used for each welding parameter are determined according to the materials and samples to be welded. Subsequently, the welding parameters used have an influence on the weld joint quality. The main process parameters are listed bellow and detailed in the next paragraphs:

1. Laser wavelength
2. Laser intensity distribution
3. Laser power
4. Scanning speed
5. Laser beam focus and beam diameter
6. Clamping pressure

The laser wavelength is conditioned by the laser system used for welding. The diode laser is the most commonly used laser technology for LTW. More than fifty works have been reported on LTW with diode lasers since 2004. The most common used wavelengths are 808, 915, 940, 970, 975 and 980 nm [Gonçalves et al., 2021]. This parameter will condition the suitability of the materials to LTW, because their optical properties depend on the laser wavelength. As mentioned before, the upper part of the assembly must be semi-transparent to the laser beam. This transparency is defined in terms of transmission factor, or transmissivity, at the wavelength of the laser beam. In the other hand, the lower part must be absorbent at this same wavelength. Thus, the laser wavelength will indicate if the upper part is transparent enough for the process, and if the lower one will be able to absorb the energy to achieve welding.

The intensity distribution of the laser heat source also depends on the laser technology used. The laser beam profile defines the laser intensity distribution, which can be Gaussian or uniform (top-hat), as shown in Figure 1.6. Most diode lasers have top-hat beam profiles, whereas the Gaussian beam profile is more common for fibers and Nd:YAG lasers. The Gaussian beam profile irradiance follows a typical Gaussian distribution curve: the laser intensity reaches a maximum at the center (peak) of the Gaussian curve and then decays exponentially on the beam axis to zero. This kind of distribution can lead to non-homogeneous heating on the weld. The middle of the weld seam will receive more energy and be heated more than on the borders. Then, an extended heat-affected zone (HAZ) can result from the elongated wings of the Gaussian beam.

Conversely, the top-hat beam profile is more uniform in irradiance across the beam cross-section. The energy distribution of the top-hat beam profile is more effective than the Gaussian one due to the absence of wings and steeper transitions. Higher energy input into the material can be reached with top hat beams and smaller HAZ. The threshold energy required for welding is better reached by top hat lasers than in Gaussian beams, where the radiation energy is wasted by the superfluous energy beyond the threshold (blue zone in Figure 1.6) and also by the energy bellow it in the outer portions of the curve (pink zone in Figure 1.6). Top hat lasers are more efficient and reduce energy waste. However, Gaussian beam profiles are easier to find and acquire and, thus, are more used on LTW.

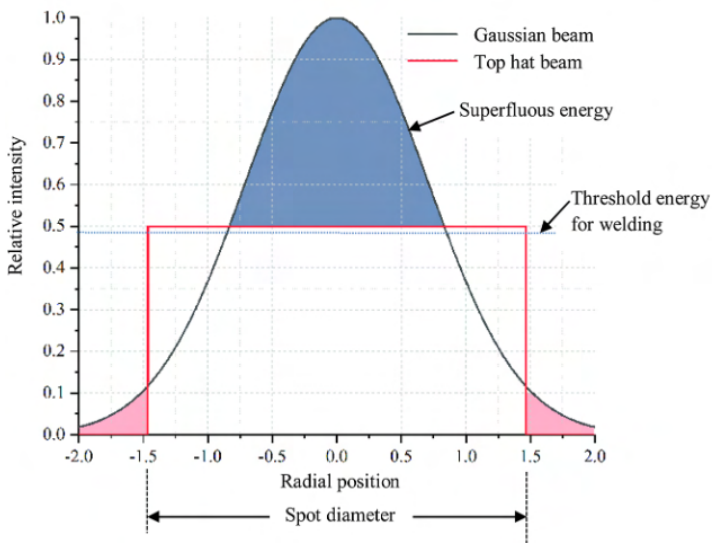

Figure 1.6: Gaussian and top-hat laser beam profiles [Acherjee, 2020].

The primary source of heat in LTW is the laser power; it determines the laser intensity and defines the heat input in the weld zone [Acherjee, 2021a]. Because of that, laser power is one of the most used parameters to control the weld temperature [Gonçalves et al., 2021]. The laser power level used for welding can determine the welding situation and material transition. Increasing the laser power induces an increase in the laser intensity and, therefore, the heat input at the weld interface. That generates melting of a higher quantity of bulk material,

resulting in a wider weld joint and enhancing the weld strength [Dave et al., 2021]. Very low laser power can result in a lack of welding. With too low laser intensity, the material may not heat enough and may not soften or melt, leading to a lack of fusion. By contrast, very high laser power can lead to material overheating, burning, and degradation, which results in a poor weld. Therefore, an optimum value or range of laser power can be identified to achieve satisfactory welding that improves weld strength and obtains the required weld joint quality. However, the laser power value used for welding is strongly related to other welding parameters, such as scanning speed and laser beam focus. The role of each parameter on the weld joint quality can be studied by keeping all other factors constant. *Acherjee et al.* [Acherjee et al., 2010] studied the contribution of these three parameters in the weld strength of laser transmission welded acrylic plates by the Taguchi method. They concluded that laser power is the main parameter that contributes to the LTW process (58 %), followed by focal distance (31 %) and scanning speed (11 %). Nevertheless, the laser power and scanning speed are deeply interrelated with the final properties of the weld.

In general, low laser power requires low scanning speeds to achieve welding. Using high laser power values allows for increasing the scanning speed for welding. The scanning speed also determines the heat input at the weld interface by defining the laser-material interaction time during laser transmission welding. Increasing the welding speed decreases the interaction time between the laser and the polymers, reducing the weld interface's heat input. If a very high scanning speed is used for welding, the lack of interaction and heat will lead to a lack of welding.

On the other hand, if very low scanning speeds are used, the interaction time will increase and may cause overheating on the parts. Therefore, a threshold value can also be determined for the scanning speed. It is essential to use the welding speed within the threshold to achieve welding and to improve the weld quality. The critical welding speed is related to the laser power but also to the thermal diffusivity and the absorption coefficient of the materials.

The laser beam focus is controlled by the working, or focal, distance between the laser-optic focusing lens and the samples. The beam focus will thus determine the beam dimensions: diameter and spot area. High attention is put on the laser beam diameter in LTW, because this parameter governs the power density at the zone of irradiation. The laser power density increases with decreasing the beam diameter, because it focuses the laser beam. High power density is obtained with a narrower beam diameter, which may lead to material burning and decomposition. A larger beam diameter generates low power density and, if the density is too low, this may lead to a lack of fusion. To obtain a more uniform distribution of the energy inside the beam spot is recommended to defocus the laser beam, this will increase the size of the beam spot and allow to reduce the energy gradient. In addition, increasing the laser beam size at the irradiated zone allows to obtain a wider weld seam, enhancing the weld strength. The laser beam size, or focal distance, have also a threshold at which the optimum weld strength can be achieved. Exceeding this optimum value, the weld strength will begin to decline. The optimum value of the lase beam size depends directly on the laser power, welding speed and even on the material properties of the samples to be welded.

As mention in section 1.1.1, to achieve welding in LTW the superposed parts must be in

close contact at their interface. This is mainly achieved, and improved, by pressing the parts to each other by means of clamping arrangements. The use of clamping system generates what is called the clamp pressure to the polymer parts. The clamp pressure is applied all along the welding process, until end of cooling, to maintain adequate contact at the welding interface. This improves heat conduction from the bottom absorbent part to the upper semi-transparent one, enhancing material softening and melting at the interface. Clamp pressure also promotes the melt flow of the melted material in the weld pool, which is necessary for diffusion of the polymer chains to form the weld joint [Potente et al., 2009].

The combination of some of the LTW process parameters generate the definition of new parameters that can be also taken into account for the welding process [Acherjee, 2021a]:

1. Laser power density: also called laser intensity (I_P) [$W \cdot mm^{-2}$] is defined as the optical power delivered per unit area. This parameter is a function of laser power (P) [W] and beam diameter (D_B) [mm], and can be calculated with Equation 1.1:

$$I_P = \frac{4P}{\pi D_B^2} \tag{1.1}$$

2. Laser-polymer interaction time (T_w) [s]: expressed as function of welding speed (V) [mm·s^{-1}] and length of weld (L) [mm], with Equation 1.2:

$$T_w = \frac{L}{V} \tag{1.2}$$

3. Laser energy density (I_E) [$J \cdot mm^{-2}$]: combines the laser power density (I_P) and the laser-polymer interaction time (T) in a single Equation 1.3:

$$I_E = I_P \times T = \frac{4P}{\pi D_B^2} \frac{L}{V} \tag{1.3}$$

For contour welding, the laser energy density can be determined with Equation 1.4 [Gonçalves et al., 2021]:

$$I_E = \frac{P}{D_B \times V} \tag{1.4}$$

For simultaneous welding (static irradiation), the energy density is calculated using Equation 1.5 [Gonçalves et al., 2021]:

$$I_E = \frac{P \times t}{S} \tag{1.5}$$

where t [s] is the irradiation time and S [mm^2] is the area of the laser beam spot.

4. Line energy (L_E): is the ratio of power to welding speed, expressed with Equation 1.6:

$$L_E = \frac{P}{V} \tag{1.6}$$

1.2 Physical phenomena involved during LTW

In laser transmission welding several key physical phenomena are involved during the process. The interactions between the light of the laser beam and the samples to be welded that depends on the material properties and the samples pre-welding conditions, conditioned to the laser wavelength. The laser intensity profile and the heat generation by this intensity, conditioned by the laser beam system and by the absorption properties of the samples. And the heat transfer that occurs at the interface, influenced by the material thermal properties.

1.2.1 Light-Matter interaction

The use of laser light as the energy source for welding polymers in LTW involves to take special consideration of the interaction of this light with the samples to be welded. The way that the light interacts with the samples can be described and quantified by the optical properties of the last ones. Therefore, the optical properties of the samples play an important role in LTW.

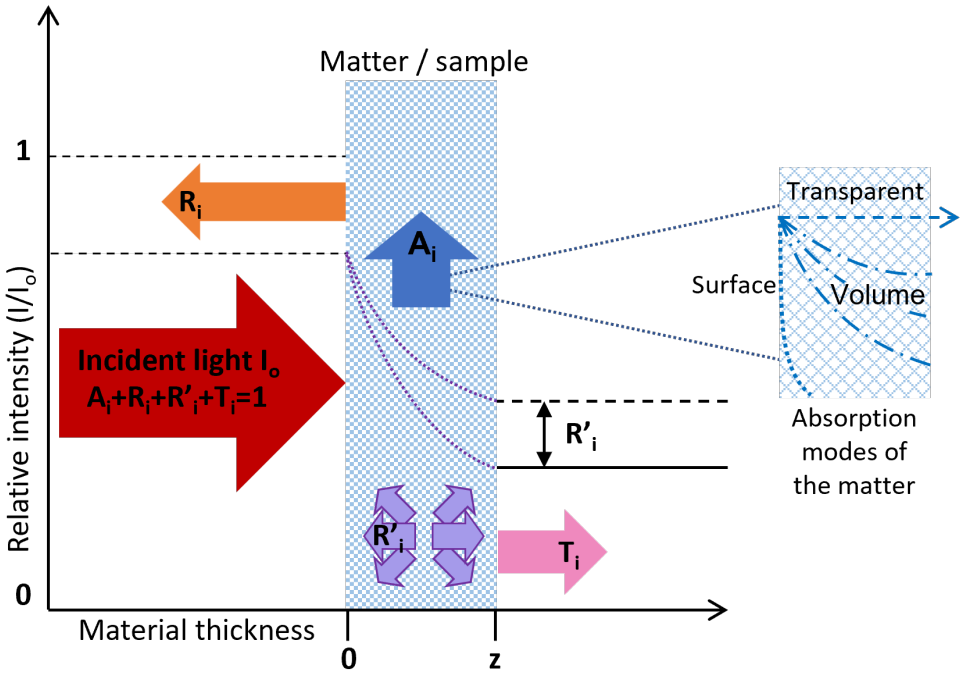

Figure 1.7: Diagram of relative intensity (I/I_o) representing the Light-Matter interaction. Insert indicates the intensity path as function of the absorption ranges on the material depth (reproduced from [Bachmann and Russek, 2002]).

When light strokes the surface of a material, it can be either reflected or penetrates into the sample [Bachmann and Russek, 2002]. The part of light that is not reflected enters the material. In this case, some part of the light will achieve to go through the material, some

other will be absorbed and some will be scattered and lost. All of these interactions between light and matter (sample) are schematically explained in Figure 1.7. As it can be seen in the diagram, the incident light (I_o) strokes the material, a part is reflected (R_i), a part will be transmitted (T_i), a part will stay inside the material and from here it can be either absorbed (A_i) or scattered (R'_i). The reflection of the light depends mostly on the sample's surface conditions (mostly the roughness and coating). The transmission, absorption and scattering are mostly determined by the material composition and morphology. Finally, the sample thickness determines mostly the transmission and absorption.

All these phenomena can be measured for a specific material at a specific wavelength to obtain the optical properties of the concerned sample. These properties are defined by the reflection, transmission and absorption factors, indicated in % of incident light. These optical factors are related between them according to the energy conservation principle indicated by Equation 1.7 [Mamuschkin et al., 2014]. Another important optical property that can be calculated is the absorption coefficient α, which depends on the sample's thickness.

$$T_i + R_i + A_i = 1 \tag{1.7}$$

1.2.1.1 Samples' surface and pre-weld preparation

The first interaction between the laser light and the matter occurs at the surface of the sample. The sample surface quality influences thus the quantity of light that will be reflected and that will not achieve to enter the material. The rest will be able to go inside the sample to be absorbed, scattered or transmitted.

1.2.1.2 Polymers' transparency

Most thermoplastics in their natural state are semi-transparent or translucent to the visible and near-infrared (NIR) radiation, in wavelengths from 0.35 to 1.4 microns [Xu et al., 2015a, Acherjee, 2020, Gonçalves et al., 2021]. In this wavelength spectrum, thermoplastics have low inherent absorption, which enables them to be welded to a thickness of several mm. In this context, almost any thermoplastic can be used as upper semi-transparent part for LTW process. However, some thermoplastics are able to naturally absorb the electromagnetic radiation between 1.4 and 2.2 microns [Devrient et al., 2011]. Thus, special care must be taken when welding polymers with laser beam within this range of wavelengths.

Thermoplastic materials can have different degree of transmissivity (light transmission capabilities) to a specific laser wavelength, depending on their morphology, composition and thickness. These transmission capabilities are determined by the transmission factor (T_i) of the material at the specified wavelength. The T_i expresses the percentage of the incident laser light that will go through the sample thickness and escapes from it, without affecting the sample.

1.2.1.3 Laser absorption by the bottom part

As the laser light passes through the sample it will be absorbed (A_i) according to the *Beer-Lambert's law* [Bachmann and Russek, 2002], indicated in Equation 1.8:

$$I(z) = I_o \times e^{-\alpha z} \tag{1.8}$$

where $I(z)$ [$W \cdot m^{-2}$] is the quantity of intensity that goes through the sample thickness, I_o [$W \cdot m^{-2}$] is the quantity of the laser radiation that achieves to enter the polymer just after reflection loss [Dave et al., 2021], α is the absorption coefficient of the sample at the laser wavelength and z is the thickness of the sample. This law indicates that, for a constant value of α, the laser intensity decays exponentially to the samples thickness (z). The absorption coefficient α depends on the material morphology and composition, on the wavelength of the incident laser beam, on temperature and other parameters. The absorption coefficient α affects the absorption mode, the way in which the light is absorbed by the sample. Its value can go from zero ($\alpha = 0$) for a fully transparent material, over a medium range (which indicates absorption on the volume of the sample), up to as high numbers as 10 000 cm^{-1}, for a material that will absorb only in the surface.

For LTW, the bottom sample must absorb the laser energy, either at the interface or in volume. Different techniques are used to achieve this. One of this technique is to fill the sample with absorbent additives, which can be colorants [Potente et al., 1999, Amanat et al., 2011] or reinforcements. The most used are carbon black (CB) [Jankus and Bendikiene, 2022], and carbon fibers (CF) [Berger et al., 2015, Korycki et al., 2022]. Another recent and less used technique is to modify the morphology of the polymer to increase light absorption intrinsically. Modify the morphology means to play with the polymer chains arrangement, which can only be possible in semi-crystalline thermoplastics, by playing with their crystalline state. Increasing the crystalline state, or degree of crystallinity, of semi-crystalline thermoplastics can lead to a morphology that interferes with the light transmission. The optical properties of semi-crystalline polymers are influenced by their crystalline structure, which imposes limitations on light transmission [Kagan and Bray, 2001]. The crystalline structure increases the light travel path, which leads to higher absorption [Kagan et al., 2002, Xu et al., 2015b].

1.2.1.4 Light scattering

Scattering (R') is only found in volume absorbers and only under certain conditions [Bachmann and Russek, 2002]. The scattering phenomena causes to the light to be deflected from its initial path, and the energy of the light is not transferred to the material, having a negligent effect on the state of the matter. Scattering is mostly caused when the light encounter the surface of particles, grains boundaries or crystals (as explained for semi-crystalline thermoplastics).

As indicated by *Russek in 2001* [Russek, 2001] the optical properties of thermoplastics can

be influenced by playing with the scattering behavior. The size, distribution and nature of the scattering centers influence the scattering properties of the polymer. In the context of semi-crystalline polymers, increasing the crystallinity of the material leads to an expansion of the laser beam. And when increasing the scattering phenomena, more line energy is necessary for welding. The scattering can thus be influenced by increasing the crystallinity of the polymer.

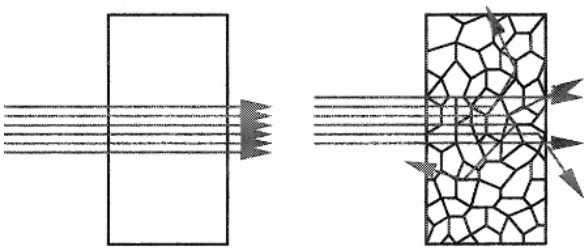

Figure 1.8: Light scattering on a) amorphous and b) semi-crystalline thermoplastics [Bachmann and Russek, 2002].

1.2.2 Laser intensity and heat generation

As mentioned in section 1.1.5, the laser beam intensity is governed by the laser beam profile. This profile can be Gaussian or top hat. For a Gaussian laser beam that irradiates the interface of the overlapped parts while it is in movement, the laser intensity is calculated using Equation 1.9 [Coelho et al., 2003]:

$$I(r,t) = \frac{4P}{\pi(\frac{D_B}{2})^2} exp\left[\frac{-2 \cdot r^2}{(\frac{D_B}{2})^2}\right] \tag{1.9}$$

where P $[W]$ is the laser beam power, D_B [mm] is the laser beam diameter, r represents the spatial coordinates, and t denotes time dependency do to the movement of the laser beam.

This laser intensity will be absorbed by the material at the interface, which will generates heat (Q $[W.m^{-3}]$) according to the absorption properties of the parts on their thickness. Q is thus the source term generated on the laser transmission welding process, and is calculated using Equation 1.10 [Coelho et al., 2003]:

$$Q(r,t) = \alpha \cdot I(r,t) \cdot exp(-\alpha.z) \tag{1.10}$$

1.2.3 Heat transfer at the interface

After the interface is irradiated, and that this laser energy is converted into heat by the lower absorbent part, the heat will be transferred to the upper part by heat conduction. This heat transfer will be governed by the degree of contact between the samples, but also by their thermal properties. The heat transfer state between the welding interfaces significantly

affects the welding quality [Wu et al., 2021]. The heat transfer rate through the materials is directly proportional to the negative gradient of the temperature, according to the heat equation statement [Dave et al., 2021]. This heat transfer is defined by the heat conduction Equation 1.11 simplified due to the mass conservation [Coelho et al., 2003], for a laser beam on a defined coordinate system r:

$$\rho(T)C_p(T)\left(\frac{dT}{dt} + v \cdot \nabla T\right) = \nabla(k(T) \cdot \nabla T) + Q(r) \tag{1.11}$$

where ρ [kg $\cdot$ m^{-3}] is the density, C_p [J $\cdot$ kg^{-1} $\cdot$ K^{-1}] is the heat capacity and k [W $\cdot$ m^{-1} $\cdot$ K^{-1}] is the thermal conductivity of the materials. Those properties of the material evolve with temperature. The term $v \cdot \nabla T$ indicates the heat carried within the material as it moves with a flow rate $\rho \cdot v$ [Dowden, 2001].

1.3 LTW of semi-crystalline thermoplastics and composites

Thermoplastics can be classified into amorphous and semi-crystalline, depending on the order of stacking of their molecules. In amorphous thermoplastics, the molecules are in disorder, and their molecular mobility remains relatively static, only vibrating around their initial position. From a microscopic point of view, amorphous polymers are isotropic, with properties that are microscopically identical at all point. In the other hand, semi-crystalline thermoplastics are composed of areas with crystalline order[1] and amorphous state, being non-homogeneous from a microscopic point of view.

When laser transmission welding semi-crystalline (SC) thermoplastics special care must be taken into account. A semi-crystalline thermoplastic has a more complex micro structure that can influence the laser welding. In addition, its ability to melt and crystallize gives special features to the welding process and conditions the weld joint final result.

1.3.1 Characteristics of semi-crystalline thermoplastics

A SC thermoplastic is composed of crystalline and amorphous domains. Their microstructure consists of an arrangement of crystallites coupled to amorphous zones. Crystallites, also called lamellae, are polymer chains that arrange themselves into meshes. These crystallites can grow and conform different kind of superstructures at the microscale form, like spherulites or shish-kebab, among others. Spherulite is the most common superstructure developed in SC thermoplastics, particularly on injected-molded samples. A spherulite is created when several crystallites grown radially from a common nucleus, as shown in Figure 1.9. The crystallites stack then in a spherical pattern which size and shape can vary, depending on the processing conditions.

[1] The crystalline order is characterized by a repetitive geometrical arrangement of the atoms over a large distance.

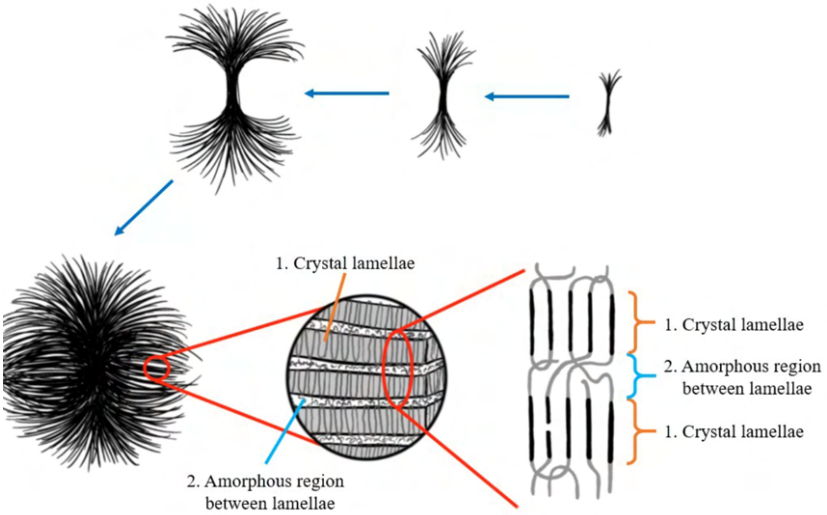

Figure 1.9: Schematic representation of the formation of a spherulite [Pérez-Martín et al., 2022].

Technically, a thermoplastic can not be fully (100%) crystallized, due to their statistical chain structure. Thus, only a fraction (percentage) of the whole polymer mass can be crystalline. This percentage of the crystallized phase on the material is the degree of crystallinity, or crystallization grade (X_c). The X_c of a material can be determined by different techniques such as density, differential scanning calorimetry (DSC), and X-Ray diffraction (XRD), as shown in *Doumeng et al.* [Doumeng et al., 2021]. The most commonly used technique, and the one used in this study to characterize the samples, is the DSC (further detailed in chapter 2, section 4.1).

The crystalline structure and X_c of a SC thermoplastic is strongly related to the thermal history of the processing conditions (such as fabrication and welding). Then, this micro structure influences the material properties. Thus, the morphology of the crystalline structure, as well as the degree of crystallinity of the material, can be varied with the process parameters, and this variation can influence the final material properties.

Semi-crystalline thermoplastics can crystallize from the melt state on cooling, or from the solid amorphous (glassy) state on heating (cold crystallization). The crystallization process can also occurs under isotherm or non-isotherm conditions. The temperature, time and/or ramp used to crystallize the material, can also vary, and they are dependent on the thermal transitions and crystallization kinetics of the polymer. Depending on the way, conditions, time and temperature, used to crystallize the polymer, the crystalline morphology and proportion will vary.

As any material, SC thermoplastics undergone phases transitions when they are heated. These transitions occur over a temperature range, characterizing the transition zones, as for all polymer materials. The transition zones are the glass transition, melting and crystallization (Figure 1.10. Semi-crystalline polymers have the dual behavior of an amorphous solid

and a crystalline solid. They therefore have well-defined glass temperature (T_g) and melting temperature (T_m). T_g is the glass transition temperature of the amorphous phase of the SC polymer. T_m, on the other hand, is the melting temperature that defines the change of state of the crystalline zones of the material. Below T_g, the SC polymer is solid and brittle, with its amorphous phase being frozen. Above T_g, the amorphous phases thaw and their macromolecules gain more mobility, changing to the cautchoutic state. At this point, the crystalline zones still exist and they act as knots. Above T_m, the crystalline zones start to vanish, to be destroyed, to melt, and the polymer becomes a viscous liquid. In the molten phase, the SC polymer can starts to degrade if the decomposition temperature (T_d) is exceeded. The melt temperature of SC thermoplastics depends on the size of the crystals and the ratio of amorphous to crystalline phases, among other factors. The range of crystallization temperatures is always lower than that of melting, so crystallization is delayed [Carrega, 2009].

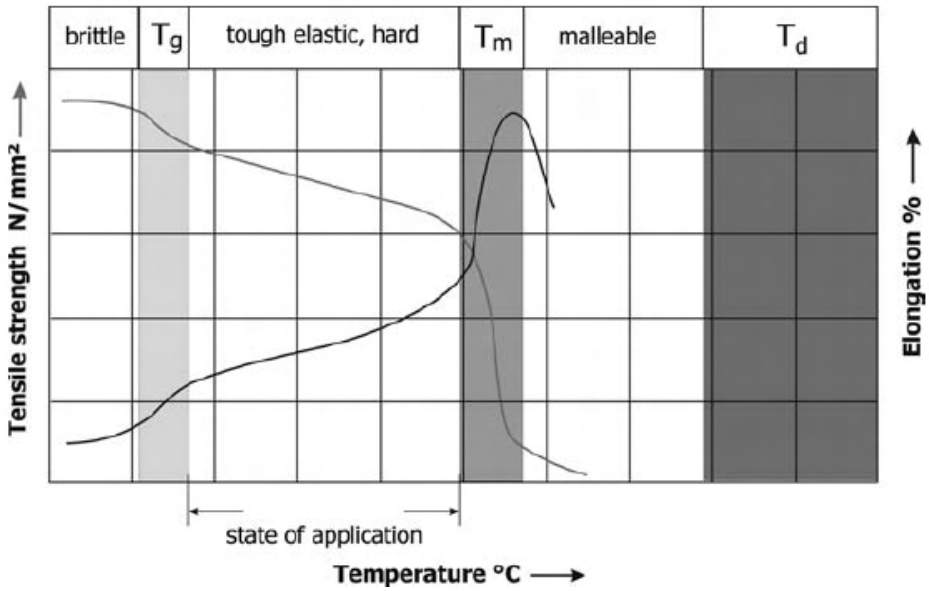

Figure 1.10: Schematic representation of the thermal transitions on semi-crystalline thermoplatics [Klein, 2012].

1.3.2 Crystalline structure and its impact on LTW

The laser interaction with SC thermoplastics is different than with amorphous polymers. The presence of crystalline zones on semi-crystalline thermoplastics make them non homogeneous, impacting the light transmission properties. Due to the differences in refractive index between the amorphous and crystalline regions, semi-crystalline polymers scatter the laser beam more than amorphous ones. Scattering of laser light prohibits a deep penetration of laser radiation, even when the absorption coefficient is low [Nonhof, 1994].

In SC thermoplastics, the reflection phenomena increases: there is specular reflection from the front surface, and this is combined with the multiple specular reflectance from the

additional components within the polymer. This last reflectance is also known as the diffuse scattering, and it is higher compared to the first reflection. This scattering causes that a substantial portion of the transmitted light through the sample may be deflected from the incident beam direction. This reduces the energy density at the back surface. Moreover, is is possible that the effective path length of the transmitted light became slightly longer than the sample's real thickness, which would increase the absorbance of the sample and reduce laser transmission [Kagan et al., 2002]. Changes in optical properties of semi-crystalline thermoplastics depend on the level of crystallinity, crystal form, the orientation of crystalline lamella, etc. [Acherjee, 2021b].

1.3.3 Laser irradiation impact on the crystalline structure

When semi-crystalline polymers are welded by laser, different micro structures produce varied morphologies and, as a result, material properties.

When the laser irradiates a semi-crystalline thermoplastic, its morphology can be easily modified, depending on the thermal transitions and crystallization kinetics of the polymer. As the laser encounters the SC material it will begin to heat. This increment in temperature can cause the polymer to soften, cold crystallize, melt or decompose. The SC polymer will only begin to soften if the reached temperatures are near the glass transition (T_g) and below the cold crystallization (T_{cc}) temperatures. If the temperatures are near or above the melting point (T_m), the material will melt and all the existent crystals will vanish. However, if the temperatures are reached an maintained between T_g and T_m, the SC thermoplastic will crystallize from the cold (according to their crystallization kinetics).

In the case that the SC polymer softens at the interface, it will be difficult to achieve molecular chain inter-diffusion, because of the low molecular mobility. Thus, welding may lack.

When the laser irradiation achieves to melt the SC thermoplastics at the interface, both will be able to entangle and to fusion to develop a weld upon cooling. Then, its crystalline state will vary upon cooling: it can stay amorphous (low crystallinity) or re-crystallizes. If the material achieve to re-crystallize or not will depend on the cooling rate of the welding process on the melted material. The crystalline structure or morphology developed in the re-crystallization will also depend on this cooling rate.

Nevertheless, if the SC polymer crystallized from the cold at the irradiation process, different case scenarios can occur. First, if the semi-transparent (upper) part crystallized when the laser is going through it, it will block the laser irradiation at no irradiation will achieve to reach the interface of the assembly. In this case, the semi-crystalline material cannot be used as semi-transparent part. This crystallization generated from cold will develop a morphology that will depend on the initial morphological structure of the polymer obtained on the manufacturing process.

1.4 LTW on poly(aryletherketone)s (PAEKs)

Poly(aryletherketone)s (PAEK)s is a family of high-performance engineering semi-crystalline thermoplastics. PAEKs have aromatic groups and both the ether and keto groups are in the backbone, existing several varieties of those structures [Fink, 2014]. The most common varieties of PAEKs are poly(etheretherketone) (PEEK) and poly(etherketone) (PEK). Other more refined forms are poly(etherketoneketone) (PEKK), poly(etheretherketoneketone) (PEEKK) and and poly(etherketoneetherketoneketone) (PEKEKK).

PAEKs thermoplastics have been used in the engineering field since 1980s, because of their excellent thermal and mechanical performances. These high performance copolymers are able to replace metals in may applications, thanks to their high mechanical and thermal properties, low density, low outgassing properties and high resistance to chemicals and oxidation due to aiging. They have many opportunities to be used in various domains like electronics, robotics, medical devices, prostheses, dentistry, food processing equipement, aerospace and automotive. The most used and studied are PEEK [Seferis, 1986, Nguyen and Ishida, 1987, Fink, 2014, Rezvani Ghomi et al., 2021, Maloo et al., 2022, Pravin et al., 2022] and PEKK [Hsiao et al., 1991a, Pritchard, 1994, Ke and Wu, 1998, Alqurashi et al., 2021, Pérez-Martín et al., 2022, Zol et al., 2023]. These two PAEK copolymers differ in the ratio and structure of ether to ketone group, which affect their thermal transitions and crystallinity. The more the ketone group, the more the polarity and rigidity, thus the more the glass transmission temperature and melting point. PEEK is a monomer unit of ether ether ketone, and PEKK is the monomer unit of ehter ketone ketone. Figure 1.11, show the chemical structure of PEEK and PEKK. The differences between PEEK and PEKK are highlighted by Maloo et al. [Maloo et al., 2022] in Table 1.4.

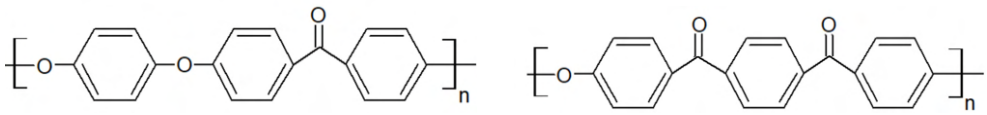

(a) (b)

Figure 1.11: Chemical structure of (a) PEEK and (b) PEKK.

PEEK	PEKK
Contains two ether group and one keto group	Contains two keto group and one ether group
Higher extrusion temperature (almost 400°C)	Lower extrusion temperature (340°C-360°C)
Lower glass transition temperature (143°C)	Higher glass transition temperature than PEEK (159°C)
Low modulus of elasticity than PEKK	Greater modulus of elasticity than PEEK
As PEEK has low modulus of elasticity, it requires surface treatment	It works if surface treatment is not done with PEKK polymer
80% straight and 20% kinked segments melt at 360°C	60% straight and 40% kinked segments melt at 305°C

Table 1.4: Differences between PEEK and PEKK copolymers [Maloo et al., 2022].

PAEK thermoplastics are used pure, but they are also used as matrix for composite materials [Veazey et al., 2017, Zeyrek et al., 2022]. Since 1988, PEKK was introduced as a "new thermoplastic matrix for high performance composites" [Chang, 1988]. In their study, they demonstrated that PEKK reinforced with unidirectional laminates of carbon fiber shown good hot-wet stability, environmental durability, interlaminar fracture toughness and damage tolerance. The presence of reinforcements modify the properties of PAEK copolymers. Chelaghma et al. [Chelaghma, 2018] demonstrated that when PEKK material contain fibers, its crystallization behavior and kinetics is modified. The crystallization of PEKK is accelerated when carbon fibers are present. Fibers act as the primary surface of germination, enhancing the development of a transcrystalline phase within them. This morphology modification leads to an alteration of the germination rate, changing also the crystallization kinetics of PEKK matrix.

The increasing use and demand for PEEK and PEKK has led to an increase in processability methods, such as joining. Few studies have demonstrated the weldability of PEEK and PEKK by the LTW process. PEEK has been the most studied for LTW, demonstrating its ability to be laser welded by applying colorants [Amanat et al., 2011, Vacogne and Wise, 2011] or reinforcements [Vacogne and Wise, 2011, Liu et al., 2022] on the lower substrate ; by using an infrared absorbent coating at the interface [Amanat et al., 2010]; and even welded with metals [Su et al., 2020].

In the other hand, welding PEKK by LTW has rarely been studied. Only one study has proven its weldability by LTW and without the use of any additives. That was the work of *Villar et al. in 2018* [Villar et al., 2016, Villar et al., 2018], where PEKK thermocompressed samples were welded with an 808 nm NIR laser device. They control the degree of crystallinity of PEKK to obtain quasi-amorphous and semi-crystalline samples, to be used as upper-transparent and lower-absorbent substrates, respectively. The focus was put on characterizing the temperature distribution along the thickness of the assembly during LTW to optimize the process parameters.

Even though PEEK is by far the most widely used PAEK polymer in the industry, PEKK is gaining presence and the need to better understand the material, its joining methods, and its quality assessment, is increasing. Regarding the joining process of PEKK by LTW, there is certainly room for improvement. The unique crystallization properties of PEKK make it a better option for the LTW process, compared to PEEK. The crystallinity of PEKK can be easily controlled by adjusting the processing parameters. This is possible thanks to the ability of PEKK to generate various co-polymers with different crystallization kinetics and properties. The crystallization mechanisms and kinetics of the material will condition their capability and reaction to the LTW process. Consequently, understanding the mechanisms and kinetics involved in the crystallization of PEKK reveals to be beneficial in the performance and managing of its joining process by LTW.

1.4.1 Crystallization mechanisms of PEKK thermoplastic

Gardner et al. [Gardner et al., 1992] studied the isothermal crystallization mechanisms of PEKKs having different terephthalic/isophthalic content (T/I ratio). His study addressed two issues: the characterization of the two crystal structures, and the effect of the T/I ratio on features of the crystallization behavior (melting temperature, double-melting behavior, crystallization kinetics and recrystallization). Its work was based on X-ray diffraction and thermal analysis studies.

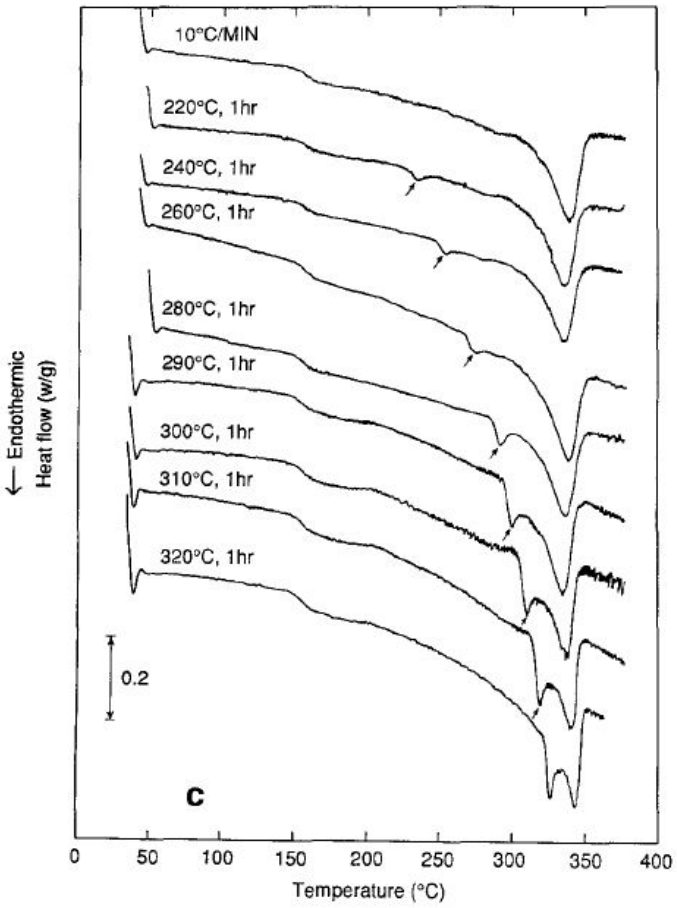

Figure 1.12: DSC scans of PEKK (70/30) specimens annealed at different temperatures [Gardner et al., 1992].

Gardner's DSC scans show a double melting behavior for TT crystals. After annealing, an additional endotherm occurs about 10°C above the annealing temperature, during melting. If PEKK (70/30) is annealed at several temperatures for 1 hour, we can notice the straightforward double-melting behavior (Figure 1.12). This peak is associated with the melting of a secondary structure withing the spherulite, being a secondary crystallization [Gardner et al., 1992].

To study crystallization kinetics of PEKK, *Gardner et al.* [Gardner et al., 1992] focused on the crystallization peak time method (time at the maximum crystallization exothermic peak), using DSC scans. He recorded the isothermal crystallization peak time to characterize the crystallization rate, as shown on Figure 1.13. There we can see that the crystallization behavior is different for TI and TT structures. Therefore, the crystallization rate increases with decreasing isophthalate content.

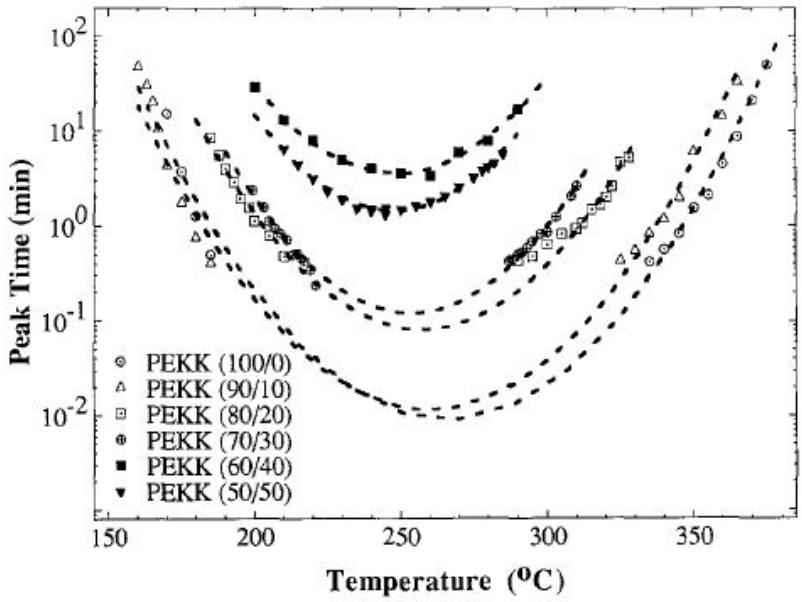

Figure 1.13: PEKKs crystallization peak time vs temperature [Gardner et al., 1992].

Choupin [Choupin, 2017] also investigated the crystallization kinetics of PEKK 70/30. He studied the PEKK 7002 provided by Arkema, and compared it with PEKKs 6002 and 8002, also from Arkema. As first approach he compared their crystallization kinetics by the use of DSC characterization. All samples where crystallized from melt at three different cooling rates: 1 $°C.min^{-1}$, 5 $°C.min^{-1}$ and 10 $°C.min^{-1}$. Then, their crystallinity X_c was measured after a heating scan at 5 $°C.min^{-1}$. The degree of crystallinity obtained for each PEKK grade at each cooling rate are shown in Table 1.5.

From the DSC heating scans (Figure 1.14) it can be noticed that PEKK 8002 crystallizes more than PEKK 7002, but this ones crystallizes more than PEKK 6002. For PEKK 7002 an additional endothermic peak appears around 260 °C, associated to the melting of a secondary crystallization. As it can be observed, PEKK 7002 shows a high crystallization rate and its crystallinity is quasi-independent of the cooling rate, for cooling rates between 1 $°C.min^{-1}$ and 10 $°C.min^{-1}$ (Table 1.5).

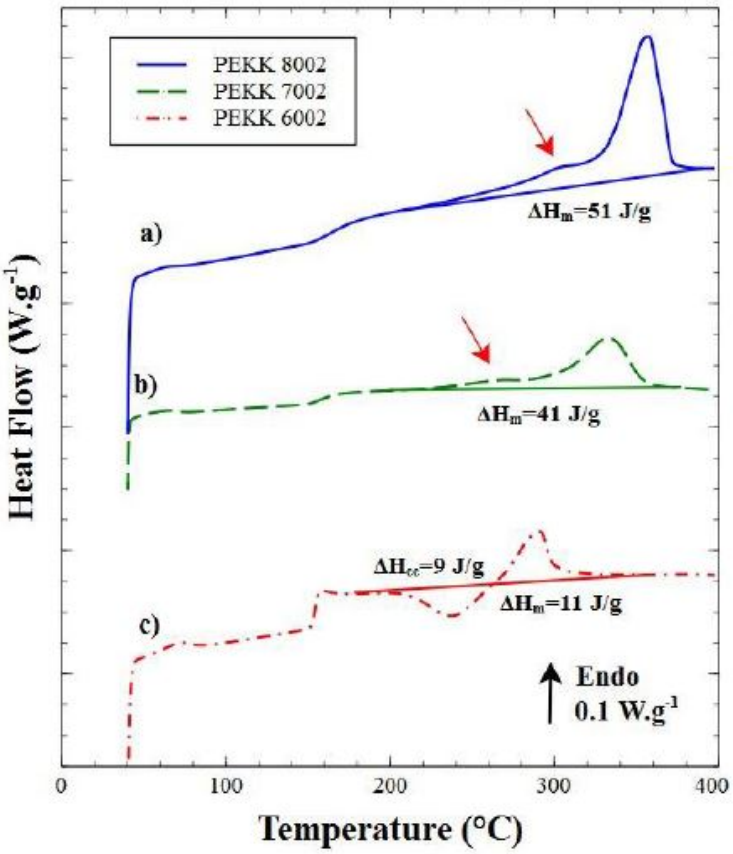

Figure 1.14: DSC heating scans after crystallization from melt at 10 $°C.min^{-1}$ of PEKK 8002, 7002 and 6002 [Choupin, 2017].

Grade	X_c (%) at V=10°C.min^{-1}	X_c (%) at V=5°C.min^{-1}	X_c (%) at V=1°C.min^{-1}
PEKK 8002	39	39	40
PEKK 7002	31	32	33
PEKK 6002	2	14	28

Table 1.5: Crystallinity Xc (%) for each cooling rate used to crystallize PEKK from melt [Choupin, 2017].

1.4.2 PEKK crystallization kinetics models

PEKK 7002 is a polymer that crystallizes from the melt with only one crystalline morphology *form 1* (spherulitic growth). It also shows an additional melting peak, associated with the melting of a secondary structure within the spherulite, which indicates a secondary crys-

tallization. Therefore, this secondary crystallization of PEKK 7002 needs to be taken into account for its crystallization kinetics modeling.

From microscopy observations *Choupin* [Choupin, 2017] found that the Avrami exponent [Avrami, 1939] for the primary crystallization n_1 is equal to 3, which corresponds to a three dimensional growth with an instantaneous nucleation. Then, the Avrami exponent for the secondary crystallization was determined with a multi linear regression fitting of the derivative Hillier model [Hillier, 1965]. Thus, the secondary crystallization Avrami exponent was found to be $n_2 = 1$, corresponding to a uni-dimensional crystallization growth with an instantaneous nucleation.

For isothermal modeling, *Choupin* established a new method using the derivative of the Hillier modified isothermal model. With this method, he modeled the isothermal crystallization of PEKK 7002 and fit it with the experimental DSC measurements for crystallization from the melt (at 250°C). He concluded that the derivative Hillier model fits well with experiments and allows rebuilding the crystallization peak beginning [Choupin, 2017]. Also, from modeling the crystallization rate constants K_1 and K_2 with the Hoffman and Lauritzen model, and the weight factor w_1 with a linear model, *Choupin* obtained their correspondent parameters.

For the modeling of non-isothermal crystallization kinetics of PEKK 7002, a new model was developed by *Choupin*. It is based on the derivative isothermal crystallization kinetic Hillier model, to take into account the primary and secondary crystallization of the material. This model was the derivative model proposed by Patel and Spruiell [Patel and Spruiell, 1991] extended to the secondary crystallization from the Hillier model. Then, this model was solved using the implicit Euler method. *Choupin* also changed some of the of the Hoffman and Lauritzen parameters for the primary crystallization process. Using the proposed model, solved by the chosen method and changing the parameters indicated, *Choupin* found a good agreement between the relative crystallinity obtained from the non-isothermal modeling and the experimental data.

Crystallization kinetics are used to predict the evolution of the relative crystallinity X_R as function of time and temperature. *Avenet* [Avenet, 2021] indicates in his work that these kinetic models are based on the next hypothesis:

- The existence of N_0 potential "germs" randomly distributed in the volume.
- The total volume of the material is constant.
- The growth of a germ is immediate.
- Germs can only disappear by activation or absorption of a crystalline entity.
- The geometry of the crystals is imposed: stick in 1D, stick or disc in 2D, stick, disc or sphere in 3D.

Thus, to describe the evolution of the relative crystallinity as function of time $X_R(t)$ The Avrami Evans [Avrami, 1939] theory is used, having as general expression:

$$X_R(t) = 1 - exp(-E(t)) \tag{1.12}$$

where $E(t)$ is dependant on the nucleation and growth modes, and on the growth geometry.

1.4.2.1 Isothermal crystallization kinetic models

For the isothermal crystallization, Avenet [Avenet, 2021] includes two more hypothesis:

- The crystallization growth rate G is constant over time.
- The frequency of germ activation q is constant and can be instantaneous.

This type of crystallization is also modeled with the Avrami theory [Avrami, 1939] using the general equation as a function of the Avrami crystallization rate constant K, of time and of the Avrami exponent n:

$$X_R(t) = 1 - exp(-Kt^n) \tag{1.13}$$

where K and n are dependant on the dimensionality of crystal growth and on the nucleation mode, having different values as shown on Table 1.6 and 1.7.

	Germination sporadique	Germination instantanée
3 dimensions	4	3
2 dimensions	3	2
1 dimension	2	1

Table 1.6: Avrami's exponent values [Avenet, 2021]

	Germination sporadique	Germination instantanée
3 dimensions	$\frac{q\pi N_0 G_g^3}{3}$	$\frac{4\pi N_0 G_g^3}{3}$
2 dimensions	$\frac{q\pi N_0 G_g^2}{3}$	$\pi N_0 G_g^2$
1 dimension		$N_0 G_g$

Table 1.7: Avrami's crystallinity rate constant values [Avenet, 2021].

Experimentally, the plot of the double logarithm of the relative crystallinity $ln[-ln(1 - X_R(t))]$ as function of $ln(t)$ gives a line with a slop n and y-interception at $ln(K)$.

This model does not take into account the secondary crystallization that can appear on the material after the first one.

Different models have been developed to incorporate the primary and secondary crystallization process into the crystallization kinetic modeling of polymers. The two most relevant models reported are from Hiller [Hillier, 1965] and Velisaris Seferis [Velisaris and Seferis, 1986] studies. Hsiao et al. [Hsiao et al., 1991b] used a modified Hillier model to investigate the isothermal crystallization kinetics of a PEKK 70/30 and compare it to the Valisaris Seferis model. The modified Hillier model used postulates that the secondary crystallization is not necessarily a first order process. They concluded that the modified Hillier model is more suitable to describe the growth of a second crystalline structure within lamellae [Choupin et al., 2017].

Hillier modified model

Choupin et al. [Choupin et al., 2017] investigated the isothermal melt and cold crystallization kinetics of a PEKK 6002, with T/I ratio 60/40, using a modified Hillier model for crystallization to predict the crystallinity evolution according to processing cycles. This crystallization kinetics was also characterized by using DSC tests.

The modified Hillier model used by *Choupin et al.* [Choupin et al., 2017] expresses the primary crystallization by an Avrami equation:

$$X_1(t) = 1 - exp(-K_1 t^{n_1}) \tag{1.14}$$

Where $X_1(t)$ is the relative volume fraction crystallinity at time t, K_1 is the crystallization rate constant depending on the annealing temperature, and n_1 is the Avrami exponent depending on the dimensionality of crystal growth and on the nucleation. At time θ occurs the secondary crystallization process, when a volume element has been included in the lamellae. This process is expressed by Hsiao et al. [Hsiao et al., 1991b] by an Avrami equation:

$$X_2(t-\theta) = 1 - exp(-K_2(t-\theta)^{n_2}) \tag{1.15}$$

Which *Choupin et al.* [Choupin et al., 2017] developed to express the secondary crystallization process at time t as:

$$X_2(t) = \int_0^t X_1(\theta) \times \frac{d}{dt}(X_2(t-\theta))\, d\theta \tag{1.16}$$

Where $X_2(t-\theta)$ is the relative volume fraction crystallinity at time t, K_2 is the crystallization rate constant and n_2 is the Avrami exponent of the secondary stage. Therefore, the total relative crystallinity $X_R(t)$ at time t is the sum of these two crystallinity process, multiplied

each one by their corresponding weight factor between primary and secondary crystallization (w_1 and w_2).

$$X_R(t) = w_1 X_1(t) + w_2 X_2(t) \tag{1.17}$$

Therefore, from equations (1.14), (1.16) and (1.17):

$$X_R(t) = w_1[1-exp(-K_1 t^{n_1})] + w_2 K_2 n_2 \int_0^t [1-exp(-K_1\theta^{n_1})](t-\theta)^{n_2-1} exp(-K_2(t-\theta)^{n_2})\, d\theta \tag{1.18}$$

Where $w_1 + w_2 = 1$ corresponding to the Avrami model hypotheses that the relative crystallinity at infinite time is unity.

Choupin [Choupin, 2017] crystallized the PEKK 6002 from the melt, using isothermal crystallization at 230 °C and 210 °C, with a cooling rate of 40 $°C.min^{-1}$. The DSC thermograms that *Choupin* obtained are shown on Figure 1.15. As it can be observed, there is a gap between the beginning of the crystallization exothermic peak and the baseline. *Choupin* attributed it to the instrumental thermal inertia switching from the cooling to the isothermal step. At 230 °C the crystallization kinetics is higher, so the gap is more important.

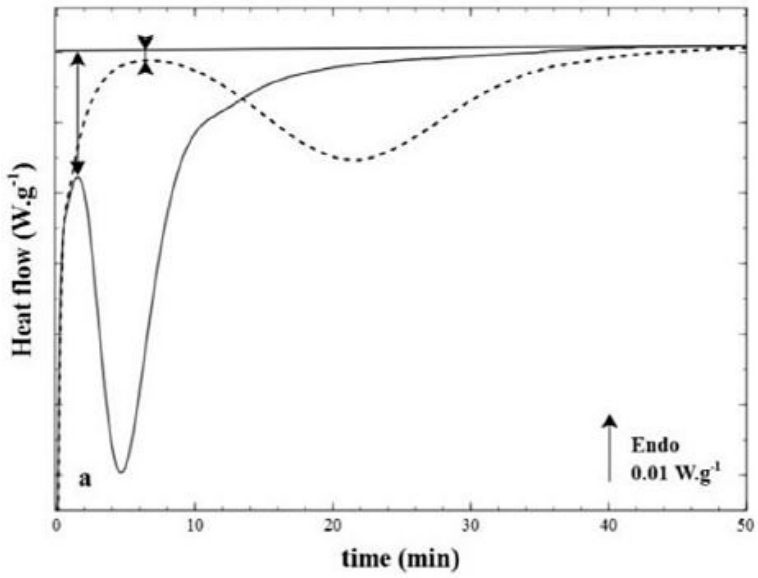

Figure 1.15: Isothermal DSC scans of crystallized PEKK 60/40 from the melt. Isothermal crystallization at 230 °C (solid line) and 210 °C (dashed line) [Choupin et al., 2017].

This gap at the crystallization peak beginning makes difficult the calculation of the area above the heat flow curve to determine the evolution of the relative volume crystallinity, which is obtained with the equation:

$$X_R(t) = \frac{\int_0^t Q(t)}{\int_0^{t\infty} Q(t)}\, dt \tag{1.19}$$

where $Q(t)$ is the heat flow measured at time t, and t_∞ is the time when the polymer is fully crystallized. Thus, it was necessary to rebuild the crystallization peak.

Choupin [Choupin, 2017] used the modified Hillier model to fit it with the relative crystallinity calculated from the extrapolated crystallization peak by a straight line. This approach gives good results regarding the fitting of the modified Hillier model with experiments. However, it gave some inconsistent results regarding the primary crystallization Avrami exponent, which is inconsistent with microscopic observations. This could be related to the linear extrapolation of the crystallization peak beginning.

Derivative Hillier model

Another approach developed by *Choupin* [Choupin, 2017] was to fit directly the Hillier model with the heat flow measured by DSC, using the derivative of Equation 1.19 :

$$X_R(t) = \frac{Q(t)}{\Delta H_c} = \frac{Q(t)}{\Delta H_m}\, dt \tag{1.20}$$

where ΔH_c is the crystallization enthalpy and ΔH_m is the melting enthalpy after crystallization.

Therefore, he used the derivative of the Hillier model, expressed by:

$$\frac{dX_R}{dt} = w_1 \frac{dX_1}{dt} + w_2 \frac{dX_2}{dt} \tag{1.21}$$

where the derivative of the primary crystallization kinetic is:

$$\frac{dX_1}{dt} = K_1 n_1 t^{n_1 - 1} exp(-K_1 t^{n_1}) \tag{1.22}$$

and the one for the secondary crystallization is expressed by:

$$\frac{dX_2}{dt} = 0^{n_2 - 1} K_2 n_2 [1 - exp(-K_1 t^{n_1})]$$
$$+K_2 n_2 \int_0^t [1 - exp(-K_1 \theta^{n_1})] exp[-K_2 (t-\theta)^{n_2}] \{(n_2 - 1)(t-\theta)^{n_2 - 2} - K_2 n_2 (t-\theta)^{2n_2 - 2}\}\, d\theta \tag{1.23}$$

For PEKK 7002, the Avrami exponents were found as follows. From the microscopy

observations *Choupin* [Choupin, 2017] found that the Avrami exponent for the primary crystallization n_1 is equal to 3, which corresponds to a three dimensional growth with an instantaneous nucleation. Then, the Avrami exponent for the secondary crystallization was determined with a multi linear regression fitting of the derivative Hillier model. The best fit of the derivative Hillier model was found for a secondary crystallization Avrami exponent $n_2 = 1$. This corresponds to a one dimensional crystallization growth with an instantaneous nucleation. Thus, by simplifying $n_2 = 1$ on equation (1.23), the derivative of the secondary crystallization kinetic becomes:

$$\frac{dX_2}{dt} = K_2[1 - exp(-K_1 t^{n_1})] + {K_2}^2 \int_0^t [1 - exp(-K_1 \theta^{n_1})] exp[-K_2(t-\theta)]\, d\theta \tag{1.24}$$

For the Hillier crystallization rate constants *Choupin* [Choupin, 2017] express them as a function of the initial number of potential nuclei (N_0) and the crystal growth rate (G) depending on the dimensionality of crystallization and the nucleation mode.

Using the Hoffmann and Lauritzen theory, the crystal growth is expressed by:

$$G_i(T) = G_{0i} exp[-\frac{n \cdot U^*}{n \cdot R(T - T_\infty)}] exp[-\frac{K_{gi}}{T \Delta T f}] \tag{1.25}$$

where G_{0i} is a pre-exponential factor independent of the temperature. The first exponential term contains the contribution of the diffusion process to the growth rate, where U^* is the activation energy of the molecular transfer through the melt crystal interface, T_∞ is the temperature below which diffusion stops ($T_\infty = T_g - 30K$) with $T_g = 155$°C and R is the gas constant ($8.314449 \pm 0.000056\ J \cdot mol^{-1} \cdot K^{-1}$ [Segovia et al., 2017]).

The second exponential term is the contribution of the nucleation process, where K_{gi} is the activation energy of nucleation for a crystal with a critical size, ΔT is the degree of supercooling ($\Delta T = T_{m0} - T$) with T_{m0} the equilibrium melting temperature and f is a correction coefficient for the temperature dependence of the melting enthalpy ($f = 2T/(T_{m0} + T)$). The index i for G_i, G_{0i} and K_{gi} is equal to 1 for primary crystallization and 2 for secondary crystallization.

Therefore, the primary rate constant is:

$$K_1(T) = K_{01} exp[-\frac{n_1 \cdot U^*}{R(T - T_\infty)}] exp[-\frac{n_1 \cdot K_{g1}}{T \Delta T f}] \tag{1.26}$$

And, the secondary crystallization rate constant is equal to:

$$K_2(T) = K_{02} exp[-\frac{n_2 \cdot U^*}{R(T - T_\infty)}] exp[-\frac{n_2 \cdot K_{g2}}{T \Delta T f}] \tag{1.27}$$

with the pre-exponential factors $K_{01} = \frac{4}{3}\pi N_{01}{G_{01}}^3$ and $K_{02} = N_{02}G_{02}$ independent of temperature.

Then, the primary crystallization weight factor was modeled by *Choupin* [Choupin, 2017] by a linear equation dependant on the crystallization temperature:

$$w_1(T) = a_1 T + b_1 \tag{1.28}$$

This derivative of the Hillier model approach was developed and used by *Choupin* [Choupin, 2017] to fit it with the heat flow measured by DSC divided by the melting enthalpy $\triangle H_m$ (Equation 1.20) for PEKK 7002 isothermal crystallization at 250°C, as shown on Figure 1.16. He indicated that 250°C is the temperature for which the crystallization kinetics of PEKK 7002 is the highest.

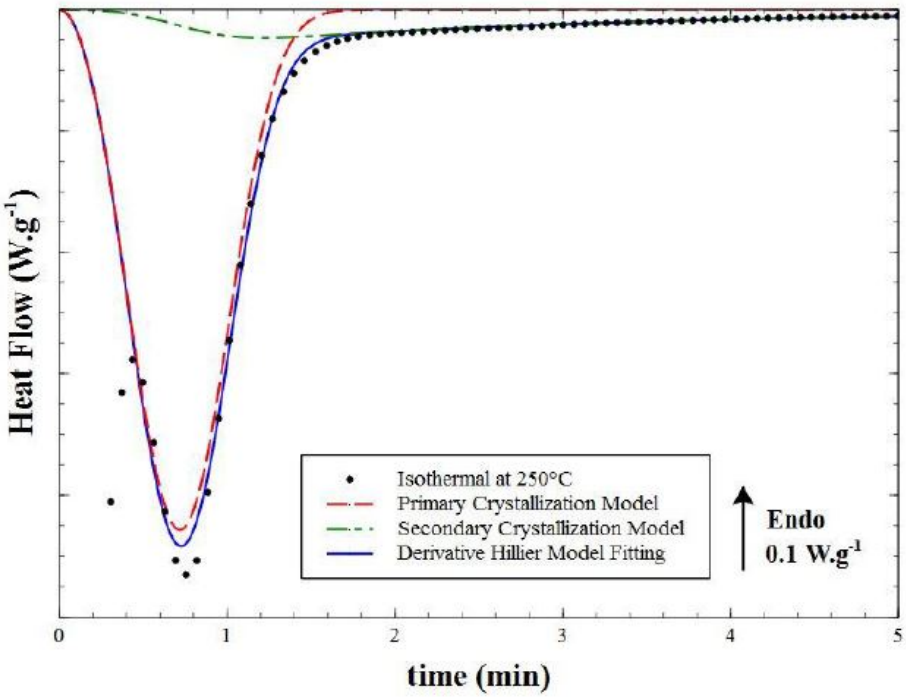

Figure 1.16: DSC thermograms of neat PEKK 7002 crystallized from the melt at 250°C with the fitting of the derivative Hillier model (solid line) and the primary (dash curves) and secondary crystallization (dash-dot curves) modeling [Choupin, 2017].

For the Hillier parameters K_1 and K_2 *Choupin* plotted their logarithm (Figure 1.17) and fitted them with the Hoffman and Lauritzen model, using equations (1.26) and (1.27), for PEKK 7002 and 6002. PEKK 7002 crystallization kinetics is the most important at 245°C. Results obteined for K_{0i} and K_{gi} are presented in Table 1.8.

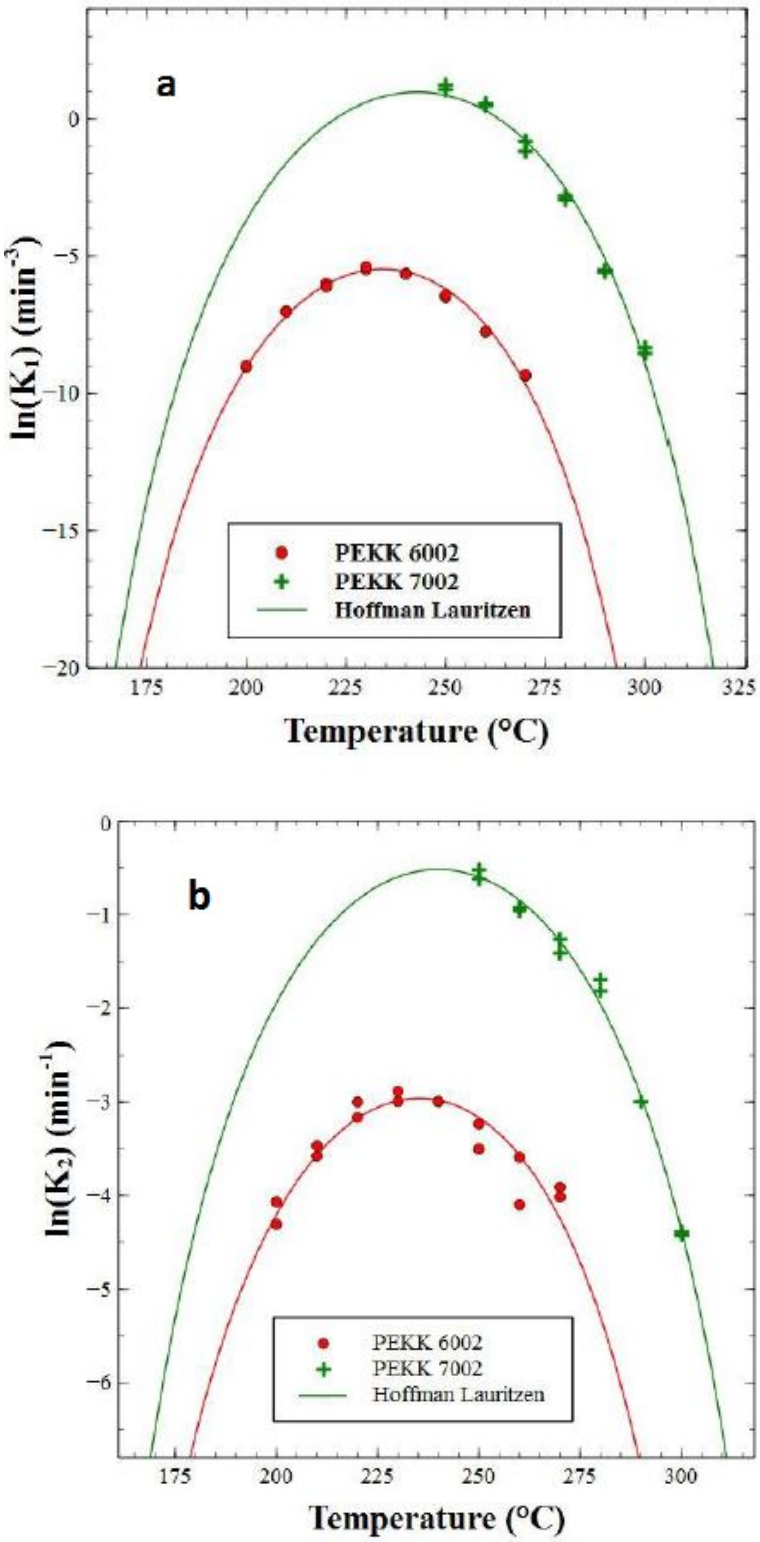

Figure 1.17: Logarithmic plot of the primary (a) and the secondary crystallization (b) rate constants vs temperature for neat PEKK 6002 and 7002 isothermal crystallization from the melt with the Hoffman and Lauritzen model fitting [Choupin, 2017].

Then, primary crystallization weight factor for PEKK 7002 was plotted as function of temperature (Figure 1.18) and fitted with the linear model from equation (1.28). a_1 and b_1 are also presented in Table 1.8. From the Figure 1.18 it is observed that the weight factor of PEKK 7002 is quasi constant as a function of temperature. Its value is around 0.78. Its weight factors are also higher than for PEKK 6002, which could be attributed to a more organized crystallization leaving less room to the growth of the secondary crystallization.

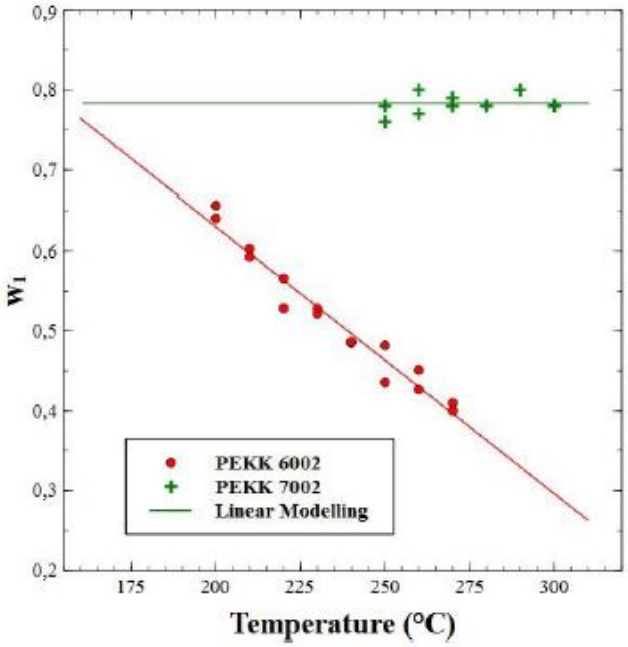

Figure 1.18: Weight factor of the primary crystallization vs temperature for PEKK 6002 and 7002 isothermal crystallization from the melt with the linear model fitting [Choupin, 2017].

Kinetic parameters	PEKK 6002	PEKK 7002
T_{m0} (°C)	340	360
K_{01} (min^{-3})	$1.1.10^{14}$	$1.79.10^{16}$
K_{02} (min^{-1})	$1.1.10^{4}$	$2.6.10^{5}$
K_{g1} (K^2)	$3.6.10^{5}$	$4.0.10^{5}$
K_{g2} (K^2)	$3.5.10^{5}$	$4.4.10^{5}$
U^* ($J.mol^{-1}$)	$4.7.10^{3}$	$4.7.10^{3}$
a_1 (K^{-1})	$-3.3.10^{-3}$	0
b_1	2.2	0.78

Table 1.8: Parameters of the kinetic models for the crystallization rate constants (K_1 and K_2) and the weight factor (w_1) for PEKK 6002 and 7002 crystallized from the melt [Choupin, 2017].

Time-Temperature-Transformation (TTT) diagrams for PEKK 7002 were also modeled by *Choupin* (Figure 1.19). The TTT diagram shows a very fast crystallization kinetics of PEKK 7002. We can notice that it fully crystallizes at 240°C in 10 minutes.

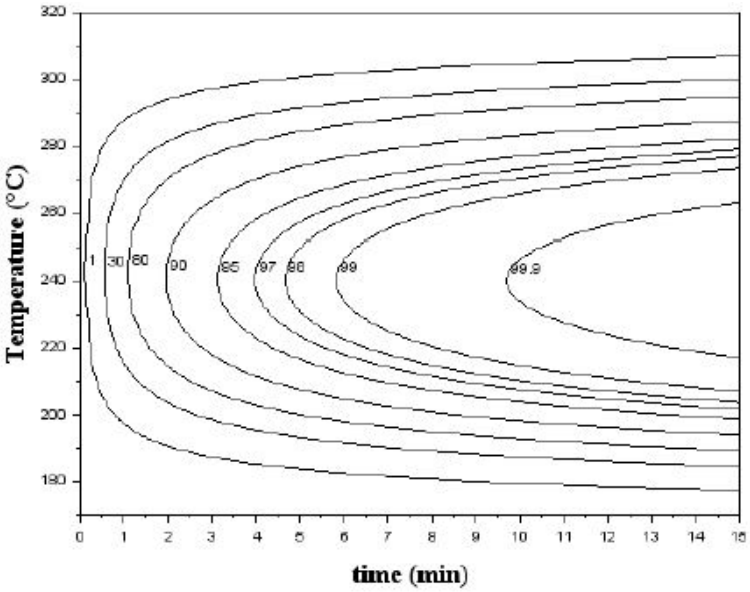

Figure 1.19: TTT diagram of the relative crystallinity for the overall crystallization for PEKK 7002 crystallized from the melt [Choupin, 2017].

1.4.2.2 Non-isothermal crystallization kinetic models

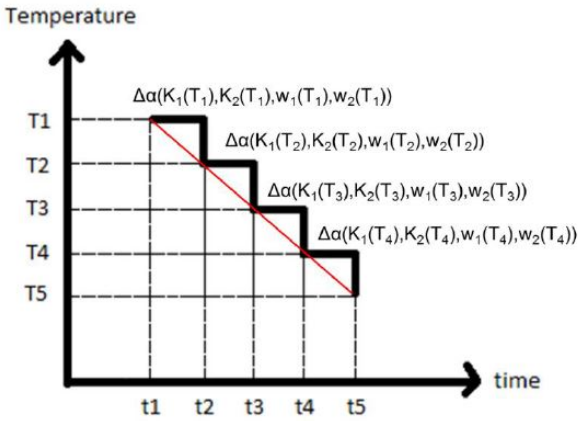

Figure 1.20: Diagram of the decomposition of a non-isothermal crystallization cycle by small isotherms [Choupin, 2017].

The non-isothermal crystallization kinetics allows to predict the crystallinity of the material for any processing cycle. Non-isothermal crystallization cycles can be considered as a succession of small isotherms that occur at a temperature T (Figure 1.20). Therefore, it is possible

to determine the relative crystallinity for non-isothermal crystallization by summing up the relative crystallinity formed during each isotherm [Choupin, 2017].

In his work, *Choupin* [Choupin, 2017] also investigated this type of crystallization for PEKK 7002. He proposed a model based on the Hillier model to take into account the primary and secondary crystallization of the material. This model was the derivative model proposed by Patel and Spruiell [Patel and Spruiell, 1991] extended to the secondary crystallization from the Hillier model, which is expressed by:

$$\frac{dX_R}{dt} = w_1 n_1 K_1(T)^{\frac{1}{n_1}} \{-ln[1 - X_1(t)]\}^{\frac{n_1-1}{n_1}} [1 - X_1(t)] + w_2 n_2 K_2(T)[X_1(t) - X_2(t)] \quad (1.29)$$

with $w_1 + w_2 = 1$. This equation allows then to determine the relative crystallinity for each isotherm at a temperature T, according to the non-isothermal crystallization kinetic principle.

From Equation 1.29 $X_1(t)$ is expressed with the initial Avrami equation for the first crystallization (Equation 1.14), and $X_2(t)$ is expressed with Equation 1.16.

The derivative of the primary crystallization is expressed with the Avrami derivative model proposed by Patel and Spruiell [Patel and Spruiell, 1991] for any cooling rate, written as:

$$\frac{dX_1}{dt} = n_1 K_1(T)^{\frac{1}{n_1}} \{-ln[1 - X_1(t)]\}^{\frac{n_1-1}{n_1}} [1 - X_1(t)] \quad (1.30)$$

where $K_1(T)$ is described by Equation 1.26, and with t coming from Equation 1.14 and being:

$$t = \left[- \frac{ln(1 - X_1(t))}{K_1(T)} \right]^{\frac{1}{n_1}} \quad (1.31)$$

Then, the derivative of the secondary crystallization kinetics equation is expressed from Equation 1.16 with $n_2 = 1$ (as determined from the isothermal model for PEKK7002):

$$\frac{dX_2}{dt} = n_2 K_2[1 - exp(-K_1 t^{n_1})] - {K_2}^2 \int_0^t [1 - exp(-K_1 \theta^{n_1})] exp[-K_2(t - \theta)]\, d\theta \quad (1.32)$$

This equation was then simplified by using Equations 1.14 and 1.16, obtaining:

$$\frac{dX_2}{dt} = n_2 K_2(T)[X_1(t) - X_2(t)] \quad (1.33)$$

with $K_2(T)$ described by Equation 1.27.

Numerical scheme for non–isothermal crystallization

To solve the non-isothermal model Equation 1.29, *Choupin* used the implicit Euler method expressed by:

$$X_R(t+\Delta t,T) = X_R(t,T) + f(X_R(t+\Delta t,T))\Delta t \tag{1.34}$$

where $X_R(t+\Delta t,T)$ is the relative crystallinity at time $t+\Delta t$, $X_R(t,T)$ is the relative crystallinity at time t, $f(X_R(t+\Delta t,T)) = \frac{dX_R}{dt}$ wiht $t = t+\Delta t$ and Δt is the time between t and $t+\Delta t$, which has to be small enough to ensure Euler hypotheses.

Applying the Euler method to the primary crystallization (Equation 1.30), and searching to solve $X_1(t+\Delta t,T)$, Equation 1.34 becomes:

$$X_1(t+\Delta t,T) - X_1(t,T) - n_1 K_1(T)^{\frac{1}{n_1}} - ln[X_1(t+\Delta t,T)]^{\frac{n_1-1}{n_1}}[1-X_1(t+\Delta t,T)]\Delta t = 0 \tag{1.35}$$

where $K_1(T)$ is determined by solving Equation 1.26.

Thus, for the secondary crystallization (Equation 1.33), Equation 1.34 becomes:

$$X_2(t+\Delta t,T) - X_2(t,T) - K_2(T)[X_1(t+\Delta t,T) - X_2(t+\Delta t,T)]\Delta t = 0 \tag{1.36}$$

where $K_1(T)$ and $K_2(T)$ are calculated with Equation 1.26 and Equation 1.27 respectively and $X_1(t+\Delta t,T)$ is the relative crystallinity from the primary crystallization, determined by solving Equation 1.35.

Finally, the total relative crystallinity for each isotherm at temperature T is expressed by:

$$X_R(t+\Delta t,T) = w_1(T)X_1(t+\Delta t,T) + w_2(T)X_2(t+\Delta t,T) \tag{1.37}$$

where $X_1(t+\Delta t,T)$ and $w_2(T)X_2(t+\Delta t,T)$ are determined by solving Equation 1.35 and 1.36 respectively, and $w_1(T)$ and $w_2(T)$ are calculated with Equation 1.28.

The continuity equation for primary and secondary crystallization needs to be used to pass from a temperature T_1 to a very close temperature T_2, which are:

$$w_1(T_1)X_1(t,T_1) = w_1(T_2)X_1(t,T_2) \tag{1.38}$$

$$w_2(T_1)X_2(t,T_1) = w_2(T_2)X_2(t,T_2) \tag{1.39}$$

Then $X_1(t+\Delta t, T_2)$ can be calculated by replacing $X_1(t,T)$ in Equation 1.35 with:

$$X_1(t,T_2) = \frac{w_1(T_1)X_1(t,T_1)}{w_1(T_2)} \tag{1.40}$$

Also $X_2(t+\Delta t, T_2)$ is calculated by replacing $X_2(t,T)$ in Equation 1.36 with:

$$X_2(t,T_2) = \frac{w_2(T_1)X_2(t,T_1)}{w_2(T_2)} \tag{1.41}$$

Then, the total relative crystallinity $X_R(t+\Delta t, T_2)$ is calculated with Equation 1.37 with $T = T_2$.

Choupin [Choupin, 2017] applied this numerical scheme of the non-isothermal crystallization to PEKK 7002 to obtain the evolution of the relative crystallinity modeling as function of temperature for different cooling rates. These modelings were also compared to the DSC thermograms obtained experimentally.

At first, *Choupin* modeled the non-isothermal crystallization of PEKK 7002 using the same crystallization kinetic parameters identified with the isothermal model form Table 1.8. But he observed that the non-isothermal crystallization kinetic modeling over-predicts the experimental results. He attribute this phenomenon to the iso-kinetic hypothesis assuming that nucleation an growth kinetics are proportional, which could not be fully true for non-isothermal crystallization. Because of that, *Choupin* modified some of the Hoffman and Lauritzen parameters for the primary crystallization process from the isothermal crystallization, to have a better correspondence between the non-isothermal crystallization kinetics modeling and experiments. These modified parameters are shown on Table 1.9.

Hoffman and Lauritzen parameters	PEKK 7002	
	Isothermal	Non-Isothermal
K_{01} (min^{-3})	$1.79.10^{16}$	$1.79.10^{16}$
K_{g1} (K^2)	$4.0.10^5$	$4.0.10^5$
U^* ($J.mol^{-1}$)	$4.7.10^3$	$4.9.10^3$

Table 1.9: Crystallization kinetic parameters modified for PEKK 7002 crystallized from the melt [Choupin, 2017].

Using the modified kinetic parameters, *Choupin* plotted the non-isothermal kinetic modeling and compared it with the DSC thermograms for different cooling rates, as shown on

Figure 1.21. As it can be seen, the relative crystallinity obtained from the non-isothermal modeling has a good agreement with the experiments for each cooling rate studied for PEKK 7002. This good agreement validates the new method for the non-isothermal crystallization kinetic modeling proposed by *Choupin* [Choupin, 2017].

Nevertheless, it is also notices that at low cooling rates (1 °C·min^{-1}) and high conversion rates, a small discrepancy occurs between data and modeling. Actually, the crystallization kinetics modeling is lower that experiments at the end of crystallization. *Choupin* indicates that it can might be due to low w_1 at high temperatures (above 270 °C), meaning that $w_1(T)$ is probably not constant for PEKK 7002. This phenomenon was not possible to identify by *Choupin* because it was necessary to make some isothermal experiments at temperatures between 280 °C and 300 °C, but it is very difficult to do such experiments at so low crystallization kinetics [Choupin, 2017].

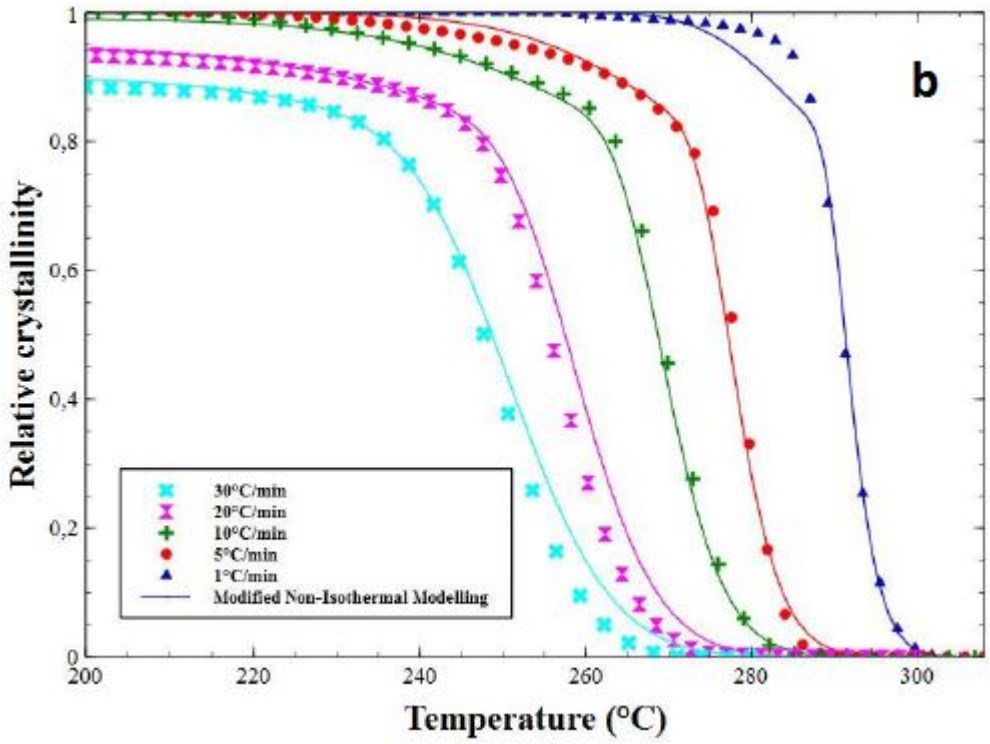

Figure 1.21: Relative crystallinity X_R against temperature for PEKK 7002 crystallized from the melt at different cooling rates with the modified non-isothermal crystallization kinetics modeling [Choupin, 2017].

Perez-Martin et al. also studied the non-isothermal crystallization kinetics of PEKK in its grade 70/30 [Pérez-Martín et al., 2022]. They used a dual Nakamura model to predict the evolution of the relative crystallinity X_R of the material for different cooling rates. The model consists in two separate Nakamura models acting in parallel to include both primary and secondary cristallization, as shown in Equation 1.42:

$$X_R(t) = w_1 \left\{ 1 - exp\left[- \left(\int_0^t K_1(T)^{\frac{1}{n_1}} dt \right)^{n_1} \right] \right\} + w_2 \left\{ 1 - exp\left[- \left(\int_0^t K_2(T)^{\frac{1}{n_2}} dt \right)^{n_2} \right] \right\} \tag{1.42}$$

where $K_1(T)$ and $K_2(T)$ are described by the crystal growth rate expressed by the Hoffmann-Lauritzen model, and already shown on Equations 1.26 and 1.27. And, in those equations, T is considered to be the temperature at time t dependent on the cooling rate r, calculated with Equation 1.43:

$$T = T_{mc} - r \cdot t \tag{1.43}$$

where T_{mc} is the melt temperature from which crystallization begins.

In their study *Perez-Martin et al.* observed that the weight factors for the primary and secondary crystallization variate with cooling rate, as shown in Figure 1.22. This variation can be taken into account by introducing the variation of w_1 with the cooling rate r, defined by Equation 1.44:

$$w_1 = -1.399 r^{-0.8707} + 1 \tag{1.44}$$

and keeping in mind that $w_1 + w_2 = 1$.

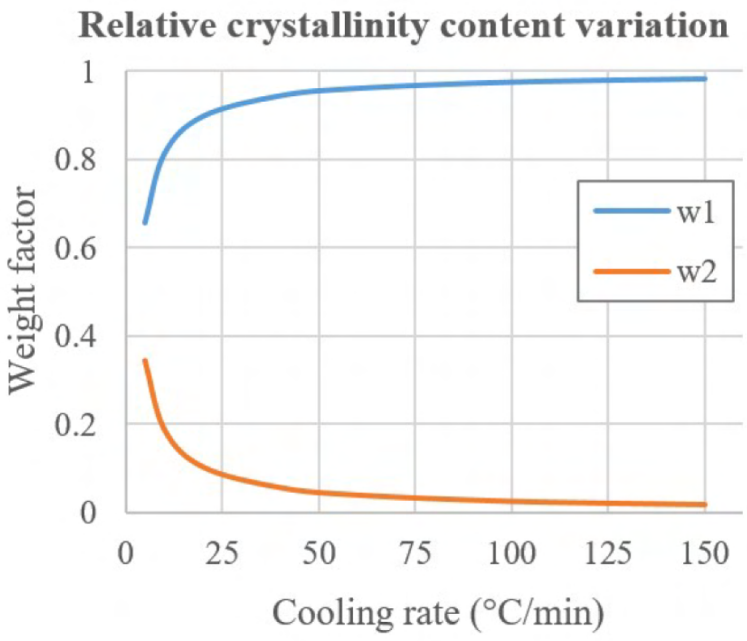

Figure 1.22: Variation of the crystallization relative content (w_1 and w_2) with cooling rate for non-isothermal crystallization kinetics of PEKK 70/30 [Pérez-Martín et al., 2022].

In addition, *Perez-Martin et al.* determined new values for the Avrami exponent (n_1 and n_2) and for the Hoffmann-Lauritzen parameters for crystal growth. The values for n_1 and n_2 were determined from modeling the isothermal crystallization kinetics of the material, being equal to 3 and 2, respectively. The parameters for the crystal growth rates were determined by the best fitting of the Hoffmann-Lauritzen models with the experimental data for each $K_i(T)$ on isothermal crystallization of PEKK. The compilation of parameters determined by *Perez-Martin et al.* for the non-isothermal modeling of PEKK crystallization kinetics are shown in Table 1.10.

Parameter	***PEKK 70/30***
n_1	3
n_2	2
w_1	$1.399r^{-0.8707} + 1$
w_2	1 - w_1
$U^*[J.mol^{-1}]$	4.7×10^3
$K_{01}[min^{-3}]$	1.5×10^{14}
$K_{g1}[K^2]$	2.486×10^5
$K_{02}[min^{-3}]$	5.041×10^7
$K_{g2}[K^2]$	2.025×10^5

Table 1.10: Parameters of the non-isothermal crystallization kinetic model for PEKK 7002. (r accounts for the cooling rate in the calculation of w_1) [Pérez-Martín et al., 2022]. U^* from [Choupin et al., 2017].

Figure 1.23 shows the final resulting fits of the dual Nakamura model to the non-isothermal crystallization experimental data of PEKK 70/30 studied by *Perez-Martin et al.*.

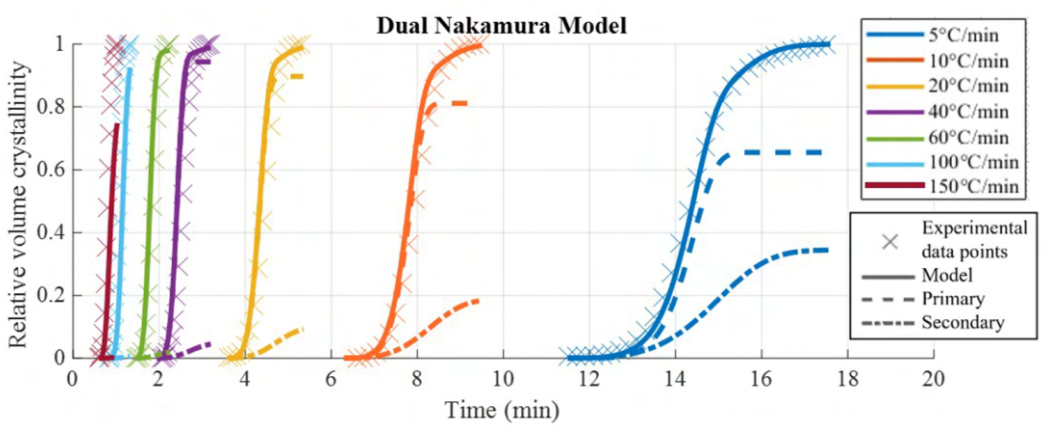

Figure 1.23: Dual Nakamura Model fist to the X_R evolution for non-isothermal crystallization of PEKK 70/30 for different cooling rates [Pérez-Martín et al., 2022].

1.5 Synthesis

This chapter has enlightened the path for welding thermoplastics by laser transmission welding. First, a brief introduction on the importance of thermoplastics on daily life an industry was given. This conducted to highlight the importance of welding these kind of polymers, putting emphasis on the laser transmission welding technique, its advantages, disadvantages, applications and fundamentals. Then, the importance of material properties and process parameters of the welding process and weld quality was described. Further description was made to explain the physical phenomena involved during LTW. To finish with a context on laser welding of semi-crystalline thermoplastics, how these materials affect the welding process, and how the welding parameters influence the material behavior.

From this state of art, it appears that from the many welding techniques explored for thermoplastic polymers, LTW rises as promising and advantageous. Understanding this welding method from its process principle, laser technologies, welding techniques and process parameters, allow to find the good combination of those factors to achieve welding of thermoplastic parts.

In addition, it has been shown that the laser transmission welding of semi-crystalline thermoplastics drives some difficulties compared to amorphous ones. Thus, understanding the material microstructure and its behavior is of importance for LTW, like described for PEKK in the present chapter. That will allow to select the optimum weld process parameters to ensure welding and obtain good weld joint quality.

Chapter 2

Material of study: PEKK samples and properties for LTW

Contents

2.1 Introduction 54
2.2 Overview of the welded material 54
2.2.1 The poly-ether ketone ketone 54
2.2.2 PEKK grade 70/30 60
2.3 Samples manufacturing for welding 60
2.3.1 Drying process for PEKK pellets 61
2.3.2 Injection molding process and parameters 63
2.3.3 Crystallization phenomena from the melt state 65
2.4 Plates characterization for LTW 68
2.4.1 Thermal transitions and degree of crystallinity by DSC 69
2.4.2 Heat capacity and thermal conductivity 72
2.4.3 Optical properties for laser welding 72
2.5 Synthesis 85

2.1 Introduction

The present chapter covers the description, fabrication, and characterization of the material of study. The aim is to establish the groundwork to study the suitability and performance of the material for the laser transmission welding process (LTW). In the first section, an overview of the studied material is presented, outlining its composition and grades. The influence of these grades on the material transitions and crystallization properties is presented to justify the final choice of material grade.

The next sections of the chapter focus on the manufacturing and characterization of the samples for welding. The fabrication process of the samples by injection molding is described, highlighting the importance of the drying conditions of the bulk material before processing, and of the injection parameters to obtain the desired crystalline states on the polymer samples. The techniques used to characterize the samples are also described, and the results on the properties of the samples are discussed. The properties characterized are those of relevance to the feasibility of the LTW process such as thermal and optical properties and their correlation with the crystallinity degree of the samples.

2.2 Overview of the welded material

The material used in this study is a semi-crystalline (SC) high-performance (HP) thermoplastic (TP): the Polyetherketoneketone (PEKK). A grade of unfilled PEKK is used to obtain different crystalline states when producing the samples. This section describes the present material and its general properties.

2.2.1 The poly-ether ketone ketone

Poly-aryl ether ketone ketone (PEKK) is a semi-crystalline thermoplastic member of the high-performance poly-aryl ether ketone (PAEK) family. As mention in chapter 1 section 3.4, there are different varieties of PAEK depending on the ratio and structure of ether to ketone group. This difference is mostly emphasized by the ketone content (percentage of ketone) which can vary from 0 in PPO to 67 % in PEKK. Table 2.1 shows the chemical structure and linkage composition of some member of the PAEK family. This ratio of ether/ketone modifies the polymer properties concerning their thermal transitions (T_g and T_m), thus affecting their heat resistance and processing temperatures, as well as their melt viscosity. Figure 2.1 shows how the T_g and T_m transition temperatures increase with increasing the ratio of ether to ketone, with PEKK reaching the highest values (theoretically).

The ketone content has also an effect on the crystallization of PAEKs. The addition of ketone linkages improves the packaging efficiency of the unit-cell structure, producing a larger crystal bonding energy (or cohesiveness) [Gardner et al., 1992]. Figure 2.2a shows the X-ray powder diffraction patterns of three members of PAEK, PEEK, PEK and PEKK,

crystallized from the melt. As seen, even if they have similar diffraction patterns, the increase in the ketone content generates a small change in peak locations to a lower angle. This shift generates systematic modifications in the unit-cell parameters, as observed in Figure 2.2b.

Structure	Name	Ketone (%)
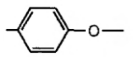	PPO	0
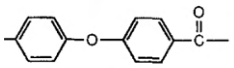	PEK	50
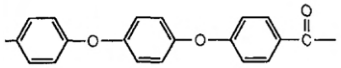	PEEK	33
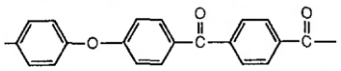	PEKK	67

Table 2.1: Some members of the PAEK family with their chemical structure and ketone contents [Gardner et al., 1992].

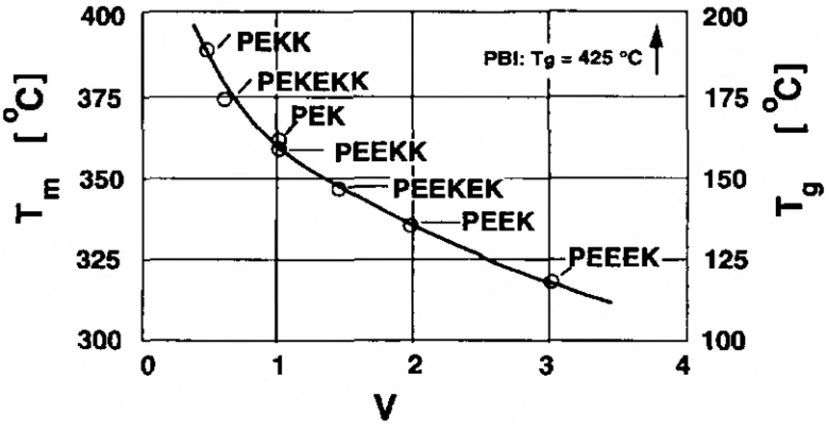

Figure 2.1: Variation of the melting and glass transition temperature of PAEK varieties as function of ether/ketone ratio (V) [Friedrich et al., 1995].

PEKK is the member of PAEKs with the highest percentage of ketone linkages of 67 %. This material is prepared from diphenyl ether (DPE) combined with terephthalic acid (T), leading to *para*-linkages, and/or with isophthalic acid (I), creating *meta*-linkages (FigureX). There are different grades of PEKK that differ from each other in their terephthalic acid/isophthalic acid (T/I) ratios [Choupin et al., 2017], as shown on Table 2.2. Because of the synthetic route, these polymers can be thought of as copolymers of the "diads" containing -DPE-T-DPE-T (TT) and/or -DPE-T-DPE-I- (TI), showing a polymer diad distribution dependant of the T/I ratios (Table 2.2) [Gardner et al., 1992].

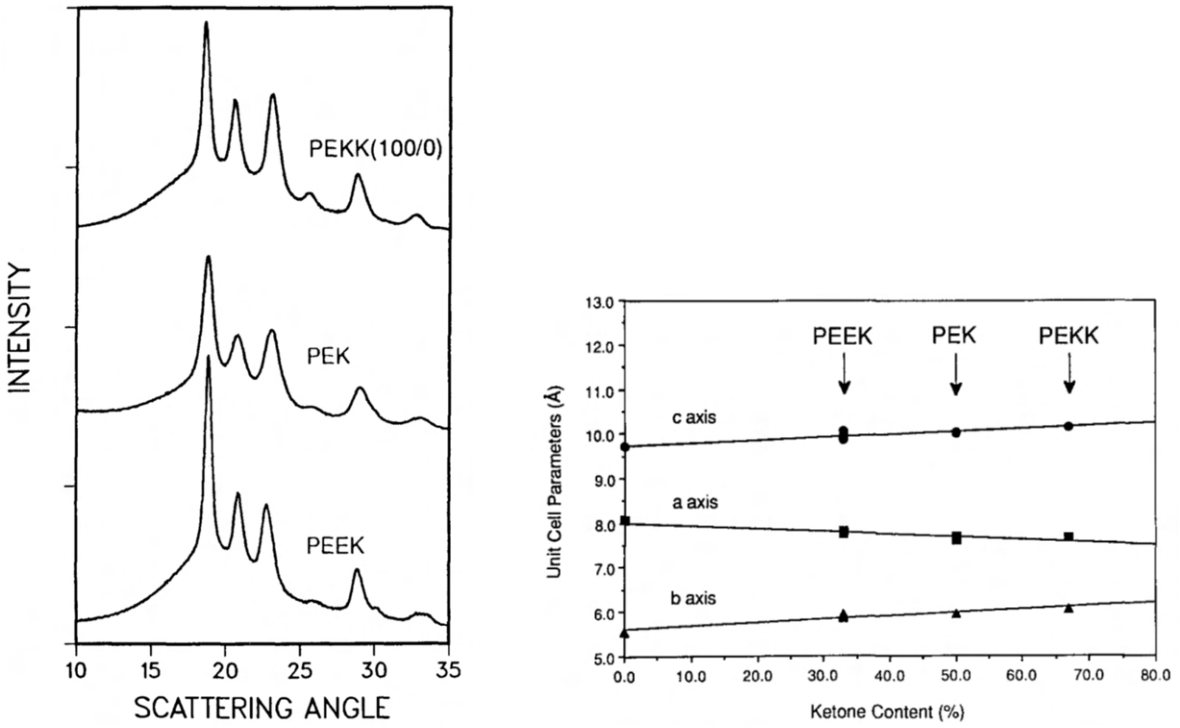

(a) (b)

Figure 2.2: PEEK, PEK and PEKK (T/I = 100) (a) X-ray powder diffraction patterns and (b) unit-cell parameters vs. ketone content [Gardner et al., 1992].

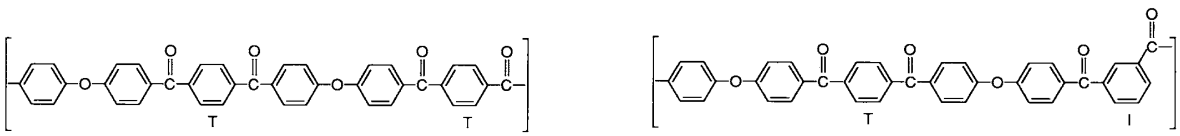

(a) (b)

Figure 2.3: PEKK chemical structure when combining DPE with (a) terephthalic (T) acid or with (b) isophthalic (I) acid [Hsiao et al., 1994].

PEKK grade[1]	T/I Ratio	TT/TI
5000	50/50	50/50
6000	60/40	20/80
7000	70/30	40/60
8000	80/20	60/40
all-para linked	100/0	100/0

Table 2.2: PEKK grades T/I ratios and their diads distribution.

[1]The grade of PEKK naming is based on the nomenclature defined by Arkema company.

The grade (T/I ratio) modifies the melting temperature (T_m) of PEKK. Incorporation of isophthaloyl (*meta* linkages) into PEKK allows the melting temperature of the material to decrease, while keeping a high glass temperature (T_g around 165°C). Gardner et al. [Gardner et al., 1992] represented this with a linear relationship between the equilibrium melting temperature and the percentage of terephthalate content in PEKK (Figure 2.4). In the Figure it is visible how the melting temperature increases with T content, whereas the glass transition remains almost constant. The viscosity of PEKK is also modified according to the T/I ratio, a low T/I ratio decreases the viscosity of the material, facilitating its processing.

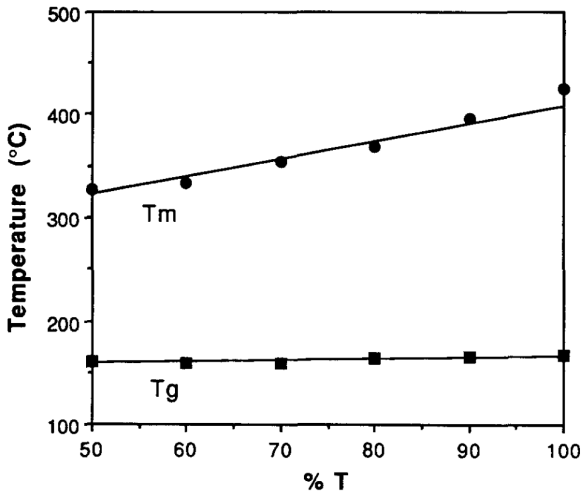

Figure 2.4: Relationship between the terephthalate content (% T) and the equilibrium melting temperature, as well as the glass transition temperatures [Gardner et al., 1992].

As for PEEK, PEKK can be obtained in amorphous form by rapid cooling or quenching. In addition, different levels of crystallinity can be reached on PEKK by alternative or subsequent processing, such as solvent casting or annealing the amorphous form, or by slow cooling the material from melt. However, PEKK is less crystalline than PEEK. Whereas PEEK can reach a high degree of crystallinity of 42 % by solvent crystallization [Avakian et al., 1990], the maximum degree of crystallinity reached by PEKK is around 27 % when annealed [Pérez-Martín et al., 2022].

The crystallinity structure of PEKK is similar to other PAEKs. PEKK copolymers, regardless of T/I ratio, develop a conventional crystalline structure *form 1*, similar to other PAEKs, from melt crystallization. In addition, they can be induced to show a second crystalline modification, *form 2*, developed by solvents or cold crystallization [Gardner et al., 1992]. *Gardner et al., 1992* attributed its existence to the high ketone content of PEKK. Figure 2.5 shows the schematic diagrams of the chain packing modes for form 1 and form 2 that predict diffraction patterns obtained by Gardner. Figure 2.6 shows the diffraction patterns obtained by *Gardner et al., 1992* on different grades of PEKK. As can be seen for melt-crystallized PEKKs (Figure 2.6a), the T/I ratio does not modify the reflection positions, thus the unit-cell parameters remain consistent. However, the crystalline phase in a melt-crystallized PEKK composition with higher T content, like PEKK 7000 (T/I ratio of 70/30),

mainly consist of TT diads (crystals). When crystallizing amorphous PEKK by solvent (exposed to methylene chloride), the diffraction patterns (Figure 2.6b) show a new reflection peak at $2\theta = 15.6°$. Gardner explained this peak as the reflection of a one-chain (metrically) orthorhombic unit cell, designated as form 2. In addition, when PEKK is cold crystallized, a mixture of form 1 and form 2 is produced in the material, as found on PEKK 50/50 by *Gardner et al., 1992*. Different morphologies are thus produced according to the crystallization conditions. *Gardner et al., 1992* created a *phase diagram* for PEKK to summarize the apparition of the two polymorphs (form 1 and form 2) in the PEKK copolymers in function of the T/I ratio and the crystallization conditions (Figure 2.7) [Gardner et al., 1994]. The two different crystal structures of PEKK are:

- A conventional form 1 structure, the same as that observed in PEEK and PEK, which has a two-chain orthorhombic unit cell (lammellae growing direction a = 0.767 nm, b = 0.606 nm and chain axis c = 1.008 nm) [Cheng et al., 1996].
- And a new form 2 structure, which can be developed from solvent or cold crystalliation. Form 2 has a one-chain (metrically) orthorhombic unit cell (a = 0.786 nm, b = 0.575 nm and c = 1.016nm). The form 2 structure is capable of converting into form 1 after melting. [Gardner et al., 1992]

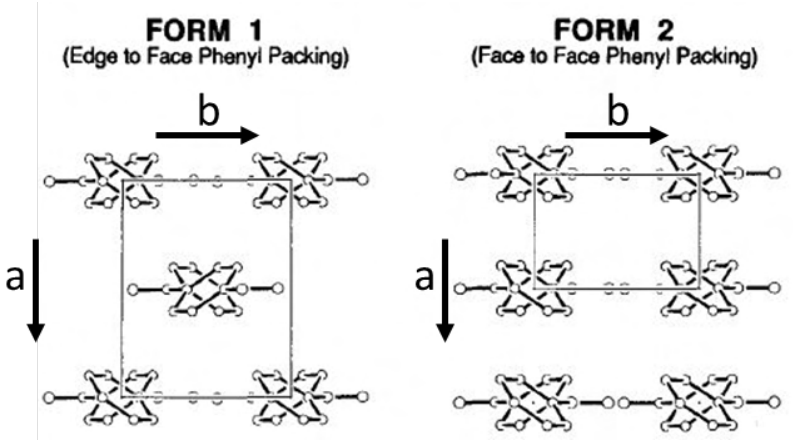

Figure 2.5: Crystal unit cells of PEKK 7002: form 1 and form 2 [Gardner et al., 1992].

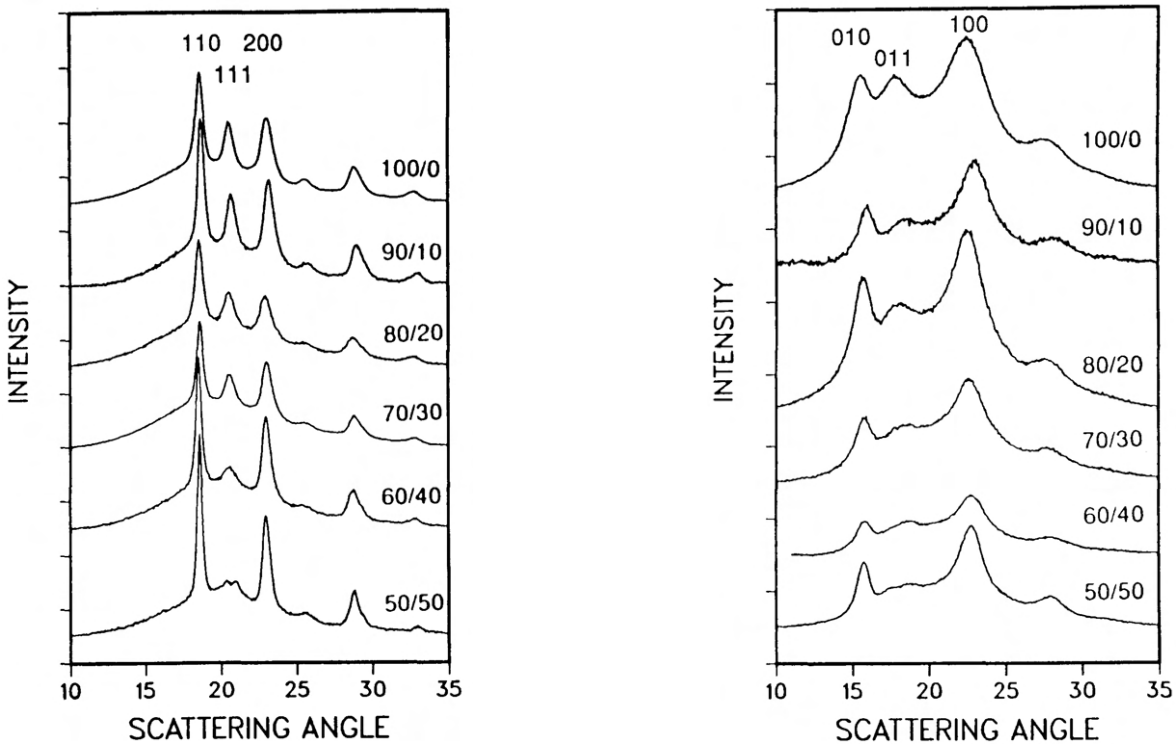

Figure 2.6: X-ray diffraction patterns of different grades of PEKK when (a) melt crystallized and (b) solvent crystallized [Gardner et al., 1992].

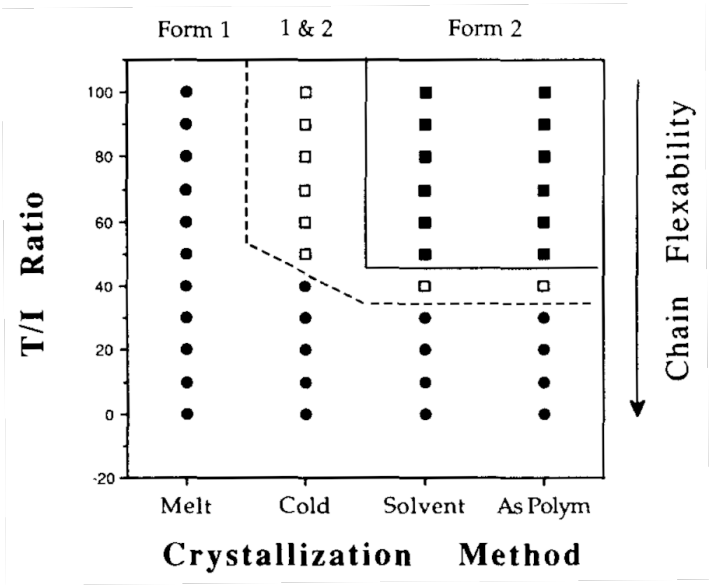

Figure 2.7: Phase diagram of PEKK [Gardner et al., 1994].

2.2.2 PEKK grade 70/30

PEKK copolymers 80/20, 70/30 and 60/40 are the most used and studied since the last two decades, and the ones that are commercialized [Arkema, 2024]. As for the melting temperature, the crystallization capabilities of PEKK are also modified by its T/I ratio. Increasing the content of para-linkages increases the chain linearity, which increases the material crystallinity and the crystallization kinetics, , thus its mechanical properties. As for any application where performance is necessary, high crystallinity of the material is desired. Increasing the crystallinity increases the strength of the material, its stiffness, toughness, and chemical resistance. Therefore, controlling this crystallinity is of importance. The crystallization rate of PEKK copolymers increases in the order (60/40) < (70/30) ≃ (80/20) < (90/10) [Gardner et al., 1992].

The three grades of PEKK mentioned are commercialized by Arkema, the main supplier of PEKK in France, under the name of Kepstan®[Arkema, 2024]. Those PEKK resins are available in pellets, powder, and compound forms (with glass or carbon fibers). In addition, three different levels of viscosity are available for the material: level 1, 2 and 3, for high, medium, and low viscosity, respectively [Inc., 2018]. Typically, the viscosity level 2 is used for the injection molding fabrication technique.

In this work, PEKK grade 70/30 is chosen as material of study, because its high tuneability thanks to it medium crystallization kinetics. Indeed, the fact that the crystallization rate of PEKK 70/30 is medium allows it to better control and modify its degree of crystallinity with controlling the processing conditions. In addition, level 2 of viscosity (PEKK 7002) is chosen to be able to fabricate the samples by injection molding.

2.3 Samples manufacturing for welding

The bulk material of the study is the Kepstan®PEKK 7002, supplied by Arkema France in pelleted form. The PEKK pellets are processed by injection molding to produce the welding samples. Square plates with dimenstion of $95 \times 95\ mm^2$ are manufactured. Two different crystalline states of unfilled PEKK are obtained in the injected plates: quasi-amorphous (PEKK-A) and semi-crystalline (PEKK-SC). The quasi-amorphous state indicates a low degree of arrangement of the semi-crystalline polymer molecules, having a molecular arrangement similar to an amorphous polymer, and a low degree of crystallinity. The semi-crystalline state denote a high degree of organization on the SC polymer molecules, which implies a high degree of crystallinity on the sample. Those two different crystalline state of the material are chosen to function as upper and lower parts on the LTW welding process. Based on previous studies of LTW of PEKK 6002 [Villar et al., 2018], the quasi-amorphous state of PEKK is suited to serve as upper semi-transparent part for LTW, whereas the semi-crystalline state is appropriate as lower absorbent part. To achieve the two crystalline states of PEKK, different cooling time and temperature are used at the cooling step in the mold, as will be later explained in Section 2.3.2.

Figure 2.8 shows the different PEKK plates obtained by injection molding. The PEKK quasi-amorphous plates are manufactured in 2 and 4 mm thick (PEKK-A2 and PEKK-A4 respectively), this to study the influence of thickness on the sample suitability as upper semi-transparent part for the LTW process. PEKK-SC plates are injected only in 2 mm thick, based on the fact that this is the minimum functional thickness for PEKK to serve as lower absorbent part [Villar et al., 2018]. After injection, the PEKK plates are cut into rectangular parts of 25 ± 3 mm width by 95 mm long, to obtain the final samples for welding (Figure 2.8c).

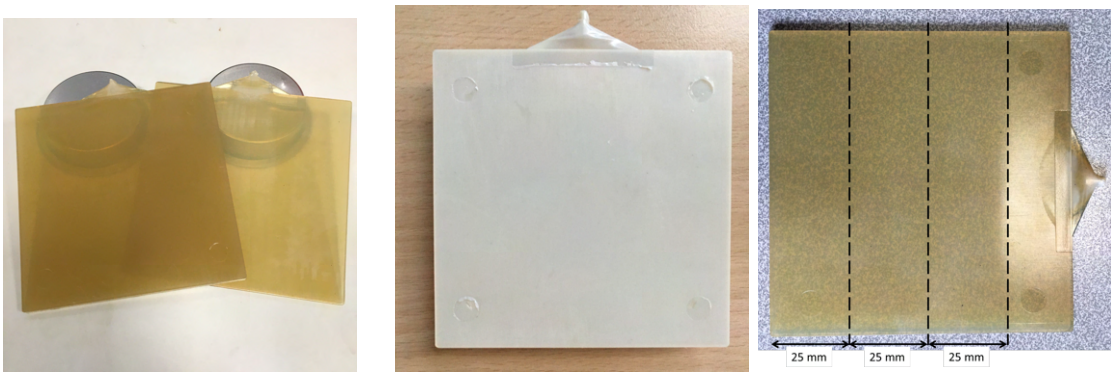

(a) (b) (c)

Figure 2.8: PEKK 7002 injected plates of 95 × 95 mm^2: (a) quasi-amorphous (4 and 2 mm thick) and (b) semi-crystalline (2 mm thick). (c) General representation of the injected plate cutting pattern to obtain the samples for welding.

The following sections of this chapter will describe the manufacturing process of the welding samples. Beginning with a study made on the pellets drying process, to ensure the correct procedure for drying. Passing through the injection molding process and the definition of the parameters for each injected plate. Finishing with the description procedure and parameters defined for the solidification step into the mold to achieve each crystalline state from the melted injected material.

2.3.1 Drying process for PEKK pellets

Before being processed, PEKK pellets need to be totally free of moisture content to avoid any defect related to air bubbles on the injected samples. In the technical data sheet of PEKK 70/30 [Arkema, 2021], the supplier recommends to dry the pellets at 120°C for 6 to 8 hours. However, the drying process is studied to determine the correct time to guarantee the maximum elimination of the moisture from the material at the indicated temperature.

The drying process of PEKK grade 7002 pellets is investigated by following the steps described in the protocol shown on Appendix A. Three representative samples of pellets are dried in an hermetic oven UFP400 from Memmert at 120°C for 30h. The mass of the PEKK

pellets is weighted over time while drying, measured with a digital scale with 0.01 mg of precision. This mass tracking allows to track the moisture content loss of the pellets. Figure 2.9 shows the mass evolution for each pellet sample in terms of percentage of the mass for each drying hour monitored, as well as the moisture content evolution. The mass tracking values for each sample for every drying hour monitored is registered in the table of Appendix B. By using the average evolution of the mass from the table on Appendix B, the mass lost and moisture content lost are calculated for each drying time monitored, as shown on Figure 2.9a.

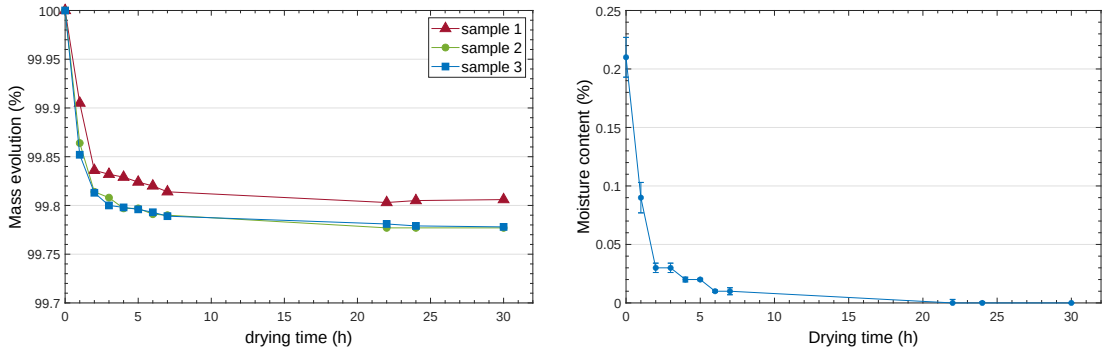

(a) (b)

Figure 2.9: Drying process study on PEKK 7002 pellets. (a) Mass lost evolution over time for three different samples; (b) moisture content evolution in the samples over time (average values).

Verifying the evolution of the mass on the samples from Figure 2.9a, it is considered that the maximum mass loss occurred at 24 hours of drying, because at that time the mass of the three samples begins to be stable. At this time PEKK pellets lose a maximum of 0.21 % of the initial mass, as shown in Figure 2.9a. It indicates that the pelleted material had initially a very low moisture content. The moisture content percentage can also be analyzed. In the first hour of drying, the pellets lost 59 % of the moisture content. This moisture lost percentage is near to the one obtained by *Ke et Wu* in 1998 when studying the desorption behaviour of PEKK films at 60°C in a solvent of $C_2H_4Cl_2$ [Ke and Wu, 1998]. In their study, PEKK films lose 50 % of the absorption weight in less than 1 hour. This allows to verify the reliability of drying the pellets in an oven. Further, at 6 hours of drying (time recommended for the supplier), only 93 % of moisture is lost. It is at 22 hours of drying that the material loses the 100 % of the moisture content, as it can be seen on Figure 2.9b.

It can be concluded that 4 to 7 hours of drying are enough to free the pellets from a high moisture percentage (maximum 95 %). However, to remove the maximum moisture content, PEKK pellets must be dried for more than 22 hours to a maximum of 30 hours (as studied), this for a drying temperature of 120 °C. This drying process must to be applied before processing the pellets in the injection molding machine.

2.3.2 Injection molding process and parameters

To produce the unfilled PEKK plates, an injection moulding machine Proxima 50 from Billion is used (Figure 2.10). The characteristics of the machine are described in Table 2.3. The process parameters to define for the injection process are: the screw temperature, the injection speed and stroke, the holding pressure, the mold temperature, and the cooling time.

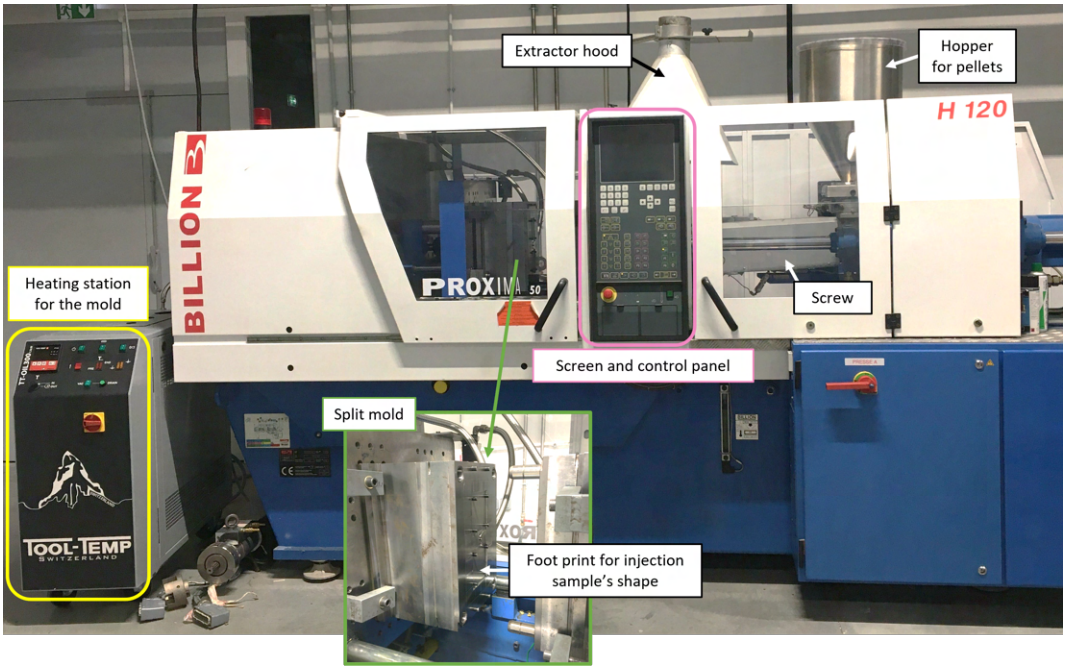

Figure 2.10: Injection molding machine.

Model	H 120 - 50
Maximum clamping force	501 kN
Screw diameter	25 mm
L/D ratio	20
Maximum operating pressure	190 bar

Table 2.3: Injection molding machine characteristics.

The process parameters are defined directly in the injection machine program, and some of them can be measured, or monitored. The *screw temperature* corresponds to the different temperatures defined for the different zones of the screw (zones 1 to 5, from rear to nozzle, respectively). The *injection parameters* corresponding to the *speed* and the *stroke* are used for the injection of the melted material into the mold. These are divided into three steps with different values that depend on the viscosity of the melted polymer and the amount of material to inject into the mold. The *hold pressure* is also a parameter for the *injection* step, it indicates the pressure to hold just after the injection of the material into the mold. The

mold temperature is defined in the pump (*as defined*), and *measured* with the thermocouples located inside the mold. Finally, the *cooling time* is the time the injected material is kept into the mold for cooling and solidification.

As mentioned, three different PEKK plates of 95×95 mm^2 are fabricated by injection molding: PEKK amorphous in 2 mm thick (PEKK-A2), PEKK amorphous in 4 mm thick (PEKK-A4) and PEKK semi-crystalline in 2 mm thick (PEKK-SC). For the injection process, the screw temperatures are set similar to the ones indicated by the supplier in the PEKK 70/30 technical data sheet [Arkema, 2021]. Table 2.4 shows the temperature settings defined for each zone of the screw. The other parameters of the injection process are defined according to the thickness of the PEKK plate and the crystalline state desired to obtain. Tables 2.5, 2.6, 2.7 specify the injection parameters identified for each PEKK plate injected.

With the parameters indicated, the injection cycle time differs for each type of plate produced. To fabricate a PEKK-A2 plate, the cycle takes 43 seconds. For a PEKK-A4 plate (the same crystalline state as PEKK-A2 but with double thickness), 55 seconds is needed. Then, the cycle time to fabricate a PEKK-SC plate (2 mm thick but high crystallinity) is 155 seconds. The cycle time increases with the injection step parameters, but also with the cooling time necessary for solidification of the samples. This cooling time into the mold after melted material injection, increases with sample thickness, but particularly with the degree of crystallinity desired to obtain in the sample.

To produce amorphous plates of 2 mm thickness, 5 kg of PEKK pelleted is used. With that amount of bulk material, 130 plates are obtained with an average mass of 27 g per plate. However, 30 samples are considered as scrap because they were obtained with some imperfections due to the initial injection tests and some difficulties that arrived on the process. In addition, more than 288 g of solid polymer is generated as scrap. For 4 mm thick amorphous plates, 4 kg of pellet polymer is used. 47 amorphous plates are produced, with an average mass of 48 kg. 30 of these plates are considered as scrap, in conjunction with 150 g of solid polymer.

To produce the semi-crystalline plates, 4.5 kg of pellet material is used. Each plate is obtained with an average mass of 27 g, as for the PEKK-A2 plates. 114 plates are fabricated, of which 42 are scrap. High quantity of scrap is obtained from this fabrication lot because of the difficulty to control the cooling and solidification of the injected material into the mold, due to the high temperature used to achieve crystallization of the material. In addition, 200 g of solid polymer is generated as scrap.

Screw zone	**Z1 (rear)**	**Z2 (center)**	**Z3 (front)**	**Z4 (nozzle)**	**Z5**
Defined (°C)	330	340	350	370	50 %
From supplier (°C) [Arkema, 2021]	320	340	350	360	-

Table 2.4: Screw temperature settings defined for the injection process of PEKK 7002.

Injection	**step 1**	**step 2**	**step 3**
speed ($mm{\cdot}s^{-1}$)	23	23	23
stroke (mm)	5	55	60
Hold pressure	80 bars per 10 s		
Mold conditions	**As defined**	**Measured**	
Temperature (°C)	80	68	
Cooling time (s)	21		

Table 2.5: Injection process parameters defined to fabricate the PEKK-A2 plates.

Injection	**step 1**	**step 2**	**step 3**
speed ($mm{\cdot}s^{-1}$)	15	20	15
stroke (mm)	20	70	98
Hold pressure	800 bars per 10 s		
Mold conditions	**As defined**	**Measured**	
Temperature (°C)	80	70	
Cooling time (s)	30		

Table 2.6: Injection process parameters defined to fabricate the PEKK-A4 plates.

Injection	**step 1**	**step 2**	**step 3**
speed ($mm{\cdot}s^{-1}$)	15	8	5
stroke (mm)	5	45	50
Hold pressure	300 bars per 10 s		
Mold conditions	**As defined**	**Measured**	
Temperature (°C)	270	240	
Cooling time (s)	120		

Table 2.7: Injection process parameters defined to fabricate the PEKK-SC plates.

2.3.3 Crystallization phenomena from the melt state

When processing PEKK by injection molding, it is important to control the process parameters and conditions to achieve the correct fabrication of the samples. For injection molding, the parameters used to melt the material are of relevance to achieve the correct melting state. Then, the parameters used for injection of the material into the mold are controlled depending on the quantity of material to inject into the mold, conditioned by the shape and size of the sample. In addition, the temperature conditions of the mold that receives the melted material are of important for the injection parameters. Moreover, mold temperature is of high

importance to ensure solidification of the sample and the obtention of the desired crystalline state.

PEKK, being a semi-crystalline thermoplastic, can crystallize after melting while cooling and solidification. The solidification conditions used will determine the crystalline state, or degree of crystallinity, of the final part fabricated. When injection molding PEKK material, the material is injected in melted form into the mold until filling the mold's footprint with the shape of a square plate (Figure 2.11). Inside the mold, the melted material begins to cool down and solidify. Depending on the temperature of the mold, and the time that the material stays inside it at the defined temperature, the final part will acquire a different arrangement of the polymer molecules and thus a different crystalline state. In the case of the present study, two different states were desired to obtain for the PEKK injected samples: a quasi-amorphous PEKK with a very low degree of crystallinity, and a semi-crystalline PEKK with a very high degree of crystallinity.

Thus, to control the final crystalline state of the injected sample it was important to define a correct temperature for the mold. Table 2.8 shows the mold temperature and cooling times defined for the solidification of the PEKK injected material into the mold. The temperature indicated is the one measured from the thermocouples while processing the material. The values indicated as *from supplier* are the parameters recommended on the material technical sheet from the supplier to facilitate skin and core crystallization. As shown in the table, the mold temperature differs according to the crystalline state desired to reach on the final sample. Furthermore, the cooling time used to solidify the material into the mold is also of importance, and it differs for each type of plate. To obtain an amorphous state (very low crystallinity degree) of the PEKK material, low temperature and time used for the mold. On the contrary, using very high temperature and high cooling time, allows the generation of a semi-crystalline state (high degree of crystallinity) on the PEKK sample. Therefore, the amorphous state is achieved by setting the mold temperature at 70 °C for a holding time of 20 to 30 seconds, whereas the semi-crystalline one is obtained at 247 ± 6 °C for 2 minutes of cooling, as indicated in Table 2.8.

Mold	Temperature (°C)	Cooling time (s)
From supplier [Arkema, 2021]	230 to 250	-
PEKK-A2	68	21
PEKK-A4	70	30
PEKK-SC	247	120

Table 2.8: Mold temperature and cooling times defined for material solidification after injection.

The temperature of the mold used for injection molding the PEKK plates can be controlled by an arrangement of pipes inside the mold structure. These pipes can transport water or oil to heat the mold to a defined temperature. The temperature is indicated in the pump used to heat and control the liquid flux into the mold pipes. In addition, the temperature of

the mold can be monitored by the thermocouples integrated behind the foot print. Figure 2.11 shows the footprint of the mold used to inject the square plates with the monitoring points available. The location of the thermocouples used to monitor the mold temperature are indicated by the colored stars with the labels *TM1*, *TM2* and *TM3*. The beginning of the polymer injection is indicated by the red circle with an arrow for the injection direction.

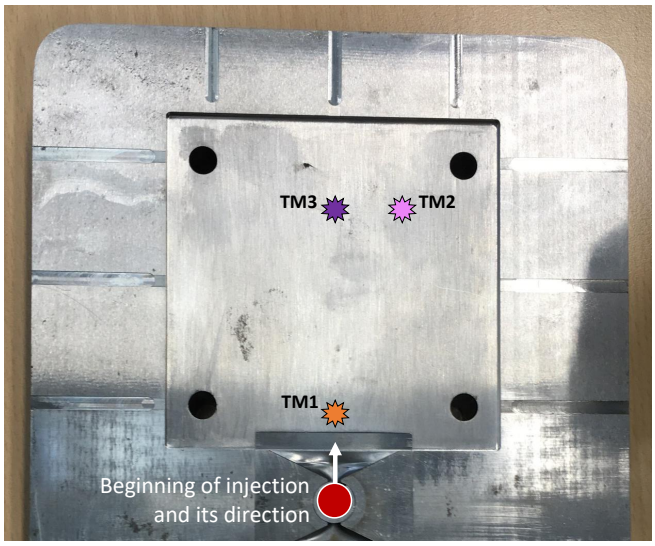

Figure 2.11: Mold footprint with the shape of a square plate and thermocouples locations.

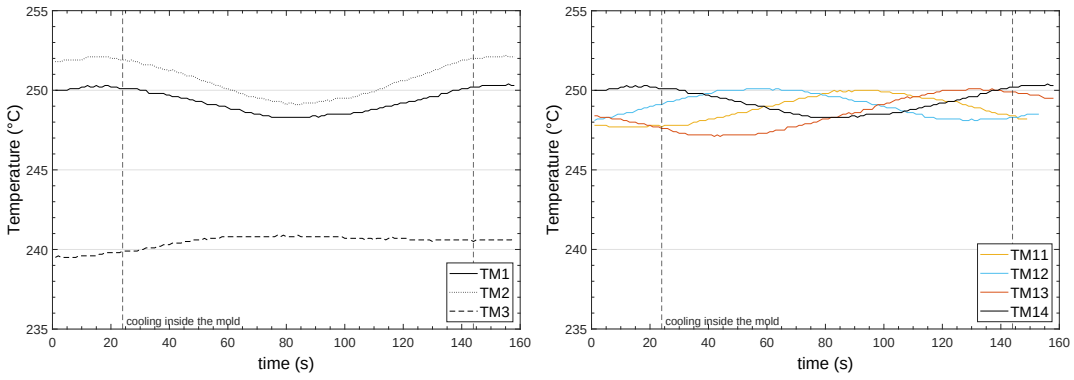

(a) (b)

Figure 2.12: Mold temperature evolution during the injection cycle of PEKK-SC plates for a) the 3 monitoring points (TM1, TM2 and TM3), and b) four measurements of TM1 point. Cooling and solidification step indicated between the vertical dashed lines.

When crystallizing the material inside the mold, the crystallization is achieved by an isotherm at a defined temperature and time. According to the isothermal crystallization kinetics of PEKK 7002 from the melt state, PEKK 7002 fully crystallizes at 240 °C in 10 minutes [Choupin et al., 2018]. That would mean that the PEKK-injected material should

stay inside the mold for a solidification time of 10 minutes at a temperature of 240 °C. However, a lower time can be used to obtain a highly crystallized PEKK sample. In the time-temperature-transformation (TTT) diagram predicted by *Choupin et al., 2018*, it is visible that when using a lower time of 2 minutes at the same temperature of 240 °C, high crystallinity can be achieved on the material (almost 90 % of the relative crystallinity of PEKK 7002) [Choupin et al., 2018].

When injecting the PEKK-SC plates, the mold temperature was monitored all along the injection cycle of one plate for ten different injected plates. The objective was to verify the temperature distribution in the mold during injection and solidification. The mold temperature was measured by thermocouples of type K, class 1 (accuracy of ± 1.5°C) positioned in three different points behind the footprint (Figure 2.11). To monitor the temperature over time, the mold thermocouples are connected to a Graphtec GL220 measuring station with a measurement. The temperature is recorded for each thermocouple all along the injection process, from the beginning of injection, until the end of cooling and ejection of the sample.

Figure 2.12a shows the temperature evolution over time for each measurement point of the mold for a cycle of one PEKK-SC injected plate. As can be seen, for a same time step the temperature values differ between the points ($TM2 > TM1 > TM3$). Although TM1 is lower than TM2 by only 2°C, there is a high difference registered between TM2 and TM3, which is around 12°C. These differences in temperature at the footprint level may lead to a differences in crystallinity inside the injected sample. Moreover, the temperature of each measurement point oscillates over time as a *sin(x)* function during the injection cycle. That generates a difference of temperature at one point along the injection process. This difference is between 1 and 3.5 °C, depending on the point. In the cooling step (between 24 and 144 s), the mold temperature varies, and this variation can have also an impact on the crystallization of the final sample. Furthermore, each injection cycle have a different oscillation cycle and amplitude, as can bee seen in Figure 2.12b, which can create a different crystallinity distribution for each injected sample. The crystallinity distribution may differ from one sample to another.

Temperature (°C)	**Max (± 1.5 °C)**	**Min (± 1.5 °C)**
TM1	250.3	247.9
TM2	252.2	248.7
TM3	240.7	239.7

Table 2.9: Maximum and minimum temperatures registered for each point of measurement in the mold at the injection process of PEKK-SC plates.

2.4 Plates characterization for LTW

As seen in Chapter 1, Section 1.4, the material properties have an influence on the LTW process feasibility and weld joint quality. Those properties concern the optical, thermo-

physical and mechanical properties of the samples (ref. Table 1.3), which are also influenced by their microstructure and composition. In the next section, the thermo-physical and optical properties of the injected PEKK plates are characterized. Different techniques and methods are used to obtain those properties and correlate them with the microstructure of each sample, thus to their crystalline state.

2.4.1 Thermal transitions and degree of crystallinity by DSC

To verify the differences in crystallinity between the injected samples and to characterize their thermal transitions,differential scanning calorimetry (DSC) test are carried out on a DSC Stare System Mettler Toledo (Figure 2.13). The untreated PEKK pellets, as well as the injected PEKK plates are studied for comparison. Samples weighing 6 ± 3 mg are extracted from PEKK pellets and plates and placed inside hermetic aluminum pans. Using ramps of 10 K·min^{-1}, samples are heated from 100°C to 390°C, cooled from 390°C to 100°C, and then heated again from 100°C to 390°C under a 50 mL·min^{-1} nitrogen flow. At the beginning of each test, samples are stabilized at 100°C for 5 minutes, and there is no hold between the heating and cooling cycles.

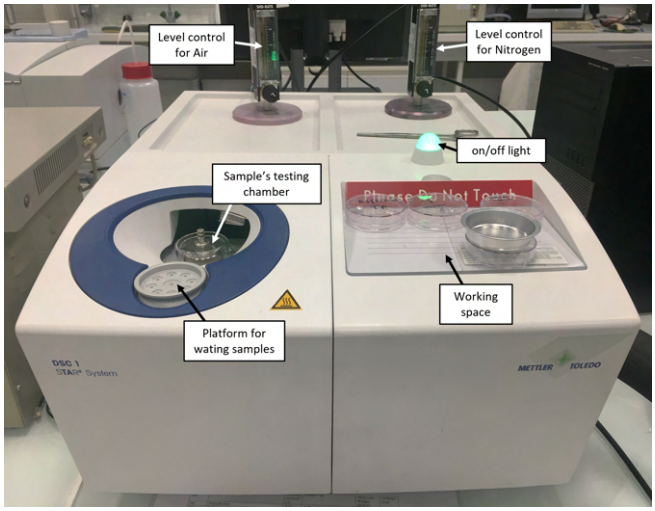

Figure 2.13: DSC 1 Stare System Mettler Toledo.

Figure 2.14 shows typical DSC thermograms of each PEKK sample studied: untreated pellet and injected plates. The first heating ramps show a slope change of the curves between 150 and 160 °C (depending on the sample), which characterize the sample's glass transition. Further, at the end of this first heating ramp, an endothermic peak is observed to begin around 300 °C, showing the endothermic reaction by melting. For some samples (Figures 2.14c and 2.14d) the first heating scans show the apparition of an exothermic peak around 200 °C. Those peaks indicate cold crystallization of the material, demonstrating that the initial state of the sample was quasi-amorphous before heating. Therefore, from the first heating ramp, glass transition temperature (T_g), melting temperature (T_m), and initial degree of crystallinity

(X_c) are obtained for each sample. In addition, cold crystallization temperatures (T_{cc}) are obtained for the PEKK-A plates.

The cooling ramp is used to obtain the crystallization temperature of the material from the melt (T_{cm}). As it can be seen in Figure 2.14, the cooling curves show an exothermic peak between 270 °C and 295 °C for all samples. This peak indicates the crystallization of the material from the melt state. Also, the maximum degree of crystallinity (X_{c-max}) that the material can achieve can be calculated from this ramp. Finally, the second heating of the DSC tests gives the maximum melting temperature of the material after crystallization from the melt. An endothermic peak appears for all samples on the second heating ramp, indicating the fusion of the crystalline zones.

Figure 2.15 focus on the DSC scans from 150 to 250 °C obtained on the first heating for each sample. After the glass transition (Tg), an exothermic peak is observed around 205°C for the amorphous samples (green and red curves). This indicates cold crystallization, occurring when the sample is not fully crystallized on cooling. Indeed, right after Tg, the macromolecules have gained enough mobility to self-organize into crystalline structures. For PEKK-SC, no peak is observed because the sample was fully crystallized during processing.

The crystallinity of the samples is calculated thanks to Equation 2.1 [Doumeng et al., 2021]. The thermal transitions and crystallinity obtained from the DSC tests are summarized in Table 2.10.

$$X_c = \frac{\Delta H_m - \Delta H_{cc}}{\Delta H_{100\%}} \tag{2.1}$$

The enthalpy of the cold crystallization peak (ΔH_{cc}) is subtracted from the melting enthalpy of the first heating (ΔH_{mc}). The result is then divided by the theoretical enthalpy of the 100 % crystallized polymer ($\Delta H_{100\%}$). This last enthalpy is unknown for PEKK, so is commonly assumed to be the same as for PEEK (130 $J{\cdot}g^{-1}$) [Blundell and Osborn, 1983]. For the calculation of the enthalpy, the correspondent peaks are integrated with a *spline* baseline predetermined on the DSC software data treatment.

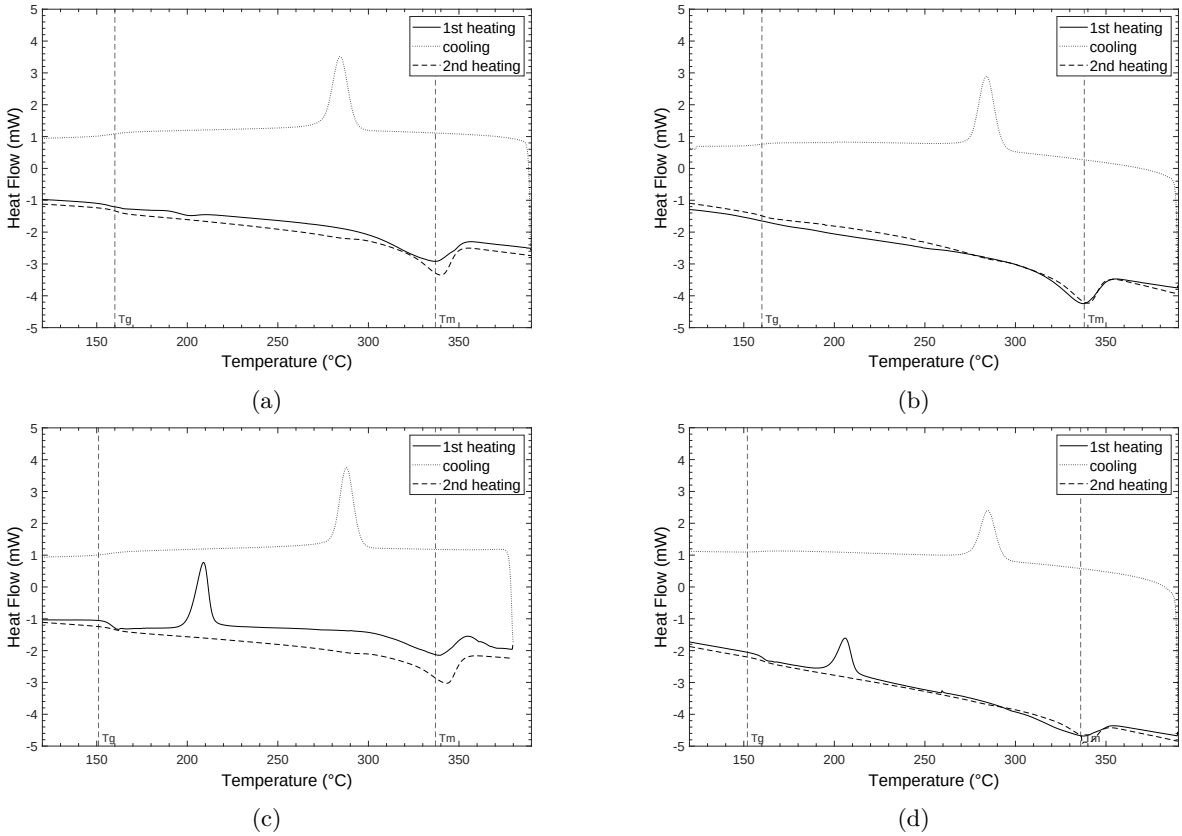

Figure 2.14: Typical DSC thermogram of PEKK 7002 a) pellets, b) semi-crystalline plates, c) amorphous plates 2 mm thick and d) amorphous plates 4 mm thick. Exothermic reaction direction goes upwards.

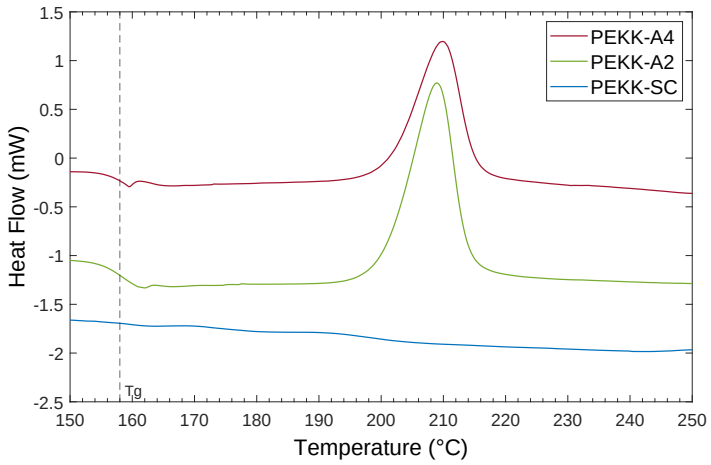

Figure 2.15: Cold crystallization peaks of PEKK injected samples.

PEKK	Pellets	A2	A4	SC
Tg [°C]	160	151	152	160
Tcc [°C]	-	204	205	-
Tm [°C]	337	337	336	338
Tcm [°C]	285	285	286	284
Xc [%]	27	5	6	24
Thick [mm]	-	2	4	2
Color	-	Yellow	Yellow	Beige/White

Table 2.10: PEKK injected plates thermal transitions, crystallinity, coloration and thickness.

2.4.2 Heat capacity and thermal conductivity

The thermal properties of the PEKK material influencing the heat transfer are also measured. Those properties concern the density, conductivity and heat capacity. In this study, the density ρ [kg·m^{-3}] of the material is taken from the material's technical datasheet given by the supplier [Arkema, 2021], and it is considered equal for all samples, regardless their crystallinity. The conductivity and heat capacity properties are characterized for each crystalline state: quasi-amorphous and semi-crystalline. Therefore, the properties obtained for the quasi-amorphous state is considered for both PEKK-A2 and PEKK-A4 samples.

The thermal conductivity k [W·m^{-1} · K^{-1}] of the samples is obtained by Hot disk method using a TPS2500 from Hotdisk Instrument. Tests are carried out at room temperature (20°C) using directly the PEKK injected plates. Three different PEKK plates are tested per crystalline state. The heat capacity C_p [J·kg^{-1} · K^{-1}] of PEKK samples is measured by a DSC TA Instrument Q200. Samples weighting 10 ± 1.5 mg are tested with ramps of 5 °C·min^{-1}. The thermal properties characterized are summarized in Table 2.11.

Property	Unity	PEKK-A	PEKK-SC
Density (ρ)	[kg·m^{-3}]	1290	1290
Specific heat (C_p)	[J·kg^{-1} · K^{-1}]	973	1138
Thermal conductivity (k)	[W·m^{-1} · K^{-1}]	0.246	0.211

Table 2.11: Thermal properties of PEKK samples.

2.4.3 Optical properties for laser welding

The optical properties of the samples at the near-infrared (NIR) light are important for laser transmission welding. As already seen in Chapter 1, the laser intensity that strokes the surface of the sample can be transmitted, reflected and/or absorbed. Moreover, the differences in crystallinity on the samples may affect their optical properties. This is evident at the visible

light: PEKK-A plates are transparent with a yellow coloration, whereas PEKK-SC plates are opaque, with a beige, milkywhite, coloration. The transparency of the sample at the NIR light of a laser beam could be different than at the visible light. The majority of polymers are semi-transparent or translucent under visible and near-infrared (NIR) wavelengths in their natural state [Xu et al., 2015a, Acherjee, 2020, Gonçalves et al., 2021]. Nevertheless, the optical properties of semi-crystalline polymers are influenced by their crystalline structure, which imposes limitations on light transmission [Kagan and Bray, 2001]. The crystalline structure increases the light travel path, which leads to higher absorption [Kagan et al., 2002, Xu et al., 2015b].

In the case of this study, quantifying the optical properties of the PEKK injected samples (amorphous and semi-crystalline) is important to confirm their suitability to be welded by LTW. The objective is to determine the transmission, reflection and absorption properties at the wavelength of the laser used in the study (975 nm), for a laser beam that is directed perpendicular to the surface of the samples, as in LTW process. For the amorphous state of PEKK, focus is put on confirming its potential as semi-transparent upper part for LTW. Additionally, quantification of the transmission capabilities modification when increasing the amorphous sample thickness (from 2 to 4 mm) is of importance to ensure adequate laser intensity at the interface regardless the thickness of the upper part. On the other hand, the optical properties of the PEKK semi-crystalline state are studied to confirm its effectiveness as absorbent lower part on LTW. Furthermore, the effect of crystallinity is correlated with the absorption properties of PEKK.

To measure optical properties of the injected plates, a FTIR spectrophotometer Bruker Vertex 70 (Figure 2.16) from IMT Mines Albi-Carmaux ICA laboratory is used. The laser source has a capacity from 0.4 to 2 μm. It is possible to obtain the transmission and reflection spectrum corresponding to the wavelength. Bidirectional and hemispherical characterization of the transmission and reflection optical properties are possible. Using an INGAAS detector (detection between 0.8 and 2 μm), the bidirectional and hemispherical transmission and reflection spectra are measured with a resolution of 16 cm^{-1}. For the bidirectional characterization of transmission and reflection factors, a diaphragm of 0.5 mm was used. And for the hemispherical characterization, the diaphragm was of 8 mm. The spectra showed at the characterization is the result of the average of 16 measurements made by the spectrophotometer on a same point. To obtain the hermispherical properties of transmission and reflection, an integration sphere with an Infragold Lambertian coating is used.

At the wavelength of interest (975 nm cf. Chapter 3), transmission (T_i) and reflection (R_i) factors are extracted from the characterized spectra. After studying the results, the chosen values for the optical factors are the ones obtained from the hemispherical characterization. This is better described in the next sections. Absorption factors (A_i) are calculated from the T_i and R_i factors, according to the energy conservation principle (Equation 5, Chapter 1, Section 2.1). The optical properties of the samples at the wavelength of interest of 975 nm are summarized in Table 2.12. The analysis and discussions made for the optical properties characterization is described in the next sections.

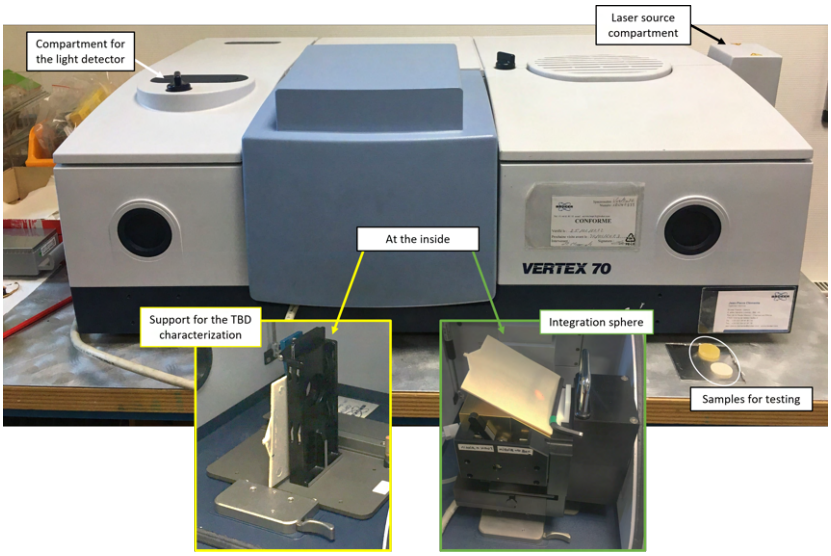

Figure 2.16: FTIR spectrophotometer Bruker Vertex 70 used for optical characterization of the PEKK injected plates at IMT Mines Albi.

PEKK	A2	A4	SC
$T_i\%$	75	62	20
$R_i\%$	13	13	48
$A_i\%$	12	25	32

Table 2.12: Optical properties of PEKK samples at the laser wavelength of interest (975nm).

2.4.3.1 Reflection properties

Bidirectional and hemispherical reflection factor can be characterized. The bidirectional reflection characterization measures the specular reflection of the material surface. Specular reflection occurs when the irradiation that arrives at the material surface at a specific angle within the Normal is reflected at the same angle at the opposite direction, as schematically represented in Figure 2.17a. This kind of reflection is going to be called "bidirectional reflection" from now on.

To characterize the portion of the light that is reflected bidirectionally on the material surface an integrated goniometer is used. The sample is positioned laid down parallel to the horizon, and the goniometer's mirrors allow the light to be directed onto the sample's surface at the chosen angle. The maximum angle possible to obtain with the horizontal is 77°. Then the portion of light that has been reflected at the same angle that the incident angle, is detected and measured.

This kind of characterization does not allow to measure the portion of light that can be diffused in the reflection. To measure the diffuse reflection (or hemispherical reflection) of the

material surface it is important to use the integration sphere as shown in Figure 2.17b (also used for the hemispherical transmission characterization). This can allow the measurement of the diffused reflection of the incident radiation.

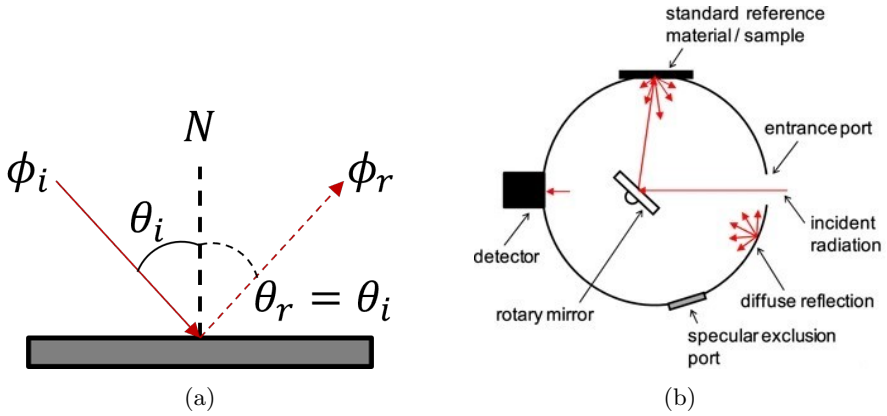

(a) (b)

Figure 2.17: Schematic representation of (a) specular reflection on the surface of a sample and (b) characterization of the diffuse (hemispherical) reflection of a sample with the integration sphere.

Figures 2.18 show the bidirectional and hemispherical reflection spectra of each PEKK injected plate characterized. The reflection factors obtained for the wavelength of interest of 975 nm are summarized in Table 2.13. As it can be noticed, for the amorphous samples of 2 and 4 mm thick, the reflection factors diverge on 1 % on the bidirectional characterization, but they show the same reflection of 13 % on the hemispherical characterization. On the other hand, the reflection characterization of the semi-crystalline samples of 2 mm thick shows a high discrepancy between the bidirectional and the hemispherical. Visualizing the bidirectional reflection factor, it seems that the semi-crystalline samples have a very low reflection of 1 %. But, when seen the hemispherical reflection is characterized, it can be noticed that the surface reflection is actually high, around 48 % for the wavelength of interest.

The hemispherical reflection is then higher than the bidirectional one, which indicates that the surface of the PEKK injected plates diffuse the NIR radiation of the laser that strokes it. Therefore, the hemispherical characterization needs to be taken into account as the one that characterize the material reflection properties. Figure 2.19 shows thus the reflection spectra of the three PEKK samples combined. It can be noticed that the apparent reflection of the semi-crystalline state of the material is higher than that of the the amorphous state. Additionally, the reflection properties of the amorphous PEKK is the same regardless its thickness. This is mostly due to the crystalline structure that can be found on the surfaces of the samples. The semi-crystalline ones have more crystalline zones on their surface, which increases the reflection surfaces. Contrary to the amorphous samples that have less crystalline zones due to their low degree of crystallinity. And both PEKK-A2 and PEKK-A4 samples seam to share a similar crystalline structure at their surfaces because they share the same reflection properties.

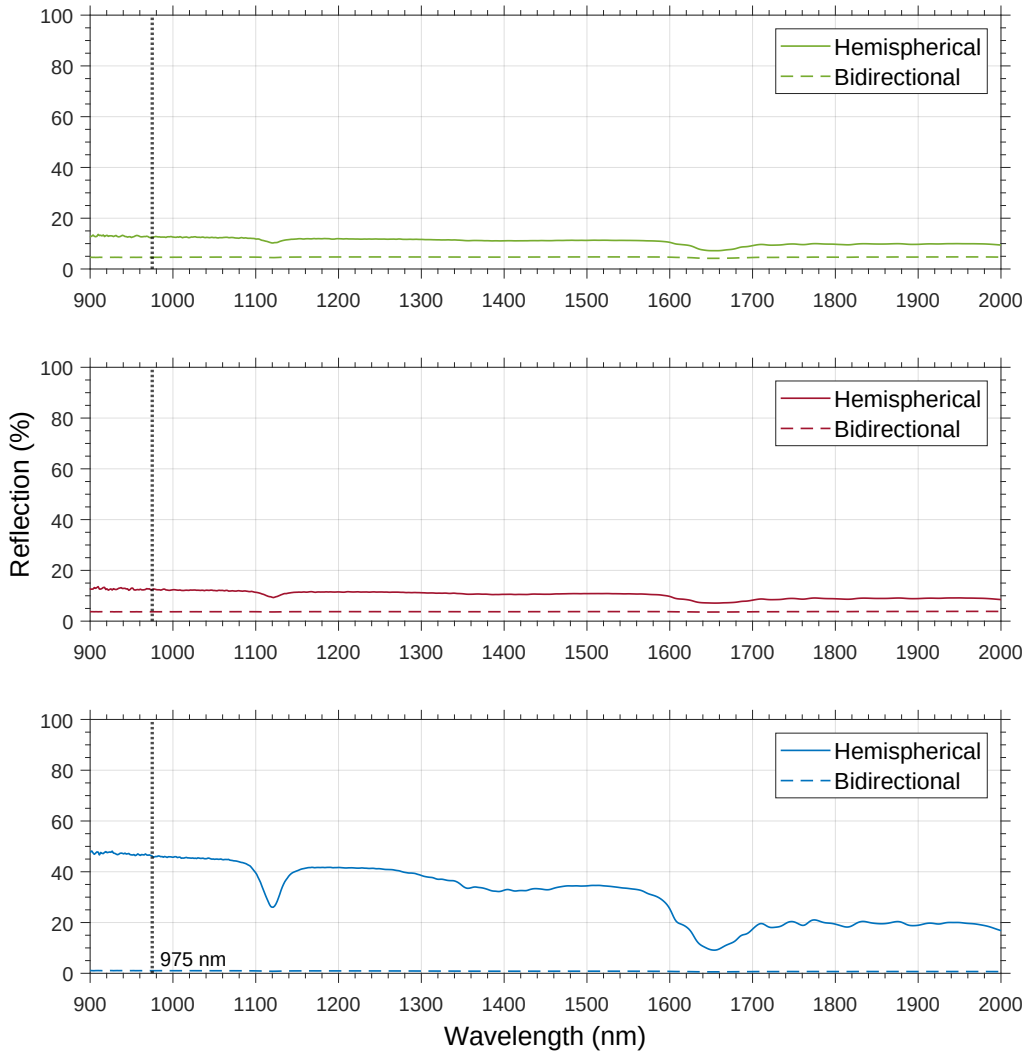

Figure 2.18: Bidirectional and hemispherical reflection spectra of PEKK-A2 (top), PEKK-A4 (middle) and PEKK-SC (bottom) injected plates.

Sample	RBD (%)	RHm (%)	Difference
PEKK-A2	5	13	8
PEKK-A4	4	13	9
PEKK-SC	1	48	47

Table 2.13: Reflection factors of PEKK injected plates at the wavelength of interest of 975 nm.

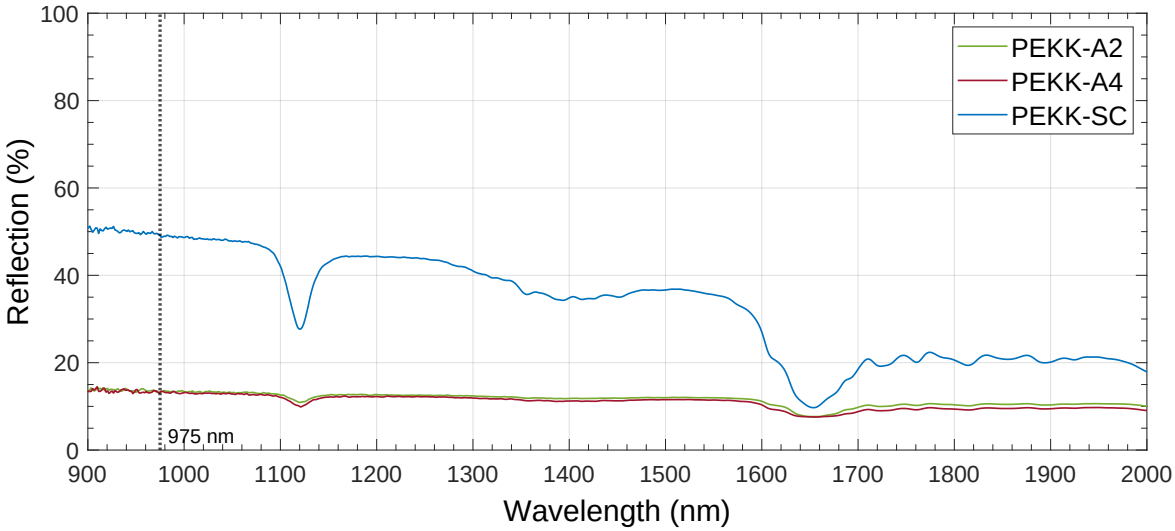

Figure 2.19: Hemispherical reflection spectra of PEKK 7002 injected plates.

2.4.3.2 Laser Transmission

Bidirectional and hemispherical transmission factors can also be measured. The bidirectional transmission (TBD) factor is the fraction of light that is transmitted normal to the sample's surface, after going through the material. To characterize it, the sample is positioned between the source and the detector, as represented in the schema of Figure 2.20a. The source sends the light flow directly to the sample, perpendicular to its surface. Then, the fraction that achieves to go through the material thickness, and that goes out following the same angle than the incident light, is detected and measured by the detector.

If the semi-transparent material is diffusant, the light that arrives to the material is going to be transmitted in all directions, not only perpendicular to the outdoor surface (Figure 2.20b. This kind of transmission is measured using the hemispherical transmission characterization with help of an integration sphere.

The bidirectional transmission measurement does not take into account the fraction of the light that diverges after going through the material. For that, hemispherical transmission (THm) factor needs to be characterized. The hemispherical transmission characterization indicates the quantity of light that can passes through the samples thickness, even if it diffuses after going through it. This is possible thanks to the use of an integration sphere as shown in Figure 2.21). The integration sphere used for the characterization of our material optical properties has an Infragold Lambertian coating, with a reflectivity of 94 %. To characterize the hemispherical transmission factor, the sample is positioned between the source and the sphere. The source sends the light flow to the sample and the fraction that achieves to going through it, in all possible directions, is detected and measured by the detector.



Figure 2.20: Schematic representation of (a) bidirectional transmission properties characterization and (b) hemispherical transmission on a diffusant material.

If the hemispherical transmission factor obtained is higher than the bidirectional one, then the studied material is diffusant. Meaning that the portion of the incident laser irradiation that will be able to go through the material will be diffused in all directions, not only normal to its surface.

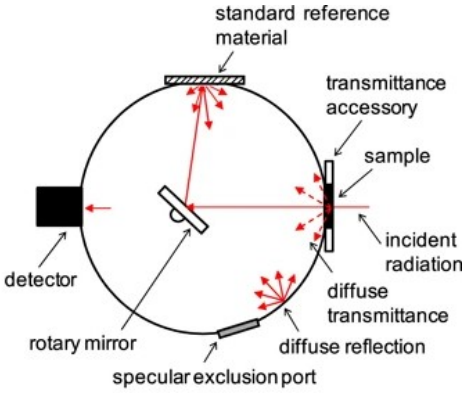

Figure 2.21: Schematic representation of the hemispherical transmission properties characterization with the integration sphere.

Figure 2.22, show the bidirectional and hemispherical transmission spectra of each sample characterized. On each graph, the wavelength of interest is indicated by a vertical dotted line. The bidirectional and hemispherical transmission factors obtained at the wavelength of interest are summarized in Table 2.14. The amorphous samples of 2 mm thick allow a transmission of 55 % of the infrared radiation (IR) in the bidirectional configuration. With the hemispherical characterization, we can notice that the same samples allow more transmission of the IR radiation, around 75 %. For the amorphous samples of 4 mm thick, the bidirectional characterization indicates a transmission factor of 47 %, while the hemispherical one gives a higher value of 62 %. The same happens for the semi-crystalline sample (2 mm thick). While the bidirectional transmission factor indicates almost null transmission (0.3 %), the hemispherical transmission factor shows that it can transmit 20 % of the IR radiation.

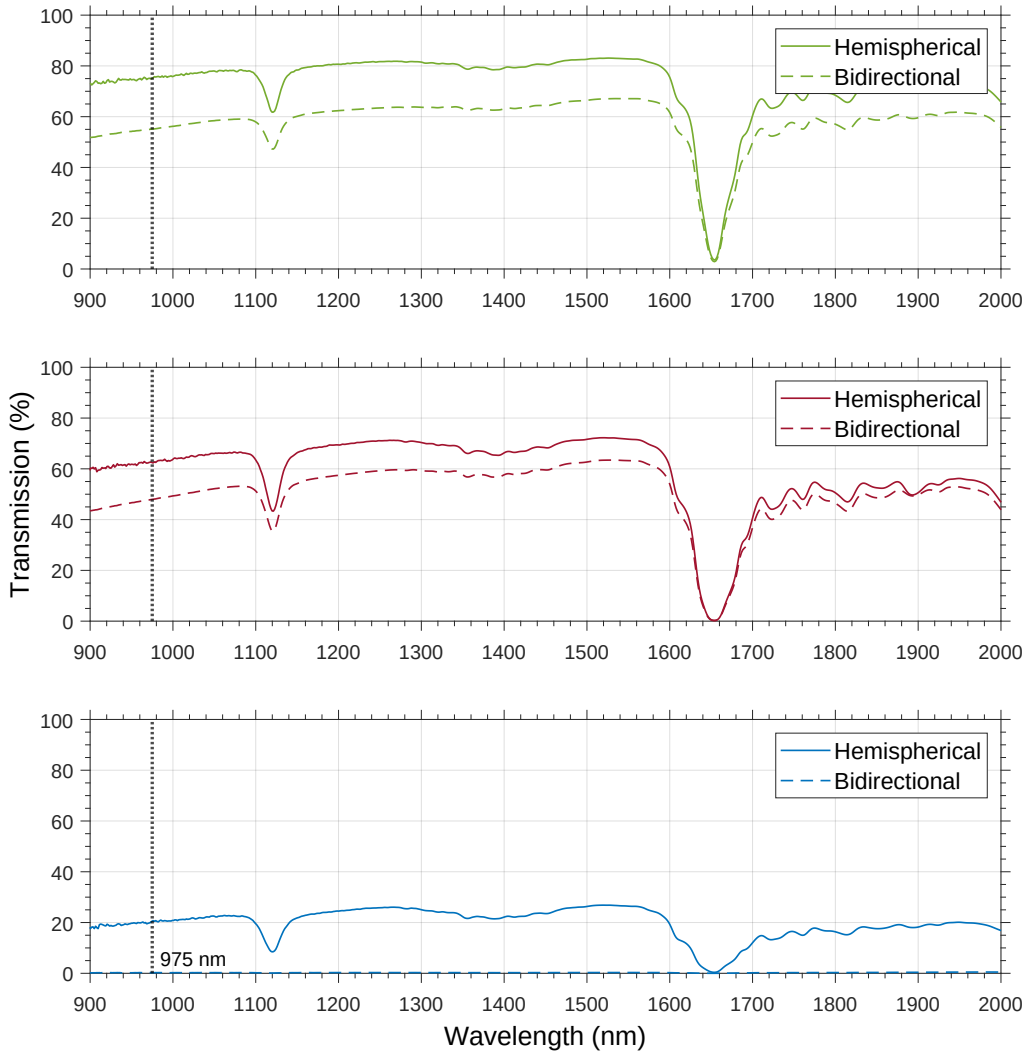

Figure 2.22: Bidirectional and hemispherical transmission spectra of PEKK-A2 (top), PEKK-A4 (middle) and PEKK-SC (bottom) injected plates.

Sample	TBD (%)	THm (%)	Difference
PEKK-A2	55	75	20
PEKK-A4	47	62	15
PEKK-SC	0.3	20	20

Table 2.14: Transmission factors of PEKK injected plates at the wavelength of interest of 975 nm.

As observed in the transmission spectra and from the transmission factors revealed at the wavelength of interest, the hemispherical transmission is higher than the bidirectional one for our PEKK samples. That indicates that the PEKK samples are diffusant and the laser beam irradiation will be transmitted in all directions when going through the thickness of the sample. Hence, it is important to consider the hemispherical characterization as the one that describes the transmission properties of the PEKK samples.

Other important information that can be revealed is that the semi-crystalline sample is also semi-transparent. With the bidirectional characterization, the TBD factor is near zero (0.3 %). However, the hemispherical characterization show that the PEKK-SC allows a portion of the incident radiation to be transmitted. Around 20 % of the radiation at the wavelength of interest. Even though, 20 % is a very low transmission factor in comparison with the amorphous (semi-transparent) samples.

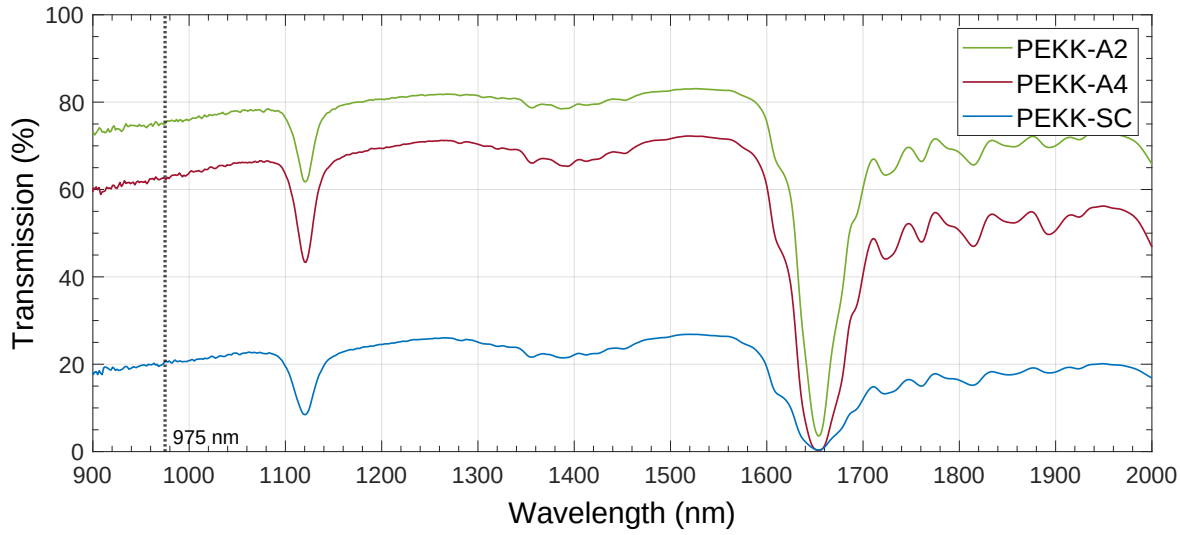

Figure 2.23: Hemispherical transmission spectra of PEKK 7002 injected plates.

Therefore, taking into account the hemispherical transmission characterization (Figure 2.23), it can be notices that the amorphous samples have a transmission factor higher than the semi-crystalline state of the material. The transmission properties of PEKK can be thus correlated with their crystallinity. For a same thickness (of 2mm), when the crystallinity (Xc) of PEKK is increased from 5 % to 24 %, the transmissivity decreases from 75 % to 20 %. Additionally, it can be seen that increasing the thickness of the amorphous sample from 2 to 4 mm, decreases the transmission factor from 75 % to 62 %. Even though, the amorphous PEKK samples show a transmissivity high enough for the feasibility of LTW. As proved by *Villar et al.* when welding PEKK 60/40 by LTW, a transmission factor of 60 % allows melting at the interface [Villar et al., 2018]. Consequently, PEKK-A2 and PEKK-A4 are adequate to be used as the semi-transparent upper part for LTW.

2.4.3.3 Absorption properties

The PEKK samples absorption properties are obtained indirectly from the measurements of the transmission and reflection properties, by applying the energy conservation principle (Equation 5, Chapter 1, Section 2.1). Table 2.15 summarizes the absorption factors (bidirectional and hemispherical) calculated for the PEKK injected plates at the wavelength of interest.

Sample	ABD (%)	AHm (%)	Difference
PEKK-A2	40	12	28
PEKK-A4	49	25	24
PEKK-SC	99	32	67

Table 2.15: Absorption factors of PEKK injected plates at the wavelength of interest of 975 nm.

The bidirectional absorption is higher than the hemispherical one, as for the reflection and transmission properties. Therefore, hemispherical factors are taken into account to define the absorption properties of the PEKK parts. If the bidirectional characterization is taken into account, it will imply that PEKK-SC absorbs 99 % of the laser irradiation at the wavelength of interests. But it would also point out that the amorphous substrates are highly absorbent, with an A_i between 40 and 50 %. But, taking into account the hemispherical absorption calculated from the hemispherical transmission and reflection measurements, it appears that the amorphous samples have, in fact, a low absorption of the laser radiation (12 and 25 %, for 2 and 4 mm thick respectively). In addition, the semi-crystalline samples have a lower absorption compared with the bidirectional factor. However, this absorptivity of 32 % is high enough to absorb the laser radiation at the interface, and maybe even on the volume. As demonstrated by *Goyal et al.* when welding 2 mm thick polycarbonate samples by LTW, an absorptivity of 30 % is high enough to achieve welding [Goyal et al., 2022]. This indicates that the PEKK-SC sample is a good candidate to be used as lower absorbent substrate for LTW.

The intrinsic properties of absorption of the PEKK samples at the wavelength of interest can be quantified from their transmission and reflection properties. The intrinsic absorption of a material is quantified with the absorption coefficient α $[m^{-1}]$. This coefficient can be calculated by using the Lambert-Beer's law for a laser beam that is directed normal to the surface of the sample. The Lambert-Beer's law is shown in Equation 6, on Chapter 1, Section 2.1. And, when having the optical factors of transmission (T_i) and reflection (R_i), the equation can be rewritten as in Equation 2.2 [Geiger et al., 2009]:

$$T_i = (1 - R_i) \times exp(-\alpha.z) \tag{2.2}$$

where z $[m]$ is the thickness of the sample. Using the corresponding values of T_i and R_i

factors of the PEKK samples at 975 nm in the equation, the absorption coefficients of each sample is obtained. The values of those absorption coefficients are summarized in Table 2.16. These absorption coefficients calculated for each welding sample will be used for numerical modeling of LTW on PEKK parts in Chapter 4.

PEKK	**A2**	**A4**	**SC**
$\alpha[m^{-1}]$	74.2	84.7	477.75

Table 2.16: Absorption coefficient α calculated for each sample.

2.4.3.4 Moisture content influence

Bidirectional transmission characterization was used to understand the influence of the moisture content on the optical properties of the semi-transparent sample. Amorphous samples of 2 mm thick were characterized. The samples to compare were a dried injected plate against an injected plate exposed to ambient humidity for more than 24 hours. The dried samples where dried at 120°C by 24 hours. The Figure 2.24 shows the transmission spectrum of the dried and humid amorphous 2 mm thick sample.

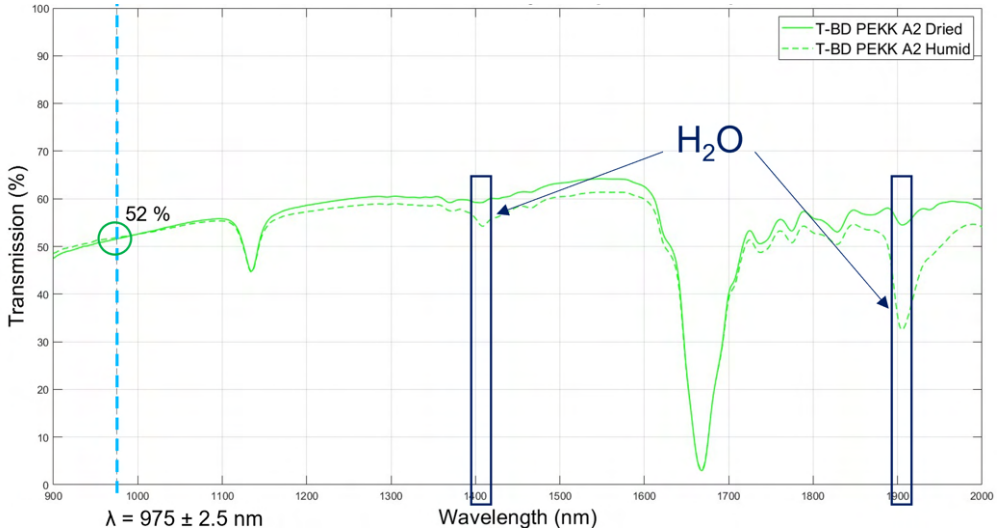

Figure 2.24: Bidirectional transmission spectra of PEKK-A2 sample. Comparison between a dried and a humid sample.

As we can see in the graph, both samples have the same TBD factor of 52 % at the wavelength of interest. For the humid sample (the dotted spectrum) we can notice two more peaks of lower transmission at 1400 and 1900 nm, corresponding to the water band, but both spectrums stay almost similar. Thus, the humidity content does not affect drastically the transmission factor of the transparent substrate of our material, specially at the wavelength of interest.

2.4.3.5 Optical anisotropy

As we notice on the transmission factor characterization, the IR radiation is diffused after passing through the injected plate. This diffusion depends on the injected plate's orientation. This can be important to understand for LTW, specially for the upper transparent substrate. It is important to know if the samples orientation affect the quantity of laser that will be transmitted and that will arrive at the interface for welding. Thus, it is important to understand the influence of the sample orientation on the transmission property of our amorphous substrate. For that, bidirectional transmission factor was characterized for different amorphous plate's samples of 2 mm thick.

Circular samples of 22 mm of diameter were characterized at three different orientation angles 0°, 45° and 90°. The zero-degree orientation is when the plate injection direction is parallel to the vertical at zero degrees. The orientation angle describes the injected plate's sample orientation from the injection direction as the zero-degree angle, as shown in Figure 2.25.

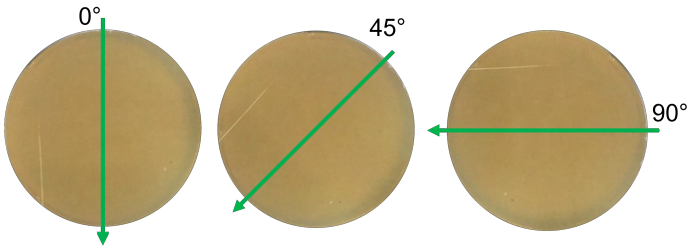

Figure 2.25: Same amorphous 2 mm thick circular sample oriented at three different angles. The green arrow indicates the injection direction.

On Table 2.17 we can see the bidirectional transmission factor measured against the sample's orientation, for the three different orientations chosen: 0°, 45° and 90°. We can notice that the TBD factor is higher at 45 DEG with 57 ± 2 % of bidirectional transmission of the incident radiation allowed. At 90 DEG we obtain a TBD factor of 56 ± 1 %, which if higher than at 0 DEG (53 ± 4 %). This indicates that more IR radiation can passes through the injected plate perpendicular to the injection direction. This confirms the IR radiation diffusion direction after passing through the injected plate, when the radiation stretches out perpendicular to the injection direction.

Sample orientation	**0°**	**45°**	**90°**	**Average**
TBD-A2	53 ± 4 %	57 ± 2 %	56 ± 1 %	55 ± 2 %

Table 2.17: Bidirectional transmission factors obtained for different sample orientation of PEKK-A2 samples.

If we take into account the uncertainty of each TBD factor obtained, we can notice that is

possible to obtain the same bidirectional transmission for the three orientations tested. But we have a higher probability to allow a higher bidirectional transmission at 90° than at 0°, and even higher at 45°.

The difference obtained on the TBD factors depending on the sample's orientation indicates that our transparent samples are optically anisotropic regarding their transmission property. Thus, the orientation of the sample has an influence on the quantity of IR radiation that our semi-transparent injected plates are going to be able to transmit. The average TBD allowed by our amorphous 2 mm thick samples is 55 %, which coincides with the TBD factor obtained when characterizing the general optical properties of the same samples.

2.4.3.6 Material variability

To verify if the optical properties of our injected plates vary on the same sample material, we test the material variability of the plate. For that, bidirectional transmission was tested and characterized at different points of an amorphous 2 mm thick injected plate. The amorphous injected plate was sectioned into nine parts to obtain a sample of each section, to characterize each part of the injected plate. Circular samples of 22 mm diameter were extracted from each section of the plate, as showed on Figure 2.26. These samples were characterized at their center with an orientation angle of zero degree.

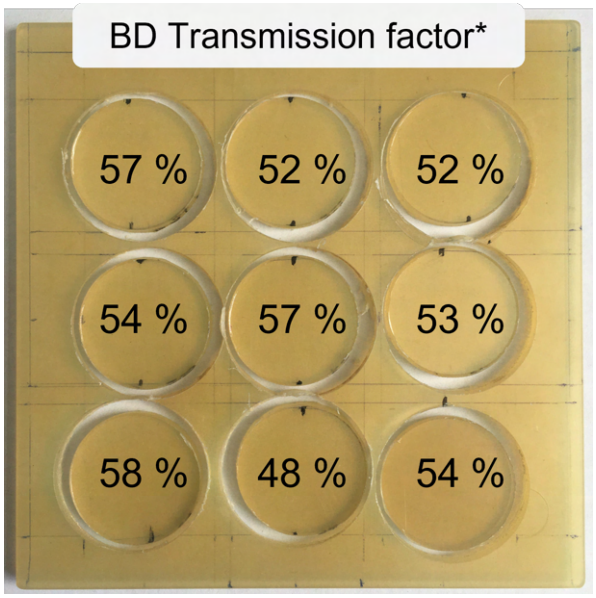

Figure 2.26: Circular samples extraction from a PEKK-A2 injected plate and their correspondent bidirectional transmission factor characterized.

The bidirectional transmission factor obtained was different for each plate's section, as showed on the Figure 2.26. The transmission percentage found within the plate has a gap of 10 %, going from 48 % to 58 %, which gives an average of 54 % for all the injected plate, with an

error of 3 %. The bidirectional transmission varies randomly within the plate. There is then a material variability on the optical properties of the injected plates, having zones with more or less transmission capability in all randomly way. Nevertheless, the different transmission percentages found within the plate are still high enough to allow the transmission of the laser radiation for LTW.

2.4.3.7 Laser scattering

A physical visualization of a red laser that is transmitted by the amorphous samples can show how the IR radiation is diffused/scattered after going through the material thickness (Figure 2.27). As it can be seen, the laser has a circular shape at the top surface of the amorphous injected plate, but after passing through the sample the laser stretches out perpendicular to the direction of the plate's injection, and its shape is deformed into an ovoid.

This phenomenon occurs with the 2 and 4 mm thick amorphous samples. And it maybe also arrives to the semi-crystalline sample, but we are not able to confirm it by physical visualization, due to the low transmission of the red visible laser by this sample.

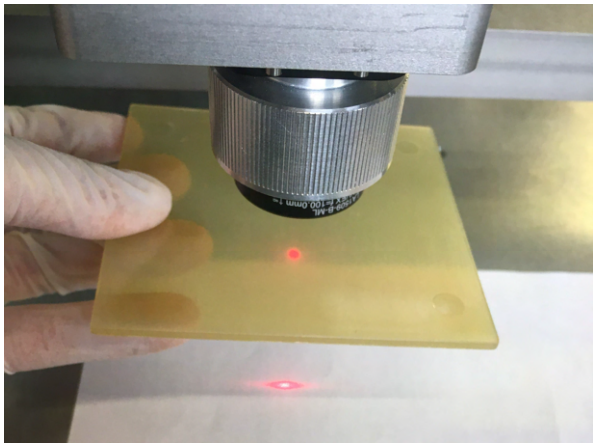

Figure 2.27: Qualitative characterization of the laser beam scattering after going through the PEKK-A2 injected plate.

2.5 Synthesis

The present chapter introduced the material of study and its relevant properties for laser transmission welding. In the first section, an overview of the PEKK welded material was presented, highlighting its interest for LTW. The second section focused on the material processing method and parameters used to obtain the samples for welding. Finally, the characterization of the injected PEKK samples was described. The properties characterized were those of importance to achieve and understand the LTW welding process on the samples, such as thermal and optical properties, as well as the effect of sample's crystallinity.

Chapter 3

Laser transmission welding of PEKK parts

Contents

3.1 Introduction 88
3.2 LTW setup and parameters 88
3.2.1 Laser welding machine device 89
3.2.2 Diode laser power source 93
3.2.3 Laser-material interaction tests for PEKK 7002 94
3.2.4 Process parameters for LTW of PEKK 7002 106
3.3 Crystallizing the welded assemblies by annealing 109
3.3.1 Preliminary annealing tests 109
3.3.2 Annealing parameters and process description 112
3.4 Weld joint characterization methods 112
3.4.1 Mechanical tests by single lap shear 112
3.4.2 Weld joint observation by microscopy 114
3.5 PEKK-A/SC assembly weld joint properties 114
3.5.1 Morphological properties 114
3.5.2 Mechanical properties 120
3.6 Synthesis 126

3.1 Introduction

In the last chapter, the suitability for LTW of PEKK injected plates was validated by characterizing their thermal and optical properties. The optical properties of the samples at the wavelength of interest indicate that PEKK amorphous samples (PEKK-A2 and PEKK-A4) are suitable as semi-transparent upper part for LTW. Their transmission factors, which are higher than 60 %, allow the laser beam to pass through the sample and irradiate the interface of the assembly, regardless of the thickness increment from 2 to 4 mm. In the other hand, PEKK semi-crystalline samples (PEKK-SC) are suitable as lower absorbent parts for LTW. The absorption factor of this sample is high enough to store the laser energy at the interface without heating the whole volume of the assembly. Therefore, the PEKK parts can be welded by LTW with the overlapped configuration where the PEKK amorphous sample is positioned over the PEKK semi-crystalline one. This assembly configuration will be designed as "PEKK-A/SC" from now on.

The present chapter focuses on the laser transmission welding process of PEKK parts. The PEKK-A/SC configuration is used to generate the welded assemblies. First a detailed presentation and description of the welding machine device and its laser source is made. Then, the study made on the interaction between the laser irradiation and the samples is detailed. Afterwards, the process parameters defined for the study, and derived from the laser-material interaction tests, are outlined. The annealing thermal treatment undergone by the assemblies after welding to enhance weld quality is presented and detailed with its protocol. Then, the characterization methods used to assess the weld joint quality, such as single lap shear (SLS) mechanical tests and microscopy observations, are described in detail. Finally, the chapter presents the results obtained from these characterization methods discussing the weld quality in terms of morphological properties and mechanical performances. These weld joint properties are discussed and correlated with the material properties and the welding parameters presented. The comparison of the joint properties is made between the just welded assemblies and those that have undergone post-weld annealing treatment, this to provide a comprehensive analysis of the weld improvements.

3.2 LTW setup and parameters

This section presents the experimental setup implemented for the laser transmission welding process of PEKK parts. The laser welding machine used for joining the parts is presented, with its components and parameters. Then a description of the studies made on the interaction between the laser beam and the material is discussed. Finally, a detailed explanation of the welding parameters defined for welding PEKK-A/SC assemblies is made.

3.2.1 Laser welding machine device

For this study, a diode laser welding machine ES Weld 200 from the supplier ES Laser [ES Laser, 2024] is used. Figure 7 shows the welding machine with its general components. The power supply switch (1) provides the electrical energy to the machine to be able to turn it on. The compressed air pump (2) allows to adjust the clamping pressure used for welding. The laser activation keys panel (3) are used to turn on-off the laser and to allow the laser beam output. This panel also contains two buttons to control the displacement of the working platform on Z direction (up and down), and an emergency stop button. The screen (4) gives access to the software that allows to control the welding procedure. The control panel (5) provides control of the X-Y displacement of the laser beam on the working space, and allows to initiate, pause and stop a welding procedure. The protection door (6) is always closed when the laser beam is activated. The observation glass (7) allows one to visualize the irradiation process from the exterior safely when the protection door is closed.

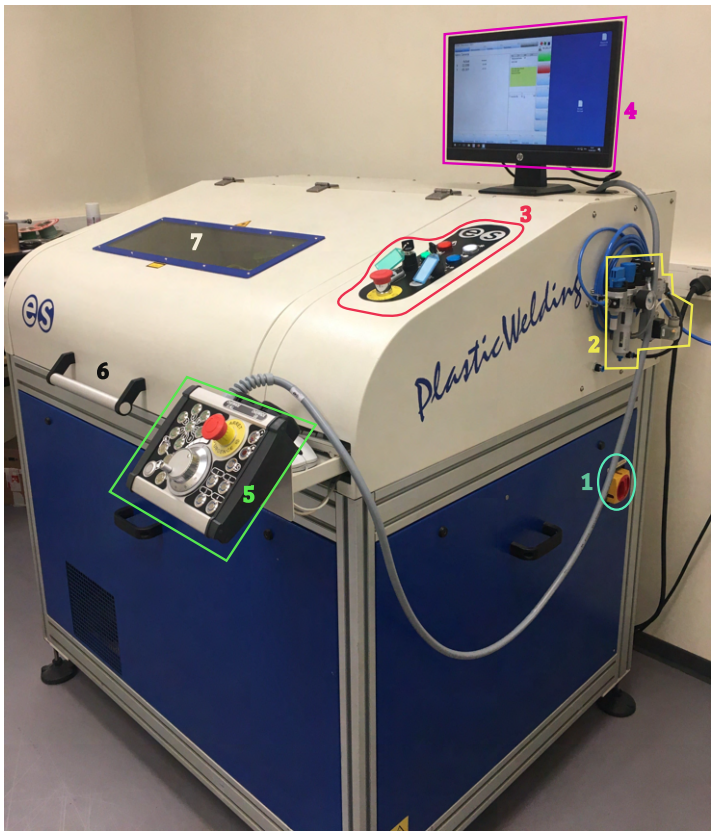

Figure 3.1: Welding machine ES Weld 200 at LGP-ENIT, exterior visualization with the components indicated by the numbers (1) power supply switch, (2) compressed air pump, (3) laser activation keys panel, (4) screen, (5) control panel, (6) protection door and (7) observation glass.

Inside the welding machine, the working space can be found, and it is visible when the protection door is opened, as shown in Figure 3.2. The first element is the diode laser source

(1). This laser source is enclosed inside a metallic device that allows to control the output of the laser beam by means of a focusing lens (2). The focusing lens can be changed to obtain different beam shapes (e.g. circular, oval, line). In this study, a circular laser beam shape is employed for all the tests. The laser source can move on the working space by means of the X-Y displacement system (3). These displacements are generated on the plan parallel to the working platform (4), where the samples are positioned for welding. The laser source cannot move automatically in the Z direction (up and down). However, the working platform can move up and down from the laser source, allowing to change the focal distance, therefore the beam focus and its dimensions.

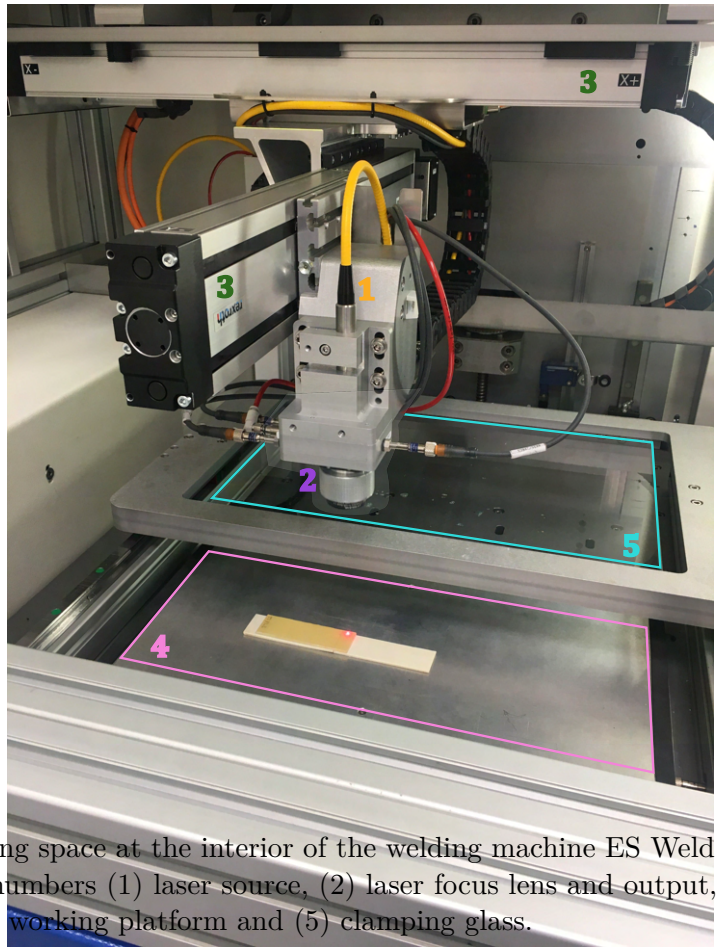

Figure 3.2: Working space at the interior of the welding machine ES Weld 200. Components indicated by the numbers (1) laser source, (2) laser focus lens and output, (3) X-Y displacement systems, (4) working platform and (5) clamping glass.

The last component of the working space is the semi-transparent clamping glass (5). This glass is positioned between the laser output and the working platform, over and parallel to this last one. The position of the clamping glass is fixed at a distance *hp* in Z over the platform, as shown schematically in Figure 3.3a. The clamping glass can slide over the working platform to open and close this space. When the glass is in an "open" position (sliding behind the working platform), one can have access to the working platform space to position the samples and assemblies on it. If the glass is in the "closed" position (over the working platform), the access to the samples is now restrained, and one can only see them through the glass. When the clamping glass is in "closed" position, the working platform can move upward to press the

samples against each other with help of the clamping glass, as seen in Figure 3.3b. Indeed, the assembly is then pressed between the working platform and the semi-transparent glass to generate the clamping pressure necessary to achieve close contact at the interface of the assembly.

The position of the clamping glass between the laser and the working platform indicated that the glass will obstruct the laser's path during sample irradiation. As shown schematically in Figure 3.3, to irradiate the samples, the laser beam will first pass through the clamping glass. This glass must thus allow a portion of the laser beam energy to pass through it to irradiate the assembly and achieve welding. The percentage of laser beam energy that the clamping glass allows to transmit is characterized by its transmissivity. The transmissivity of the clamping glass was experimentally measured using a Gentec Pronto-500 power-meter, by comparing the output power measured before and after going through the glass. Figure 3.4 shows the laser power values in watts measured before and after going through the clamping glass for each power percentage indicated in the welding machine, at the laser wavelength of interest (975 nm). At this wavelength, it was found that the clamping glass has a transmissivity of 0.83 ± 0.01. That means that 83 % of the output laser power value will be transmitted by the clamping glass to the top surface of the assembly. This transmissivity of the clamping glass must be taken into account when welding the samples.

The physical components of the welding machine and set-up are of importance, but also the welding parameters. The parameters for welding that can be defined on the welding machine are the clamping pressure, laser beam focus, laser power, scanning speed and welding path. The clamping pressure value is adjusted with the compressed air pump (Figure 7), placed in the exterior of the welding machine. The laser beam focus can be adjusted manually by moving up and down (Z direction) the working platform (with the clamping glass fixed over it). This movement will allow to modify the focal distance between the laser source and the samples positioned on the working platform. In this study, the focal distance is considered as the distance between the laser output and the interface of the assembly, where the laser must irradiate. Thus, this focal distance will determine the laser beam diameter at the interface of the assembly. For this study, the value of the focal distance is calculated by the addition of the distance between the laser output (focus lens) and the clamping glass (h_w in Figure 3.3), the clamping glass thickness (15 mm) and the upper part thickness. Therefore, in the welding machine, the distance that can be easily controlled is the height h_w.

The laser power value, scanning speed and welding path are defined in the software of the welding machine. These parameters are indicated by programming in G-code inside the software. Thanks to this definition method, any path can be developed for welding, and different scanning speeds and laser powers can be implemented in the welding procedure. The scanning speed is indicated in $mm.min^{-1}$, and the welding path is programmed by a series of defined coordinates from the starting point (also defined). The output laser power value is indicated by a percentage of the maximum power capabilities of the laser source.

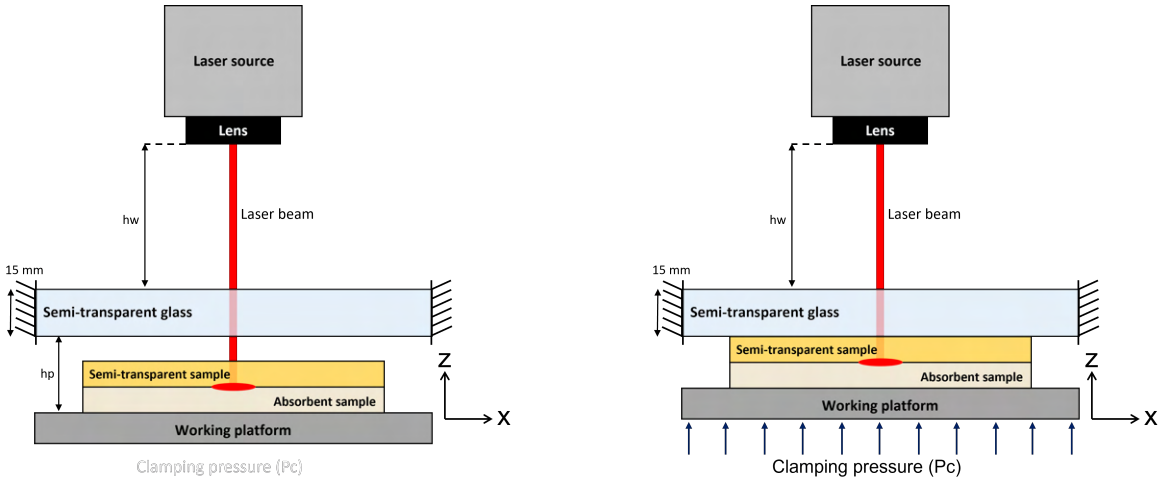

Figure 3.3: Schematic representation of the workspace inside the welding machine, showing an assembly between the working platform and the semi-transparent clamping glass: (a) before and (b) after applying the clamping pressure.

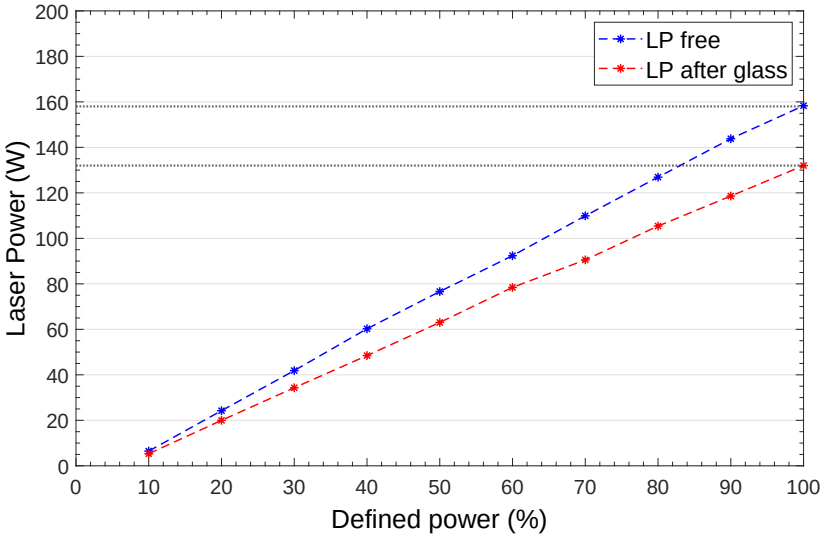

Figure 3.4: Output laser power value in watts measured for each power % defined in the welding machine. *LP free* [1] indicates the output laser power before glass and *LP after glass* indicates the laser power that achieves to go through the clamping glass. Dashed lines used to guide the eye.

[1] In the present plot it can be noticed that the *LP free* measured at 100 % is around 160 W. However, in the next section it is indicated that the output laser power at 100 % = 222 W. The discrepancy in the values came from specific experimental conditions that were not controlled at the moment of measuring the laser power to quantify the glass transmissivity. The laser power measurements were realized with a partially opened laser output gate, which was blocking the correct laser output. That was caused for an error on the positioning of this gate at the moment of the measurements. Nevertheless, the problem was solved after these tests and a complete opening of the laser output gate is employed in the following sections.

3.2.2 Diode laser power source

The diode laser from the ES Laser Welding machine has a working wavelength of 975 nm. The output laser power can be adjusted between 0 and 222 Watts, with a precision of ±3 W. The wavelength of the laser source determines the value on the electromagnetic spectrum at which the energy must be transmitted and absorbed by the samples, as already characterized in Chapter 2. The laser power value will determine the heat input at the irradiated zone, and the fact that it can be modulated gives an advantage to modify and control this heat depending on the sample's properties. The laser beam has a Gaussian intensity profile, as shown in Figure 3.5. This profile was characterized qualitatively with an OPHIR LT665 Laser Beam Profiler.

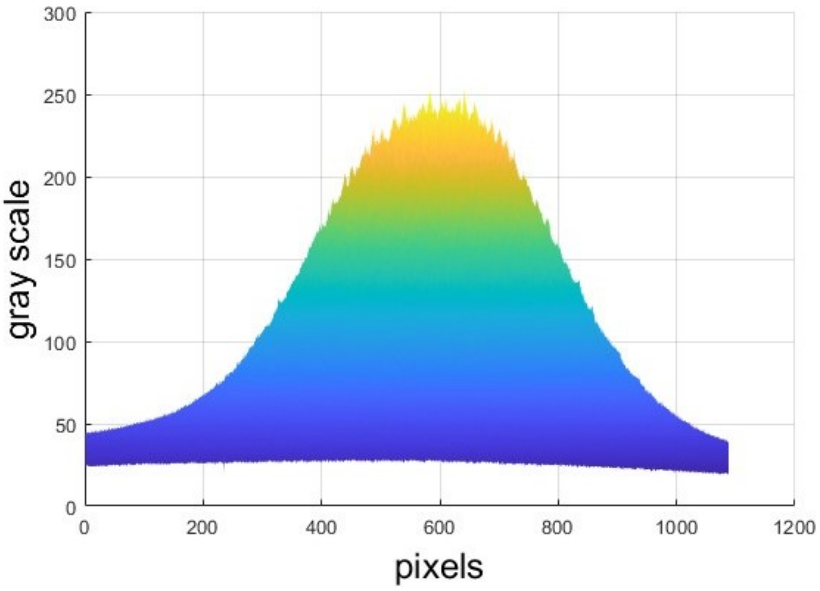

Figure 3.5: Gaussian intensity profile of the laser beam from the welding machine ES Weld 200 characterized experimentally.

The output laser power value is defined in the welding machine software by a G-code defined for the irradiation procedure. The power value is indicated by a percentage of the maximum power in watts of the machine. This percentage follows a linear relationship with the maximum power value in watts of the laser source. To found the linear relationship, laser power measurements are made for different power percentages for the study. For that, the output laser power value in watts is measured with a Gentec Pronto-500 power-meter for different power percentages indicated in the G-code. Table 3.1 show the laser power values in watts obtained from those measurements. Making a linear interpolation of the power values characterized Equation 3.1 is obtained to calculate the output power value in watts (P_o) from the power percentage ($P_{\%}$) defined in the G-code.

$$P_o = 2.4P_{\%} - 14.7 \tag{3.1}$$

P (%)	Po (W)	Error (%)
10	9	2
20	32	1
30	56	0.4
40	80	1
50	106	2
60	131	1
70	154	2
80	179	1
90	201	1
100	222	1

Table 3.1: Output laser power values in watts for some laser power percentages indicated in the G-code of the welding machine.

3.2.3 Laser-material interaction tests for PEKK 7002

The suitability of the PEKK samples for laser transmission welding process has been validated theoretically with the characterization of their thermal and optical properties. However, to achieve welding, the operation points of the welding process must also be determined. The operation points are the values of the welding parameters that are susceptible to allow welding on the studied samples. In Chapter 1, it was seen that the welding parameters involved in LTW are the laser wavelength, the intensity distribution, the laser beam focus and diameter, the laser power value and scanning speed used for irradiation, and the clamping pressure applied to keep the samples in contact all along the process. The laser wavelength and beam intensity profile are fixed parameters that depend on the type of laser used. The laser used for this study is a diode laser with a wavelength of 975 nm and a Gaussian beam profile, as detailed in Section 3.2.2. The other welding parameters can be varied within a range limited by the capacities of the laser and welding machine. The limits of those welding parameters imposed by the laser and the welding machine used for this study are mentioned in Table 3.2.

Welding parameter	Value(s)
Laser wavelength	975 [nm]
Laser intensity profile	Gaussian
Laser power	0 to 222 [W]
Scanning speed	0 to 1200 [mm·min^{-1}]
Beam diameter	2 to 6 [mm]
Clamping pressure	0 to 12 [MPa]

Table 3.2: Welding parameters values and limits imposed by the laser and welding machine used for the study.

To determine the operation points able to weld the PEKK samples of the study, it is important to understand how the samples react to the irradiation of the laser beam used for the study. This can be determined for different values of welding parameters and for different pre-welding conditions of the samples. For that, laser-material interaction (LMI) tests are carried out. The LMI tests involve exposing the samples to the irradiation of the laser beam, with welding parameters defined for irradiation. Different values of the welding parameters can be tested to define a process window for the studied assembly configuration. In addition, some pre-welding conditions of the samples can also be explored to determine the optimal pre-welding conditions to allow welding.

For the LMI study on PEKK samples the explored welding parameters are the irradiation time, laser power value and beam diameter. The irradiation time is established in seconds for the static irradiation condition and as the scanning speed for the dynamic irradiation. The laser power value is established as the output laser power percentage ($P_{\%}$) from the welding machine. The beam diameter is defined at the desired surface to irradiate, and it depends on the focal distance between the laser beam and that surface. Two focal distances are explored for the LMI tests: 78 mm, to obtain a focused beam with a diameter of 2 mm; and 161 mm, obtaining the maximum defocused laser beam with 6 mm of diameter. The LMI tests are first made on the PEKK-SC sample, and then transposed to the PEKK-A2/SC and PEKK-A4/SC configurations. For all tests, the desired surface to irradiate is the top surface of the PEKK-SC lower sample. In addition, the samples are irradiated with the clamping glass positioned between the laser and the sample, to simulate real irradiation conditions for final welding.

To better analyze the results of the interaction between the laser beam and the samples, laser power values in watts are verified and compared for each tests. As seen in the last section, the laser output power P_o value in watts can be calculated from the laser power percentage $P_{\%}$ with Equation 3.1. Then, the laser power value decreases when it goes through the thickness of another element (like the clamping glass or the upper semi-transparent part) before reaching the surface desired to irradiate. For the LMI tests on PEKK-SC samples its top surface was irradiated with the laser beam going through the clamping glass. In this case, the laser power value will decrease according to the clamping glass transmissivity. The power in watts that irradiates the PEKK-SC top surface is calculated with Equation 3.2:

$$P_s = P_o \times 0.83 \tag{3.2}$$

For the LMI tests on the PEKK-A/SC overlapped configuration, the desired surface to irradiate was placed between the overlapped samples, at the interface. Also, the clamping glass was positioned over the overlapped configuration, to simulate real welding conditions. In that case, the output laser power (P_o) will first go through the clamping glass and then through the transparent substrate. Therefore, the output laser power value will decrease after going through each layer, according to the transmission factor of each layer. Hence, the power reaching the assembly interface will be the percentage of output power that the glass and the transparent substrate will allow to transmit. At our laser wavelength, the transmissivity of

the clamping glass is 0.83, as already evaluated with the power-meter. Then, the transmission factor of the transparent-upper substrate depends on its thickness: 0.75 for PEKK-A2, and 0.62 for PEKK-A4, as seen in Chapter 2, section 4.3. Thus, the power at the interface (P_{int}) can be calculated using Equation 3.3 and Equation 3.4 for PEKK-A2/PEKK-SC and PEKK-A4/PEKK-SC, respectively. Therefore, to achieve each laser power required to irradiate the interface, the output laser power will differ depending on the upper part. This will be seen in the LMI tests results.

$$P_{int(A2)} = P_o \times 0.83 \times 0.75 \tag{3.3}$$

$$P_{int(A4)} = P_o \times 0.83 \times 0.62 \tag{3.4}$$

To analyze the different operation points explored on LMI tests, the irradiated zone is visually observed. If the employed parameters leave a mark on the sample surface in the irradiated zone, the values are confirmed. Then, the limits of the process parameters range on which the samples are susceptible to be welded are delimited by:

1. A visual alteration of the sample at the irradiated zone. This alteration of the sample indicates that it has been affected by the laser, which could suggest that the material heated to temperatures higher than its glass transition. The parameters values are thus confirmed as positive or optimal.

2. If the irradiated zone present signs of burning or degradation. This can be identified during the irradiation process, if the irradiated zone shines, indicating material burning. Or after irradiation, is the irradiated zone has acquired a brow or black coloration, or if it has a lot of irregularities. Same criteria can be found after separating the weld. In this case, the operational points used are classified as non-optimal.

Further, some pre-welding conditions of the samples are also explored: the sample orientation and the humidity content. These parameters are studied for the dynamic irradiation condition. The optimal pre-welding conditions on the samples are chosen from the visualization of the irradiated zone. In this case, observations of the irradiated zone under a numerical microscope were necessary to visualize the details of that zone.

3.2.3.1 LMI static conditions

The first LMI tests are made in static condition on the samples. The aim of these test is to understand how the laser irradiation physically affect the samples. Furthermore, to define the operation points limits concerning the laser power and irradiation time that allow material transition at the irradiated zone. Static irradiation conditions consist in irradiating the sample

surface at a specific point for a defined time. Because in the study a circular laser beam is used, the laser will irradiate only the area touched by its area.

The first tests were performed on the PEKK-SC samples with a focused laser beam (beam diameter of 2 mm). The initial operation points were set according to the minimal working values found in the literature for LTW of PAEK materials. *Amanat et al., 2010* used a minimum power value of 10 W when welding PEEK films of 0.25 mm [Amanat et al., 2010]. In our machine, a $P_{\%}$ of 10 % is the nearest power to 10 W. For the irradiation time, *Villar et al.* welded PEKK 6002 thick samples of 2 mm under static conditions using a minimal irradiation time of 8 s [Villar et al., 2018]. Therefore, those parameters were chosen as initial operation points. However, different values were added along the initial LMI tests to increase the testing window, as shown in Table 3.3.

Operation point	**First limits**	**Adjusted**
P_o[%]	10 to 20	15 to 25
Irradiation time [s]	8, 10, 12, 16, 30	2 and 4

Table 3.3: Initial operation points for LMI tests on PEKK-SC.

Therefore, different irradiation times were tested for laser power outputs percentages between 10 and 20 %. For laser power values of 10 and 11 %, the irradiated zone did not show marks or heat effect, regardless of the irradiation time. When using power values between 12 and 20 %, the samples burned for times longer than 10 s, and heat effect (melting) occurred throughout the thickness of the sample. Therefore, the operation points were adjusted taking into account these first results and in order to improve the irradiation. Lower irradiation times were defined to avoid burning, setting two operation points: 4 and 2 s. Then, higher power values were chosen, to allow heat effect at low times, between 15 and 25 %. For an irradiation time of 4 s, a power working window between 17 and 19 % was obtained (Figure 3.6a). Employing 2 s of irradiation allowed for a larger power range window, from 19 to 23 % (Figure 3.6b). Therefore, 2 s are chosen as the optimum irradiation time for static irradiation of PEKK-SC, with its corresponding power range.

With this first LMI test, it was observed that a good visual aspect of the heat-affected zones (HAZ) is found when the irradiation time is decreased and the laser power increases (up to certain limits). Therefore, an optimal irradiation time must be short, not exceeding 10 s, and better if it is less than 4 s. Also, it was seen that the laser power value has a better impact on the irradiated zone than the irradiation time. In the case of the PEKK samples of this study, it is more viable to define a large process window on laser power for a same irradiation time, than the opposite.

The irradiated zones obtained from the LMI tests on PEKK-SC samples with an irradiation time of 2 s for different power values between 16 and 24 % are observed in Figure 3.7. The limits of the optimal process window for these irradiation conditions are defined in Table 3.4. The HAZs obtained by those limits are observed under numerical microscope and studied. As it can be noticed, the laser irradiation allowed the sample to be melted in

the targeted zone. This can be noticed by the change in coloration of the PEKK-SC sample, which acquires a yellow tone. This can indicated rapid melting and cooling, inducing the PEKK-SC sample to become amorphous (yellow) after irradiation. This visualization results validate the process parameters working points. However, it is seen that the size of the heat-affected zone is shorter than the beam sizes used for irradiation. For 19 % of power, the HAZ diameter reaches 548 μm, being almost 4 times shorter than the original beam size. For the higher power used of 23 %, the HAZ diameter is around 995 μm, less than the half of the original beam size. This can be explained by the type of intensity profile of the laser beam, where the maximum point is reached at the center of the irradiated zone and it decays to the borders of the beam area. It is an important point that must be taken into account when welding. Increasing the beam size can help to increase the HAZ.

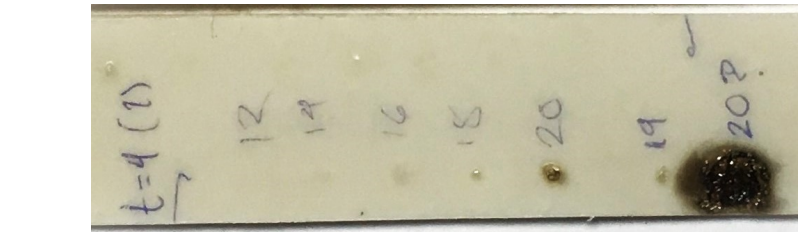

(a)

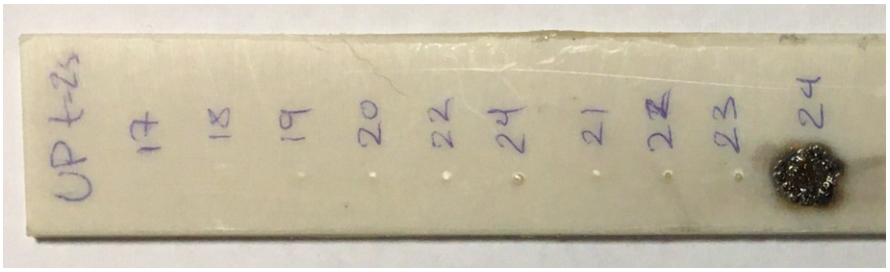

(b)

Figure 3.6: LMI tests static conditions on PEKK-SC sample. Different laser powers tested for an irradiation time of (a) 4 s and (b) 2 s.

Operation point	**Minimum**	**Maximum**
P_o [%]	19	23
P_o [W]	31	41
P_s [W]	26	34
HAZ size (diameter) [mm]	0.548	0.995

Table 3.4: Process window for a suitable LMI on PEKK-SC for an irradiation time of 2 s and a beam diameter of 2 mm.

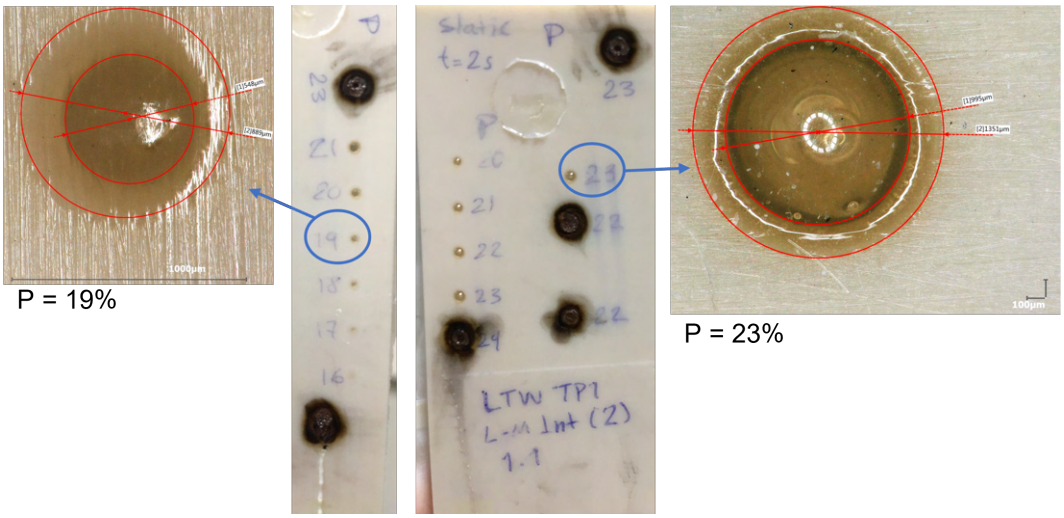

Figure 3.7: Irradiated zones from LMI tests in static condition on PEKK-SC sample. Irradiation time = 2s. $P_{\%}$ between 16 and 24 %.

For the same irradiation time defined for PEKK-SC samples, different output power values were tested to find the process window for the overlapped configuration of PEKK-A/SC parts. Power values from 22 to 36 % are explored. For 2 s of irradiation, the optimal operations points limits defined from this tests are indicated in Table 3.5 for each overlapped configuration. As it can be seen, the optimal power percentage range differs for each overlapped configuration, being higher for the PEKK-A4/SC than for the PEKK-A2/SC. This is because the desired irradiated zone is now at the interface of the overlapped configurations. And the laser power to irradiate the desired zone must go first through the upper PEKK-A part to reach the top surface of the PEKK-SC sample. Taking into account that the laser power decreases while going through the upper part due to its transmissivity, the quantity of power that achieves to irradiate the interface is lower than the output power. Then, knowing from the optical characterization of the samples (ref. Chapter 2), increasing the thickness of the PEKK-A upper part reduces its transmissivity, which indicates that less power will reach the interface on the PEKK-A4/SC configuration compared to the PEKK-A2/SC one. Therefore, more output power is necessary to use on the PEKK-A4/SC configuration to achieve enough heating than on the PEKK-A2/SC one. However, analyzing the power values P_{int} reached at the interface from the P_o it can be noticed that both overlapped configuration share the same power range.

Figures 3.8 and 3.9 show the irradiated zones obtained on PEKK-A2/SC and PEKK-A4/SC overlapped samples, respectively. In this case, various test per operation point were made to test replication. As it can be seen, the laser irradiation leave marks on both samples on the surfaces that generated the interface of the overlapped configuration. This indicates good heat absorption and conduction properties from the PEKK-SC sample to the PEKK-A sample at the interface. Those results validate qualitatively the possibility to weld the PEKK-A parts to the PEKK-SC ones by LTW.

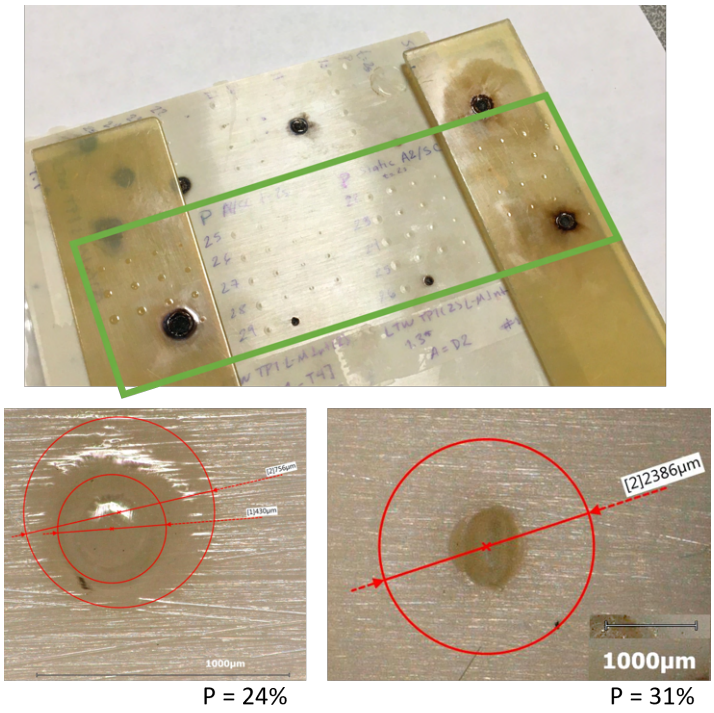

Figure 3.8: Irradiated zones from LMI tests in static condition on PEKK-A2/SC configuration. Irradiation time = 2 s. $P_{\%}$ between 22 and 29 %.

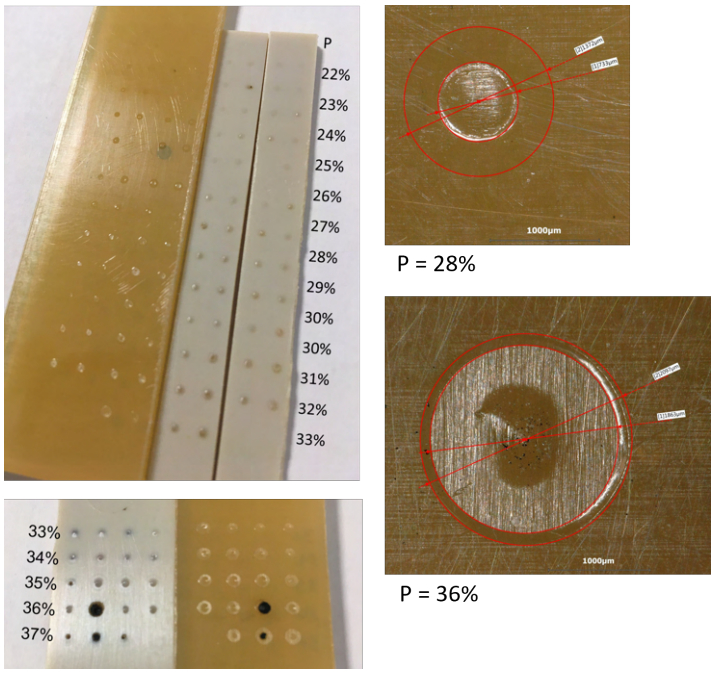

Figure 3.9: Irradiated zones from LMI tests in static condition on PEKK-A4/SC configuration. Irradiation time = 2 s. $P_{\%}$ between 22 and 37 %.

Configuration	P_o [%]	P_o [W]	P_{int} [W]	HAZ size (diameter) [mm]
PEKK-A2/SC	24 to 31	43 to 60	27 to 37	0.756 to 2.386
PEKK-A4/SC	28 to 36	52 to 72	27 to 37	0.733 to 1.863

Table 3.5: Process window for a suitable LMI on PEKK-A/SC overlapped configuration for an irradiation time of 2 s and a beam diameter of 2 mm.

3.2.3.2 LMI dymanic conditions

To test the samples irradiation in dynamic conditions, a linear movement of the laser is chosen. The laser irradiates the sample while moving from a starting point to an end point defined by a length path L_i. The movement of the laser beam is conditioned by the scanning speed. Therefore, for the dynamic LMI tests, the parameters that will be explored are the scanning speed and the laser power. In addition, two beam diameters will be investigated, 2 and 4 mm, obtained from maximum focus and defocus, respectively. At the end, the optimal process window for dynamic irradiation will be defined for PEKK-A/SC overlapped configuration.

From the LMI static irradiation conditions was found that the optimal irradiation time to obtain a good visually altered HAZ on the sample is 2 s (for powers percentages over 19 %). If we take into account that 2 s were used to irradiate 2 mm of distance (from the beam diameter), the optimal scanning speed for dynamic irradiation should be 1 mm·s^{-1}. However, a quick verification of this hypothesis was made, by testing different scanning speed for a same laser power percentage of 20%. The scanning speed explored were 1200, 240, 120, 75 and 60 mm·min^{-1}. Figure 3.10 show the irradiated zones on PEKK-SC samples when testing the mentioned scanning speed at 20 % of laser power. As it can be seen, the scanning speed of 1 mm·s^{-1} achieved to good heat affect the sample at the irradiated zone. Therefore, 1 mm·s^{-1} is defined as the optimal scanning speed for irradiating the PEKK samples.

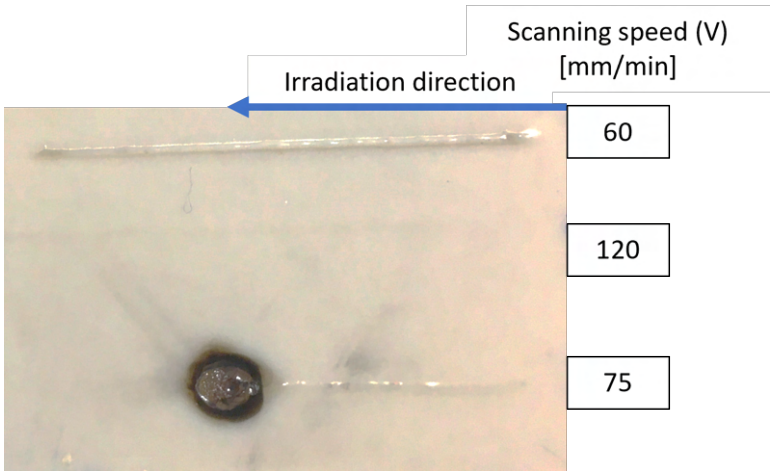

Figure 3.10: LMI tests in dynamic condition with a beam diameter of 2 mm. Tests made on PEKK-SC samples for different scanning speed and $P_{\%} = 20$ %.

Different laser power percentages were explored for the chosen scanning speed to find the optimal range. Table 3.6 indicates the optimal operation points found for PEKK-SC sample and PEKK-A2/SC configuration. In the case of PEKK-SC sample irradiation, the process window obtained for a suitable LMI is between 18 to 22 %. For the irradiation of the overlapped configuration of PEKK-A2/SC, the power range is delimited from 20 to 23 %. Figure 3.11a shows the HAZs obtained on the PEKK-SC samples for dynamic irradiation. The width of the HAZ line generated is less than a half of the beam diameter. A width of 0.262 mm is obtained when irradiating at 18 % of power, and of 0.59 mm for the maximum power of 22 %. The width of the irradiated zone is of importance to the quality of the final weld joint. This width, combined with the length path, generate the area of welding, which determines the contact surface for the mechanical performances. Having an irradiated zone with a width as little as that could cause problems on the quality of the final weld joint. Because of that, it was considered important to increase the beam diameter to improve the irradiated zone area, therefore aiming for an improvement of the weld joint quality. Hence, for the next LMI dynamic tests a beam diameter of 6 mm is then used. This beam size is obtained at maximum defocus of the laser beam, with a focal distance of 161 mm.

Configuration	P_o [%]	P_o [W]	P_{int} [W]	HAZ size (width) [mm]
PEKK-SC	18 to 22	29 to 38	24 to 32	0.262 to 0.59
PEKK-A2/SC	20 to 23	33 to 40	21 to 25	NA

Table 3.6: Process window for a suitable LMI on PEKK-SC samples and PEKK-A2/SC overlapped configuration for a scanning speed of 1 mm·s^{-1} and a beam diameter of 2 mm.

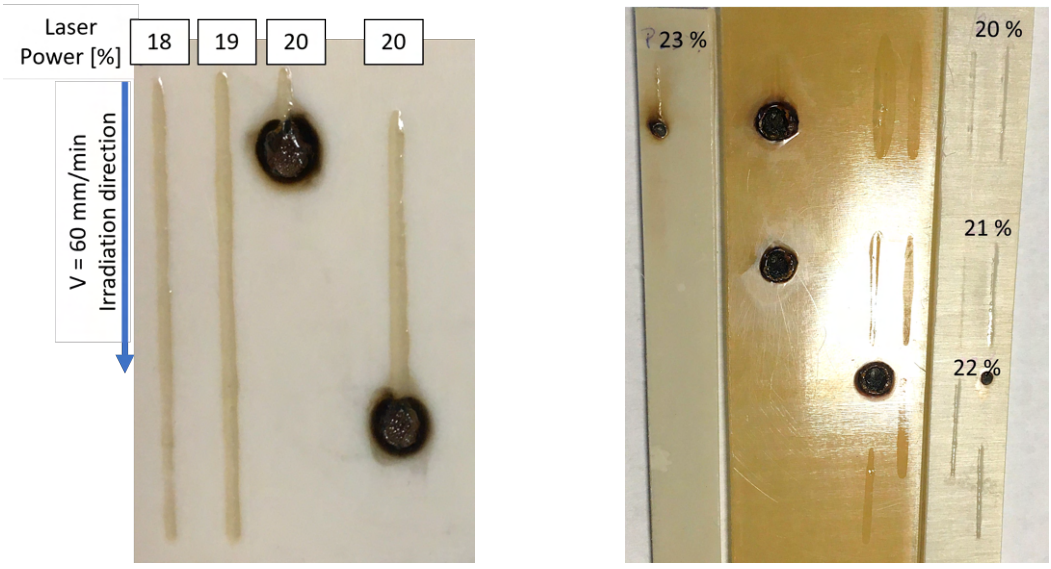

(a) (b)

Figure 3.11: LMI tests in dynamic condition with a beam diameter of 2 mm. Tests made for a scanning speed of 1 mm·s^{-1} and different power values on (a) PEKK-SC samples and (b) PEKK-A2/SC overlapped configuration.

The dynamic irradiation with a beam diameter of 6 mm is first tested on PEKK-SC sample. First, the power range obtained from the last tests is explored (18 to 22 %). With that power range no interaction between the laser and the material is generated. Thus, the power range is increased periodically until obtaining a suitable LMI (identified by the criteria already indicated at the beginning of the section). The optimal laser power range obtained for the PEKK-SC sample is between 32 and 45 %. These power percentages give a power range in watts of 54 to 78 to irradiate the sample surface. This power range will tried to be transposed to the PEKK-A/SC overlapped configuration, as made for the static tests.

For the LMI dynamic tests on PEKK-A/SC overlapped configuration, clamping pressure was applied while irradiation to test the real welding conditions and ensure the optimal parameters for welding. In that case, two more criteria are added for the validation of the operation points: (1) the samples stay together after irradiation, and (2) it isn't easy to separate the welded samples by hand.

The dynamic irradiation was thus tested on PEKK-A2/SC configuration using the same power range in watts obtained in PEKK-SC samples. However, the interface of the assembly started to be heat affected by the laser power when reaching 72 W at the interface. The need of a higher power at the interface when the upper part is over the PEKK-SC sample can be due to the scattering of the laser beam by the upper part. The laser power value obtained here at the interface is theoretically calculated by taking into account only the transmissivity of the upper part. However, the scattering phenomena and coefficient is not considered, because quantitative characterization was not possible to realize. Figure 3.19 show the heat-affected zones obtained for a dynamic irradiation on PEKK-A2/SC configuration for a beam diameter of 6 mm. Laser powers that achieve to generate heat effect at the interface were defined between 54 and 72 %, which in watts is transposed to 72 to 98 W at the interface.

The power range obtained for the PEKK-A2/SC configuration was then transposed to the PEKK-A4/SC configuration, with adding ± 2 W to each limit. That allowed to define the power range for the last welding configuration which goes from 70 to 95 W. All the process windows found for each tests are detailed in Table 3.7. As it can be noticed, the power range share for both assemblies configuration is from 72 to 95 W. However, a last test was made to investigate the lower laser power values effect to ensure the optimal minimal value for welding. As is shown on Figure 3.13, the minimum value of 72 W (54 %) heat affected the interface, but did not generated melting on the whole irradiated zone. The power value that achieved melting of the whole irradiated area is 75 W (56 %). Therefore, the optimal process window to weld PEKK-A/SC samples by LTW in dynamic conditions when using a scanning speed of 1 $mm{\cdot}s^{-1}$ and a beam diameter of 6 mm is for a power range of 75 to 95 W at the interface.

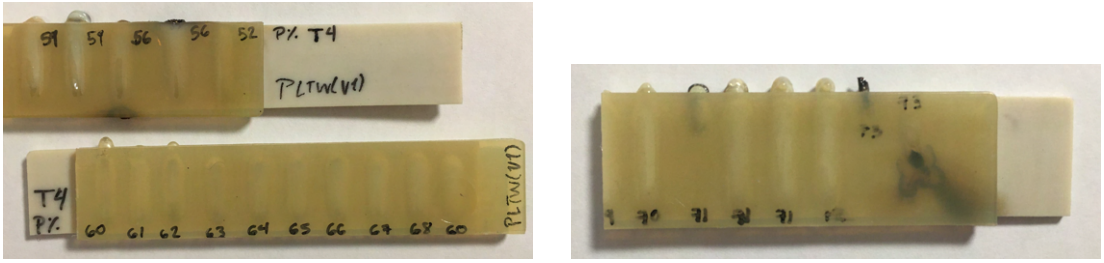

(a) (b)

Figure 3.12: LMI tests dynamic conditions on PEKK-A2/SC assembly configuration. Laser powers tested from (a) 52 to 68 % and (b) 69 to 73 %.

Configuration	P_o [%]	P_o [W]	P_{int} [W]
PEKK-SC	33 to 45	65 to 93	57 to 78
PEKK-A2/SC	54 to 72	115 to 158	72 to 98
PEKK-A4/SC	62 to 84	134 to 187	70 to 95

Table 3.7: Process window for a suitable LMI on PEKK-SC samples and PEKK-A2/SC overlapped configuration for a scanning speed of 1 mm·s^{-1} and a beam diameter of 6 mm.

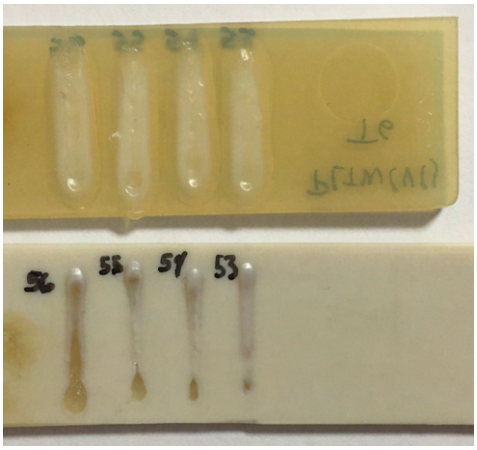

Figure 3.13: LMI tests dynamic conditions on PEKK-A2/SC assembly configuration for the lower laser powers between 53 and 56 %.

3.2.3.3 LMI for pre-welding conditions of samples

Two pre-welding conditions of the samples were investigated for the LMI tests: the humidity content and the sample orientation. LMI tests are made in dynamic conditions on the PEKK-SC sample, using the optimal irradiation parameters defined in the last section for a focused laser beam of 2 mm: scanning speed is set to 60 mm·min^{-1} and laser power to 20 %. For each

pre-welding condition, two values are explored, as shown in Table 3.8. The humidity content refers to the sample's exposure to moisture. The first studied condition is when the samples is free of moisture, which is achieved by drying the samples at 120°C for 24h before welding. The other condition is for a sample exposed to ambient humidity for more than 2 h and it is not dried before welding. The sample orientation corresponds to the injection direction of the PEKK plates, when injecting them. In this case, two orientations of the sample are explored for the dynamic irradiation: parallel and perpendicular to the weld path.

Figure 3.14 shows micrographs of the irradiated zones obtained on the pre-welding conditions LMI tests. As it can be noticed, bubbles appear on the HAZ when the samples are exposed to ambient humidity and not dried before irradiation. On the opposite side, if samples are dried before irradiation, the HAZ shows a minimal quantity of bubbles (only one) make it clean of voids. This aspect is important to take into account for the welding tests of PEKK samples to avoid voids on the weld and avoid the alteration of the weld joint quality. Then, focusing on the sample orientation parameter, it can be seen that the thickness of the HAZ generated is more regular when the weld is made parallel to the sample orientation, than perpendicular. This indicates the importance of well orient the sample with the welding path. Therefore, to obtain the optimal pre-welding conditions on the samples they must be dried before welding and the irradiation must be made parallel to the sample orientation, to the injection direction.

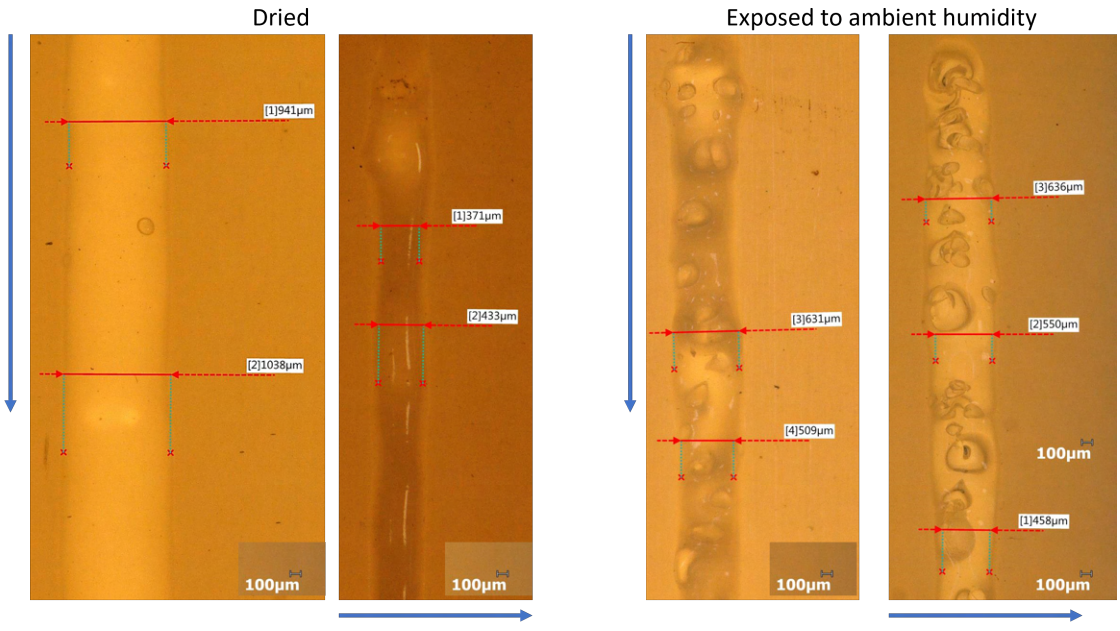

Figure 3.14: Micrographs of the irradiated zones from LMI tests for the pre-welding conditions on PEKK-SC sample. Scanning speed = 60 mm·min^{-1}. $P_{\%} = 20$ %. Arrow indicates injection direction.

Sample orientation	• Parallel to the irradiation path • Perpendicular to the irradiation path
Humidity content	• Sample dried (at 120°C for 24h) • Sample exposed to ambient humidity (for more than 2h on the laboratory)

Table 3.8: Pre-welding conditions of the samples explored on the LMI tests.

Table 3.9 summarizes the operation points of the welding parameters defined by the LMI tests to achieve welding of PEKK-A/SC parts by LTW with a diode laser of 975 nm.

Process parameter	**Limits**
Focal distance	161 mm
Beam diameter	6 mm
Scanning speed	60 mm·min^{-1}
P_{int} [W]	75 to 95
Sample orientation	parallel to the irradiation path
Sample humidity content	to dry at 120°C for 24h before irradiation

Table 3.9: Operation points to achieve LTW of PEKK-A/SC parts with a diode laser of 975 nm.

3.2.4 Process parameters for LTW of PEKK 7002

As already mentioned, PEKK 7002 injected samples are welded on an overlapped configuration where the PEKK amorphous (PEKK-A) is positioned over the PEKK semi-crystalline (PEKK-SC) sample (PEKK-A/SC assembly). Also, two different thicknesses are used for the upper amorphous sample 2 and 4 mm thick (PEKK-A2 and PEKK-A4, respectively). Each upper part (2 and 4 mm) is thus paired with the lower absorbent PEKK-SC part, resulting in two types of assemblies: PEKK-A2/SC and PEKK-A4/SC. The configuration used for welding is the lap-joint (Figure 3.15), with an overlap of 12.5 mm, as indicated in ISO 4587:2003. This configuration is used to allow the assemblies to be mechanically tested by single lap shear (SLS) tests.

The welding parameter varied on the study is the laser power value used to irradiate the interface of the assemblies. The laser intensities are chosen from the power-range that allows melting at the interface without burning, that is between 75 and 95 Watts. This power-range was determined from previous laser-material interaction tests. To narrow the study, four laser power intensities were selected, based also on preliminary welding tests: 75, 85, 88 and 95 W. Amanat et al. studied the welding process of PEEK-injected plates of 0.7 mm thickness [Amanat et al., 2011] they found that laser power is a crucial parameter for weld strength, whereas irradiation time has little effect. Other works on PEEK and their composites, have

also focused on laser power [Liu et al., 2022, Korycki et al., 2022].

Therefore, the two parameters varied and studied for the welding process are the thickness of the upper semi-transparent part and the laser power used to irradiate the assembly. The two types of assemblies (PEKK-A2/SC and PEKK-A4/SC) are welded using four laser powers to obtain 8 assembly combinations, as detailed in Table 3.10.

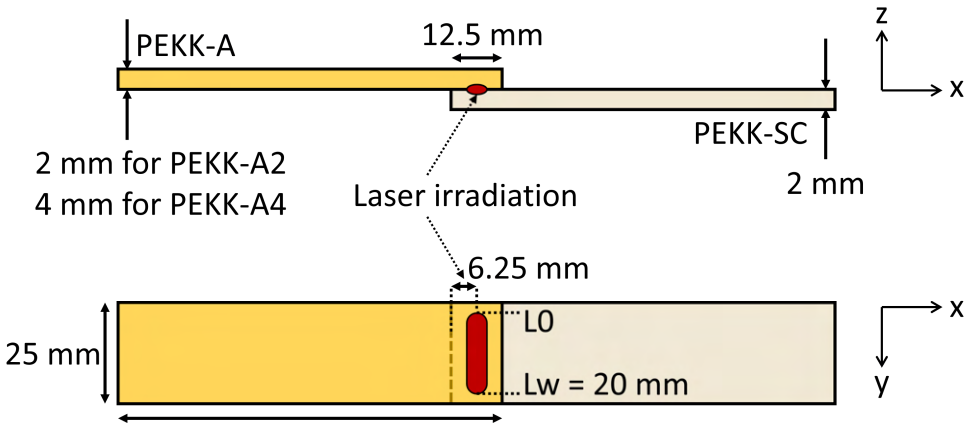

Figure 3.15: Schematic representation of lap-joint configuration used for welding PEKK-A/PEKK-SC.

Laser power	75 W	85 W	88 W	95 W
PEKK-A2/SC	A2/SC-P1	A2/SC-P2	A2/SC-P3	A2/SC-P4
PEKK-A4/SC	A4/SC-P1	A4/SC-P2	A4/SC-P3	A4/SC-P4

Table 3.10: Assembly combinations for the study

Inside the welding machine, the assembly configuration is kept fixed on the welding machine working platform. A support is placed under the amorphous sample to keep the interface parallel to the platform. The 15 mm thick semi-transparent clamping glass plate is positioned over the assembly to apply the clamping pressure necessary to ensure intimate contact at the joint interface. Clamping pressure is constantly applied at 3.8 MPa thanks to the glass plate. A circular shape laser beam is used with a beam diameter of 6 mm, obtained at maximum laser defocus (h_w = 161 mm). The weld is created at the center of the overlap area using a moving laser. Thus, the interface is heated as the laser beam moves over the samples following a predefined welding path. This LTW technique is known as contour welding.

The welding path is a straight line: the laser beam moves from its initial position (L0) until the indicated weld length (Lw) of 20 mm, as shown in Figure 3.15. When a constant speed is used to irradiate the interface from L0 to Lw, an ovoidal weld bond is created instead of a thick line, as shown in Figure 3.16A. To obtain a more homogeneous weld bond along the line laser path, like in Figure 3.16B, a procedure combining static and dynamic irradiation is applied. The procedure starts by statically irradiating the interface for 2 seconds at L0.

Then, the laser moves to irradiate at the given speed, from L0 to Lw. Finally, the laser statically irradiates the interface for 1 second at Lw. That allows to melt the interface all along the welding path in a more homogeneous shape of the weld bond (Figure 3.16B). The optimum welding speed to achieve the melting at the interface, regardless of the laser power, is 60 mm·min^{-1}, as determined by previous tests. Thus, welding speed is kept constant for all welds. After irradiation, clamping pressure is maintained for 120 seconds while cooling.

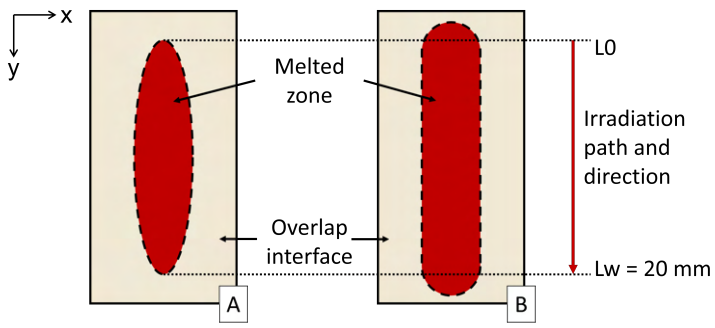

Figure 3.16: Schematic diagram of the melted zone's shape created at the interface when irradiating with (A) dynamic procedure, (B) static and dynamic procedure.

For welding, as seen on the LMI tests, the interface of the assembly will be irradiated by the laser beam after going through the clamping glass and then through the upper part. Therefore, the output laser power value will decrease according to the transmissivity of each semi-transparent object until reach the interface. Hence, to achieve each laser power chosen for the study to irradiate the interface (indicated in Table 3.10), the output laser power will differ depending on the upper part. The power at the interface (P_{int}) can be calculated using Equation 3.3 and Equation 3.4 for PEKK-A2/PEKK-SC and PEKK-A4/PEKK-SC, respectively. Table 3.11 indicates the output laser power used for each type of assembly to obtain the desired power at the interface for each targeted power. Table 3.12 shows a summary of the welding parameters defined and used for welding PEKK-A/SC.

	P_o [W]		**P_{int} [W]**
	for A2/SC	for A4/SC	For both
P1	123	148	75
P2	139	168	85
P3	144	175	88
P4	154	188	95

Table 3.11: Laser power values used for LTW of PEKK-A/SC

Parameter	Value	Unity
Beam shape (Bs)	circle	-
Laser focus height (h_w)	161	[mm]
Beam diameter (D_B)	6	[mm]
Welding path	line	-
Weld length (Lw)	20	[mm]
Power at interface (P_{int})	75 to 95	[W]
Scanning speed (V)	60	[mm.min^{-1}]
Clamping pressure (P_c)	3.8	[MPa]
Welding procedure	2s static irradiation at L0 + dynamic irradiation at V from L0 to Lw + 1s static irradiation at Lw	-
Cooling time after irradiation (with P_c)	120	[s]

Table 3.12: Welding parameters used to LTW PEKK-A/SC injected plates.

3.3 Crystallizing the welded assemblies by annealing

After welding, some of the assemblies undergo an annealing treatment to increase the crystallinity of the welded zone. The annealing is performed in an oven UFP400 from Memmert at the cold crystallization temperature for a defined time. The welded assemblies are placed inside a fabricated mold to avoid sample deformation. This section describes the preliminary annealing tests performed to define the annealing parameters and protocol.

3.3.1 Preliminary annealing tests

The annealing process aims to turn the amorphous state of the material to crystallization to its maximum degree. The effectiveness of annealing on promoting crystallization has already been proven by Liu et al. on PEEK/PEEK-CF LTW assemblies [Liu et al., 2022]. The annealing temperature must be between Tg and Tm to achieve crystallization in isothermal conditions from the amorphous state, as stands by *Quiroga Cortés et al., 2016* [Quiroga Cortés et al., 2016]. As seen in Figure 3.17, PEKK-A crystallizes during the first heating ramp after the glass transition temperature. This crystallization is assessed by the exothermic peak after Tg, namely cold crystallization temperature (Tcc). The crystallization of the amorphous form of the material starts with the development of the first germs. This first crystal germination occurs at the beginning of the exothermic peak when heating. The cold crystallization peak observed in Figure 3.17 seems to start around 190 °C. Thus, 190 °C is the temperature established for the annealing process of the welded assemblies.

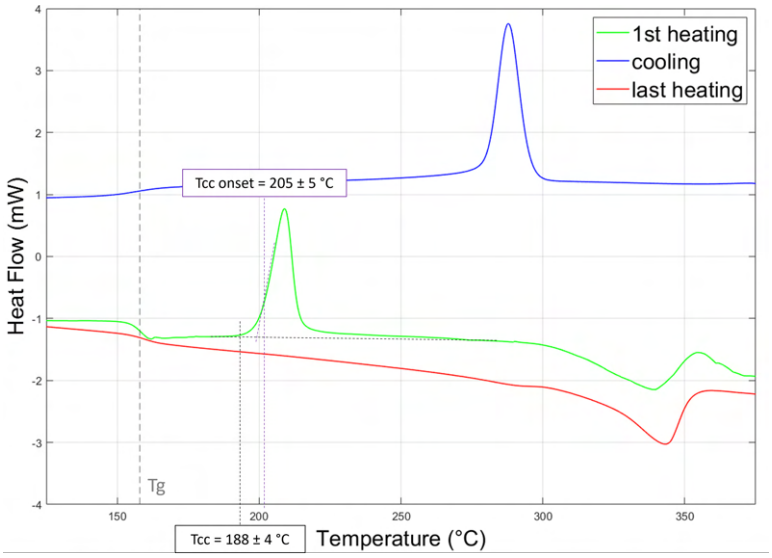

Figure 3.17: Typical DSC thermogram of PEKK-A (amorphous) samples. Cold crystallization temperature (T_{cc}) values are indicated in the plot. Heating and cooling ramps at 10 °C·min^{-1}.

Preliminary annealing tests were carried out in PEKK-A/SC trial assemblies to observe the physical effect of the thermal treatment on the assemblies. The trial assemblies represented the overlapped section of the lap-joint assemblies, with dimensions of 25 × 12 mm^2 with the respective thickness of the samples, as shown in Figure 3.18a. These preliminary annealing tests were carried out at 190 °C for 5 minutes.

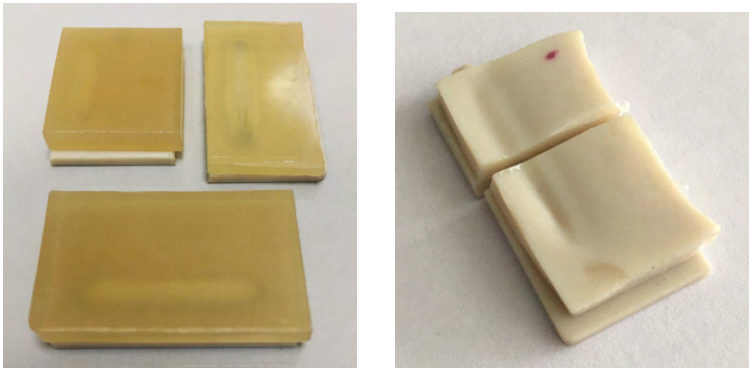

(a) (b)

Figure 3.18: Preliminary annealing tests: PEKK-A/SC trial (a) welded assemblies and (b) after annealing.

Figure 3.18b shows one of the welded assemblies after annealing. As can be noticed, when annealing the assemblies, the PEKK-A sample (upper part) acquired a milky-white coloration similar to the PEKK-SC sample, indicating an increment in the crystallinity of the PEKK-A sample. Additionally, the PEKK-A sample swells and deforms under the effect

of crystallization. Despite this sample deformation, it was verified that the weld joint did not separate during the annealing process, validating the feasibility of the annealing process without damaging the weld joint.

However, avoiding sample swells and deformation during annealing is important to conserve the assembly shape and performance. For that, the assemblies can be restrained inside a mold with the shape of the assemblies. Therefore, a mold was fabricated to avoid deformation of the assembled parts while ensuring homogeneous annealing of the assemblies. The mold consisted of two thick aluminum plates of 10 mm superposed, with the lap-joint assemblies between them. Figure 3.19a shows the fabricated mold in an opened configuration with eight PEKK-A2/SC assemblies already annealed. The PEKK-SC sample of the lap-joint assembly is positioned on the bottom plate, and a metallic sheet 2 mm thick is positioned under the PEKK-A sample of the assembly and another one over the PEKK-SC sample to balance the differences in height between the welded parts caused by the lap-joint configuration. The assemblies are positioned with a separation of 10 mm between them to avoid the samples merging when being softened by heat, and PEKK-SC samples of 10 mm width are used in between the PEKK-A samples to restrain their deformation. The aluminum plates are clamped by four screws on each corner to keep the assemblies constrained, as shown in Figure 3.19b. The mold can hold eight assemblies at a time.

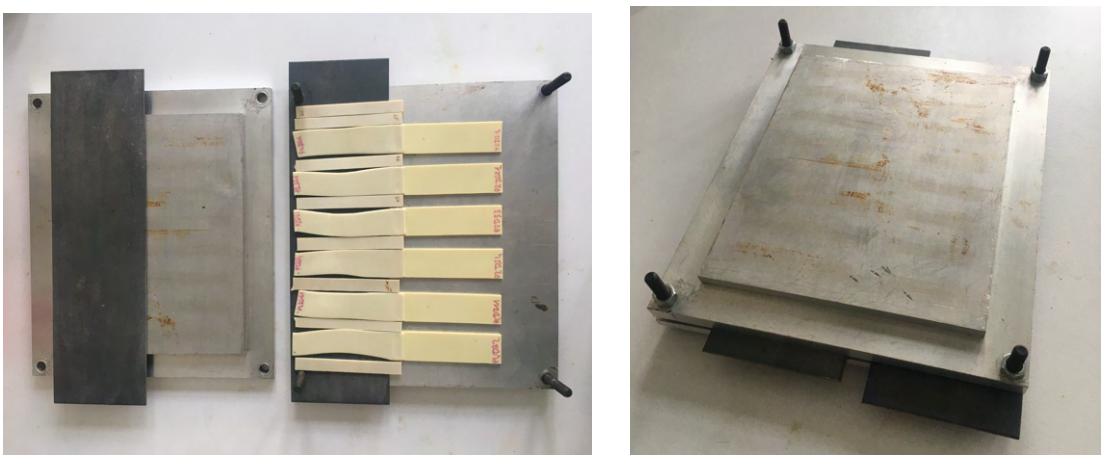

(a) (b)

Figure 3.19: Mold fabricated for the annealing tests (a) opened and (b) closed.

To determine the annealing time, preliminary welding tests were carried out on eighth PEKK-A/SC assemblies inside the mold, as shown in Figure 3.19a. *Quiroga Cortés et al., 2016* [Quiroga Cortés et al., 2016] investigated the impact of annealing on the physical structure of PEKK 60/40. They observed that prolonged annealing duration or annealing at higher temperatures led to a significant increase in crystallinity. They also associated the crystal improvement with the increment of the annealing time at a given temperature, resulting from conformational reorganizations during annealing. In the present study, annealing times between 1 and 4 hours were tested. The assemblies were inspected visually after each annealing

treatment to observe the PEKK-A sample coloration. It was observed that an annealing time of 3 hours was enough to obtain a similar color than the PEKK-SC sample. Therefore, 3 hours is the time defined for the annealing process.

3.3.2 Annealing parameters and process description

Annealing is performed at 190°C for 3 h inside an oven UFP400 from Memmert. Eight welded assemblies are placed into the fabricated mold to avoid sample deformation. The mold is pre-heated in the oven at the annealing temperature. After annealing, the assemblies are slowly cooled inside the mold up to room temperature. Then, they are stored in a desiccator before further testing. The welded assemblies that have undergone annealing post-welding are named "PEKK-Ac/SC" to distinguish them from the non-annealed ones (PEKK-A/SC).

The study of annealing is carried out on the following specimens: P2 (85 W) and P4 (95 W). These two powers are chosen from the results obtained in the mechanical characterization of PEKK-A/SC welds (ref. Section 3.5.2). Upon annealing, not only the weld joint is crystallized, but also the whole specimens. After crystallization, the assemblies are characterized visually and mechanically.

3.4 Weld joint characterization methods

3.4.1 Mechanical tests by single lap shear

Different mechanical tests are carried out to quantify the resistance of welded samples by LTW: DCB [Juhl et al., 2013b, Chabert et al., 2020], wedge [Villar et al., 2018], and single-lap shear (SLS) tests [Amanat et al., 2010, Juhl et al., 2013b, Juhl et al., 2013a, Wippo et al., 2016, Asseko et al., 2016, Korycki et al., 2022]. SLS is the easiest and most used test.

The lap-joint assemblies are characterized by SLS tests as shown in Figure 3.20. A tensile machine INSTRON 550R is used with a load cell of 50kN and a cross-head load rate of 2800 N.min^{-1}. Eight assemblies are tested for each parameter for the PEKK-A/SC non-annealed welds. Three samples are tested per parameter for the annealed assemblies. All the assemblies are tested until failure. After failure, samples are inspected to identify the failure type. To identify their failure type, four failure types are defined (Table 3.13) inspired by the classification proposed by *Amanat et al., 2010* [Amanat et al., 2010] for LTW on PEEK.

Within the PEKK assemblies, two main failure types are observed: the Cohesive (CI) and the Substrate Near Joint (SNJ). When the assembly fails in CI type, it means that the assembly separates by shear at the interface within the weld joint. In-plan shear failure mode is achieved, which is the failure mode that gives the real weld strength. The SNJ failure indicates that the bulk sample breaks near the weld joint heat-affected zone (HAZ). This suggests that the assembly failed by tensile mode within the bulk.

The force at failure (F_f) is thus recorded for each assembly, regardless the failure type. For the assemblies that failed in CI type, the F_f corresponded to the force at which the assembly separated at the interface within the joint. For SNJ failure type, the F_f is the one obtained when one of the bulk samples breaks near the weld joint. To quantify the mechanical results, the force at failure (F_f) is considered to calculate the weld strength. Two types of stresses are calculated, the failure stress (σ_f) and the lap shear stress (LSS). For both, the (F_f) is divided by the contact area (A_c). The A_c is different for each stress, depending on the zone where the failure occurred.

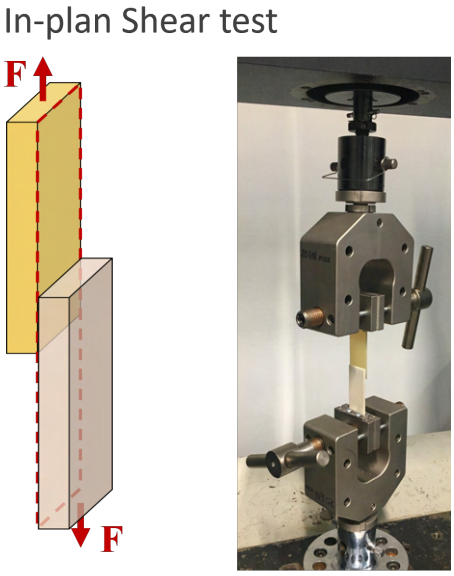

Figure 3.20: Single lap shear test on PEKK-A/SC welded assemblies.

Failure type	Appearance	Inference	Description
Interfacial		Bond strength << substrate strength	Assembly fails at the interface because no real material cohesion was created at the irradiated interface. Most undesired result.
Cohesive		Bond strength ~ substrate strength	Assembly fails at the interface within the weld bond created.
Substrate near joint (SNJ)		Bond strength > substrate strength	Failure within the substrate but near the interfacial region and weld bond intact (or mostly).
Bulk substrate		Bond strength >> substrate strength	Bulk substrate results in tensile yield and brakes far from the weld bond. Most desired result.

Table 3.13: Failure types definitions for LTW assemblies tested by SLS.

3.4.2 Weld joint observation by microscopy

Numerical optical microscope VHX-6000S from Keyence is used to visualize the weld joint. The assemblies are observed to characterize the weld joint cross-section along the weld path. These weld cross-sections are cut, embedded in an epoxy resin, and polished before microscopy observations. The post-failed CI-type assemblies are characterized at the separation zone (the irradiated interface) to study their failure zones.

3.5 PEKK-A/SC assembly weld joint properties

3.5.1 Morphological properties

The welds obtained from PEKK-A/SC assemblies are shown in Figure 3.21. The weld joint cross-section along the weld path is visible for each assembly combination before and after welding. The weld joint heat-affected zone (HAZ) is recognizable as the oval shape with the color gradient. Prior welding, the interface line is easily noticeable between the overlapped samples. Then, for each power used for welding, a HAZ is developed at the location of the previous interface line. All the cuts exhibit a similar HAZ: an oval shape with a color gradient from yellow to white, transitioning from bottom to top. As it can be noticed, a portion of the PEKK-SC bottom sample has now turned yellow. On the other hand, the PEKK-A top sample has acquired a white coloration at the top of the developed HAZ. These color changes on the samples suggest a modification on their crystalline state at the weld joint HAZ. As a result, an anisotropic weld joint in terms of crystallinity is generated after welding.

Given that PEKK is a semi-crystalline thermoplastic, its initial polymer microstructure can be significantly altered during laser welding, as proven by *Ghorbel et al., 2009* in the case of semi-crystalline polypropylene (PP) polymers [Ghorbel et al., 2009]. The different thermal gradients that the material experiences at the welding process can modify the crystalline microstructure of the injected samples. In case of PEKK 7002, change in crystallinity is easy to be identified by the coloration of the material. By examining the HAZ obtained on the different assemblies, two principal zones can be identified in Figure 3.22, which can be related to the thermal history of the welding process.

Zone 1 is the yellow portion of the HAZ that has replaced the interface line that existed prior to welding. The yellow coloration of this zone indicates low crystallinity or an amorphous state, as observed in the PEKK-A sample with a comparable color. It can be inferred that, during the irradiation process, both parts melted within this zone, allowing the macromolecules to diffuse and entangle to develop the weld joint. Then, when cooling, the material did not crystallize due to the fast cooling rate compared to the crystallization kinetics of PEKK from the melt. As measured by *Villar et al., 2018* when LTW of PEKK 60/40, the samples cool down at a rate of 300 °C·min^{-1} after irradiation [Villar et al., 2018]. Indeed, for PEKK 70/30 to crystallize from the melt, a slow cooling ramp, lower than 40 °C·min^{-1}, is necessary [Quiroga Cortés et al., 2016]. As proven by *Quiroga Cortés et al.,*

2016, when PEKK 70/30 crystallizes from the melt at high cooling rates ($40°C \cdot min^{-1}$) it exhibits cold crystallization endotherms [Quiroga Cortés et al., 2016]. It means that a partial crystallization occurs on cooling. The crystallinity of PEKK 70/30 decreases from 28 % to 15 % with increasing the cooling rate from 10 to $40°C \cdot min^{-1}$. Therefore, the crystallinity change after LTW process has already been proven by *Liu et al.* on PEEK/CFR-PEEK thin films. They correlated the crystallinity of the weld joint with the laser power [Liu et al., 2022]. Their results reveal a reduction of the crystallinity with the rapid cooling rate of the welding process. Zone 1 can also be considered as the "molten layer" (ML) of the HAZ.

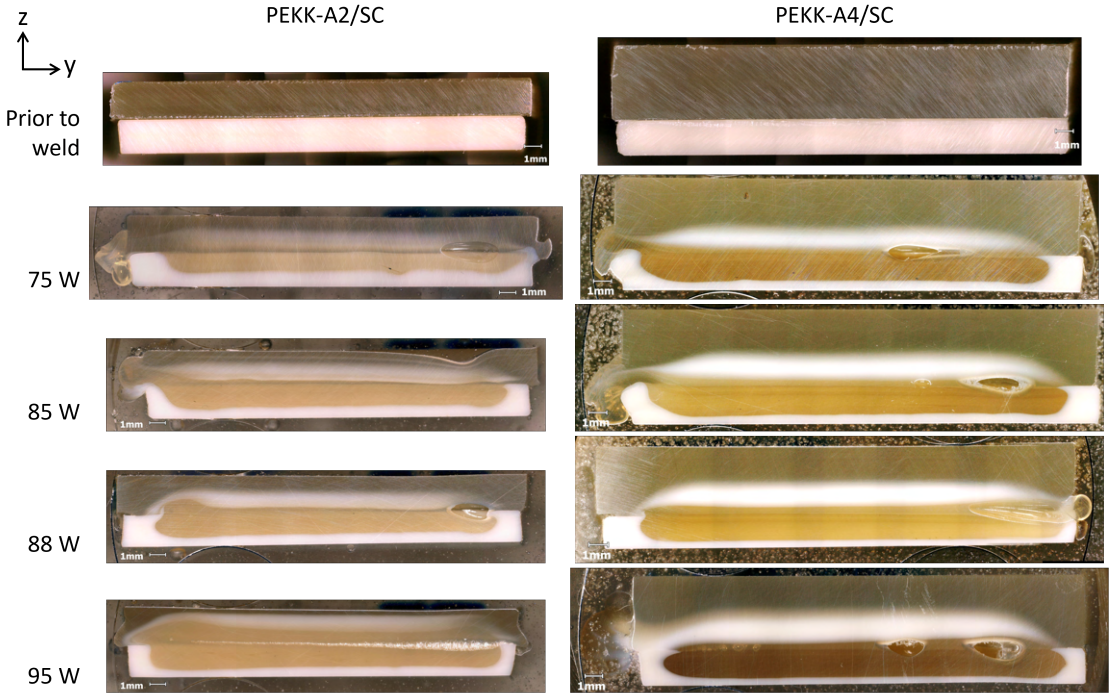

Figure 3.21: Representative micrographs of the weld joints cross-sections along the weld path of the PEKK-A/SC assemblies.

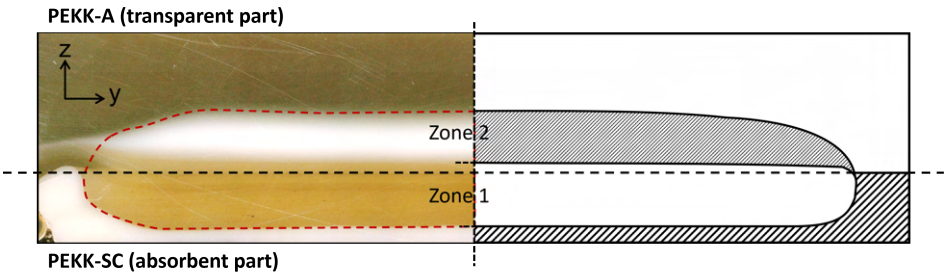

Figure 3.22: Representative micrograph of the weld joint cross-section with a schematic representation of the different zones inside the weld joint HAZ. The interface location prior to weld is identified by the horizontal dotted line.

Zone 2 of the weld joint HAZ is represented by the white portion developed over zone 1, inside the bulk PEKK-A sample. This white coloration indicates material cold crystallization. In this zone, a high temperature was achieved by thermal conduction of the interface irradiation. It can be inferred that the maximum temperature reached was between Tg and Tm, because the amorphous form of PEKK achieved to crystallize from the amorphous state. This is possible due to the fact that the molten layer (ML) generated is thick and the conductivity of the material is low, so the energy transferred by conduction from the ML to the bulk PEKK-A sample is stored for a long time, having enough time to crystallize. This zone 2 can also be called the "semi-crystalline layer" (scL) of the HAZ.

As illustrated in Figure 3.22, it is obvious that the molten layer (ML) extends over both samples, although the depth of melting varies between them. The PEKK-A samples melted within a minimal depth, remaining close to the interface. The average depth of this ML on PEKK-A samples for both types of assemblies is 0.4 ± 0.1 mm. On the other hand, the ML of PEKK-SC sample has a significant depth inside its thickness, nearly reaching the bottom of the substrate. This suggests that the laser irradiation penetrated the sample, as noted by *Jones et al.* [Jones, 2002], and was absorbed within the volume, rather than solely at the interface. The maximum depth that this ML achieves in the PEKK-SC sample is 1.6 mm for the A4/SC-P4 assembly. Welding substrates thinner than 1.6 mm would be tough with the parameters of this study. This asymetric distribution of the ML was also observed on *Abed et al.*'s work when welding natural PP to PP pigmented with carbon black [Abed et al., 2001]. An asymmetric shape of the weld seam into the two materials was observed when the lower part is filled with a low pigment content (less than 1 %), resulting in low absorbing properties. They indicated that this allowed most of the energy to go deep inside the absorbing material, leading to a limited heat transfer to the upper part, obtaining moderated temperatures at the interface and lower dimensions of the meltpool. Even if the PEKK-SC sample melted with a significant depth in its thickness, it did not melt up to the bottom of the sample. The bottom of the PEKK-SC sample was in contact with the welding platform made of aluminum, which allows rapid heat dissipation.

Figure 3.23 shows the HAZ layers (ML and scL) depth dimensions for each assembly combination. (ML) indicate the molten layer, and (scL) the semi-crystalline layer. The values below the interface line indicate the ML depth in the PEKK-SC sample. And, the values above the interface line indicate the ML and scL depths on the PEKK-A samples. Focusing on the ML depths, a notorious increment of the molten depth is seen in both bulk samples when increasing the laser power. Inside the PEKK-SC sample the ML covers 53 % to 70 % of the original sample thickness of 2 mm when welded with PEKK-A2. When PEKK-SC is welded with PEKK-A4, this percentage increases, going from 74 % to 81 % of its thickness. On the other side, the melted layer in the PEKK-A sample is thin with almost the same dimensions for both types of assemblies. In the PEKK-A2 assemblies, the ML covers around 15 % of the original sample thickness when welding with P1, P2 and P3, and 40 % when using P4. In the PEKK-A4 samples, the thickness of the ML goes from 7 % to 9 % of the original thickness of 4 mm. As already proven by *Acherjee et al.* who studied LTW of polycarbonate (PC), the molten depths in transparent and absorbing parts increase when increasing laser power and welding time [Acherjee et al., 2011, Acherjee et al., 2012]. The increase in laser

power results in greater heat input, leading to more molten material which generates larger weld dimensions. This was further demonstrated by *Asséko et al., 2015* when welding and simulating the LTW of glass fiber PC over carbon black PC [Asséko et al., 2015]. They found that the weld pool depth increases with exposure time in both parts, but is deeper at the absorbent part, generating an asymmetric distribution of the melted zone.

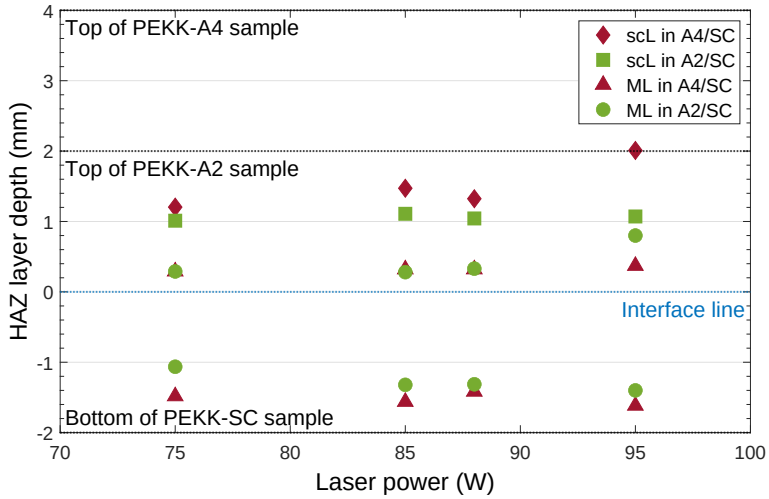

Figure 3.23: Weld joint HAZ layers depths inside the thickness of each bulk sample for each PEKK-A/SC assembly combination.

The scL depth within the HAZ also exhibits a notable correlation with both laser power and assembly type, as seen in Figure 3.23. In the case of PEKK-A2/SC assemblies, the scL depth increases from 1.01 to 1.07 mm, covering more than 50 % of the thickness of the PEKK-A2 bulk sample. For PEKK-A4/SC assemblies, the scL depths increase from 1.2 to 2.01 mm, covering between 30 % and 50 % of the PEKK-A4 bulk sample thickness. Notably, only welding with the higher power value (P4) achieves a scL depth that covers 50 % of the PEKK-A4 sample thickness, while using lower laser powers yields scL depths that cover less than 37 % of the PEKK-A4 thickness. To date, no other study has documented the apparition or development of a scL within the HAZ over the ML, rendering it challenging to draw comparison with existing data.

The HAZ length is measured for each assembly combination and plotted with the power used for welding in Figure 3.24. The HAZ length is the maximum length measured along the Y axis inside the ML of the PEKK-SC sample. A notorious increment on the HAZ length with the power is noticed. This increment is almost linear for three of the four intensities (75, 85 and 95 W). The HAZ length obtained at 88 W does not follow the regular trend, that can be explained by the uncertainty of the power in the welding machine. Indeed, the values of power are defined with ± 3 %. Thus, the data obtained for 85 and 88 W are expected to be close to each other. Nevertheless, the increment of the HAZ length with laser power can be explained by the fact that increasing the laser power maximizes the heat input which leads to a greater volume of melted material at the interface, resulting in a higher welded zone. As it can be seen, the HAZ length of PEKK-A2/SC improves considerably with laser intensity,

with a gap of 1.6 mm between the higher and lowest power. The HAZ length of PEKK-A4/SC assemblies also increases, but this increment is meanly notorious, with only 0.3 mm of difference from the lowest to the highest power, the HAZ lenght of these assemblies is quite the same. Moreover, this HAZ length is higher than the welding path used for welding (20 mm) in all the configurations. That indicates that the irradiation procedure used, combining static and dynamic irradiation, had a positive impact on the melting at the interface.

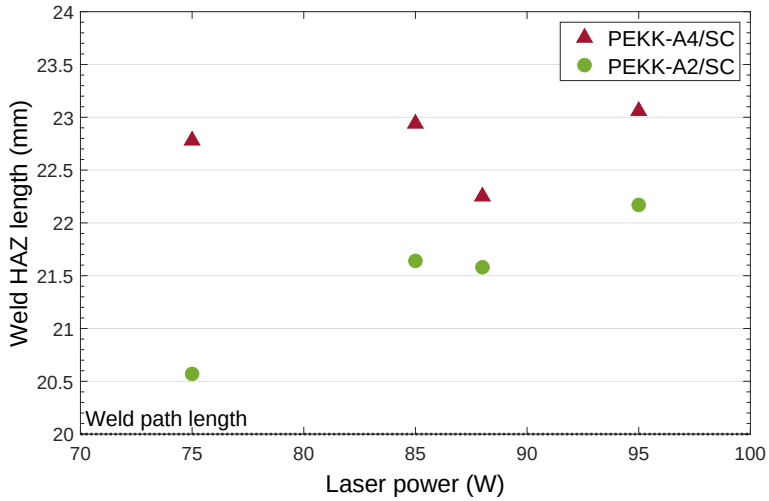

Figure 3.24: Weld joint HAZ length plotted against laser power used for welding.

The HAZ length also increase with the increase of the transparent substrate thickness for each laser power. This can be caused by the scattering of the laser irradiation through the samples. Thus, PEKK-A4 seems to scatter more the light than PEKK-A2, which increases the distribution of the energy over a longer area.

From Figure 3.21 it can be seen that most of the cross-sections show a void on the left side of their HAZ, near its end. This void was not caused by water evaporation, because samples were dried before welding, but mostly from flowing matter that escaped from the other side, as it can be clearly seen on the pictures. On the right side of the cross-section, outside the border, an extra of the material can be seen. This implies that the material that melted at the irradiation-welding process flowed from the interface line opposite to the welding trajectory.

Annealed assemblies weld joint morphology

As it can be recalled, when welding PEKK-A/SC the weld joint obtained is heterogeneous in terms of crystallinity, as it can be seen on Figure 3.25b. With the annealing process, crystallization is enhanced and a fully crystallized weld joint is obtained, as in Figure 3.25c. The cross-section of the weld joint shown on Figure 3.25c has a more homogeneous color on its HAZ, compared to the HAZ obtained only after welding (Figure 3.25b). Indeed, the full cross-section of the crystallized assembly shows only one coloration, which is beige. Having this color on the PEKK 70/30 samples indicates that the material has a high crystallinity.

Thus, it can be inferred that the weld joint obtained after annealing is homogeneous in terms of crystallinity.

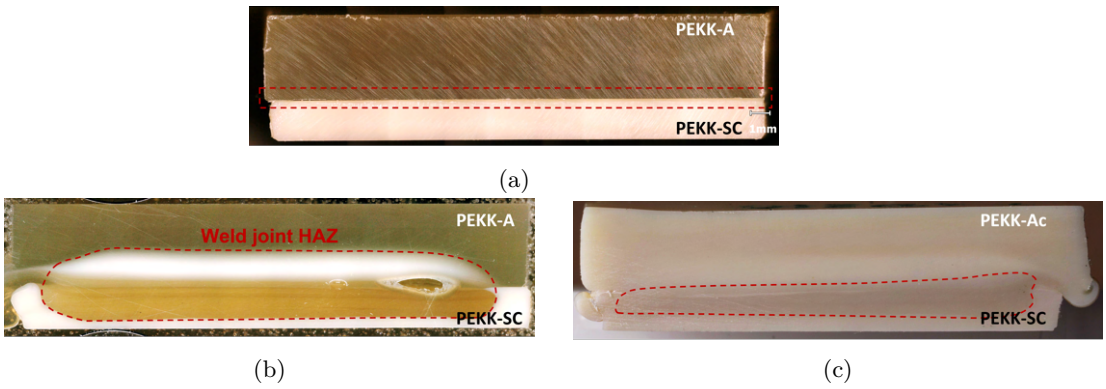

Figure 3.25: PEKK-A/SC weld joint cross section a) before welding, b) after welding and c) after annealing process.

Although, as seen in Figure 3.26, a darker region of beige coloration can be noticed on the crystallized weld cross-section for all assembly configurations. This darker region could be the amorphous zone (Zone 1) of the initial weld joint that crystallized during annealing. The crystallization generated gave a darker color because it was obtained from cold crystallization. It can be inferred that the crystalline structure obtained here is different from the PEKK-SC bulk sample. As already proven by different authors, PEKK exhibits two crystal polymorphisms (forms I and II) [Gardner et al., 1992, Gardner et al., 1994, Ho et al., 1994] that can develop depending on the crystallization conditions [Gardner et al., 1994, Ho et al., 1994, Ho et al., 1995, Cheng et al., 1996]. *Gardner et al.* [Gardner et al., 1994] suggested that under conditions of fast nucleation, such as cold crystallization with a significant degree of supercooling, form II is favored. They also identified that when PEKK 70/30 crystallizes from the cold, both forms I and II structures appear, contrary to crystallization from the melt which favor form I. This can indicate that the weld joints crystallized by annealing can have a mixture of forms I and II, thus the colors observed are darker than the PEKK-SC sample.

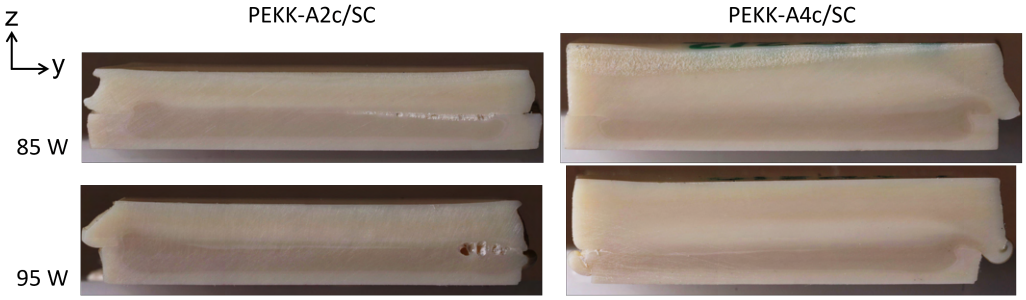

Figure 3.26: Weld joints cross-section along the weld path of the crystallized assemblies (PEKK-Ac/SC).

3.5.2 Mechanical properties

The results of the SLS mechanical tests are analyzed in correlation with the welding parameters for the PEKK assemblies. Initially, the focus is placed on the non-crystallized (NC) assemblies, namely PEKK-A/SC. Figure 3.27 shows the load at failure (F_f) for all assembly combinations within the non-crystallized group. Notably, it is observed that the failure force increases when doubling the PEKK-A thickness for each power tested. Additionally, the breaking load increases with power for the first three power values, nearly doubling from 75 W to 88 W. For the PEKK-A2/SC assemblies, the load at failure escalates from 0.8 kN to 1.4 kN, representing an increment of 75 %. While for the PEKK-A4/SC assemblies, the force increases from 1 kN to 1.9 kN, marking a 90 % rise. However, at the highest power value, there is a subsequent decrement in the failure force, dropping by 21 % for the A2/SC, and 11 % for the A4/SC assemblies. The maximum failure force is thus recorded at 88 W of laser power, reaching 1.4 kN for A2/SC and 1.9 kN for A4/SC assemblies. These results are similar to those obtained by *Goyal et al.* when welding transparent polycarbonate samples of 2 mm thick with a fiber laser of 1080 nm wavelength [Goyal and Kant, 2023]. In their work, the maximum breaking load of 1.18 kN was achieved at 100 W and a welding speed of 400 mm·min^{-1}.

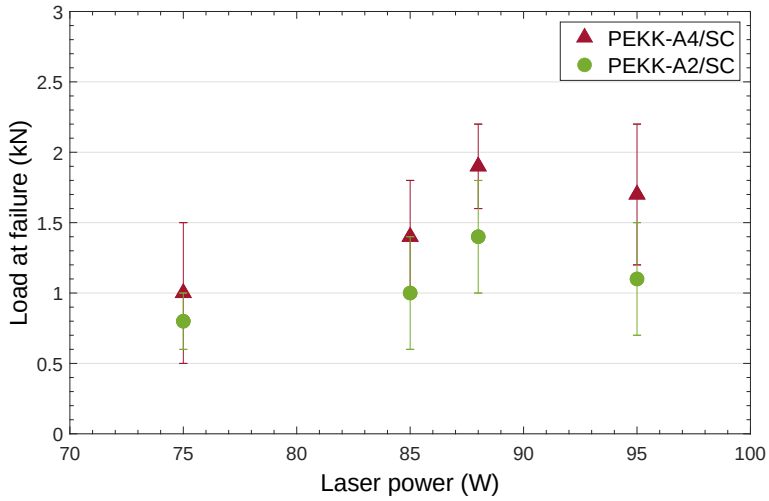

Figure 3.27: Mechanical tests results showing the load at failure (F_f) for all PEKK-A/SC assemblies combinations. Error bars indicate standard deviation[2].

As mentioned on section 3.4.1, two failure types were observed within the PEKK assemblies: the CI and SNJ (refer to Table 3.13). A high percentage of the assemblies tested failed in substrate near joint (SNJ) type (see Table 3.13): 82 % for the PEKK-A2/SC, and 44 % for the PEKK-A4/SC. These assemblies failed within the bulk, really near the weld joint, they are thus considered as if the weld joint is stronger than the bulk material, as hypothesized by *Amanat et al.* [Amanat et al., 2010] when welding PEEK films. However, the failure stress

[2]Number of welded assemblies tested per parameter: for PEKK-A2/SC P1 = 6, P2 = 8, P3 = 10, and P4 = 9. For PEKK-A4/SC P1 = 7, P2 = 8, P3 = 8, and P4 = 9.

σ_f can be calculated for the SNJ failed assemblies by dividing the F_f to the failure zone area A_f. The failed area is the section of the bulk sample that broke on the test. Figure 3.28 shows the failure stress σ_f calculated for the assemblies that failed in SNJ type. The failure stress follows a similar tendency that the F_f, but, opposite to it, the σ_f is higher for the PEKK-A2/SC assemblies. This is because the PEKK-A2/SC assemblies have a smaller failure zone that the PEKK-A4/SC. Even if the PEKK-A2/SC assemblies failed within the amorphous or semi-crystalline bulk sample, their thickness is 2 mm. On the other side, the PEKK-A4/SC assemblies failed mostly in the amorphous sample, with a thickness of 4 mm. That means that the contact area that failed was higher, and even twice, of the area on the PEKK-A2/SC assemblies. And, to obtain a higher failure stress, the failure load should also be at least twice. But this was not the case, the failure force of the PEKK-A4/SC assemblies was just 47 % higher than the F_f of the PEKK-A2/SC assemblies.

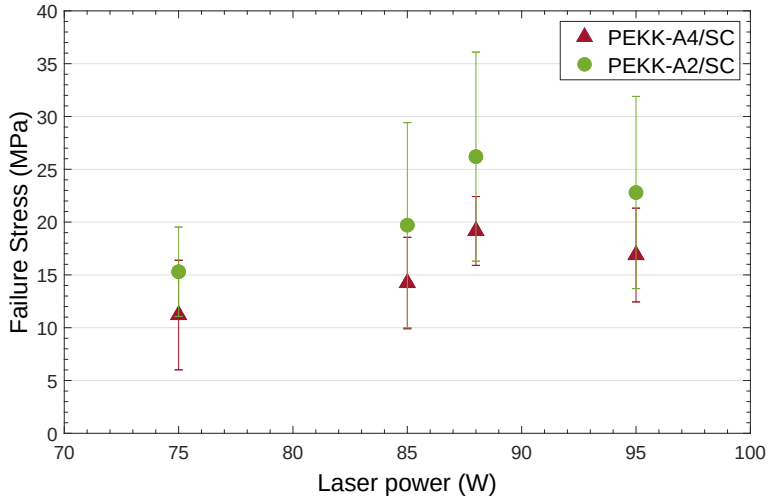

Figure 3.28: Mechanical test results showing the failure stress for the SNJ failed assemblies for each PEKK-A/SC assembly combinations. Error bars indicate standard deviation[3].

CI type failure is achieved within a few assemblies: 18 % for the PEKK-A2/SC, and 64 % for the PEKK-A4/SC. When welding PEEK films with LTW, *Amanat et al.* obtained some CI failure in the crystalline group (only 38 %) [Amanat et al., 2010]. The CI failed weld joints are characterized by optical microscopy, as shown in Figure 3.29. The HAZ of the weld joint is seen at the overlapped zone, the interface plane. This HAZ appears with a yellow coloration, as for Zone 1 of the weld joint defined in section 3.5.1. This indicates melting and change in the crystalline state of the PEKK-SC sample, becoming amorphous after welding. For each assembly combination, the weld joints show signs of sheared material. This indicates that the samples were melted and fused together at the irradiated zone and that the bonds were sheared during test, confirming a continuous material at the weld joint in the assembly by optical microscopy and used to calculate the real lap-shear-strength (LSS) of the CI failed assemblies.

[3]Number of welded assemblies per parameter: for PEKK-A2/SC P1 = 5, P2 = 7, P3 = 9, and P4 = 7. For PEKK-A4/SC P1 = 5, P2 = 7, P3 = 7, and P4 = 8.

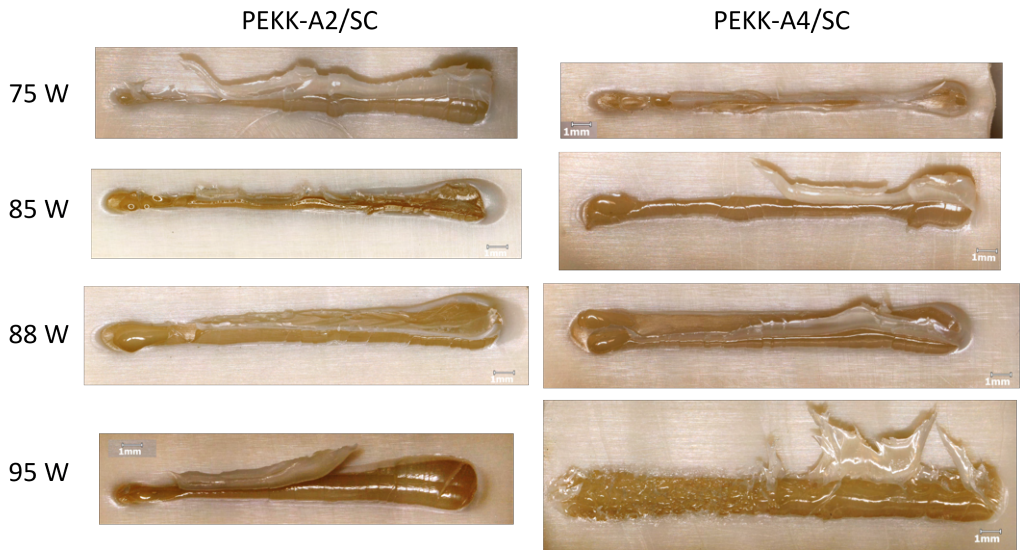

Figure 3.29: Representative micrographs of the failed weld joint of assemblies failed with CI type for each assembly combination. Visualizations are made at the overlapped zone of the PEKK-SC sample.

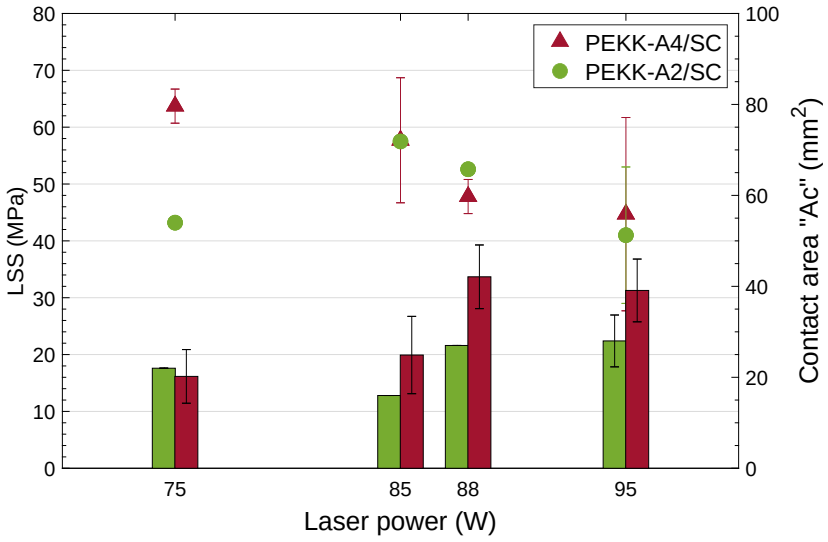

Figure 3.30: Mechanical test results showing the lap shear stress (LSS) with their respective contact area (Ac) for the CI failed assemblies for each PEKK-A/SC assembly combinations. Error bars indicate standard deviation[4].

The mean LSS of the CI failed assemblies is plotted with laser power in Figure 3.30 with their respective A_c. The strength obtained for both types of assemblies (A2/SC and A4/SC) at one laser power is relatively the same, excepted for 75 W. However, contrary to the force

[4]Number of welded assemblies per parameter: for PEKK-A2/SC P1 = 1, P2 = 1, P3 = 1, and P4 = 2. For PEKK-A4/SC P1 = 2, P2 = 6, P3 = 4, and P4 = 3.

at failure, LSS considerably decreases from 85 W. The maximum strength is reached at 85 W, with a value of 57 MPa, for both types of assemblies, whereas the minimum strength is obtained at 95 W, with 43±2 MPa. LSS decreases by 25 % between the maximum and minimum values for both types of assemblies. The explanation is that a high power intensity used for irradiation creates a bigger weld joint, obtaining a higher contact area. And, whereas the force at failure increases with power, the LSS will decrease because of the increment of contact area, this is noticeable in Figure 3.30. Overall, the strength obtained in the assemblies is higher than those achieved by *Potente et al., 2001* when welding PEEK T-joint specimens with similar thicknesses for the transparent substrate [Potente et al., 2001]. They achieved a maximum strength of 40 MPa.

Annealed assemblies mechanical properties

Two powers are studied for the annealing process: 85 and 95 W, which are compared with the NC assemblies. Compared to the NC-PEKK assemblies, the annealed cold-crystallized (CC) ones, labeled as PEKK-Ac/SC, they all failed in SNJ type. In this case, the PEKK-A2c/SC failed within the PEKK-SC bulk sample, and the PEKK-A4c/SC failed at the initially (but now crystallized) PEKK-A4 amorphous bulk sample. Cohesive failure is not achieved when the crystallization is enhanced after welding. Nevertheless, the mechanical results can be studied and compared to the NC assemblies for the two laser powers mentioned and the two sample's thicknesses.

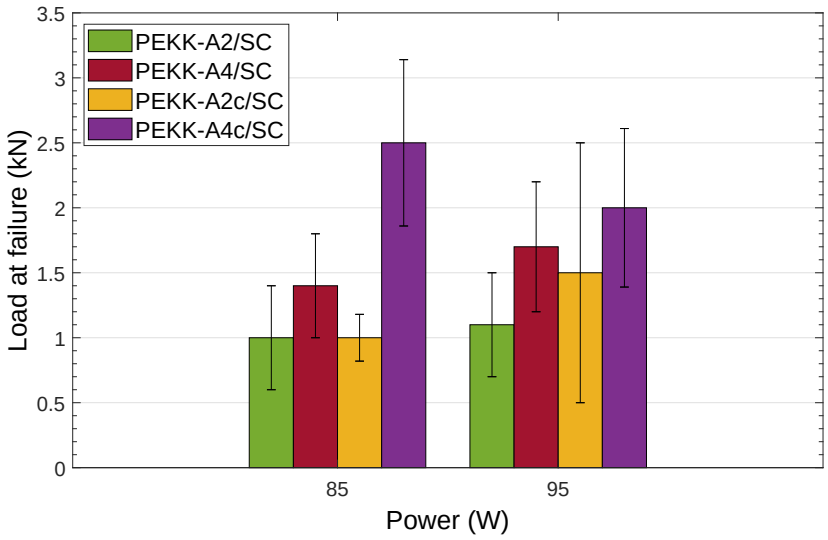

Figure 3.31: Mechanical results of the PEKK annealed assemblies (PEKK-Ac/SC) showing the F_f compared with the corresponding PEKK non-annealed assemblies (PEKK-A/SC) F_f. Error bars indicate standard deviation [5].

Figure 3.31 compares the failure force with power for the NC and CC assemblies. The CC assemblies have a similar behavior as the NC ones: when the thickness of the PEKK-A

[5]Number of welded assemblies tested per parameter: for PEKK-A2/SC P2 = 8 and P4 = 9. For PEKK-A4/SC P2 = 8 and P4 = 9. For PEKK-A2c/SC and PEKK-A4c/SC P2 and P4 = 3.

increases, the resistance to the break load increases. Furthermore, the load at failure increases with crystallization whatever the power. For A2/SC assemblies, a 35 % increment is observed between the non-crystallized and crystallized assemblies at 95 W, while at 85 W, the load at failure remains relatively the same. For the A4/SC assemblies, the breaking load increases by 19 % when welding with 95 W, and 81 % when using 85W. This suggests a positive effect of annealing: the crystallized weld joints exhibit a higher resistance compared to the non-crystallized ones.

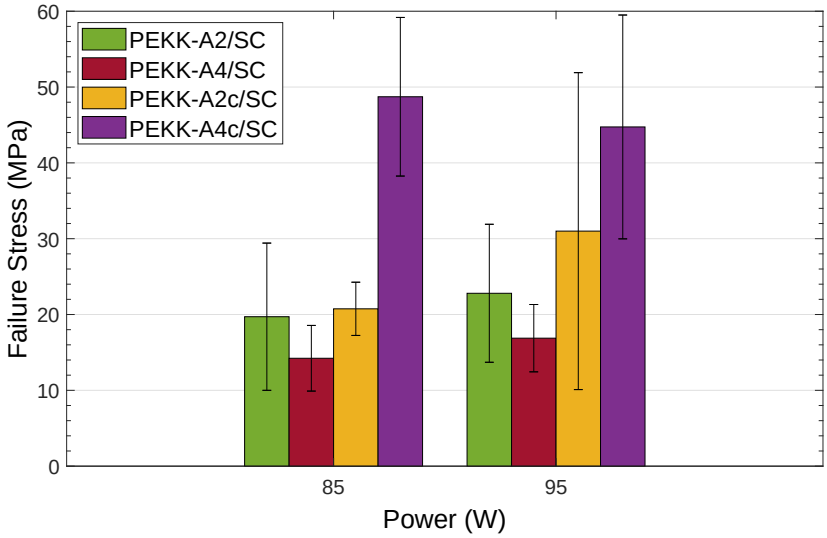

Figure 3.32: Mechanical test results showing the failure stress of the PEKK annealed assemblies (PEKK-Ac/SC) compared with the corresponding PEKK non-annealed assemblies (PEKK-A/SC). Error bars indicate standard deviation[6].

As previously, the failure stress can be calculated for the CC assemblies using the F_f and the A_f. Figure 3.32 illustrates the failure stresses of both crystallized and non-crystallized assemblies. Similar to the trend observed for load at failure, the failure stress increases with the sample's thickness. Compared to the NC assemblies, the failure stress increases when enhancing crystallinity by annealing. However, contrary to the non-crystallized assemblies, it can be noticed that the failure stress is higher for the PEKK-A4c/SC than for the PEKK-A2c/SC. This change in the tensile resistance is due to the fact that, for CC assemblies, the load at break for the PEKK-A4c/SC is more than 70 % higher than for the PEKK-A2c/SC. Even though the PEKK-A4c/SC assemblies failed at the PEKK-A4 sample, the break load was high enough to achieve a high failure stress with a large failure area $A_f = 48 \pm 3\ mm^2$.

[6]Number of welded assemblies tested per parameter: for PEKK-A2/SC P2 = 7 and P4 = 7. For PEKK-A4/SC P2 = 7 and P4 = 8. For PEKK-A2c/SC and PEKK-A4c/SC P2 and P4 = 3.

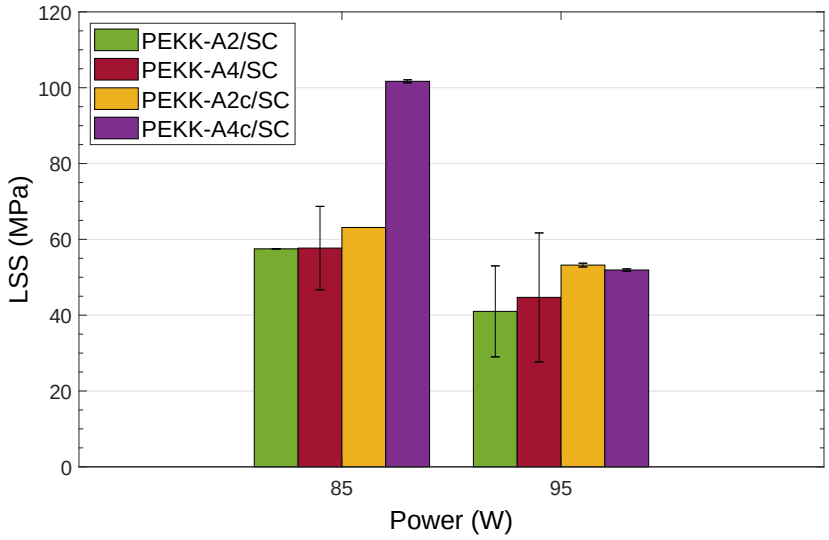

Figure 3.33: Mechanical test results showing the lap shear stress (LSS) of the PEKK annealed assemblies (PEKK-Ac/SC) compared with the corresponding PEKK non-annealed assemblies (PEKK-A/SC). Error bars indicate standard deviation[7].

To obtain the weld strength of the CC assemblies, the force at failure is divided by the contact area of the weld. Because the welds are made in the same conditions as the initial non-crystallized (NC) ones, we assume the same contact area for all types of assembly. The average values of the PEKK-A/SC weld contact areas obtained for each laser assembly configuration were used to calculate the LSS for the crystallized assemblies. These LSS values are displayed in Figure 3.33 and compared to the ones obtained for the PEKK-A/SC NC assemblies. The weld strength decreases with power for each assembly combination. Nevertheless, higher strength values are obtained for the crystallized assemblies. The strength of the assemblies increases by more than 10 % when fully crystallized. The higher increment is achieved for the PEKK-A4c/SC at 85 W, increasing by 76 % when crystallizing the weld joint, obtaining the maximum strength value at this power, reaching 102 MPa. The minimum weld strength obtained is 52 MPa, being also higher than the minimum value obtained for the NC ones (41 MPa). To date, only one work in the literature reports the effect of annealing on LTW assemblies on similar material (PEEK) by *Liu et al.* in 2022 [Liu et al., 2022]. In this work, the crystallized assemblies showed lower LSS values than the non-crystallized ones. More importantly, increasing the crystallinity of the weld joint had a negative impact on its strength. They obtained a maximum decrement of 7 % on the weld strength between the non-crystallized and the maximum crystallized weld joint. Their findings are opposite to the results obtained in the present work.

[7]Number of welded assemblies tested per parameter: for PEKK-A2/SC P2 = 1 and P4 = 2. For PEKK-A4/SC P2 = 6 and P4 = 3. For PEKK-A2c/SC and PEKK-A4c/SC P2 and P4 = 3.

3.6 Synthesis

This study provides a comprehensive analysis of LTW of PEKK assemblies, in an amorphous over semi-crystalline configuration (PEKK-A/SC). Through experimental characterization, the relationships between material crystallinity, process parameters and weld joint properties are assessed. The process parameters influence the joint morphology and mechanical resistance of welds. The effect of crystallinity on the weld joint strength is clarified by conducting post-weld annealing in some welds. The following conclusions can be outlined from the results:

- The weld joint shows an heterogeneous distribution of the crystallinity within its HAZ. Two different zones are identified in the weld joint HAZ that are correlated with the thermal history of the welding process: an amorphous zone 1, also named "molten layer"(ML); and the cold-crystallized zone 2, named "semi-crystalline layer" (scL).
- The depth and morphology of the molten and semi-crystalline layers show significant variations depending on laser power and semi-transparent part thickness.
- Mechanical testing revealed two failure types: cohesive (CI) and substrate near joint (SNJ), which reveal the weld properties, as well as the failure mechanisms.
- The mechanical strength of the PEKK-A/SC weld joints decreases with laser power. High values are reached between 41 and 64 MPa.
- Crystallization of the welds is achieved by annealing the assemblies at 190 °C, without joint separation. The annealing process generates an increment of the crystallinity in the weld joint HAZ with different crystalline structure, due to cold crystallization of the ML.
- Enhancing the crystallinity of welds by annealing improves their mechanical strength, demonstrating the potential of post-weld treatments to optimize weld performance. Higher values of LSS are thus obtained, between 52 and 102 MPa.
- Overall, controlling the crystallization properties and kinetics of PEKK is crucial to achieve optimal welding and to predict the weld joint properties.

Chapter 4

Modeling the laser transmission welding process for PEKK parts

Contents

4.1 Introduction 128
4.2 Models and equations for the LTW of PEKK 129
4.2.1 Thermo-optical model 129
4.2.2 Laser energy absorption in the semi-transparent part 131
4.2.3 Crystallization model for PEKK 132
4.2.4 Model assumptions 133
4.3 Finite difference method and discretizations for the modeling 134
4.3.1 Geometry definition and discretization 134
4.3.2 Discretization of the time domain 135
4.3.3 Heat equation discretization by FDM 136
4.3.4 Crystallization model discretization by FDM 137
4.4 Modeling the LTW of an overlapped configuration 138
4.4.1 Study on the laser irradiation, temperature field and melted zone 141
4.4.2 Study on the crystallinity evolution of the weld joint 144
4.4.3 Predicting the weld joint morphology of PEKK-A2/SC assemblies 147
4.5 Synthesis 153

4.1 Introduction

In this study, during welding PEKK-A/SC thermoplastic parts by LTW, modifications on the crystalline structure of the samples were observed. The laser irradiation allowed material to melt at the interface, which enabled the samples to weld. However, the weld joint developed resulted in a more complex morphology because of the different responses of each sample to the laser irradiation. The PEKK-SC absorbent sample melted and remained amorphous after welding and cooling. In the other hand, PEKK-A semi-transparent sample crystallized from the cold, near the interface, during irradiation. These modifications of the crystalline structure of the material generate questions about the interactions between the laser parameters and the response of the PEKK parts during LTW.

Experimental methods are not well suited to answer these questions. Monitoring the temperature at the weld interface and measuring the weld joint crystallinity developed as a result of the thermal gradients are hard to characterize. To overcome these challenges, modeling the LTW process has emerged as a functional tool.

Computational models to simulate the LTW process of thermoplastics have been used and studied since the beginning of the 2000s [Becker and Potente, 2002]. Numerical models and simulations have been used to provide insights that are difficult to obtain through experimental methods alone. In addition, models can be used to predict the influence of various parameters on weld properties and can help optimize the process for different materials and geometries [Hu et al., 2023].

Numerical simulations are a great tool and area for investigating the LTW process and parameters. When trying to determine the process parameters for welding, numerical simulations can provide a more systematic and efficient approach compared to conventional trial-and-error methods. In addition, numerical simulations can help to understand the welding mechanisms by analyzing the impact of material properties and process parameters on the temperature distribution, stress concentration, or weld joint dimensions. That can lead to optimization of the welding process and improvement of weld joint quality. The use of numerical simulation approach provides a solid theoretical basis for anticipating ideal conditions and optimizing LTW operations.

In the case of the present study, computational modeling is employed to gain insight into the intricate mechanisms of crystallization observed in the laser transmission welding experiments of PEKK-A/SC parts. The LTW process is simulated using MatLab software by solving the different models with the finite difference method. The modeling process and steps are described in the present chapter for the PEKK-A/SC assemblies. First, an overview of the equations and models that govern the welding process is presented. Then, a description of the finite difference method principle used to solve the equations is given. Then, the geometry developed for the simulations is presented, as well as the parameters used for welding. The 3D thermo-optical model results are shown in conjunction with the different choice made to improve the model. The same is shown when the crystallization model is incorporated. In the end, the weld joint morphology predicted by the simulations made for PEKK-A/SC

assemblies is shown and discussed.

4.2 Models and equations for the LTW of PEKK

As described in Chapter 1, Section 2, different physical phenomena are involved during LTW of thermoplastics. These phenomena can be described by physical laws that allow to simulate the welding process in conjunction with the material properties and welding parameters. The models used in this study to describe the phenomena involved during LTW are the "thermo-optical" and "crystallization" models. The models and their equations are going to be recalled and narrowed for this study, for the PEKK material, in the following sections.

4.2.1 Thermo-optical model

To simulate the laser transmission welding process of the overlapped samples, the heat transfer model is used. For LTW, the heat transfer model will allow to obtain the temperature evolution of the static materials on the basis of the laser energy absorption with the subsequent heat conduction involved within the samples. Therefore, the heat conduction Equation 1.11 (ref. Chapter 1, Section 2.3) can be simplified to Equation 4.1 [Cosson et al., 2009] when the materials are not in motion:

$$\rho C_p \frac{dT}{dt} = k \cdot \nabla^2 T + Q(r) \tag{4.1}$$

hence, $Q(r)$ corresponds to the external heat generated by the laser irradiation, and ρ, C_p and k are respectively the density, heat capacity and thermal conductivity of PEKK. Those thermo-physical properties of the material are of big importance for the thermal modeling of the welding process. In semi-crystalline thermoplastics, the thermo-physical properties tend to evolve with temperature, as seen for PA66 [Aden et al., 2013]. In the case of PA66, the density and heat conductivity decrease with temperature until stabilization near the melting point. However, this decrement is low compared to the temperature change, being of 160 $\mathrm{kg \cdot m^{-3}}$ for the density and 0.045 $\mathrm{W \cdot m^{-1} \cdot K^{-1}}$ for the thermal conductivity. On the other hand, the heat capacity of the material has a mayor modification with temperature. The heat capacity of PA66 increases with temperature from 1500 to 2600 $\mathrm{J \cdot kg^{-1} \cdot K^{-1}}$ after the melting point. In addition, this heat capacity shows a high peak at the melting point, increasing by 6000 $\mathrm{J \cdot kg^{-1} \cdot K^{-1}}$]. Taking into account that PA66 is a semi-crystalline thermoplastic with similar working temperatures than PEKK, it can be consider that the thermal properties of PEKK could have similar behaviors that those of PA66. In that case, the density and thermal conductivity of PEKK can be considered as constant in temperature and time for simulations, using the values characterized for the PEKK plates on Chapter 2. On the other hand, the heat capacity of the material should be considered as dependent on temperature, due to the behavior of observed in the C_p of PA66. However, for this study, the Cp evolution in temperature of PEKK was not characterized. Nevertheless, a similar behavior

than that observed for PA66 can be defined for PEKK. For that, Equation 4.2 is defined and implemented for calculations:

$$C_p = 20000\frac{1}{\sigma_T\sqrt{2\pi}}\left[exp\frac{-(T-Tm)^2}{2{\sigma_T}^2}\right] + C_{p0} \qquad C_p(T > Tm) = C_{p0} \tag{4.2}$$

with $\sigma_T = 6$ and C_{p0} being the C_p of the PEKK-A sample characterized in Chapter 2, and indicated in Table 4.1. C_{p0} was chosen to be the one of PEKK-A sample because after melting all the crystals vanish from the material, acquiring a crystalline state more similar to the PEKK-A sample than to the PEKK-SC one.

The laser welding heat source $Q(r)$ is a crucial component of a precise LTW process modeling. Accurate description of the heat source at the weld interface is essential because it influences the accuracy of temperature estimations and the finite element computations of the welding temperature field [Kumar and Bandyopadhyay, 2021, Hu et al., 2023, Asseko and Cosson, 2023]. For this study, a volumetric heat source is used to describe the volumetric heat generation rate due to laser absorption throughout the thickness of the samples, modeled by Equation 4.3 [Acherjee et al., 2012]. $Q(r)$ is calculated for the whole volume of the assembly sample:

$$Q(r) = Q(x, y, z, t) = \alpha \cdot (1 - R) \cdot I(r, t) \cdot exp(-\alpha.z) \tag{4.3}$$

where α is the absorption coefficient of the material, and z represents the spacial position in the direction of the thickness of the sample. In this study, α evolves with the crystallinity of the samples $\alpha(X_c)$. This evolution will be described by a linear correlation, which will be detailed in the next section.

The laser intensity $I(r, t)$ is the initial intensity of the laser beam, which depends on the type of laser profile. In this study, the laser beam used has a Gaussian profile, as characterized in Chapter 3. And, it travels on the (x,y) plan to irradiate the interface of the assembly. Hence, the intensity $I(r, t)$ Equation 1.9 (ref. Chapter 1, Section 2.2) became Equation 4.4 [Akué Asséko et al., 2015]:

$$I(r, t) = I(x, y, t) = \frac{P}{2\pi.\sigma^2}exp\left[\frac{-[(x - v \cdot t)^2 + y^2]}{2\sigma^2}\right] \tag{4.4}$$

where P [W] is the output laser power at the top surface of the upper part, σ is the third of the laser beam radius, v is the welding speed, t is the time, and x and y are the spatial coordinates.

The thermo-optical model is used to simulate the temperature field during welding and

obtain the melted zone.

4.2.2 Laser energy absorption in the semi-transparent part

In most studies found from the literature, the heat source model is defined differently for the semi-transparent and absorbent parts when simulating LTW [Acherjee et al., 2013, Acherjee, 2019, Asseko and Cosson, 2023]. In the semi-transparent upper part, the heat source is considered null as the hypothesis of full transparency is used. Then, the heat source is just considered at the absorbent part, taking into account its absorption properties (absorption coefficient α). However, in the case of PEKK samples used for the present study, the PEKK-A sample used as upper part is not fully transparent to the laser beam. As seen in Chapter 2, PEKK-A has a transmissivity that varies according to its thickness, being 75% when 2 mm thick, and 62% when 4 mm thick. This upper part is thus considered as semi-transparent, because, even if a high quantity of the laser energy can go through it, a part of the laser energy will be absorbed by the sample. Therefore, it is important to consider the absorption properties of the upper part in combination with that of the bottom part. This can be made with a correlation of the α coefficient with the degree of crystallinity of the material.

To take into account the absorption properties of the upper semi-transparent sample, the alpha coefficients calculated in Chapter 2, Section 2.4 (Table 2.16), are employed and defined for each sample on the modeling. Going further, the absorption coefficient can be determined as function of the degree of crystallinity of the samples. As characterized in Chapter 2, PEKK-A samples have a degree of crystallinity different from zero, and very low compared to PEKK-SC samples. Therefore, for samples that share the same thickness of 2 mm (PEKK-A2 and PEKK-SC) but differ in their degree of crystallinity (X_c of PEKK-A2 = 0.05, X_c of PEKK-SC = 0.24), α can be correlated with the evolution of X_c. A linear interpolation can be used to determine the parameters of the linear function for $\alpha(Xc)$ (Equation 4.5).

$$\alpha(X_c) = aX_c + b \tag{4.5}$$

Therefore, considering the PEKK samples with the same thickness and their absorption coefficients ($\alpha = 74.2\ m^{-1}$ for PEKK-A2, and $\alpha = 477.75\ m^{-1}$ for PEKK-SC), the parameters of Equation 4.5 are $a = 2124$ and $b = -32$. Figure 4.1 shows the plot of α as function of X_c used for the study. As it can be noticed on the plot, the defined equation can return negative values of α. A negative value for the absorption coefficient is not physically possible, the lower value of α can be zero, as for a fully transparent material. In that case, α must be conditioned to avoid negative values, using Equation 4.6:

$$\alpha(X_c) = \begin{cases} aX_c + b & \textbf{if} \quad X_c > -b/a \\ 0 & \textbf{if} \quad X_c \leq -b/a \end{cases} \tag{4.6}$$

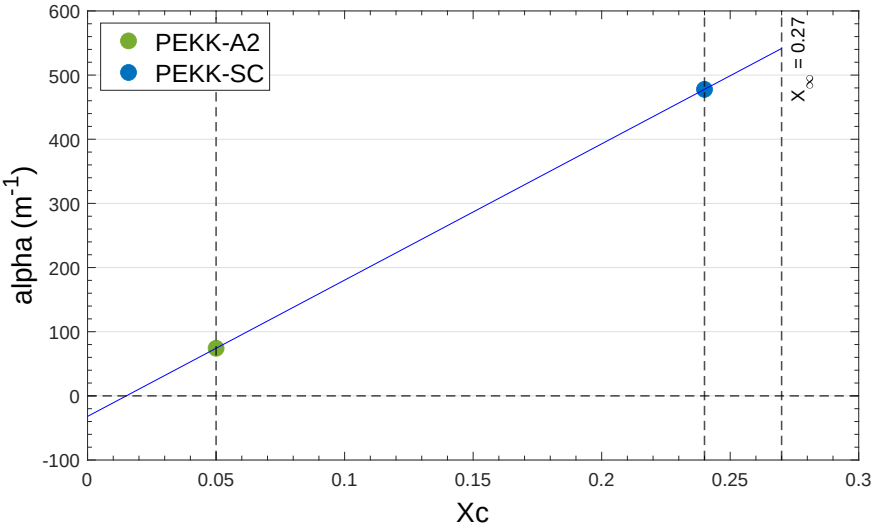

Figure 4.1: Plot of $\alpha(X_c)$ for PEKK injected plates for the study.

4.2.3 Crystallization model for PEKK

To model the evolution of the crystallinity X_c of the samples due to the laser beam irradiation, a crystallization kinetic model was implemented. The crystallinity of the samples evolved in time with the evolution in temperature due to the laser irradiation and heat conduction. The crystallization models described in the literature [Avrami, 1939] predict the evolution of the relative crystallinity X_R of the material (going from 0 to 1) as function of time and temperature. To obtain the real crystallinity evolution X_c, the X_R is multiplied by the maximum crystallinity possible to achieve by the material X_∞, as indicated by Equation 4.7:

$$X_c(t) = X_R(t) \cdot X_\infty \tag{4.7}$$

In the case of PEKK samples of the study the maximum degree of crystallinity possible to achieve is 27%, as characterized by DSC in Chapter 2. Therefore, $X_\infty = 0.27$, giving $0 \geq X_c \leq 0.27$.

In PEKK 7002, primary and secondary crystallization take place [Gardner et al., 1992], each of which has different weight in the final crystallinity X_c. Therefore, the X_R will be the addition of these two crystallinities developed, as indicated by Equation 4.8:

$$X_R(t) = w_1 \cdot X_1(t) + w_2 \cdot X_2(t) \tag{4.8}$$

where w_1 and w_2 are the weight factors of the primary and secondary crystallization in the relative crystallinity X_R of the material. Therefore, $w_1 + w_2 = 1$, corresponding to the Avrami model hypotheses that the relative crystallinity at infinite time is unity [Avrami, 1939].

To solve the crystallinity evolution for the simulations, the derivative Hillier model is used. This allow to express the crystallization kinetic model with derivatives. Therefore, Equation 4.7 combined with Equation 4.8 and expressed with derivatives became Equation 4.9:

$$\frac{dX_c}{dt} = \left[w_1 \cdot \frac{dX_1}{dt} + w_2 \cdot \frac{dX_2}{dt} \right] X_\infty \tag{4.9}$$

where $\frac{dX_1}{dt}$ and $\frac{dX_2}{dt}$ correspond to the derivatives of the primary and secondary crystallization, respectively. The equations of these derivatives will depend on the model used to calculate them, which can be found in the literature.

For the present study, the model used to predict the evolution of X_c as function of time and temperature is the one developed by *Choupin* in his thesis [Choupin, 2017]. The derivative of the Hillier model developed by Choupin predicts the non-isothermal crystallization of PEKK 7002, where the derivative of the primary and secondary crystallization kinetic are described by Equations 1.30 and 1.33 (ref. Chapter 1, Section 1.4.2.2). With the Avrami exponent for the primary crystallization $n_1 = 3$, indicating a three dimensional growth with an instantaneous nucleation, as determined experimentally by Choupin for PEKK 7002. And for the secondary crystallization, $n_2 = 1$, corresponding to a one dimensional crystallization growth with an instantaneous nucleation. Additionally, the weight factors for each crystallization are $w_1 = 0.78$ and $w_2 = 1 - w_1$, as calculated by Choupin. The additional parameters needed for the crystal growth will be given in section 4.4.2.

4.2.4 Model assumptions

Some assumptions are made to simplify and achieve the numerical simulations of the PEKK parts:

- A perfect contact at the assembly interface is assumed to consider qualitatively the clamping pressure of the experiences.
- The density and thermal conductivity of the samples are constant (no temperature dependency).
- Dirichlet boundary conditions are specified. The temperature of the top surface of the upper part, and the bottom surface of the lower part of the model are fixed at ambient temperature (20°C) for all the calculations. This to take into account the contact of the samples with the clamping glass (top surface of the upper part), and with the working platform (bottom surface of the lower part).
- Only the geometry of the overlapped section of the assembly is modeled in 3D space domain.
- Laser irradiation is applied at the top surface of the PEKK-A upper part.

4.3 Finite difference method and discretizations for the modeling

The models and equations describing the physical phenomena involved during LTW must be solved to properly simulate the dynamic laser transmission welding in thermoplastics. The used approach in this study is solving the equations by finite difference method (FDM). FDM is a numerical technique to solve differential equations by approximating derivatives with finite differences. FDM is one of the two commonly used approaches for solving engineering problems governed by differential equations [Özişik et al., 2017]. This method is relatively simple to learn and use, easy to expand to two- or three-dimensional situations for simple geometries, like in the case of this study, and simple to formulate.

To apply the finite difference method to solve the heat transfer and crystallization equations, the spatial and temporal domains are discretized. The domain is divided into a grid with nodes at discrete points in space and time. Then, the heat transfer and crystallization equations are discretized using the finite difference (FD) approximation for each derivative of the equations. For the discretization an explicit time integration scheme is used.

4.3.1 Geometry definition and discretization

The geometry of the model is defined in the 3D space (x,y,z). Only the overlap section of $25 \times 12.5\ mm^2$ with the corresponding thickness of each sample, is modeled to restrict the calculations. The spatial discretization is made for all the defined 3D geometry. A spatial step size is defined for each geometry dimension in x,y,z according to the grid points number desired. A meshgrid is generated with the discretization of the geometry for each dimension in the 3D space. The length Lx of the model goes from 0 to 25 mm with a spatial step $\Delta x = 0.0002$ m in X. Its width wy goes from 0 to 12.5 mm, with a spatial step $\Delta y = 0.0002$ m in Y. The thickness thz of the model goes from -2 mm (the thickness of PEKK-SC sample) to 2 or 4 mm (thickness of PEKK-A2 or PEKK-A4 samples) with a spatial step of $\Delta z = 0.0001$ m in Z. The chosen spatial steps ensure both good convergence and an accurate representation of the temperature gradient resulting from laser irradiation. This is validated when calculating the stability of the numerical model by the Courant-Friedirichs-Lewy (CFL) criteria in Section 4.3.3.

The spatial discretization defined for the model is relatively thin. A thin spatial discretization is chosen because of the thermal gradients that occur in the LTW process. If high values are used for the spatial discretizations, the temperature field and melted zone are not well predicted. Figure 4.2 shows the temperature fields and melted zones obtained in the thermo-optical simulation developed for the study when using high values of $\Delta x, \Delta y$ and Δz, such as 0.001 m. If these values are used as indicated, combined with a high Δt = 0.2 s (Figure 4.2a) the predictions on the temperature field and the melted zone are less accurate. Even if the maximum temperature value is correct, the temperature distribution is sharp, which generates a less well-defined melted zone. A similar effect happens even when

improving the time discretization step from 0.2 to 0.002 s, as seen in Figure 4.2b. Because of that, the spatial discretization step must be thin enough, and this must be combined with a low time discretization step.

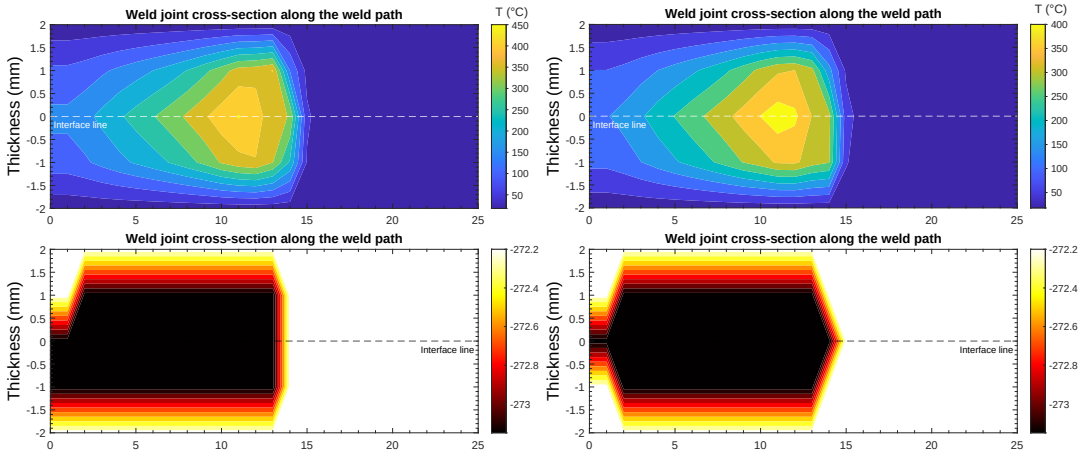

(a) (b)

Figure 4.2: Temperature field and melted zone simulated for a high value of spatial discretization ($\Delta x, \Delta y, \Delta z = 0.001$ m) for (a) $\Delta t = 0.2$ s and (b) $\Delta t = 0.002$ s when LTW modeling of PEKK parts. $P_{top} = 100$ W.

4.3.2 Discretization of the time domain

As for the spatial discretization step values, the time step value is of big importance to achieve accurate modelization of the temperature field. Figure 4.3 shows the temperature field and melted zone obtained from the thermo-optical numerical modeling when using the optimal values for the spatial discretization (defined above) but a high Δt value of 0.2 s. As it can be seen, the temperature field is less well predicted by the model than seen before in Figure 4.3a. All the geometry is subjected to temperatures higher than the melting point, as can be seen from the melted zone obtained. Then, extremely high temperature values reaching $2.5{\times}10^{63}$ °C are predicted all around the geometry combined with negative values, and the temperature distribution is compleatly inaccurate. Combine a thin spatial discretization with a high time step creates computational errors. Therefore, thin spatial discretization must be used in combination with a low time step to improve the calculations of the temperature at each point of the discretized geometry.

Therefore, for the temporal discretization, the time is divided into steps with a defined time step $\Delta t = 0.002$ s. This time step ensures good convergence of the numerical model, which is validated when calculating the stability of the model by the Courant-Friedirichs-Lewy (CFL) criteria in Section 4.3.3.

For the LTW modeling, the total simulation time t_{final} will correspond to the addition of the irradiation time t_w and the cooling time t_c, as indicated in Equation 4.10:

$$t_{final} = t_w + t_c \tag{4.10}$$

The irradiation time t_w is calculated with Equation 4.11:

$$t_w = \frac{Lw}{V} \tag{4.11}$$

where Lw is the length of welding, and V the scanning speed of the laser beam in movement. In this case, the length of welding corresponds to 20 mm and $V = 1mm \cdot s^{-1}$, as for the experimental tests.

The cooling time t_c is the time defined after irradiation for the samples to be kept in contact and cool down the irradiated zone. Here, $t_c = 120s$, as used on the experimental tests. An explicit Eulerian time integration scheme is used to solve the heat transfer and crystallinity equations.

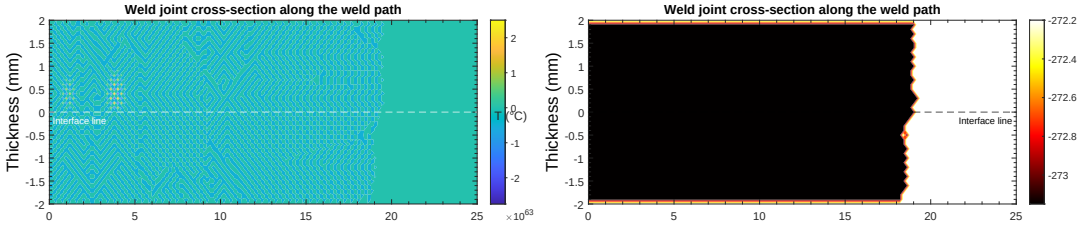

(a) (b)

Figure 4.3: (a) Temperature field and (b) melted zone simulated for a high value of $\Delta t = 0.2$ s and a good spatial discretization (Δx and $\Delta y = 0.0002$ m, $\Delta z = 0.0001$ m) when LTW modeling of PEKK parts. $P_{top} = 100$ W.

4.3.3 Heat equation discretization by FDM

The heat conduction equation coupled with an energy absorption term that represents the laser heating must be solved to properly simulate the dynamic laser transmission welding in thermoplastics. For the present study, the heat transfer equation is solved in a 3D geometry with a volumetric heat source. Therefore, Equation 4.1 became Equation 4.12:

$$\rho C_p \frac{\partial T}{\partial t} = k \times \left(\frac{\partial^2 T}{\partial x^2} + \frac{\partial^2 T}{\partial y^2} + \frac{\partial^2 T}{\partial z^2} \right) + Q(x, y, z, t) \tag{4.12}$$

To discretize the heat equation, the finite difference (FD) approximation is used for each derivative in the heat transfer equation. The FD approximations are defined according to Equation 4.13 for the time derivative, and to Equation 4.14,4.15 and 4.16 for the spatial derivatives.

$$\frac{\partial T}{\partial t} \approx \frac{T_{i,j,k}^{n+1} - T_{i,j,k}^{n}}{\Delta t} \tag{4.13}$$

$$\frac{\partial^2 T}{\partial x^2} \approx \frac{T_{i+1,j,k}^{n} - 2T_{i,j,k}^{n} + T_{i-1,j,k}^{n}}{\Delta x^2} \tag{4.14}$$

$$\frac{\partial^2 T}{\partial y^2} \approx \frac{T_{i1,j+1,k}^{n} - 2T_{i,j,k}^{n} + T_{i,j-1,k}^{n}}{\Delta y^2} \tag{4.15}$$

$$\frac{\partial^2 T}{\partial z^2} \approx \frac{T_{i,j,k+1}^{n} - 2T_{i,j,k}^{n} + T_{i,j,k-1}^{n}}{\Delta z^2} \tag{4.16}$$

Where $T_{i,j,k}^{n}$ represents the temperature at each grid point (i, j, k) of the spatial domain at the time step n. i, j and k are the indices in the x, y, z directions of the geometry.

Substituting the discretized derivatives into the heat transfer equation and rearranging to solve for the temperature evolution ($T_{i,j,k}^{n+1}$), Equation 4.17 is obtained:

$$T_{i,j,k}^{n+1} = T_{i,j,k}^{n} + \frac{\Delta t}{\rho C_p} \times \left[k \left(\frac{\partial^2 T}{\partial x^2} + \frac{\partial^2 T}{\partial y^2} + \frac{\partial^2 T}{\partial z^2} \right) + Q_{i,j,k}^{n} \right] \tag{4.17}$$

The stability of the numerical model is verified by the Courant-Friedirichs-Lewy (CFL) criteria by calculating ε with Equation 4.18:

$$\varepsilon = \frac{k \times \Delta t}{\rho \times C_p \times (\Delta x^2 + \Delta y^2 + \Delta z^2)} < \frac{1}{2} \tag{4.18}$$

where k is the conductivity, ρ the density and C_p the heat capacity of the studied material. For this calculation C_p is used as the constant value from the material properties, just to verify the stability criteria. And Δt, Δx, Δy and Δz are the discretization parameters for time and space defined for the model. Using the PEKK properties and discretization parameters of the study a $\varepsilon = 0.0044$ is obtained. This value is lower than 0.5, indicating that the numerical model is conditionally stable.

4.3.4 Crystallization model discretization by FDM

In addition to the thermo-optical model, the crystallization kinetics model is implemented and solved to simulate the crystallinity evolution of the samples according to the laser irradiation. For that, Equation 4.9 is discretized as for the heat conduction equation. The time derivative FD approximation for each crystallization derivative is defined according to Equation 4.19:

$$\frac{dX_x}{dt} \approx \frac{{X_x}_{i,j,k}^{n+1} - {X_x}_{i,j,k}^{n}}{\Delta t} \tag{4.19}$$

Substituting the discretized derivative into the crystallization equation and rearranging to solve for the crystallinity evolution ($X_{c_{i,j,k}}^{n+1}$), Equation 4.20 is obtained:

$$X_{c_{i,j,k}}^{n+1} = X_{c_{i,j,k}}^{n} + \left[w_1 \cdot \frac{dX_1}{dt} + w_2 \cdot \frac{dX_2}{dt} \right] \cdot \Delta t \cdot X_\infty \tag{4.20}$$

And when adding also the discretized derivatives for the primary and secondary crystallization derivatives, Equation 4.21 is obtained:

$$X_{c_{i,j,k}}^{n+1} = X_{c_{i,j,k}}^{n} + \{ w_1 \cdot [{X_1}^n + X_1(t) \cdot \Delta t] + w_2 \cdot [{X_2}^n + X_2(t) \cdot \Delta t] \} \cdot \Delta t \cdot X_\infty \tag{4.21}$$

where $X_1(t)$ and $X_2(t)$ depend on the crystallization model chosen to solve them.

4.4 Modeling the LTW of an overlapped configuration

The different models and equations are solved by the use of MatLab software for the dynamic laser irradiation of the PEKK-A/SC assembly. The following steps are implemented on the subroutine to model the LTW process:

1. The overlapped geometry of the assembly is defined and discretized as indicated in Section 4.3.1.
2. Material properties are defined for each up and bottom sample, including their initial degree of crystallinity (X_c).
3. When incorporating the crystallization model, the crystallization parameters for the kinetic model are defined. Also, primary and secondary crystallizations are initialized (X_1 and X_2 respectively).
4. Welding parameters are defined.
5. The initial temperature distribution $T_{i,j,k}^0$ is set for all grid points, which is equal to the ambient temperature.
6. The equations describing the physical phenomena involved during LTW are iterated over time steps Δt from t = 0 to t_{final}. This is made by the use of a *while* loop with the condition "*while* $t_n <= t_{final}$", and increasing the time t_n for each loop with $t_n = t + \Delta t$.
7. For each time step t_n from 0 to t_{final}:

- The laser intensity $I(x, y, t)$ is initialized at the beginning of the *while* loop with the first calculation at t = 0 s.
- Then, the laser intensity $I(x, y, t)$ is updated according to its movement in X axis with Equation 4.4. That for all time step inferior to the total irradiation time t_w.
- The absorption coefficient α is updated according to the crystallinity of the samples with Equation 4.5.
- The heat source $Q(x, y, z, t)$ is updated according to the updated calculation of $I(x, y, t)$ and α. $Q(x, y, z, t)$ is calculated according to Equation 4.3 for each Δz step.
- The new temperature $T_{i,j,k}^{n+1}$ is computed for each interior grid point using Equation 4.17.
- When including the crystallization model, the crystallinity of the samples is updated according to temperature evolution and time by means of Equation 4.9.
- Boundary conditions are updated.
- Time is updated with $t_n = t + \Delta t$.

8. After a time step completed the calculations move to the next time step.
9. After all time steps are completed, the calculation results are visualized and analyzed.

Figure 4.4 shows the schematic representation of the modeling of the welding process. The 3D geometry, dimensions, and orientation defined for the samples overlapped with the laser beam are shown in Figure 4.4a. The boundary conditions at time t = 0 s are represented in Figure 4.4b.

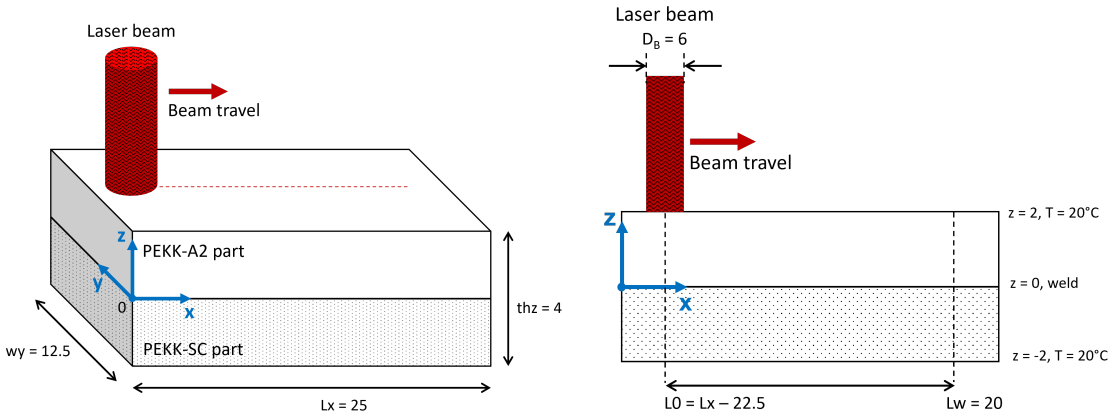

Figure 4.4: Schematic representation of the model geometry: (a) overlapped parts and laser beam orientations and (b) boundary conditions at time t = 0s. Dimensions are in millimeters.

The material properties used in the modeling are those already measured in Chapter 2 for the PEKK plates. A summary of these properties is shown in Table 4.1.

Property	Unity	PEKK-A2	PEKK-A4	PEKK-SC
T_g	[°C]	151	152	160
T_m	[°C]	337	336	338
T_{cc}	[°C]	195	196	-
T_{ch}	[°C]	293	293	293
X_c	[%]	5	6	24
ρ [Arkema, 2021]	$[\mathrm{kg \cdot m^{-3}}]$	1290	1290	1290
k	$[\mathrm{W \cdot m^{-1} \cdot K^{-1}}]$	0.246	0.246	0.211
C_{p0}	$[\mathrm{J \cdot kg^{-1} \cdot K^{-1}}]$	973	973	1138
T_i	[%]	75	62	20
R_i	[%]	13	13	48
A_i	[%]	12	25	32
α	$[m^{-1}]$	74.2	84.7	477.75

Table 4.1: Summary of the PEKK 7002 injected plates properties.

The welding parameters specified for the simulations are those used in the experimental tests to weld PEKK-A/SC samples. These parameters are summarized in Table 4.2.

Parameter	Value
Welding speed (V) $[mm.s^{-1}]$	1
Beam diameter (DB) $[mm]$	6
Weld length (Lw) $[mm]$	20
Cooling time (tc) $[s]$	120
Laser power (P) $[W]$	P_{top}

Table 4.2: Welding parameters for LTW modeling.

As for experimental tests, most of the welding parameters stay constant, except for the laser power P. The power value will be defined according to the assembly combination type (ref. Table 2 of Chapter 3, Section 3.2.4) desired to simulate. In experimental tests, the laser power defined is the output power value P_o from the laser system. This P_o is specified according to the power value desired to reach the interface of the assembly after going through the clamping glass and the PEKK-A upper part (ref. Table 3 of Chapter 3, Section 3.2.4). However, in the simulations, the laser irradiation is applied directly at the top surface of the PEKK-A upper part. The clamping glass is not taken into account to simplify the modeling. Therefore, the laser power used in the simulations is the power value after going through the clamping glass in the experimental tests. Thus, the power value that strokes the top surface of the PEKK-A upper part P_{top}. This laser power P_{top} can be calculated with Equation 4.22:

$$P_{top} = P_o \times 0.83 \tag{4.22}$$

where P_o is the output laser power values defined in Chapter 3.

To test the simulations developed in the next sections, laser welding process will be modeled for the PEKK-A2/SC-P1 assembly type. Therefore, $P_{top} = 100$ W, at the beginning.

4.4.1 Study on the laser irradiation, temperature field and melted zone

The first model developed for the study focused on the simulation of thermal and optical phenomena during laser transmission welding. The laser irradiation is modeled at the center of the interface plan with a movement on the X axis from X = 2.5 mm to X = 22.5 mm, to create a weld path length of 20 mm, as for the experimental welding tests. The laser intensity is calculated according to the laser parameters (output power and beam diameter) and to its movement in time on the X axis ruled by the scanning speed v. Therefore, Equation 4.4 can be detailed for the desired laser position and movement as in Equation 4.23:

$$I(x,y,t) = \frac{P_{top}}{2\pi.\sigma^2} exp\left[\frac{-(x - v\cdot t - 0.0025)^2 + (y - \frac{wy}{2})^2}{2\sigma^2}\right] \tag{4.23}$$

The laser intensity $I(x,y,t)$ is then used to calculate the heat source $Q(x,y,z,t)$ with Equation 4.3. The heat source is generated as a result of the absorption of the laser intensity through the thickness of the samples. Therefore, Q will evolve with the laser intensity, but also with the absorption properties of the samples.

As specified in the model assumptions (Section 4.2.4), the laser irradiation is applied at the top surface of the PEKK-A upper part. As in real experimental conditions, the laser intensity will first go through the upper part to reach and irradiate the interface of the assembly. When going through this upper part, the laser energy will decrease according to the transmission properties of the sample (as seen in Chapter 2). The energy that is not transmitted will therefore be absorbed by the sample, according to its absorption properties (conditioned by its α coefficient). The energy that reaches the assembly interface will then be absorbed by the bottom part, this also according to its absorption properties. As indicated in Section 4.2.2, the absorption properties of the PEKK overlapped samples can be described as function of their degree of crystallinity with Equation 4.6. This evolution of $\alpha(X_c)$ must be then integrated to the calculation of the heat source. Therefore, Equation 4.3 became Equation 4.24:

$$Q(x,y,z,t) = \alpha(X_c)\cdot(1-R)\cdot I(x,y,t)\cdot exp(-\alpha(X_c)\cdot z) \tag{4.24}$$

When the laser energy is absorbed by the samples it is then converted into heat. This

causes the samples to heat, incrementing their temperature. With the appropriate combination of welding parameters, the laser energy will allow the samples to heat over their melting temperature. Therefore, the materials will melt at the heated zone. For a semi-crystalline polymer like PEKK, melting phenomena indicate that the existent crystals on the samples are fully vanished. This indicates that the degree of crystallinity of the samples became null when reaching the melting temperature. To represent this in the model, X_c must be zero when T > Tm. However, if Xc is zero, Equation 4.5 became negative, according to the defined constants a and b. This will cause problems on the computation. To avoid errors on the calculations, α can be redefined by its minimum value possible, which is obtained when $Xc \geq -b/a$. Therefore, a modification of the α condition is made for $Xc \leq -b/a$ so it became minimal if the temperature rises above Tm. First, the degree of crystallinity of the samples will be near zero when the temperature rises above Tm, conditioned by Equation 4.25. Then, Equation 4.6 became Equation 4.26:

$$X_c = \left\{ -\frac{b}{a} \quad \textbf{if} \quad T > T_m \right. \tag{4.25}$$

$$\alpha(X_c) = \begin{cases} aX_c + b & \textbf{if} \quad X_c > -b/a \\ a(b/a + 0.005) + b & \textbf{if} \quad X_c \leq -b/a \end{cases} \tag{4.26}$$

This condition implemented for the evolution of α allows to simulate the melting phenomenon on the samples, improving the calculation of the temperature field. Figure 4.5 shows the temperature fields obtained by the simulations for the PEKK-A2/SC-P1 assembly type before and after including this condition for α. The temperature field is represented on the weld cross section perpendicular to the irradiation path, at the center of the weld path, at 10 s of irradiation. When the condition is not applied to the simulation (Figure 4.5a), the temperature of the samples reaches extremely high values (around 1200°C). However, having the condition of α becoming minimal for temperatures higher than the melting temperature of the material (Figure 4.5b), the temperature field obtained in the samples decreases to 400°C.

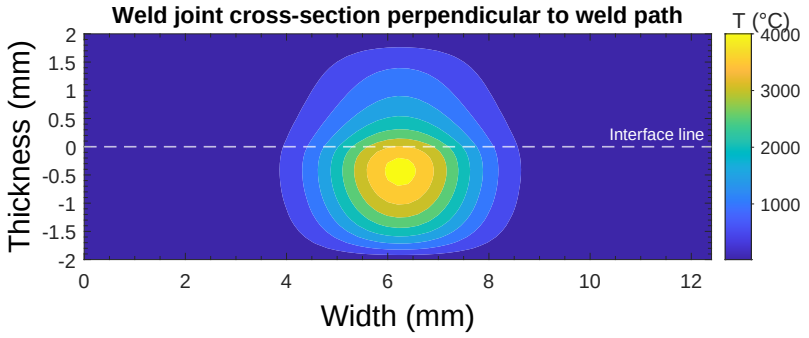

(a)

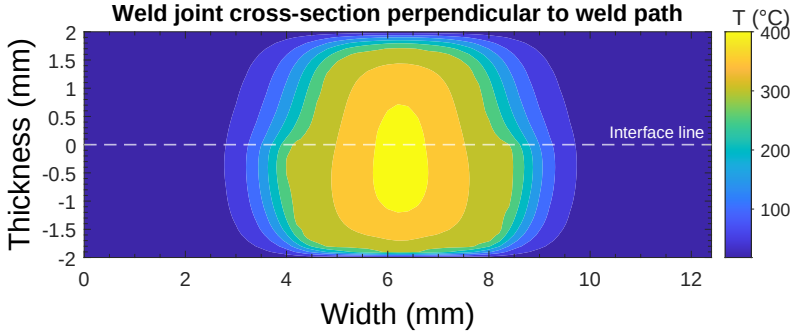

(b)

Figure 4.5: Simulated temperature field at the weld joint cross-section perpendicular to the weld path (a) before and (b) after implementing the condition for α. Laser power P_{top} = 100 W and irradiation time t = 10 s.

Figure 4.6 shows the simulated melted zone at the weld joint cross-section along the weld path for two different P_{top} values implemented. As it can be noticed in Figure 4.6a, even if the temperature field decreases with the applied condition for α, the melted zone obtained when using 100 W for P_{top} covers almost all the assembly thickness. The high-temperature gradient caused by laser power significantly alters the material's properties, making their exact values elusive. Studies have proven that thermal properties, such as the melting point of thermoplastic materials, decrease with high heating rates. Bölle et al. [Bölle et al., 2022] in 2022 demonstrated how the heating rate influences the melting peak position in PA66. The melting temperature of PA66 is modified at high heating rates, decreasing 7°C between a speed of 1 and 100°C/s. In addition, the simulations developed in the present study are based on a 1D absorption model perpendicular to the input surface with integration in Z. The existing scattering in the parts is not incorporated in the model. A lower power value must then be used to best reproduce the results obtained in the experimental tests for the PEKK-A2/SC-P1 assembly type in terms of weld joint morphology (in this case the melted zone). This power value corresponds to the power required to melt the volume of polymer within

the weld seam, as calculated using known thermal properties. In the preliminary simulations tests, 20 W was determined as the power value that allowed the welding tests to be explained in terms of weld joint melted zone (Figure 4.6b). This power value is also chosen on the basis of a known model and parameters for semi-crystalline polymers [Wang et al., 2016]. Therefore, from now on, 20 W are going to be applied on the simulation for P_{top} to try to reproduce the results for the PEKK-A2/SC-P1 assembly type.

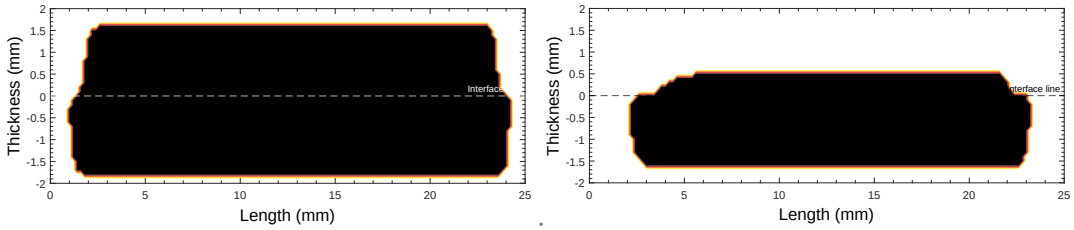

(a) (b)

Figure 4.6: Simulated melted zone at the weld joint cross-section along the weld path obtained after irradiation (t = 20 s) for a laser power P_{top} = (a) 100 W and (b) 20 W.

4.4.2 Study on the crystallinity evolution of the weld joint

The thermo-optical simulation developed is improved by adding the crystallization kinetics model of the material. When welding parts by LTW, the process is non-isothermal, due to the variations of temperature with time. Therefore, a non-isothermal crystallization model is important to use for the correct modeling of the LTW process. To validate the modeling, the simulations results will be compared with the experimental results(ref. Chapter 3, Section 3.2.1).

For the case of PEKK, two non-isothermal crystallization models are found in the literature [Choupin, 2017, Pérez-Martín et al., 2022]. The model developed by *Choupin* in his thesis is described by Equation 27 (ref. Chapter 1, section 4.2.2) [Choupin, 2017]. And the crystallization kinetic model developed by *Perez-Martin et al.* in 2022 is described by Equation 40 (ref. Chapter1, section 4.2.2) [Pérez-Martín et al., 2022]. The crystallization parameters defined on each study are summarized in Table 4.3.

In both models, the degree of crystallinity X_c is obtained by the addition of the first and secondary crystallization evolution in time and temperature. Therefore, in the simulation, both crystallizations are calculated separately. The computation of each one is conditioned between the glass and melting temperatures. This is because the crystal growth parameters are only valid between that range of temperatures [Choupin, 2017, Pérez-Martín et al., 2022]. Conditioning in this way the crystallization kinetics calculations allow to obtain the correct evolution of the crystallinity of the samples.

Parameter	*Choupin thesis* [Choupin, 2017]	*Perez-Martin et al.* [Pérez-Martín et al., 2022]
n_1	3	3
n_2	1	2
w_1	0.78	$1.399r^{-0.8707} + 1$
w_2	0.22	1 - w_1
$U^*[J.mol^{-1}]$	4.9×10^3	4.7×10^3
$K_{01}[min^{-3}]$	1.79×10^{16}	1.5×10^{14}
$K_{g1}[K^2]$	4×10^5	2.486×10^5
$K_{02}[min^{-3}]$	2.6×10^5	5.041×10^7
$K_{g2}[K^2]$	4.4×10^5	2.025×10^5

Table 4.3: Parameters of the non-isothermal crystallization kinetic model for PEKK 7002. (r accounts for the cooling rate in the calculation of w_1).

Figure 4.7a shows the results obtained on the crystallinity field of the assembly from the first simulation developed. For this simulation, the crystallization model used was that from Choupin, with its corresponding parameters for non-isothermal kinetics. It can bee seen that the crystallinity of the samples is not modified after irradiation and cooling. Particularly, the PEKK-SC bottom sample does not show any melted zone after irradiation. The melted zone on this part should be recognizable by a high decrement on the crystallinity, as observed on experimental tests. This lack of crystallinity modification on the samples occurs because the crystallization kinetic model only predicts the new germs developed from the melt or cold states. The model does not predicts the fusion of the crystals caused by the increment in temperature on the material. In this case, the effect of the melting phenomena on the crystallinity of the material must be also simulated. To achieve this, a condition is added to the crystallinity as indicated for α in the last section. In this case, the crystallinity X_c must became minimal when the temperature reached in the samples are above the melting point of the PEKK material. With that, it is indicated that the crystals are vanished when the melting point is reached. This is specified by modifying Equation 4.25 to became Equation 4.27 in the model:

$$X_c(t) = \left\{ -\frac{b}{a} + 0.01 \quad \textbf{if} \quad T > T_m \right. \tag{4.27}$$

where a and b are the constants from Equation 4.5 that describes the evolution of $\alpha(X_c)$. After including this condition on the model, melting phenomena effect on the crystallinity can be seen on the crystallinity field, as shown in Figure 4.7b. Therefore, the crystallinity field evolves as function of temperature and time.

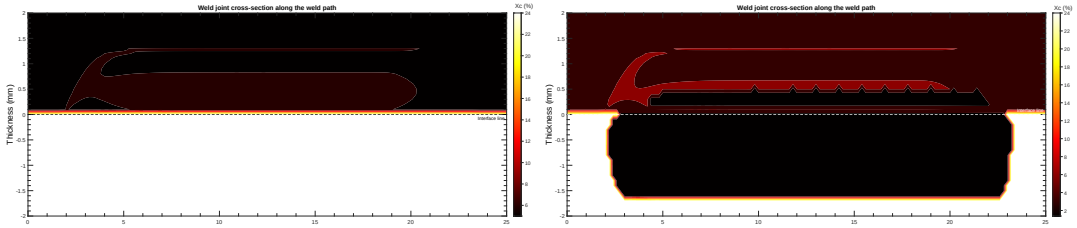

(a) (b)

Figure 4.7: Simulated crystallinity field at the weld joint cross-section along the weld path obtained after irradiation and cooling (t = 140 s) (a) before and (b) after adding the condition from Equation 4.27 (for P_{top} = 20 W).

The two models found in the literature are tested and compared to choose the one that reproduced at best the crystallinity field for the PEKK-A/SC LTW assemblies. For that, the models were tested to try to reproduce the morphology of PEKK-A2/SC-P1 assembly type. Figure 4.8a shows the weld morphology obtained on PEKK-A2/SC-P1 assembly type by the simulations when using the model and parameters of Choupin. As it can be seen, the weld joint shows only a melted zone. The weld joint did not crystallize from the cold on PEKK-A2 sample, as expected from the experimental tests.

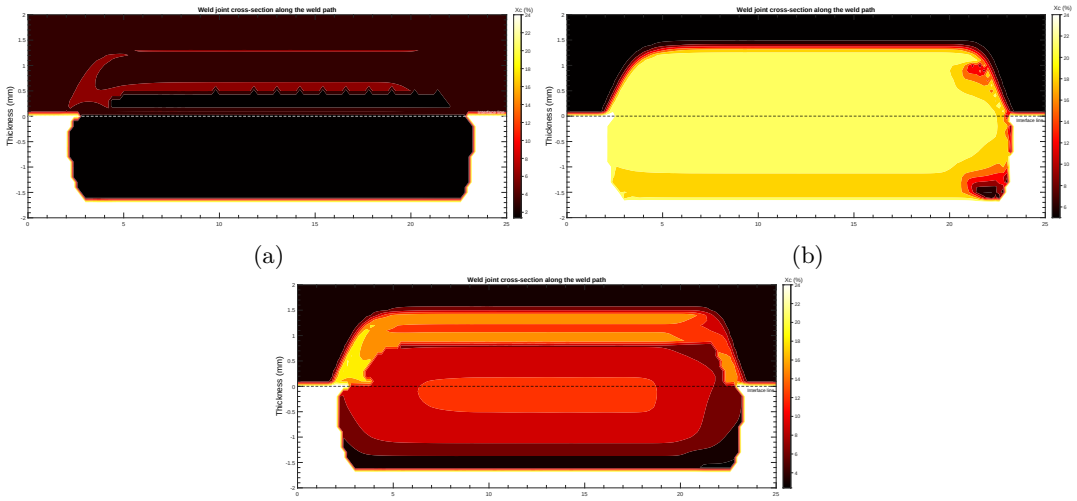

(a) (b)

(c)

Figure 4.8: Simulated crystallinity field at the weld joint cross-section along the weld path obtained after irradiation and cooling (t = 140 s) when using the crystallization model of (a) Choupin, (b) Perez-Martin and (c) Choupin with Perez-Martin parameters. (P_{top} = 20 W).

Figure 4.8b shows the weld morphology obtained for the same assembly when using the crystallization model developed by *Perez-Martin et al.* in 2022 [Pérez-Martín et al., 2022], with the parameters found for PEKK 7002. In this case, the weld joint crystallized more than expected. Crystallization from the melt and from the cold evolves at the same rate, which is not realistic compared to the experiments carried out in this study. In this study, experimental

conditions showed that when LTW PEKK-A/SC, crystallization from the cold appears sooner than from the melt (ref. Chapter 3, Section 3.5.1). During the welding process of PEKK-A/SC samples, it was observed that the PEKK-A upper part acquired milky-white coloration after irradiation. This change in coloration of the upper part occurs at the irradiated zone and follows the laser beam movement, separated by some seconds. On the other hand, the melted zone did not crystallize upon cooling, as observed after welding in the weld joint cuts (ref. Figure 3.19).

Because both models alone gave results very different between them and to the experimental results, another approach was tried. In this case, the the model developed by *Choupin* in his thesis is applied combined with the crystal growth parameters obtained by *Perez-Martin et al.* in 2022 [Pérez-Martín et al., 2022] for PEKK 7002. Combining these models allowed to obtain a better modeling of the crystallinity field for the PEKK-A2/SC-P1 assembly type, as shown in Figure 4.8c. Table 4.4 summarizes the crystallization parameters used for the modeling.

Parameter	**PEKK 7002**
n_1	3 [Choupin et al., 2018]
n_2	1 [Choupin et al., 2018]
w_1	0.78 [Choupin et al., 2018]
w_2	0.22 [Choupin et al., 2018]
$U^*[J.mol^{-1}]$	4.9×10^3 [Choupin et al., 2018]
$K_{01}[min^{-3}]$	1.5×10^{14} [Pérez-Martín et al., 2022]
$K_{g1}[K^2]$	2.486×10^5 [Pérez-Martín et al., 2022]
$K_{02}[min^{-3}]$	5.041×10^7 [Pérez-Martín et al., 2022]
$K_{g2}[K^2]$	2.025×10^5 [Pérez-Martín et al., 2022]

Table 4.4: Parameters for the crystallization kinetic model.

4.4.3 Predicting the weld joint morphology of PEKK-A2/SC assemblies

After all the adjustments implemented to the model from the studies on the laser irradiation, temperature field, melted zone and crystallinity evolution of the weld joint, simulations were lunched to predict the weld joint morphology on PEKK-A2/SC assemblies.

Figure 4.9 shows the temperature fields for two assembly views: the cross-section along the weld path and the assembly interface plan. The temperature is also shown for two different times of the simulated welding process: Figure 4.9a corresponds to the first second of irradiation (t = 1s), and Figure 4.9b shows the last second of irradiation (t = 20s). The cross-section along the weld path shows that the temperature field is non homogeneous between the upper and lower parts. At the beginning of irradiation (t = 1s) (Figure 4.9a), the highest temperatures are reached in the PEKK-SC bottom sample due to its high absorption properties compared to the PEKK-A upper part. It is also noticeable in the temperature

distribution that the PEKK-SC part absorbed the energy in the volume, not only at the interface, as for the experimental tests. Then, this temperature field expands as the laser moves. As it can be seen at the end of the weld path (Figure 4.9b), the PEKK-A sample now reaches high temperatures in its thickness and not only at the interface, but this thickness is still lower than that of the PEKK-SC sample. That indicates that both the PEKK-SC and PEKK-A melted in their volume at the irradiation process but within a different thickness, as observed experimentally with the ML of both parts. When visualizing the assembly interface plan, it can be noticed how the temperature evolution caused by the laser beam passes from a circular shape at the first second of irradiation to a comet shape at the end of the irradiation. The observed temperature distribution and its evolution along the welding process are primarily attributed to the variation of the laser energy deposition at the assembly interface. The modification of the sample's crystallinity caused by the increasing temperatures of the welding process makes the absorption coefficient evolving. This evolution in absorption capacities directly influences the energy deposition dynamics throughout the welding process.

Figure 4.10a shows two views of the weld joint HAZ after irradiation and cooling: the cross-section along the weld path and the interface plan. The isovalues indicate the crystallinity (Xc) of the samples. These numerical visualizations are comparable to those observed on the PEKK-A/SC NC assemblies. As observed experimentally in Cahpter 3, two identifiable zones are also obtained in the simulations when visualizing the cross-section along the weld path (Figure 4.10a top). An amorphous zone 1 covering both samples, and a cold crystallized zone 2 developed over zone 1. Then, when observing the HAZ at the interface plan for the CI failed assemblies in Figure 27 from Chapter 3, Section 5.2, it can be noticed that the weld joint is amorphous, as predicted by the numerical simulations at the bottom in Figure 4.10a. Also, both experimental and numerical results indicate that the semi-crystalline polymer remains crystallized in the bottom zone. This behavior is attributed to the applied boundary conditions (T=20°C) in the simulation. In the experiment, it is likely due to heat transfer with the metallic support, which keeps this area near room temperature.

Figure 4.10b plots the temperature and crystallinity evolution in time for the two points indicated in the weld joint cross-section along the weld path of Figure 4.10a: the center point of the assembly at the interface on the PEKK-SC part (wcp-int) with coordinates (x,y,z) = (12.5,0,0) mm, and the center point at the scL developed (wcp-scL) with coordinates (x,y,z) = (1.25, 0, 1.2) mm. At the interface, the temperature increases from ambient temperature (20°C) to its maximum value (around 314°C) in less than 4s, indicating a heating rate of 4380 °C·min^{-1}. The highest temperature reached is 314°C, allowing melting of the material, as defined in the model, and as observed experimentally in Cahpter 3. Then, at the scL, the maximum temperature reached is about 285°C, being lower than the melting temperature. That indicates that the PEKK-A sample did not melt in this zone. However, the elevated temperatures allowed the material to cold crystallize, agreeing with the experimental findings in Chapter 3.

The variation of crystallinity (Xc) of the PEKK-SC (at the wcp-int) shows a drastic change from 24% to almost zero when the melting temperature is reached. Then, with the temperature decrease, the crystallinity slightly increases up until it stabilizes at 10%. That

shows that the PEKK-SC sample melted upon irradiation and did not crystallize during cooling, staying amorphous. On the other side, at the PEKK-A sample (the wcp-scL point), the crystallinity increases with temperature, reaching a maximum of 14.5%. This indicates that the PEKK-A part achieved cold crystallization during irradiation, achieving a semi-crystalline state as stated in the scL.

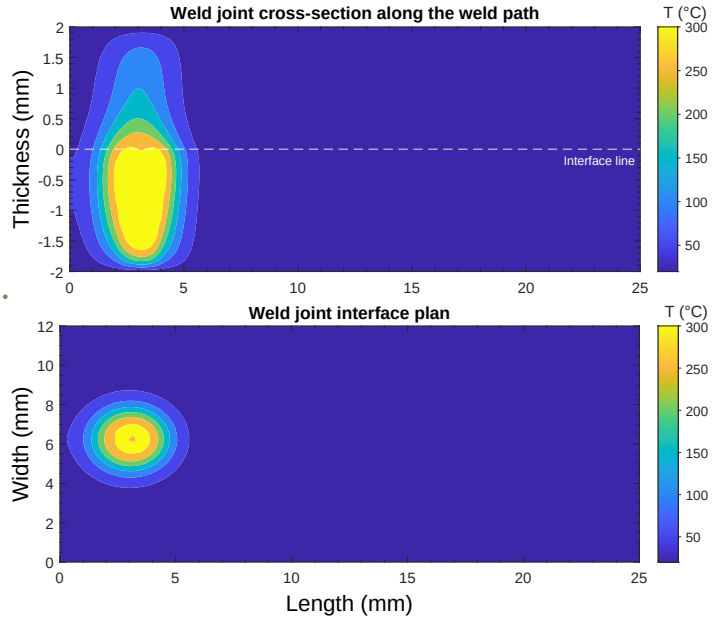

(a)

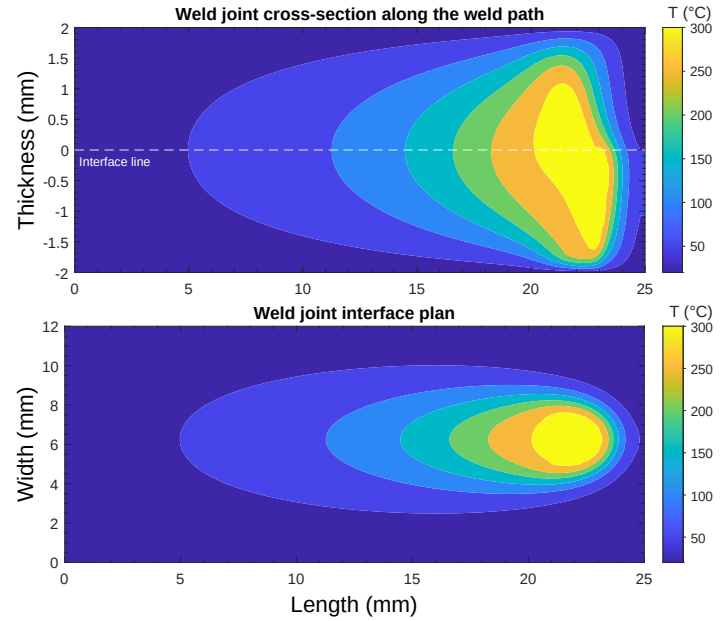

(b)

Figure 4.9: Simulations results: Temperature field on the weld joint at (a) 1s and (b) 20s of irradiation.

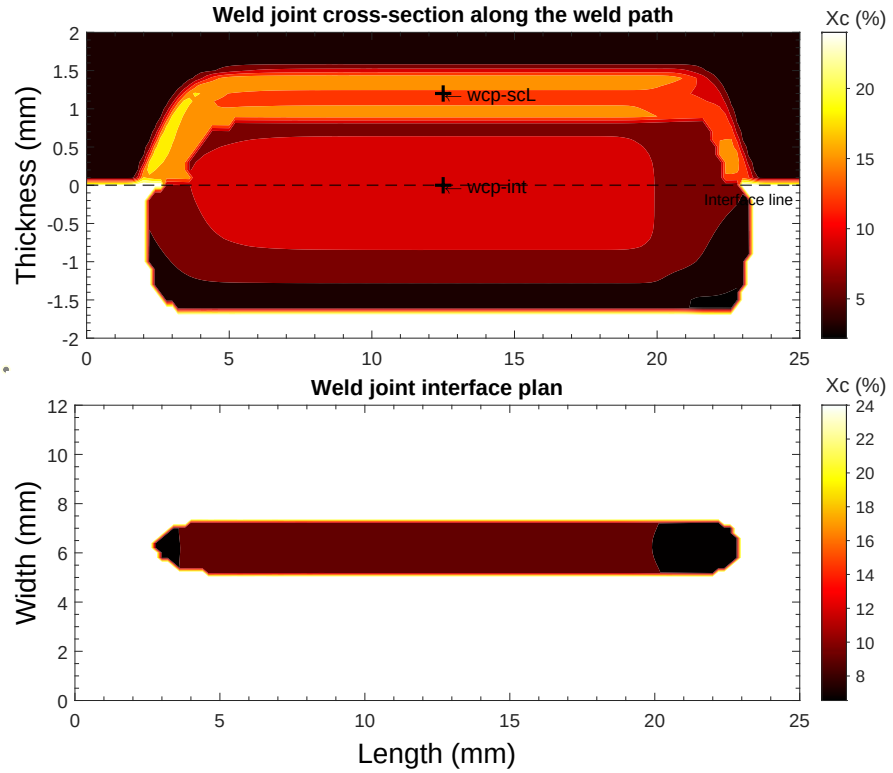

(a)

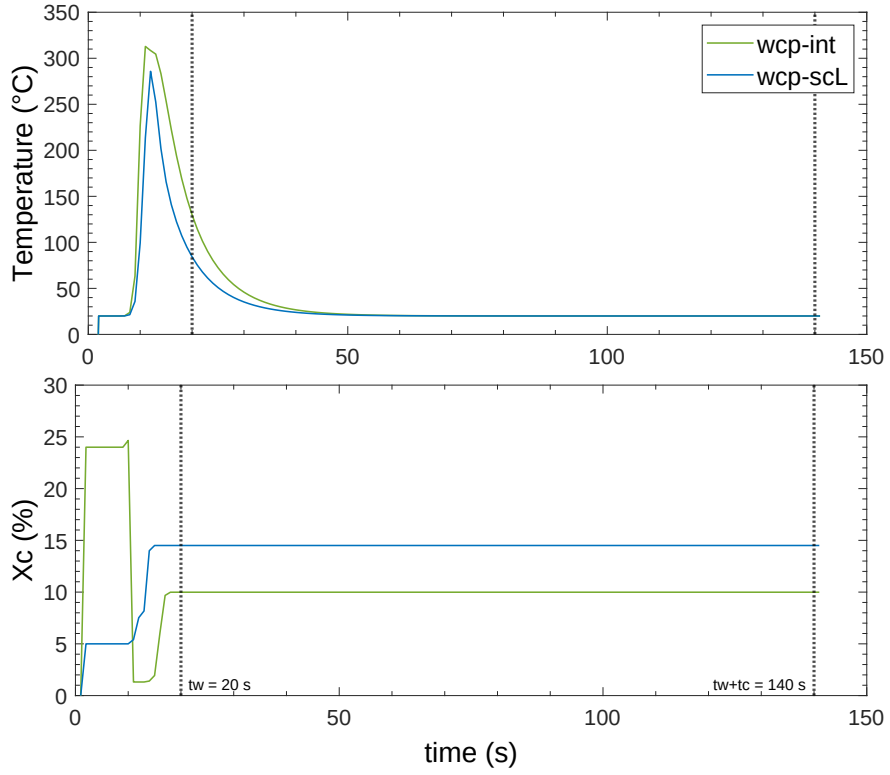

(b)

Figure 4.10: Simulations results: (a) weld joint HAZ isovalues of the crystallinity after welding process, along the welding path and at the interface plans, and (b) plots of the temperature and the crystallinity degree over time.

The weld joint morphology predicted by numerical modeling are in accordance and comparable with the experimental results obtained when LTW of PEKK-A2/SC. The simulations can be executed for different laser powers within a power range of 15 to 30 W for P_{top}. Where 15 W is the minimum laser power that allows melting at the interface, and 30 W the maximum laser power before melting all the thickness of the PEKK-A2 sample. To compare the numerical results with the experiments, four different laser powers were chosen between that power range to simulate the four laser powers studied experimentally. The chosen laser powers are the ones that represented at best the experimental results: 16, 18, 19 and 20 W as P1, P2, P3 and P4, respectively for P_{top} in the simulations. Figure 4.11 shows the weld joint crystallinity field obtained on the PEKK-A2/SC simulations for the four different laser powers, and they are compared with their corresponding experimental weld joint cross-section. As it can be noticed, the simulated weld joint HAZ shape is similar to the experimental one: an oval shape with a crystallinity gradient, from low to high X_c transitioning from bottom to top. Thus, the two zones defined inside the weld joint HAZ (ref. Figure 20 from Chapter 3, Section 5.1) are detectable in the four assemblies simulated. Those zones change in depths with power value, as observed experimentally.

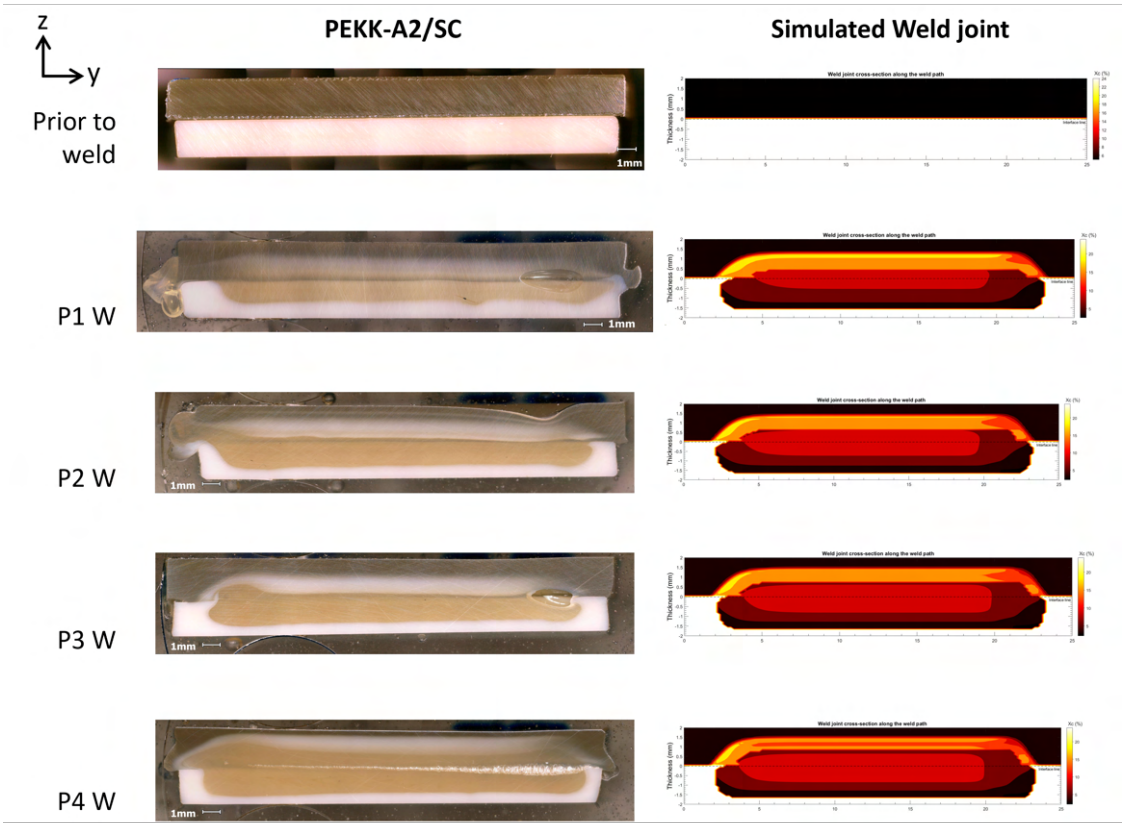

Figure 4.11: PEKK-A2/SC weld joint morphology at its cross-section along the weld path. Comparison between experimental micrographs and simulated crystallinity fields.

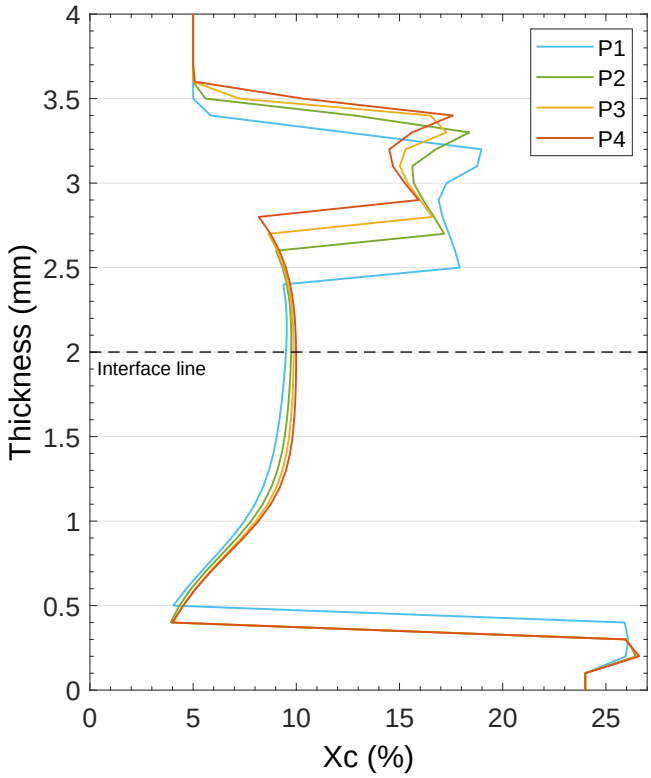

Figure 4.12: Simulated distribution of the X_c in the thickness of the PEKK-A2/SC assemblies for different laser powers.

HAZ depths	**Experimental**				**Numerical**			
Power [W]	**P1**	**P2**	**P3**	**P4**	**P1**	**P2**	**P3**	**P4**
scL-A [mm]	1,3	1,4	1,37	1,87	1,2	1,3	1,4	1,4
ML-A [mm]	0,3	0,28	0,33	0,8	0,4	0,6	0,7	0,8
ML-SC [mm]	-1,06	-1,32	-1,31	-1,4	-1,5	-1,6	-1,6	-1,6

Table 4.5: Weld joint HAZ depths obtained for 4 laser powers. Comparison between experimental and numerical results.

Figure 4.12 plots the degree of crystallinity distribution in the thickness of the assemblies for the 4 laser powers simulated. In the Y axis is represented the thickness of the assembly, the PEKK-SC part covers from 0 to 2 mm, and the PEKK-A2 from 2 to 4 mm. The interface line is identified at 2 mm by the dashed line. The distribution of the degree of crystallinity plotted is extracted from the center of the weld joint at (x,y) = (Lx/2, wy/2). The X_c distribution plots on the thickness allowed to determine the depths of the weld joint zones (defined in Chapter 3, section 5.1). Table 4.5 shows the values of the weld joint HAZ depths obtained for the 4 laser powers simulated. They are compared with the values obtained experimentally (ref. Figure 21, Chapter 3, Section 5.1). The depths of the HAZ are the ones of the semi-crystalline layer (scL), molten layer in PEKK-A2 (ML-A) and molten layer

in PEKK-SC (ML-SC). A good approximation of the simulated values is found with the experimental results obtained. When increasing the laser power, the HAZ depths increase. However, some of them are over estimated, like the ones of the ML-SC, which reached the maximum depth obtained experimentally, but on the PEKK-A4/SC assemblies. Further work must be done to better predict those depths, like increasing the grid points on the samples thickness to improve the calculations.

4.5 Synthesis

The laser transmission welding process of two overlapped PEKK parts was simulated in this chapter. The aim was to reproduce the results obtained experimentally with respect to the morphology of the weld joint when PEKK parts were welded. Focus was put on achieving the simulation of the crystallinity evolution of the weld joint during irradiation and cooling. Therefore, the modeling process and path followed to arrive there was detailed in this chapter.

In the first part, a remainder of the equations and models governing the LTW process was given. Those models were also narrowed and better detailed for the present study, such as energy absorption by the upper part. modeling assumptions were included to restrict the models in the simulations. Then, a brief explanation on the approach used to solve the different equations, the finite difference method, was made. The definition and discretization of space and time domains, as well as the equations to solve, was explained. Finally, the modeling process was detailed step by step, as well as the evolution and changes made until reaching the final objective for the simulation. Changes were made when studying the laser irradiation process, the temperature field development during irradiation, the melted zone generated, as well as the crystallinity field evolution. This modeling process allowed to successfully predict the weld joint morphology and crystallinity of the PEKK-A2/SC assemblies.

Modeling the LTW process by finite difference method on PEKK parts allows to better understand the complex mechanism of crystallization observed during welding experiments. The possibility of predicting the weld joint morphology depending on material properties and process parameters is demonstrated with the simulations developed.

Chapter 5

Welding PEKK composite by LTW

Contents

5.1 Introduction 156
5.2 The PEKK composite material 157
5.2.1 PEKK grade 80/20 157
5.2.2 PEKK-carbon fibers samples 157
5.2.3 Material properties 157
5.3 Welding set-up for PEKK composite 159
5.3.1 Laser-material interaction tests 159
5.3.2 Welding parameters for LTW of PEKK-A/CF 160
5.4 PEKK-A/CF weld joint properties 163
5.4.1 Morphological properties 163
5.4.2 Mechanical properties 169
5.5 Synthesis 171

5.1 Introduction

The present chapter describes the study made on laser transmission welding process of PEKK composite material. The composite samples destined to be welded are PEKK 8010 plates filled with 30 % short carbon fibers (CF), named PEKK-CF for the study. Until now, no studies have been found in the literature for welding PEKK carbon fiber samples by LTW. However, some studies have been performed on LTW of PEEK CF samples [Vacogne and Wise, 2011, Liu et al., 2022, Korycki et al., 2022], semi-crystalline thermoplastic from the same family as PEKK (ref. Chapter 1, Section 4). *Vacogne and Wise* welded amorphous PEEK films of 300 microns to PEEK with long carbon fiber films of 175 microns [Vacogne and Wise, 2011]. *Liu et al.* studied the LTW process between PEEK resin and unidirectional carbon fiber reinforced PEEK using 0.2 mm thick films for both samples [Liu et al., 2022]. *Korycki et al.* welded 1.2 and 4 mm thick PEI to 1 mm thick carbon fiber PEEK. In all of those studies, the carbon fiber PEEK samples were used as the lower absorbent part for the LTW process [Korycki et al., 2022]. Hence, to achieve laser transmission welding of carbon fiber composite samples, they must be welded with an amorphous or semi-transparent thermoplastic sample on the top. As a consequence, for the present study, PEKK-CF samples are welded to PEKK-A ones in an overlapped configuration where the PEKK-A is placed over the PEKK-CF. This assembly configuration is named "PEKK-A/CF" for the study. PEKK-CF plates are provided by Arkema company in 2 mm thick. PEKK-A injected plates are obtained in 2 and 4 mm thick, named PEKK-A2 and PEKK-A4, respectively (ref. Chapter 2, Section 3). Therefore, two assembly configurations are studied: PEKK-A2/CF and PEKK-A4/CF.

Before welding, a laser-material interaction (LMI) campaign is carried out on the PEKK-A/CF overlapped configuration. The LMI tests allowed to define the process weldability window for LTW of PEKK-A/CF. Then, the welding parameters for the study concerning the scanning speed and laser power are delimited from the LMI test and process window defined. Three different laser intensities are studied to irradiate the assemblies interface: 12 W (P1), 18 W (P2), and 24 W (P3). Welding is made at a constant speed of 10 mm·s^{-1} with a beam diameter of 6 mm. Five welds are made per assembly type and power to compare those welding parameters influence on the weld joint quality. The irradiated zones of post-welded assemblies are observed under microscope through the PEKK-A sample to characterize the shape and dimensions of the weld joints. Then, all assemblies are tested mechanically by single lap shear (SLS) test. The mechanically failed assemblies are inspected visually to identify their failure type from the definitions made on Chapter 3, Section 4.1. Most of the PEKK-A/CF assemblies failed at the PEKK-CF bulk, adjacent to the weld joint. This type of failure is called "substrate near joint (SNJ)", as defined in Chapter 3, Section 4.1. However, PEKK-A2/CF assemblies welded with P3 failed inter-facially (on these assemblies, the irradiated zone burned when welding). The post-failed SNJ assemblies were used to study the weld cross-section along the weld path under microscopy. A relationship between welding parameters and weld joint quality is established in this study for PEKK-A/CF LTW welded assemblies.

5.2 The PEKK composite material

5.2.1 PEKK grade 80/20

As mentioned in Chapter 2, PEKK is synthesized from diphenyl ether (DPE) and terephthaloyl chloride (T) and/or isophthaloyl chloride (I). The T/I ratio can be modified in PEKK, generating the different PEKK copolymers. PEKK grade 80/20 indicates an 80 % of terephtalic acid combined with a 20 % of isophtalic acid in PEKK. This PEKK grade is the highest commercialized for the industry and is typically used for injection and extrusion. PEKK 80/20 is the grade of PEKK with the highest crystallization kinetics and transition temperatures, compared to the 60/40 and the 70/30 grades [Quiroga Cortés et al., 2016].

5.2.2 PEKK-carbon fibers samples

PEKK 80/20 can be combined with short carbon fibers by injection molding to create composite samples. For this study, the composite samples used were injected and provided by Arkema company from the KEPSTAN®PEKK 8010C30 compound. PEKK 8010C30 is a carbon fiber reinforced compound based on the PEKK resin 8010 combined with a 30 % of mass load of short carbon fibers. The injected plates are square with a dimension of 90 × 90 mm^2 and a thickness of 2 mm. The coloration of the samples to the visible like is black, do to the high content of carbon fibers. These square plates are cut into rectangular samples of 2.5 mm width to obtain the samples for welding. The KEPSTAN®PEKK 8010C30 injectes samples will be named PEKK-CF from now on.

5.2.3 Material properties

The technical data sheet of the material provide some important properties for the LTW process [Arkema, 2023], summarized in Table 5.1. It is also indicated that the samples must be dried at 120°C for at least 6 to 8 hours before processing.

Property	**Unity**	**Value**
Density (ρ)	[kg·m^{-3}]	1800
Specific heat (C_p)	[J·kg^{-1} · K^{-1}]	840
Thermal conductivity (k)	[W·m^{-1} · K^{-1}]	8.36

Table 5.1: KEPSTAN®PEKK 8010C30 properties from technical data sheet [Arkema, 2023].

For the LTW welding process, it is also important to know the samples thermal transitions. In this case, the thermal transitions of the PEKK-CF injected plates are characterized by DSC, as for the PEKK-A and PEKK-SC samples. DSC tests were carried out in a DSC Mettler Toledo with samples weighting around 10 mg. Ramps of 10 K/min are used for

heating from 100°C to 420°C and cooling from 420°C to 100°C. Glass transition and melting temperatures are obtained on the first heating. Melt crystallization temperature is obtained on cooling. Figure 5.1 shows a typical DSC thermogram of the PEKK-CF samples. The first heating shows a glass transition temperature around 160°C and a melting peak around 360°C. No cold crystallization peak is observed on this curve, indicating that the samples are fully crystallized in their natural state after injection. The cooling ramp shows the melt crystallization peak around 310°C.

Table 5.2 summarizes the transition temperatures collected from the DSC curves for PEKK-CF and compared with the data from the PEKK 7002 plates (PEKK-A2, PEKK-A4 and PEKK-SC). As is noticeable, PEKK-CF samples have higher temperature values in their thermal transitions, compared with the PEKK 7002 amorphous and semi-crystalline samples. This is due to the PEKK grade used as resin for the PEKK-CF composite plates, the 8000, which has a higher T/I ratio than the 7002 grade. As already proven by *Gardner et al.* [Gardner et al., 1992] and *Quiroga Cortés et al.* [Quiroga Cortés et al., 2016], increasing the T/I ratio of PEKK increases the melting temperature and even the glass transition temperature.

PEKK	**CF (8010C30)**	**A2 (7002)**	**A4 (7002)**	**SC (7002)**
Tg [°C]	160	151	152	160
Tcc [°C]	-	204	205	-
Tm [°C]	360	337	336	338
Tcm [°C]	310	285	286	284
Thick [mm]	2	2	4	2
Color	Black	Yellow	Yellow	Beige/White

Table 5.2: PEKK injected plates thermal transitions characterized.

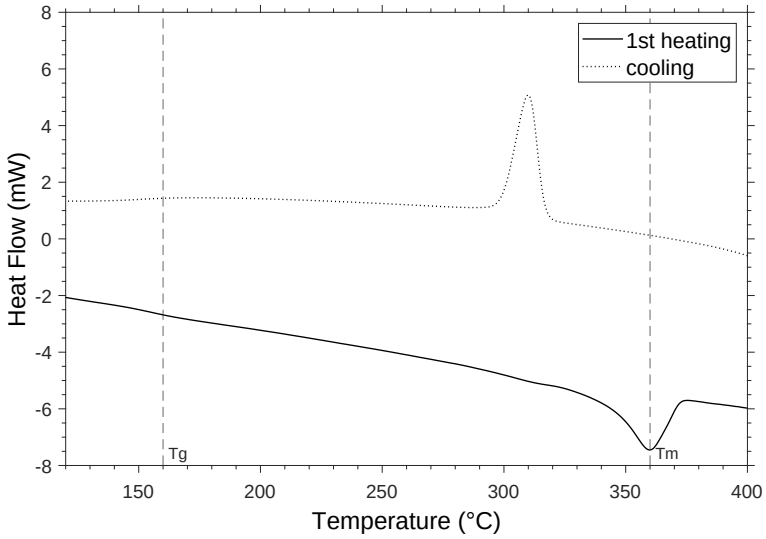

Figure 5.1: Typical DSC thermogram of PEKK-CF injected plates.

5.3 Welding set-up for PEKK composite

5.3.1 Laser-material interaction tests

The welding parameters used for welding PEKK-A/SC (ref. Chapter 3) are inappropriate for welding PEKK-CF. The laser power intensity is so high that the material burns directly when the laser irradiates its surface, even when testing the lowest power with a higher speed of 100 mm·s^{-1}. For this reason, laser-material interaction (LMI) tests were necessary to find the suitable operation points, the ones susceptible to allow welding. These operation points must heat the irradiated surface enough to allow the material to melt.

Static and dynamic irradiation were studied for the LMI tests. Static irradiation was carried out on the surface of the PEKK-CF sample. Dynamic irradiation was applied at the interface of the PEKK-A2/CF assembly type. Two process parameters were tested: the irradiation time and the power intensity to irradiate the sample's defined surface. The irradiation time was established in seconds for static tests and as welding speed for dynamic tests. The irradiated zone was visually observed to confirm the operation points. The parameters are confirmed if:

- They leave a mark on the irradiated zone
- The samples stay together after irradiation
- It isn't easy to separate the welded samples by hand

The limits of the process parameters range on which the samples are susceptible to be welded are defined by:

1. A visual alteration of the sample surface at the irradiated zone. This alteration indicates heat affectation by the laser, which could show the beginning of the polymer glass transition.
2. If the irradiated zone presents signals of burning or degradation. This can be noticed when the irradiated zone shines. Or after irradiation, if the irradiated zone has a lot of irregularities. Or after separating the weld, if the irradiated acquired a brown or black coloration.

The LMI tests allowed to define a process window for welding PEKK-A/CF by LTW, shown in Figure 5.2. Three zones of processability were defined from the combination of laser power and welding speed values. The zones are: no-welding, welding, and burning. The no-welding zone goes from zero power to the values of power shown in blue and indicated for each laser scanning speed. This zone designates the process parameters combination that does not achieve to create a weld. That can be caused by a lack of or shallow thermal interaction of the laser with the samples at the interface. The burning zone begins at the red points

and can go until the maximum values possible. The values of this zone generate material burning when irradiating the interface. Then, the welding zone is between the non-welding and the burning zones, identified by the values in green. This zone indicates the power and welding speed values that can melt the materials at the interface without burning. Power and welding speed values must be selected within this green zone to achieve welding. Table 5.3 represents a combination of process parameters selected from the green zone. A power-value range (P-range) is shown within the green welding zone for a specific welding speed. These power ranges differ for each welding speed.

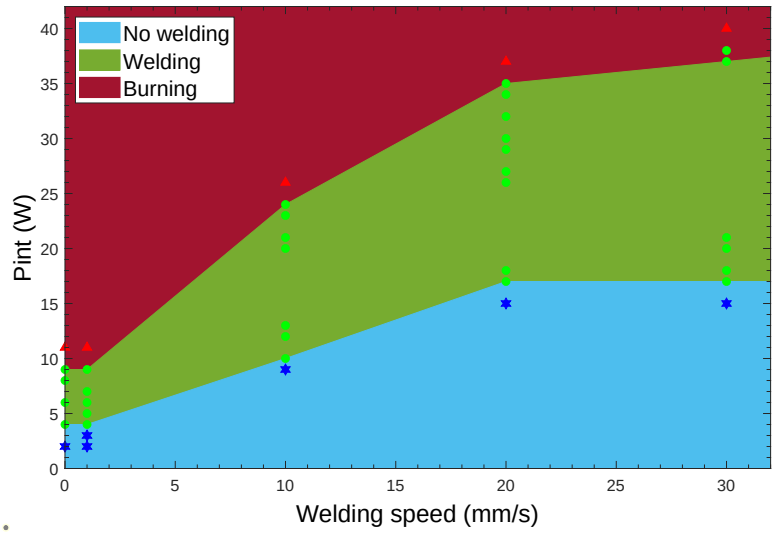

Figure 5.2: Process window for welding PEKK-A/CF by LTW.

V ($mm{\cdot}s^{-1}$)	P-range (W)
10	10 to 24
20	15 to 35
30	17 to 38

Table 5.3: Power range (in Watts) that allows material melting at the irradiated zone for a fixed welding speed ($mm{\cdot}s^{-1}$).

5.3.2 Welding parameters for LTW of PEKK-A/CF

The same welding machine ES weld 200 from ES Laser is used for LTW of PEKK-A/CF samples. Samples for welding are cut from the injected plates with dimensions of 95 x 25 mm^2. PEKK-A sample is welded over the PEKK-CF sample in lap-joint configuration. This configuration was used to test the assemblies in single lap shear (SLS) test for the mechanical characterization. An overlap of 12.5 mm is used, as indicated on ISO 4587:2003. For welding, the laser irradiates the center of the overlap area from Lo to Lw. Configuration for welding with the irradiated zone is shown in Figure 5.3.

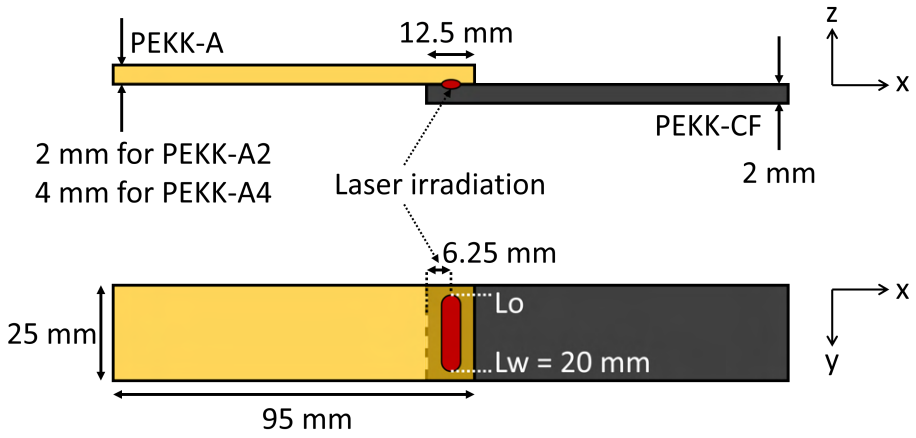

Figure 5.3: Assembly configuration for welding PEKK-A/PEKK-CF. Schematic representation not to scale.

A second LMI campaign showed that the welding speed of 10 mm·s^{-1} and its corresponding power-range (from Table 5.3) generated larger and regular heat-affected zones (HAZ). From visual inspection, they were considered better than the ones generated by the 20 and 30 mm·s^{-1} speeds. Because of that, the welding speed of 10 mm·s^{-1} was selected as the fixed parameters for the study. Then, three power intensity values were chosen from its power-range (indicated in Table 5.3). The minimum, maximum, and medium values of the power-range were chosen for the study (12, 18 and 24 W, respectively). These power values were used to irradiate the interface of each assembly (Pint).

As seen on Chapter 3 for PEKK-A/SC assemblies, to irradiate the interface of the PEKK-A/CF assemblies the output laser power (Po) will first go through the clamping glass and then through the PEKK-A semi-transparent part, as shown in Figure 5.5. Therefore, the output laser power value will decrease after going through each upper component, according to the transmission factor of each one. Hence, the power reaching the assembly interface will be the percentage of output power that the glass and the semi-transparent part will allow to transmit. At our laser wavelength (975 nm), the clamping glass has a transmissivity of 83 %, as evaluated with the power-meter. Then, the transmission factor of the transparent-upper substrate depends on its thickness: 75 % for PEKK-A2, and 62 % for PEKK-A4, as charactereized in Chapter 2, Section 4.3. Figure 5.4 shows the transmission spectra obtained for PEKK-A plates in Chapter 2. Thus, the power at the interface (Pint) can be calculated using Equation 5.1 and Equation 5.2 for PEKK-A2/PEKK-CF and PEKK-A4/PEKK-CF, respectively. Table 5.4 indicates the output laser power value (Po) necessary to use for each assembly type (A2/CF and A4/CF) to obtain the same power value at the interface (Pint).

$$P_{int(A2)} = P_o \times 0.83 \times 0.75 \tag{5.1}$$

$$P_{int(A4)} = P_o \times 0.83 \times 0.62 \tag{5.2}$$

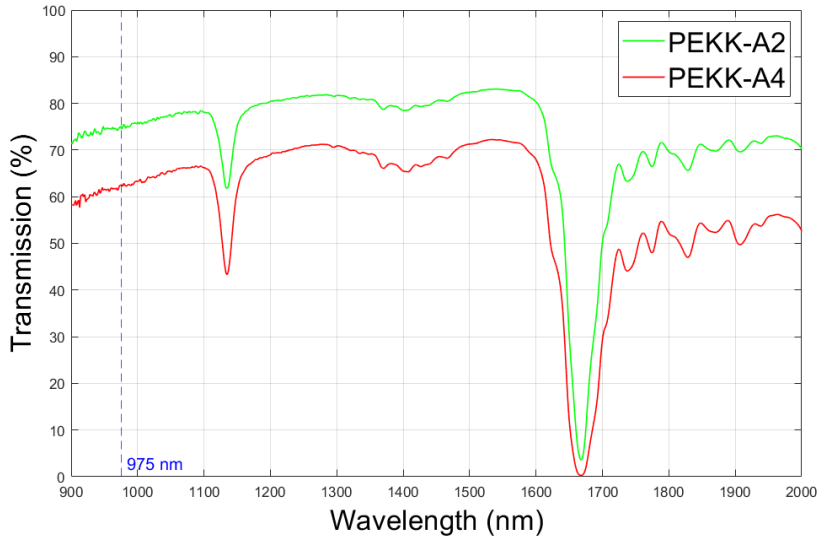

Figure 5.4: Transmission spectra of PEKK 7002 amorphous injected plates. Vertical line indicates the wavelength of interest at 975 nm.

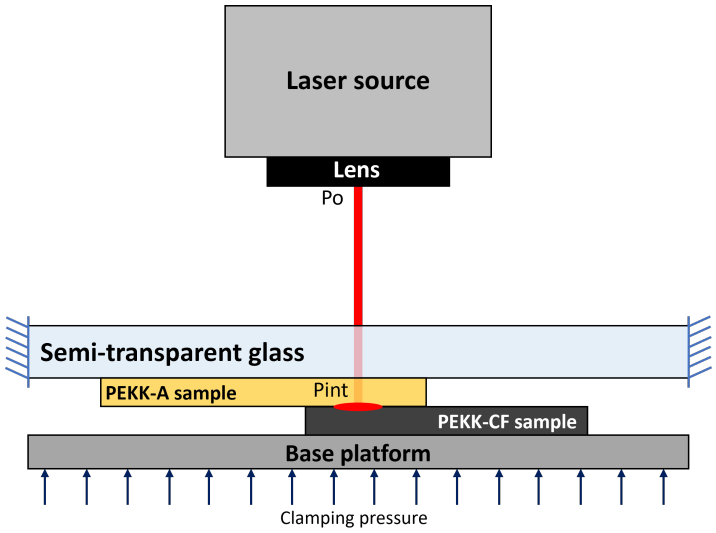

Figure 5.5: Laser welding set-up with power transmission. Schematic representation not to scale.

	Po [W]		Pint [W]
	For A2/CF	**For A4/CF**	**For both**
P1	19.4	24.5	12
P2	29.5	34.6	18
P3	39.4	47	24

Table 5.4: Laser power used for LTW.

5.4 PEKK-A/CF weld joint properties

5.4.1 Morphological properties

The welds were visually inspected with a numerical optical microscopy VHX-6000S from Keyence. The overlapped zone of post-welded assemblies was observed from above the PEKK-A sample. The weld joint heat-affected zone (HAZ) was visible through the PEKK-A sample at the interface. Those visualizations were made to characterize the shape and dimensions of the weld joint HAZ developed at the interface. The cross-section of post-failure assemblies was observed to characterize the weld along the welding path.

Figures 5.7, 5.8 and 5.9 show the micrographs of the irradiated zones observed through the PEKK-A upper sample for each welded assembly generated. A representative weld-joint HAZ for each assembly created is observed in Figure 5.10 for comparison. The weld joints obtained on the PEKK-A2/CF assemblies have a comet shape, with their width increasing in length. On the PEKK-A4/CF assemblies, the weld joints have a more constant width along their length. For these assemblies, it is also notable how the weld joint increases in width and length with power. The weld joint area observed for 12 and 18 W in both types of assemblies is mainly black and homogeneous. At P3 (24 W), the weld joint area is less homogeneous, showing some yellow areas inside it, especially on the PEKK-A2/CF assembly. Those yellow areas can indicate the presence of voids in the weld joint. Those voids were possibly generated by material burning during irradiation, creating a lack of welding at the affected zone.

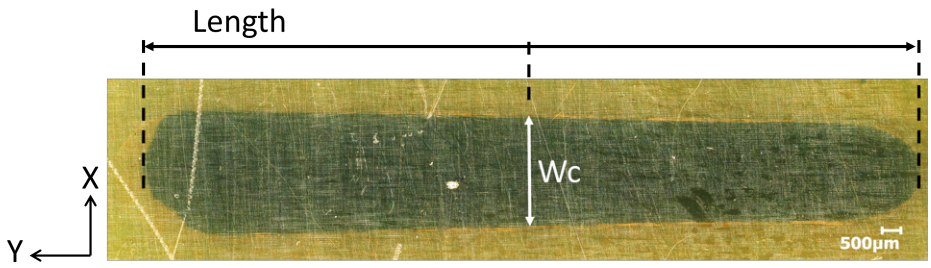

Figure 5.6: Representation of the weld joint HAZ dimensions on PEKK-A/CF-P1 post-welding assembly. Observation made at the interface through the PEKK-A sample.

The dimensions of the weld joint were measured as shown in Figure 5.6. The weld length (Lw) corresponds to the maximum length of the HAZ observable in the Y-axis. The weld width (Wc) is the width measured on the X-axis at the center of the weld joint length. The HAZ area was obtained by multiplying the weld length and width for each weld joint.

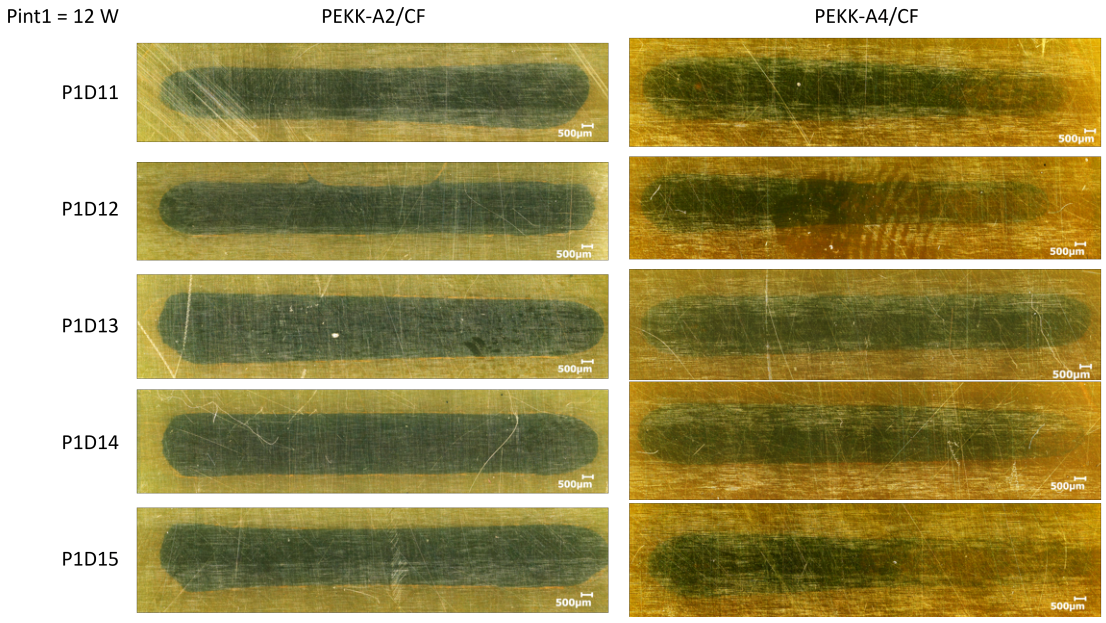

Figure 5.7: Optical micrographs of PEKK-A/CF assemblies welded with P1.

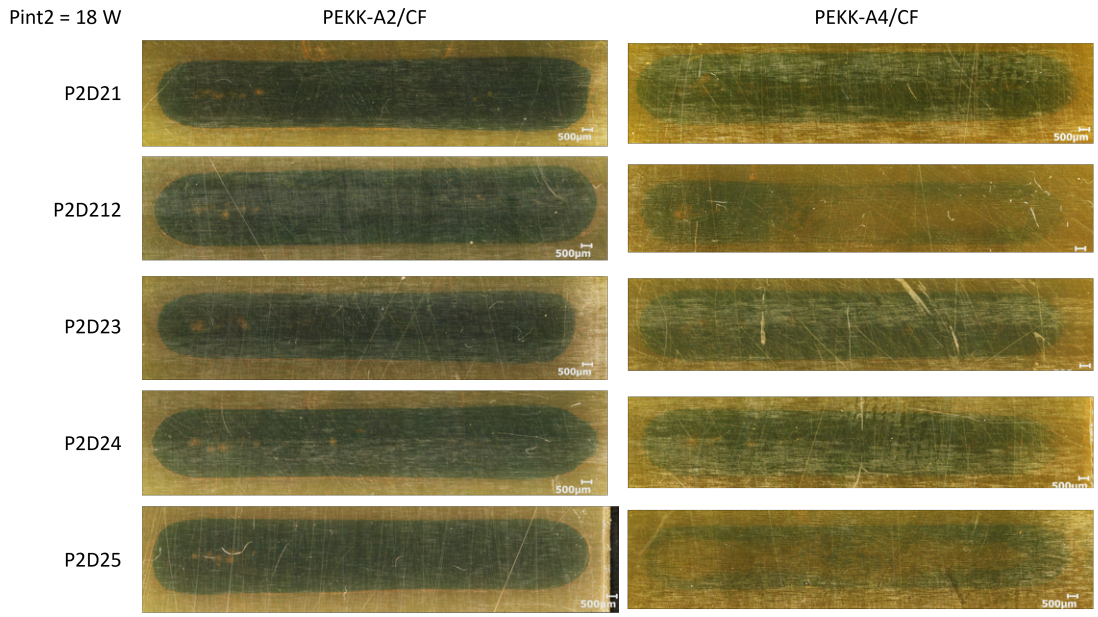

Figure 5.8: Optical micrographs of of PEKK-A/CF assemblies welded with P2.

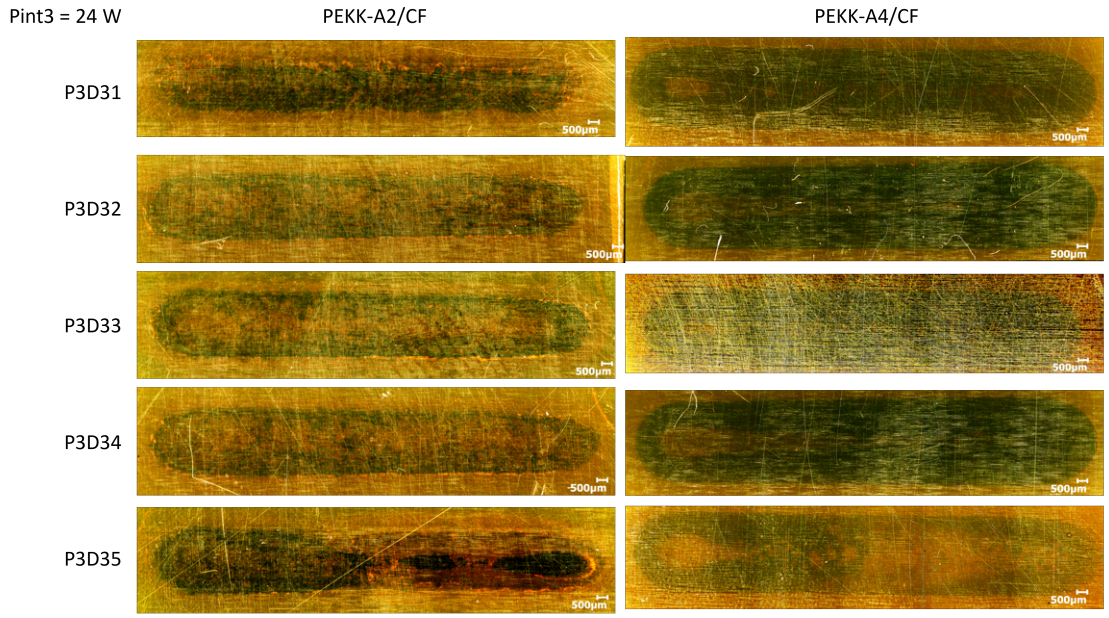

Figure 5.9: Optical micrographs of of PEKK-A/CF assemblies welded with P3.

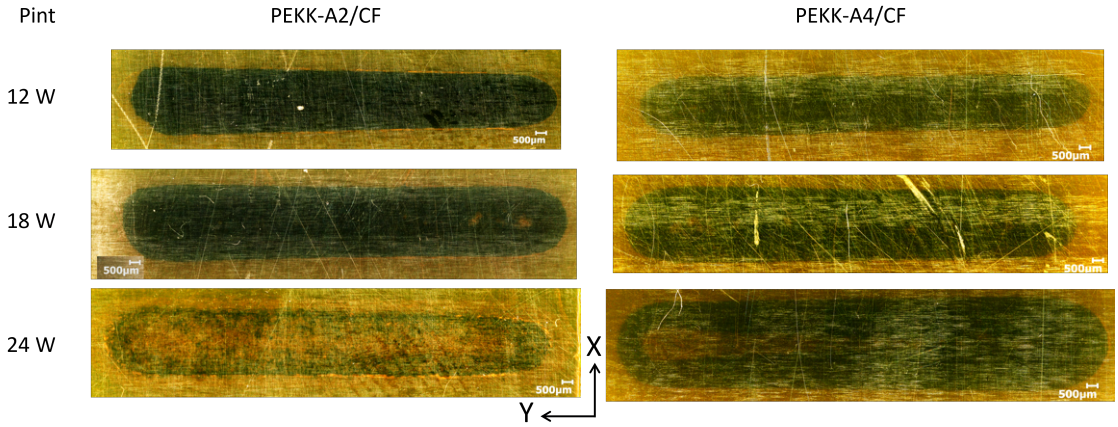

Figure 5.10: Optical micrographs of representatives weld-joints HAZ of post-welding assemblies for each weld combination. Observations were made at the weld interface through the PEKK-A sample. Images were treated differently to allow a better visualization of the HAZ.

The dimensions measured of the weld joints were plotted with the power used for welding. The length of the welds is plotted for each power in Figure 5.11(a). Globally, the weld length increases with power. For PEKK-A4/CF, the weld length increases linearly with power, from 21 mm at P1 to 23.1 mm at P3, an increment of 10 %. In PEKK-A2/CF assemblies, the weld length increases by 6 % from P1 to P2, going from 21.2 to 22.5 mm. Then, it decreases by 5 % from P2 to P3. It can also be noticed that the lengths of the PEKK-A2/CF welds are 1 % longer than the PEKK-A4/CF welds for each power (without considering P3). Nevertheless, the weld lengths obtained are longer than the initial welding path length of 20 mm. This

could be related to a possible scattering of the laser beam by the fibers inside the PEKK-CF sample.

Figure 5.11(b) plots the weld width with power. As for the length, the width increases with power for both types of assemblies, except at P3 for PEKK-A2/CF, when it decreases. For PEKK-A4/CF, the weld width increases linearly from 2.6 to 4.1 mm, an increment of 60 %. For PEKK-A2/CF, the width begins to increase 30 % from P1 to P2, going from 2.7 to 3.6. Then, it drops 22 % at P3. However, the width obtained on all the welds is smaller than the beam diameter of 5 mm that was used for welding. This could be derived from the fact that the laser beam has a Gaussian profile. A Gaussian beam propagation indicates that the peak irradiance is localized at the center of the beam spot. Moreover, the relative irradiance decreases from the center to the edge of the beam spot. So, the irradiance differs inside the beam area. This can decrease the real irradiated zone, which differs for each power intensity applied.

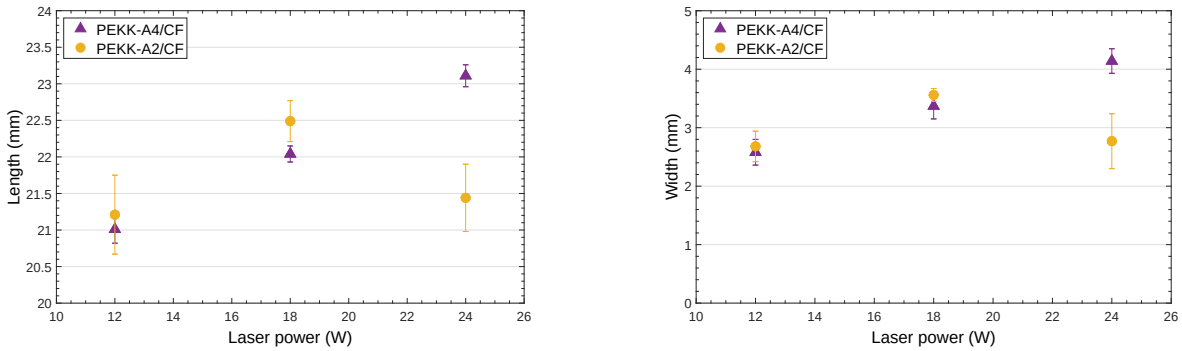

(a) (b)

Figure 5.11: Weld joints HAZ dimensions plotted with the power used for welding: (a) maximum length of the weld and (b) width at the center of the weld length. Error bars indicate standard deviation [1].

The weld joint HAZ areas calculated are plotted against power in Figure 5.12. As for the weld length and width, the weld joint areas increase linearly with the power used for welding, except for P3 in PEKK-A2/CF, where it drops. For PEKK-A4/CF, the area increases from 54.2 mm^2 to 95.7 mm^2, an increment of 77 % from P1 to P3. On PEKK-A2/CF assemblies, the area increases by 38 % from P1 to P2, going from 56.7 mm^2 to 80 mm^2. Then, it drops by 26 % from P2 to P3.

[1] From 5 welded assemblies characterized per parameter (for PEKK-A2/CF and PEKK-A4/CF P1, P2 and P3).

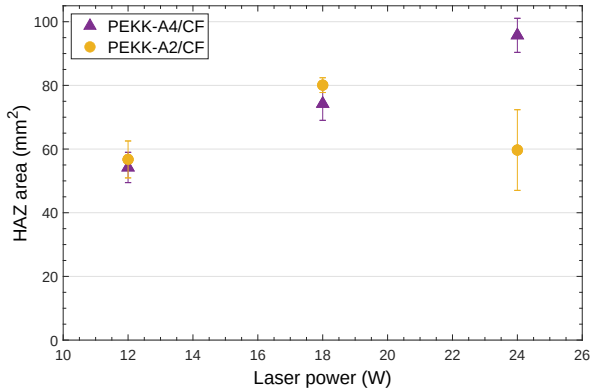

Figure 5.12: Weld joints HAZ area plotted against the power used for welding. Error bars indicate standard deviation[2].

The weld joint cross-section was characterized along the weld path. Cross-sections of the weld joint were obtained from the post-failed assemblies. One cross-section was studied for each assembly combination made. Visualizations were made by transparency, applying a gray scale filter. Figure 5.13 shows the differences between visualizing the sample with the (a) accurate color approximation and the (b) grayscale filter. When applying the filter, the PEKK-A yellow sample turns gray, which allows better observation of the PEKK-CF sample (in black). This is more notorious when visualizing the details at the interface line between the samples.



(a) (b)

Figure 5.13: Weld joint cross-section along the weld path of PEKK-A2/CF-P1 assembly. Observations made with (a) the accurate colors of the samples, (b) at gray scale.

Figure 5.14 shows a representative weld cross-section of the assemblies with its details. At the borders of the cross-section (Figure 5.14(b1) and (b2)), it can be noticed how, at some point, the PEKK-CF sample enters into the PEKK-A sample at the interface (indicated by the white arrows in the Figure). A thin polymer layer from the PEKK-CF sample appears to merge with the PEKK-A sample at the interface, allowing the fibers to go inside the PEKK-A sample within this thin layer. This phenomenon is more notorious in Figure 5.14 (c1.1) and (c1.2), where carbon fibers can be seen randomly oriented, with an inclination from the interface. Here, bubbles are also visible in the weld depth.

[2]From 5 welded assemblies characterized per parameter (for PEKK-A2/CF and PEKK-A4/CF P1, P2 and P3).

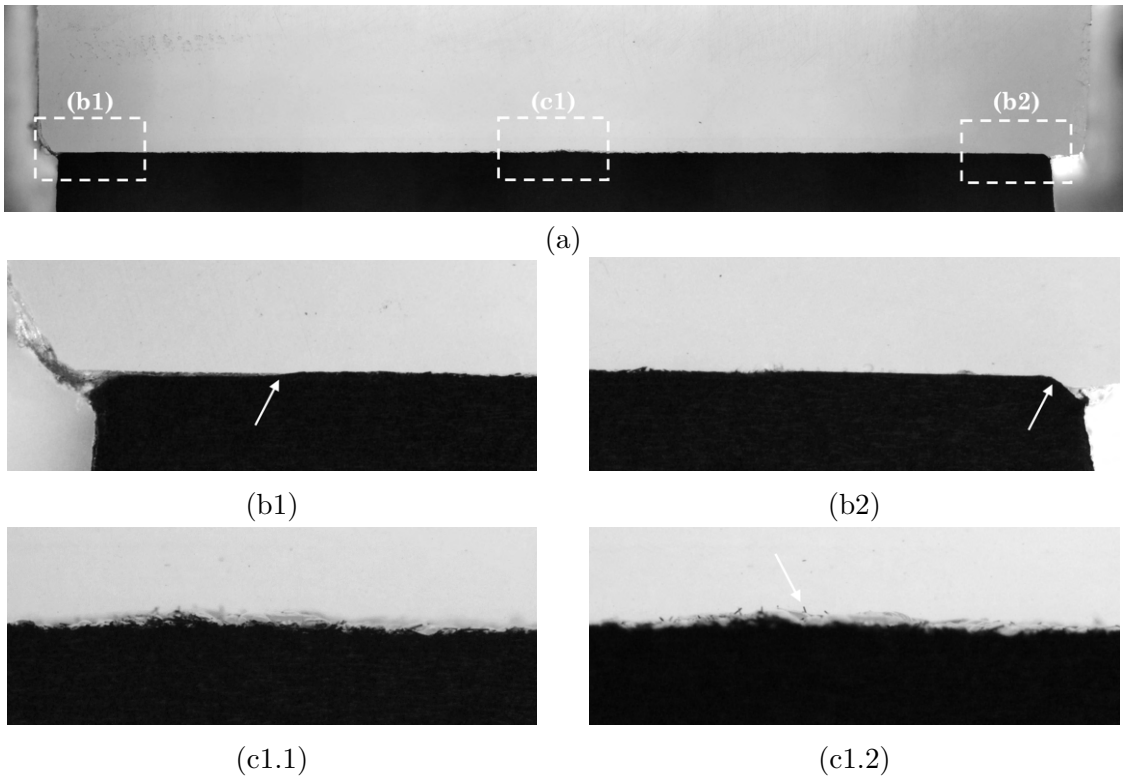

Figure 5.14: Weld joint cross-section and details of PEKK-A4/CF-P2 assembly. (a) Whole cross-section along the weld path. Details at the borders: (b1) left border, end of the weld; (b2) right border, weld starting point. Details at center: (c1.1) focusing on the cross-section surface, (c1.2) focusing on the cross-section depth.

Figure 5.15 shows a visualization of the depth of the weld-cross section center. This micrograph allows to identify the short carbon fibers detached from the PEKK-CF sample and oriented randomly into the PEKK-A sample. It is also visible how bubbles were developed at the weld joint because they appear to be all along the depth. The visible bubbles seem to have a micrometric size, not more significant than the short fibers from the PEKK-CF sample. Other studies also show the apparition of bubbles at the weld joint. They mainly attributed it to the lack of sample drying before welding. However, in the present study, the samples were dried for more than 8 hours before welding, and that drying time allowed all the moisture to evaporate from the samples. Here, bubbles could be generated by the evaporation of the solvent used to clean the samples before welding (acetone) that remained in the sample surface, as theorized by Amanat et al. when welding PEEK films with Clearweld [Amanat et al., 2010]. Another possible explanation could be that the shortest polymeric chains are vaporized under the high heating ramp caused by laser irradiation when welding. This phenomenon can generate air bubbles at the weld joint, as attributed by Ussing et al. when welding PETG to join micro-parts [Ussing et al., 2007].

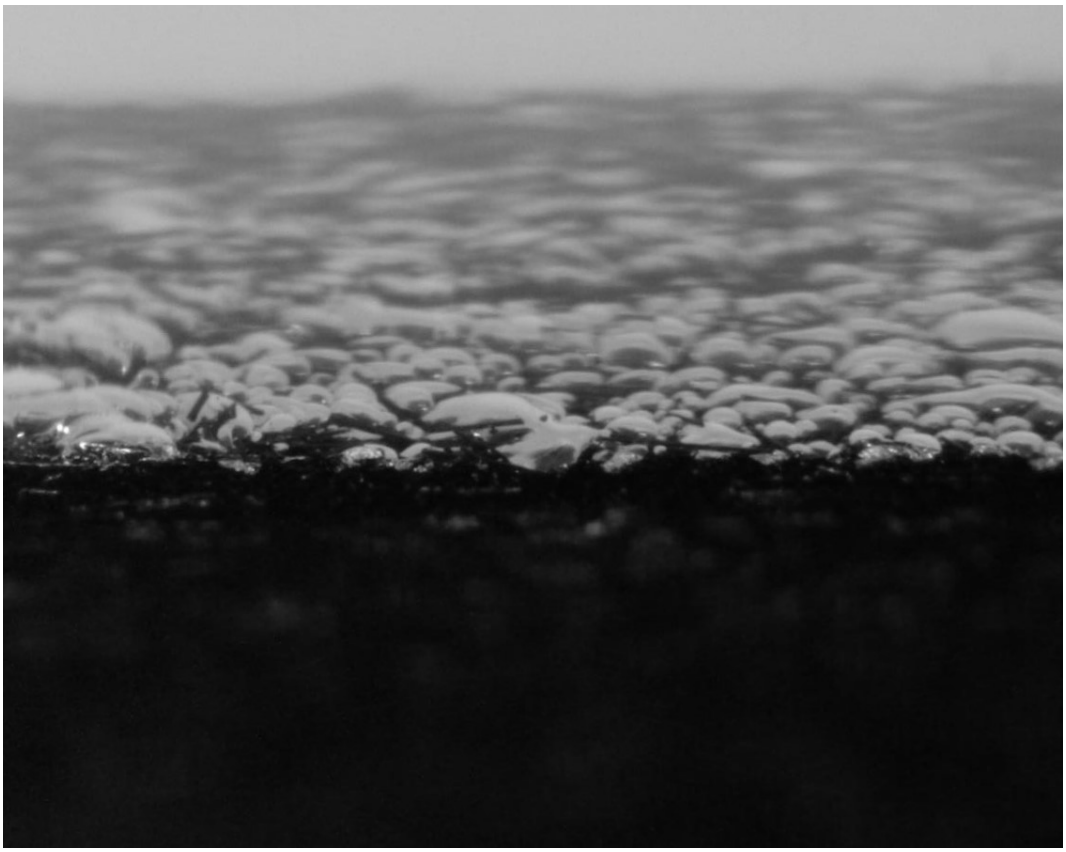

Figure 5.15: Micrograph of the weld joint interface line observed in the depth.

5.4.2 Mechanical properties

Welded assemblies were tested in single-lap shear mechanical tests to quantify the weld strength. An INSTRON 550R tensile machine was used with a load cell of 50 kN and a cross-head load rate of 2800 $N \cdot min^{-1}$. Five assemblies are tested for each welding parameter (upper part thickness and laser power). Each assembly was tested until failure, and the force at failure Ff [N] was recorded. The normalized lap-shear strength LSS [MPa] was obtained by dividing the force at failure by the contact area Ac [mm^2]. The Ac used was the HAZ area calculated with the length and width measured by microscopy.

Post-failed assemblies were inspected to identify their failure type. The failure type was chosen from the "Failure types definitions for LTW assemblies tested by SLS" made when welding PEKK-A/SC samples (ref. to Table 13 from Chapter 3, Section 4.1) The failure type obtained in most of the PEKK-A/CF assemblies tested was "substrate near joint" (SNJ). This type of failure indicates that the bulk sample breaks at the limit of the weld joint generated. In all the SNJ failed assemblies, the substrate that failed was the PEKK-CF sample. Interfacial failure was obtained on the PEKK-A2/CF assemblies welded with P3.

Figure 5.16 shows the mean force at failure obtained for each assembly combination. As

for the weld dimensions, the Ff increases linearly with power on the PEKK-A4/CF assemblies. Meanwhile, for the PEKK-A2/CF assemblies, the Ff increases from P1 to P2, then drops at P3. The higher value of Ff obtained for both types of assemblies is reached in P2, being 2.4 kN for A2/CF and 1.9 kN for A4/CF.

The failure forces obtained were used to calculate the LSS for each assembly, which gives the assembly strength. For both types of assemblies, the strength increases from P1 to P2, where the maximum LSS value of 25 MPa is achieved. Then, it decreases from P2 to P3. This decrement is different for each assembly type. For PEKK-A4/CF, the decrement is low, of 9 %. Whereas for the PEKK-A2/CF assembly, the decrement is higher, of 63 %. The strength obtained in both types of assemblies is similar for P1 and P2. The difference between both types of assemblies is less than 10 % : 1.64 MPa at P1, and 0.1 MPa at P2. For the P3, the difference in strength is higher: 13.57 MPa.

The PEKK-A2/CF assemblies welded with P3 experienced low burning during irradiation. That phenomenon did not allow the weld generation between the samples. Not real inter-diffusion occurred at the interface when welding. In contrast, interfacial adhesion occurred between the samples. The interfacial adhesion allowed the samples to stay together at the interface but were easily split. No high load was needed to separate them in the mechanical tests (0.7 kN was recorded as the maximum force at failure in one assembly from the SLS tests). Those assemblies separated easily, even by hand. Moreover, the type of failure obtained was interfacial. All of the last mentioned can explain the low dimensions, force, and LSS values on the PEKK-A2/CF-P3 assemblies.

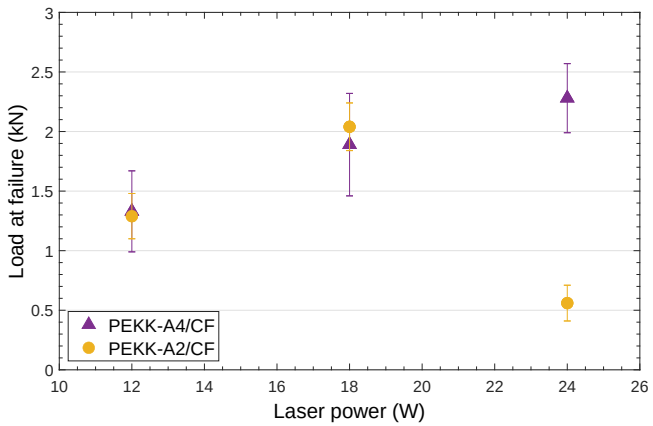

Figure 5.16: Mean force at failure values plotted with the power used for welding for each assembly type. Error bars indicate standard deviation[3].

[3]From 5 welded assemblies tested per parameter (for PEKK-A2/CF and PEKK-A4/CF P1, P2 and P3).

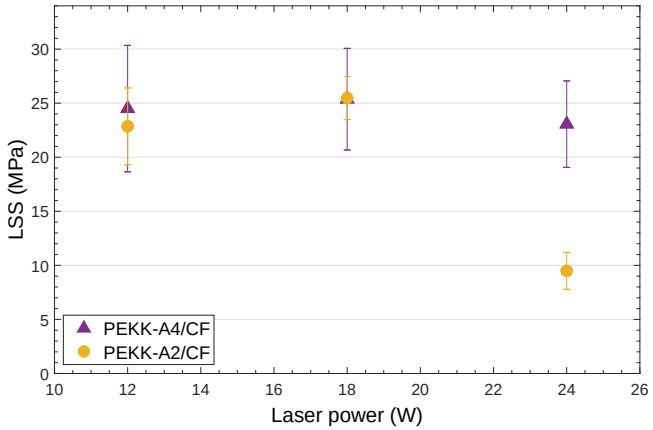

Figure 5.17: Mean lap-shear strength values plotted with the power used for welding for each assembly type. Error bars indicate standard deviation[4].

5.5 Synthesis

This chapter focused on studying the joining process of PEKK composite parts by laser transmission welding. Injected plates of PEKK 80/20 filled with 30 % of short carbon fibers were welded to amorphous PEKK plates on a amorphous/composite (PEKK-A/CF) configuration. Before welding, laser-material interaction tests were carried out to define the assembly process window for LTW. The process window defined the combination of welding speed and power to irradiate the assembly interface that generates welding, non-welding, and burning. Then, from the defined weldability window, welding parameters were chosen to be studied. Three laser powers were selected to irradiate the interface (12, 18 and 24 W) at a scanning speed of 10 mm·s^{-1}. These laser powers were combined with two thicknesses of the semi-transparent upper part, 2 and 4 mm. Therefore, 6 assembly combinations were tested, which allowed to study the influence of process parameters on the weld joint quality. The welded joints were characterized in terms of morphology and strength. The assemblies were observed under optical microscopy and tested by single-lap shear mechanical test.

The shape and dimensions of the weld joint HAZ were characterized by microscopy observation through the PEKK-A sample. Weld joint dimensions mainly increase with the power used for irradiation. The mean lengths of the weld joints are longer than the welding path length, attributed to the laser beam scattering by the fibers inside the PEKK-CF lower sample. On the contrary, the mean widths of the weld joints are thinner than the laser beam diameter used for welding, which is mainly attributed to the Gaussian irradiation profile of the laser beam. In addition, the HAZ has a quasi-homogeneous shape (concerning its dimensions) along the weld path. The weld joint cross-section along the weld path was also analyzed under a microscope. Bubbles appeared at the weld interface, and this phenomenon was attributed to possible solvent evaporation or material degradation.

[4]From 5 welded assemblies tested per parameter (for PEKK-A2/CF and PEKK-A4/CF P1, P2 and P3).

In the study it was observed that when welding PEKK-A2/CF assemblies with the maximum laser power defined for the study (24 W), the samples burned at the interface. Because of that, welding was not achieved; instead, a low interfacial adhesion was generated. This caused the development of a weld joint with shorter dimensions, non-homogeneous area, and with low mechanical properties.

The mechanical characterization of the assemblies allowed to conclude that high mechanical properties can be achieved on LTW assemblies made with amorphous over carbon-fiber PEKK plates. The values of LSS obtained on the welded assemblies were between 22 and 25 MPa. However, these strength values are still low compared to those obtained when welding PEKK amorphous over semi-crystalline plates. Values of LSS were obtained between 40 and 60 MPa on LTW of PEKK-A/SC (ref. Chapter 3 Section 3.5.2). Further work is necessary to explain the differences in strength and to improve the weld strength of PEKK-A/CF samples.

A potential explanation is that the presence of carbon fibers on the lower part reduces macromolecule mobility within the composite, limiting the number of macromolecules that may traverse the interface. Furthermore, PEKK grade 8000 may have shorter polymer chains and lower molecular weight, which causes less entanglement and decreases fracture strength. These factors most likely contribute to the decrease in weld strength in PEKK-A/CF assemblies observed in this study.

General conclusion & perspectives

Conclusion

This doctoral thesis presents the research made on the joining process of PEKK thermoplastic parts by laser transmission welding. As it was established in the introduction and from the literature review, welding is becoming an important assembling method for the joining thermoplastic materials in the industry. Welding provides many advantages compared to common assembly methods like mechanical fastening or adhesive bonding. Assembling parts by fusion bonding (welding) offer various benefits in terms of weight, material and costs savings.

One of the welding techniques that stands out due to its simplicity, precision, flexibility and ability to create joints of high quality is the laser transmission welding (LTW). However, it has been seen that LTW is a welding method with low research work when applied to high-performance semi-crystalline thermoplastics. One of the materials that has been less studied is the polyetherketoneketone (PEKK), from the polyaryletherketone (PAEK) family. PEKK material, compared to the polyetheretherketone (PEEK), shows better capabilities to be welded by LTW because of its possibility to control its crystallinity with the manipulation of the process parameters. Most studies on LTW of high-performance semi-crystalline thermoplastics have focused on PEEK, letting the path to PEKK as an area of opportunity. Therefore, this PhD thesis contributes to widening the knowledge on welding PEKK by LTW.

The objectives of this thesis project were focused on improving the LTW process of PEKK parts and on achieving to predict the weld joint properties. This prediction was intended to be related to material properties, welding parameters and the thermal history that the material undergone during the welding process. Experimental and numerical approaches were implemented to reach the objectives.

Firstly, **Chapter 1** established the basis of the laser transmission welding process, the importance of material properties and welding parameters, the physical phenomena associated in the process, and the relevant information for welding semi-crystalline thermoplastics, like PEKK. The aim of this chapter was to highlight the strengths and weaknesses of the process, and the areas of opportunity for research.

With the state of art, PEKK grade 70/30 (PEKK 7002 from Arkema, France) was chosen as material of study, thanks to its medium crystallization kinetics that allows for a better control of its crystallinity when processing it. Then, in **Chapter 2**, the fabrication and characterization of the PEKK 7002 parts allowed to obtain the appropriate samples to achieve the welding of PEKK material by LTW. In addition, the PEKK properties relevant for the laser transmission welding process (thermal and optical properties), were correlated to the crystallinity of the material.

Injection molding of the PEKK 7002 material allowed to obtain the samples for welding. And, by controlling the injection and cooling parameters, two different crystalline states of PEKK were obtained on the injected samples: a quasi-amorphous state (PEKK-A), characterized by its low crystallinity, and a semi-crystalline state (PEKK-SC), with a high crystallinity. PEKK-A samples were injected in 2 and 4 mm thick, named PEKK-A2 and PEKK-A4 respectively. PEKK-SC samples were obtained in 2 mm thick. The samples crystallinity and thermal transitions were characterized by DSC. The glass transition, melting, cold crystallization and melt crystallization temperatures were determined for each sample. This gave knowledge of the temperatures needed to be achieved on the welding process to achieve welding without damaging the samples.

The optical properties of the PEKK samples were characterized by spectrophotometry at the wavelength of the laser used for welding (975 nm), and for a laser beam that is directed perpendicular to the surface of the samples, as in LTW process. These properties were the transmissivity, reflectivity and absorptivity to the laser irradiation. This characterization allowed to validate the suitability of the PEKK parts for the feasibility of the LTW process. PEKK-A2 and PEKK-A4 samples are suitable to be used as upper part for the welding configuration, thanks to their transmissivity of 75 % and 62 %, respectively. A transmission factor of 60 % allows melting at the interface for LTW on PEKK parts [Villar et al., 2018]. Thus, the suitability of PEKK-SC sample as lower absorbent part for LTW is validated with its absorption factor of 32 %. An absorptivity of 30 % is high enough to achieve welding [Goyal et al., 2022]. Additionally, the optical properties were correlated with the degree of crystallinity of the PEKK material. When increasing the crystallinity of PEKK, the transmissivity decreases, but the absorptivity increases. For a same thickness (of 2mm), when the crystallinity (Xc) of PEKK is increased from 5 % to 24 %, the transmissivity decreases from 75 % to 20 %, and the absorptivity increases from 12 % to 32 %.

After validating the PEKK samples properties compatibility to the LTW technique, the LTW process of PEKK amorphous/semi-crystalline (PEKK-A/SC) parts is studied and optimized in **Chapter 3**. The appropriate welding parameters to achieve the assembly of PEKK parts by LTW were determined by laser-material interaction tests on the samples. Afterwards, some parameters were chosen to be studied to find the correlation between those parameters, material properties and weld joint quality. The studied parameters for welding were the thickness of the upper semi-transparent part (2 and 4 mm) and the laser power used to irradiate the interface of the assembly (from 75 to 95 W). The other process parameters, like the scanning speed (1 $mm{\cdot}s^{-1}$), beam diameter (6 mm), clamping pressure (3.8 MPa), etc., were kept fixed for the study.

The welded assemblies generated were analyzed in terms of morphology and mechanical properties. Morphologically, the weld joints were studied at their cross-section along the weld path. This cross-section was chosen to obtain better information of the weld joint properties all along its structure. It was seen that the thermal gradients and kinetics of the welding process generated an anisotropic heat affected zone (HAZ) in terms of crystallinity. The PEKK-SC sample turned amorphous after melting, whereas the PEKK-A undergone cold crystallization over the melted zone. The length and width of this HAZ were seen to increase

with laser power and with the thickness of the transparent substrate.

The mechanical properties of the PEKK-A/SC welded assemblies were characterized through single-lap shear test. All the assemblies were tested until failure and the breaking force (F_f) was recorded. Then, the failed assemblies were visually inspected to identify their type of failure. Two types of failure were obtained within the assemblies: cohesive (CI), with an assembly that separates by shear at the interface within the weld joint, and substrate near joint (SNJ), indicating that the bulk sample breaks near the weld joint heat-affected zone (HAZ). Then, the failure stress and normalized lap-shear strength (LSS) were calculated. It was observed that the thickness of the upper part has a minimal effect on the weld strength for a same laser power. However, the mechanical strength of the assemblies decreases with as laser power increases. The increment in power intensity produces bigger weld joints, which result in higher contact areas (A_c), reducing the LSS. From those morphological and mechanical analyses of the welded assemblies, the optimal welding parameters were able to be identified. The highest strength of 60 MPa is obtained when welding with 85 W for both types of upper part thicknesses.

After welding, it was intended to improve the weld joint strength. In high-performance thermoplastics, the crystallinity has a strong influence on chemical and mechanical properties [Vodicka, 1996]. In general, the crystallinity tends to improve the stiffness and tensile strength of the samples [Martineau et al., 2019]. Hence, it was hypothesized that increasing the crystallinity of the samples could also improve the LSS of the weld joint. To improve this crystallinity two options were considered, to crystallize the weld joint in-situ (while welding) or to crystallize it after welding. Crystallizing the weld joint in-situ (during welding) revealed to be difficult due to the thermal gradients needed to be controlled. The LTW process induces rapid heating and cooling of the samples at a locally restricted area (the irradiated interface). These thermal gradients generated, and their kinetics are difficult to control during welding. Therefore, a post-weld heat treatment of annealing was thought to improve the weld joint quality. Annealing was made at the cold crystallization temperature of PEKK parts (190°C) to enhance crystallinity from the amorphous state, and for a defined isotherm of 3 h, to give enough time to the assemblies to fully crystallize and reach a high crystallinity. The welded assemblies that undergone annealing are called “PEKK-Ac/SC”.

The annealed welded assemblies (PEKK-Ac/SC) were also characterized morphologically and mechanically as made with the just-welded ones (PEKK-A/SC). The weld joint properties of the PEKK-Ac/SC assemblies were compared to those of the PEKK-A/SC assemblies to validate the improvement of the weld joint quality generated by the heat-treatment. Annealing the assemblies allowed to obtain a more homogeneous weld joint HAZ in term of crystallinity. Moreover, the strength of the assemblies increased by more than 10 % when annealed. The maximum increment was achieved on the PEKK-A4c/SC welded at 85 W, with a strength that increased from 63 to 102 MPa after annealing.

In **Chapter 4**, the LTW process of PEKK parts is simulated by finite differences method using MatLab software. Heat transfer by conduction is modeled, considering the heat source generated by the laser irradiation and the energy absorption properties of the samples as function of their crystallinity. This is coupled with the crystallization kinetics model of the

PEKK material, which makes evolving the degree of crystallinity of the samples with temperature. Numerical modelling allowed to gain insights on the thermal history undergone by the samples during the laser transmission welding process, and on the intrinsic mechanisms related to crystallinity. The thermal gradients and kinetics observed in the numerical simulation confirmed the HAZ developed during welding and observed on experimental results. At the interface, as defined in the model, the highest temperatures reached are the ones that allow material melting (between 305 and 314 °C), allowing the generation of the melted zone. Then, over the melted zone on the PEKK-A2 sample, temperatures between 204 and 285 °C are reached. These temperatures allowed the PEKK amorphous sample to crystallize from the cold over the melted zone. Additionally, high heating and cooling rates are observed during the welding process, the laser irradiation heats the assembly at a rate of 3600 $K \cdot min^{-1}$, and the heated zones cool at 360 $K \cdot min^{-1}$. The developed simulation allows to predict the evolution of the weld joint crystallinity as function of welding parameters.

After validating and studying the LTW process of PEKK polymer, the LTW study extends to PEKK composites reinforced with short carbon fibers in **Chapter 5**. That represented a novel area of research, with no prior studies found on LTW of PEKK-CF composites. For joining PEKK-CF samples, the quasi-amorphous PEKK is used as upper part for the overlapping configuration, to allow joining by LTW. The process window for scanning speed and laser power that allow welding of PEKK-CF is determined by laser material interaction tests on the parts. The welding of PEKK-CF samples by LTW is optimized by new experimental trials, obtaining the optimal combination of scanning speed and laser power to generate a high-quality joint. Weld joint quality is evaluated under mechanical tests and microscopy observations, as made for the PEKK polymer welds.

Welding PEKK amorphous/carbon fiber (PEKK-A/CF) parts by LTW is possible for scanning speeds between 10 and 30 $mm \cdot s^{-1}$ with their respective power-ranges between 10 and 38 W. LTW of PEKK-A to PEKK-CF allows for a more extended weldability window than when welding PEKK-A/SC. The differences lie on the absorptivity and thermal conductivity of the lower absorbent parts used. Whereas PEKK-SC samples absorb the laser irradiation in the volume, the PEKK-CF allows for surface absorption at the interface. Additionally, the thermal conductivity of the PEKK-CF sample of 8.36 $W \cdot m^{-1} \cdot K^{-1}$ is 39.6 times higher than that of the PEKK-SC part ($k = 0.211$ $W \cdot m^{-1} \cdot K^{-1}$). Those differences on thermal and optical properties of the PEKK-CF samples improve the laser energy absorption at the interface and heat transfer to the upper part. Indeed, less energy is needed to be deposited at the interface to achieve melting of the materials. This increases the possibilities of combining different laser powers and scanning speeds to achieve the same energy deposition.

For this thesis, the LTW of PEKK-A/CF parts was studied only for a scanning speed of 10 $mm \cdot s^{-1}$ with powers between 12 and 24 W. The best joint quality was obtained when welding at 18 W, achieving a weld strength of 25 MPa. Nevertheless, the weld strength of the PEKK-A/CF assemblies was lower than the one obtained on the PEKK-A/SC welds. This was mostly caused by the low breaking load reached in comparison to the high contact areas obtained on the PEKK-A/CF weld joints. In the PEKK-A/CF assemblies the contact areas obtained at the weld joint interface were about three times that of the PEKK-A/SC assemblies. However,

the increment in contact areas did not result in a proportionally higher breaking load, since both assemblies (PEKK-A/SC and PEKK-A/CF) demonstrated comparable breaking loads, which generated a decrement on the LSS of the PEKK-A/CF assemblies. To improve weld strength, welds must have a higher breaking load resistance proportional to the increment of the contact area.

Based on those findings, the primary contribution of this PhD thesis is a deeper comprehension of the laser transmission welding process applied to PEKK polymers and composites. The relationship between material properties, welding parameters and the morphology and mechanical resistance of the weld joints was established. More precisely, this work has made major advancements related to:

1. The optical properties of the PEKK 70/30 polymer in a large wavelength range, correlated to the crystallinity, the water content and the sample orientation. The influence of the optical properties on the weldability.
2. The welding parameters definition for PEKK-A/SC samples that allow to generate a reliable and strong weld joint, with strengths between 40 and 60 MPa.
3. The influence of welding parameters on the weld joint morphology, from a thermal and crystallinity point of view.
4. The capability to improve the quality of the PEKK-A/SC LTW assemblies by crystallizing them by annealing at the cold crystallization temperature. A more homogeneous weld joint HAZ in terms of crystallinity is obtained, and the weld strength can increase by more than 10 %.
5. The possibility to predict the weld joint morphology as function of the welding parameters by numerical simulations made with finite differences method.
6. The optimal welding parameters for joining PEKK 80/20 reinforced with a 30 % weight of short carbon fibers with PEKK-A 70/30 by LTW. Reaching high weld strengths between 22 and 25 MPa.
7. The importance of the absorptivity and thermal conductivity of the PEKK lower part for LTW, which strongly influences the weld joint morphology and welding parameters.

Perspectives

The results of this doctoral work have contributed to the improvement and better understanding of the laser transmission welding process for semi-crystalline thermoplastics, with specific application on the PEKK material. However, some areas of opportunity were found in the approaches given in the study from which several perspectives can be developed.

During the present work, the optical properties of PEKK 70/30 were correlated with the degree of crystallinity of the material. However, the correlation obtained was made with only two points of data, because only two crystalline states were obtained on the PEKK samples: the quasi-amorphous (PEKK-A) and the high-crystallized one (PEKK-SC). Therefore, a detailed characterization on the influence of the degree of crystallinity on the optical properties of the material will be of interest. To achieve that, one can obtain various PEKK samples with different degree of crystallinity and characterize their transmission and reflection by spectrophotometry. To obtain the various degree of crystallinity on the PEKK samples a viable option can be to crystallize the amorphous samples from the cold by annealing at the cold crystallization temperature (T_{cc}) for different times. This will allow to crystallize more or less the samples depending on the annealing time. Having the various PEKK annealed samples, their degree of crystallinity and optical properties can be characterized and correlated. This characterization will give more information on the PEKK material behavior with respect the laser irradiation. Additionally, this more detailed correlation can feed the numerical model to improve the prediction of the weld joint crystallinity.

The LTW process of PEKK-A/SC parts generated a weld joint HAZ heterogeneous in terms of crystallinity. This was characterized qualitatively from the coloration observable in the HAZ and compared to the colors of the bulk samples. Because the color of the PEKK 70/30 samples change according to their crystallinity, correlation between color and crystallinity was possible, which gave information on the crystallinity of the weld joint according to the obtained colors after welding. However, to really convince about the influence of the welding parameters on the weld joint morphology, a deeper characterization of this last one can be made. On one hand, further qualitative characterizations would be interesting to conduct to further validate the crystalline states of the zones identified in the weld joint HAZ. One can try to observe the crystal morphology of the material, the spherulitic microstructure, on the weld joint HAZ. This can be achieved by observations under polarized optical microscopy in transmission mode of a thin layer (less than 40 microns) of the weld joint cross-section. This could allow us to better distinguish the crystalline and amorphous phases on the weld joint zones and quantify their ratio. On the other hand, measuring the degree of crystallinity of the weld joint zones can allow to correlate the weld joint crystallization with the welding parameters and with the assembly strength. This characterization should be done by non-destructive methods to avoid alterations of the crystallinity before the quantification. A method that appears interesting and possibly efficient is the X-Ray diffraction (XRD). Obtaining a mapping of the weld joint HAZ degree of crystallinity could be helpful. This can also be applied to the PEKK-Ac/SC assemblies to verify quantitatively the crystallinity of the annealed weld joints.

Because the obtained weld joint HAZ had a variation in crystallinity, it was thought that improving its crystallinity homogeneity would improve the weld joint quality. Therefore, to improve the weld joint quality (morphologically and mechanically), the choice was made to increase the crystallinity of the weld joint. For that, an annealing post-weld heat treatment process was chosen. However, this process is long and needs a mold with the shape of the assemblies to avoid sample deformation when crystallizing. Therefore, crystallizing the weld joint in-situ during the welding process can be tried. Thus, a study can be conducted on crystallizing the weld joint in-situ during LTW of PEKK-A/SC. Quasi-simultaneous LTW variant can be reproduced by increasing the number of scans and the scanning speed. This welding strategy could allow for better control of the heating and cooling phases undergone by the assembly's interface. The approach can consist of scanning the interface at a higher speed at various times and using different laser powers. That will allow the heat created at the interface to be preserved and kept at high temperatures, near the melt crystallization temperature (295°C), for weld joint crystallization after material melting. The study can be improved if the temperature at the interface is monitored to reach the targeted temperature with more accuracy. In addition, the simulations created for the LTW of PEKK-A2/SC parts can be a valuable tool to identify those quasi-simultaneous welding parameters before experimental trials. Even though this approach may initially be time-consuming due to the necessity of finding the ideal welding parameters by trial and error, it eventually will save time. Welding can be completed quickly and effectively once the ideal parameters are determined.

In addition, the simulations of LTW of PEKK-A/SC parts can also be improved by implementing other models and numerical strategies. For example, use the Monte-Carlo model to include the scattering of the laser beam radiation from the PEKK samples. The model can also be alimented with an artificial intelligence (IA) that will predict the laser travel path on the thickness of the assembly.

Finally, the LTW process of PEKK composites can be studied in detail, by testing a larger combination of welding parameters. This could help to improve the weld joint mechanical properties and to define the optimal welding parameters.

Besides high-performance polymers, joining biobased thermoplastic and composite materials and recycled materials appears relevant to address the issues of climate change and overconsumption. Assembling these types of polymers by LTW will be even more challenging due to their higher sensitivity to thermo-oxidative degradation.

List of publications

In the context of this doctoral thesis, two peer-reviewed publications were produced and some are planned for the near future. The accepted and published works are listed below:

Published papers

- [Matus-Aguirre et al., 2024]: Marcela Matus-Aguirre, Benoît Cosson, Christian Garnier, Fabrice Schmidt, André Chateau Akué-Asséko, France Chabert, **Characterization and modeling of laser transmission welded polyetherketoneketone (PEKK) joints: Influence of process parameters and annealing on weld properties**, *Journal of Advanced Joining Processes, Volume 10, 2024, 100252, ISSN 2666-3309*, https://doi.org/10.1016/j.jajp.2024.100252
- [Matus Aguirre et al., 2023]: Marcela Matus Aguirre, Christian Garneir, Rémi Gilblas, Benoît Cosson, André Akué, Fabrice Schmidt, France Chabert, **Laser transmission welding of PEKK: Influence of material properties and process parameters on the weld strength**, *Materials Research Proceedings, Vol. 28, pp 1829-1840, 2023*, https://doi.org/10.21741/9781644902479-198

Dissemination

Part of the content of this doctoral thesis was presented to the scientific community in the following conferences and seminars:

National and international conferences

- M. Matus-Aguirre, C. Garnier, R. Gilblas, B. Cosson, A. Akué, F. Schmidt, F. Chabert, **Laser transmission welding of PEKK: influence of material properties and process parameters on the weld strength**, *ESAFORM 2024*, Krakow, Poland, April 2024.
- M. Matus-Aguirre, C. Garnier, R. Gilblas, B. Cosson, A. Akué, F. Schmidt, F. Chabert, **Laser transmission welding of high performance thermoplastic materials**, *SAMPE concours sélection France*, Bayonne, France, May 2024.
- M. Matus-Aguirre, C. Garnier, R. Gilblas, B. Cosson, A. Akué, F. Schmidt, F. Chabert, **Influence of material properties and process parameters on the weld strength of laser transmission welding of semi-crystalline thermoplastics**, *2ème Congrès des Jeunes Chercheurs en Mécanique (MECA-J)*, France, August 2024.
- M. Matus-Aguirre, C. Garnier, R. Gilblas, B. Cosson, A. Akué, F. Schmidt, F. Chabert, **Material properties and process parameters influence on PEKK parts assembled by laser transmission welding**, *Polymères & Composites (P&C)*, Toulouse, France, September, 2024.
- M. Matus-Aguirre, C. Garnier, R. Gilblas, B. Cosson, A. Akué, F. Schmidt, F. Chabert, **Joining high-performance thermoplastic parts by LTW: relationship between material properties, process parameters and weld quality**, *3rd international conference on Advanced Joining Process (AJP)*, Braga, Portugal, October 2024.

Awards from seminars

- Best poster award of the *XIVèmes Journées de l'école doctorale Sciences de la Matière*, ENSIACET, Labège, France, May 2022.
- Winner of the contest *Ma thèse en 180 secondes* organized by the CERI Matériaux et Procédés of the IMT Nord Europe, Douai, France, December 2023.

French abstract

Titre de la thèse en français - Soudage laser par transmission de thermoplastique semi-cristallin PEKK : prédiction de la cristallinité du joint de soudure et de la résistance mécanique des assemblages.

Ce projet de thèse a été lancé grâce à une collaboration entre trois laboratoires : le Laboratoire Génie de Production (LGP) (EA1905) de l'École Nationale d'Ingénieurs de Tarbes (ENIT-INPT), le Centre d'Enseignement de Recherche et d'Innovation Matériaux et Procédés (CERI-MP) de l'école d'ingénieurs IMT Nord Europe, et l'Institut Clément Ader (ICA) (CNRS UMR 5312) de l'école d'ingénieurs IMT Mines Albi, en France. Le projet a reçu un financement de la Région Occitanie, France et d'IMT Nord Europe. Les travaux de recherche de ce projet ont été menés dans les trois laboratoires mentionnés ci-dessus. Différentes méthodes et ressources ont été fournies par chaque laboratoire afin de réaliser le travail de thèse dans les meilleures conditions. La société Arkema, France, a fourni le granulé du polymère PEKK 7002 et les plaques injectées du composite PEKK 8010-C30 pour l'étude.

Introduction

Il devient de plus en plus courant de souder des matériaux thermoplastiques dans l'industrie, en réponse à la nécessité de structures à la fois légères et solides. Le soudage laser par transmission (LTW en anglais) représente une méthode performante pour assembler ces matériaux, en générant des soudures de précision et de grande qualité. Le procédé de soudage laser par transmission utilise un laser proche de l'infrarouge pour assembler deux pièces thermoplastiques qui se superposent, comme montré dans la Figure 1a. La pièce supérieure doit être semi-transparente au laser, tandis que l'inférieure doit absorber le laser. Le faisceau laser irradie et fait fondre l'interface après avoir traversé la partie supérieure. Lors du refroidissement, l'interdiffusion moléculaire des chaînes de polymères génère un joint de soudure (Figure 1b). L'efficacité du procédé LTW dépend des propriétés thermiques et optiques des matériaux à souder. De plus, la qualité des assemblages LTW est influencée par les paramètres de soudage.

Ce projet de doctorat se concentre sur l'étude du procédé de soudage laser par transmission (LTW) d'un matériau thermoplastique semi-cristallin, le PEKK. L'objectif principal est de prédire la morphologie cristalline et la résistance mécanique des joints soudés. Pour cela, il est également nécessaire de prévoir l'histoire thermique subie par les échantillons pendant le soudage et les zones affectées thermiquement (ZAT) par le procédé. Pour y parvenir, des approches expérimentales et numériques seront utilisées pour cette étude. Le travail expérimental étudiera l'influence des paramètres du procédé et des propriétés des matériaux sur la morphologie et la résistance du joint de soudure. Ensuite, des simulations numériques du procédé seront développées et validées avec les résultats expérimentaux. La simulation

finale est destinée à devenir un outil numérique permettant de prédire le développement des joints de soudure.

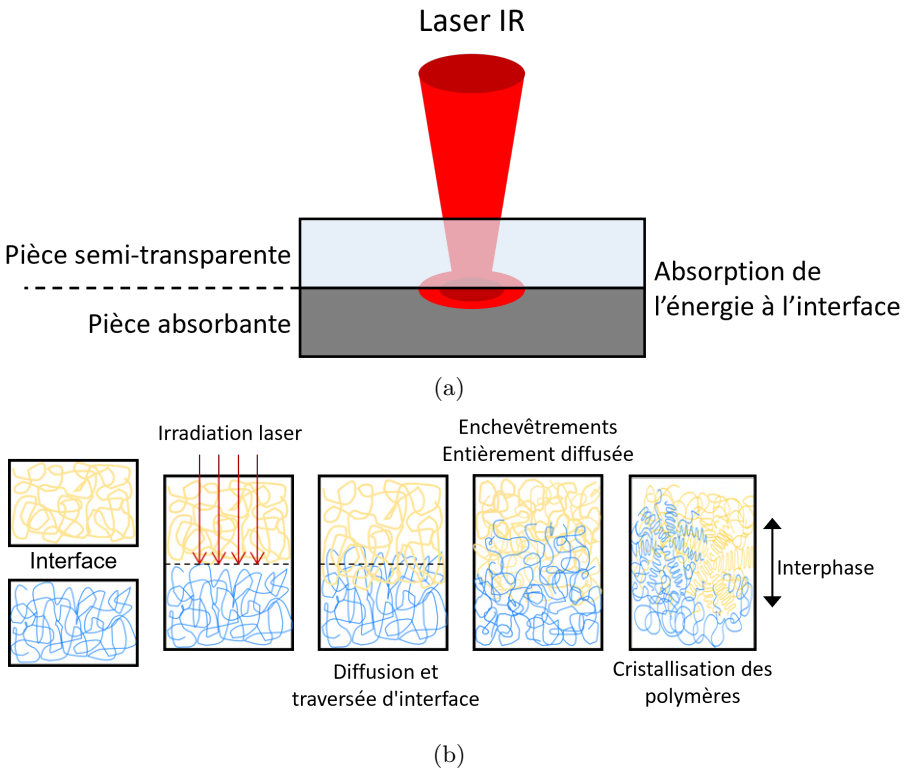

Figure 1: Soudage laser par transmission (a) principe and (b) mécanisme d'interdiffusion macromoléculaire.

Les travaux de thèse ont débuté par une étude bibliographique sur le procédé de soudage. Des articles et des revues sur le soudage laser par transmission des polymères ont été lus. Cette étude bibliographique a révélé que le procédé LTW est principalement utilisé pour le soudage des thermoplastiques communs. Peu de travaux ont étudié le soudage laser par transmission de thermoplastiques hautes performances. En outre, il a été constaté qu'une seule étude portait sur le polymère polyéthercétonecétone (PEKK en anglais). Cela indique qu'il existe une grande opportunité pour étudier le LTW sur le matériau PEKK. C'est donc ce matériau qui a été choisi pour l'étude. Cependant, le PEKK a différents grades, et le choix du grade approprié pour le procédé était également important. Pour ce faire, les différents grades de PEKK ont été comparés. Cette comparaison nous a permis de trouver le grade de PEKK le plus approprié pour le LTW : le grade 70/30, grâce à sa cinétique de cristallisation moyenne. L'objectif du choix de ce matériau et de son grade était d'obtenir des échantillons avec le taux de cristallinité le plus faible et le plus élevé possibles afin de les utiliser comme échantillons pour le soudage, en suivant l'approche d'une précédente thèse effectué au LGP, soutenue en 2018 [Villar et al., 2018].

Matériau d'étude PEKK et ses propriétés pour le soudage laser par transmission

Après avoir choisi et acquis le matériau d'étude, il était temps de fabriquer les échantillons. Les échantillons pour le soudage ont été obtenus par moulage par injection. Les granulés de PEKK ont été mise en forme dans une presse à injecter Proxima 50 de Billion (Figure 2). Des plaques injectées de 95x95 mm² ont été produites avec différentes épaisseurs. Différents paramètres de procédé et vitesses de refroidissement ont été utilisés pour obtenir des plaques avec des degrés de cristallinité faibles et élevés, comme le montre la Figure 3. Une température de moule et un temps de refroidissement faibles ont été utilisés pour obtenir des plaques à faible degré de cristallinité. Les plaques obtenues étaient transparentes à la lumière visuelle avec une coloration jaune. Ces plaques ont été considérées comme amorphes et appelées *PEKK-A*. Une température de moule et un temps de refroidissement élevés ont été utilisés pour obtenir le taux de cristallinité le plus élevé, ce qui a permis d'obtenir des plaques mates avec une coloration beige, presque blanche. Ce sont les plaques semi-cristallines, ou *PEKK-SC*. Les PEKK-A ont été injectés à des épaisseurs de 2 et 4 mm, tandis que les PEKK-SC n'avaient qu'une épaisseur de 2 mm. La température du moule a été surveillée et étudiée au cours du procédé d'injection afin de contrôler la température en temps réel utilisée pour l'injection et le refroidissement.

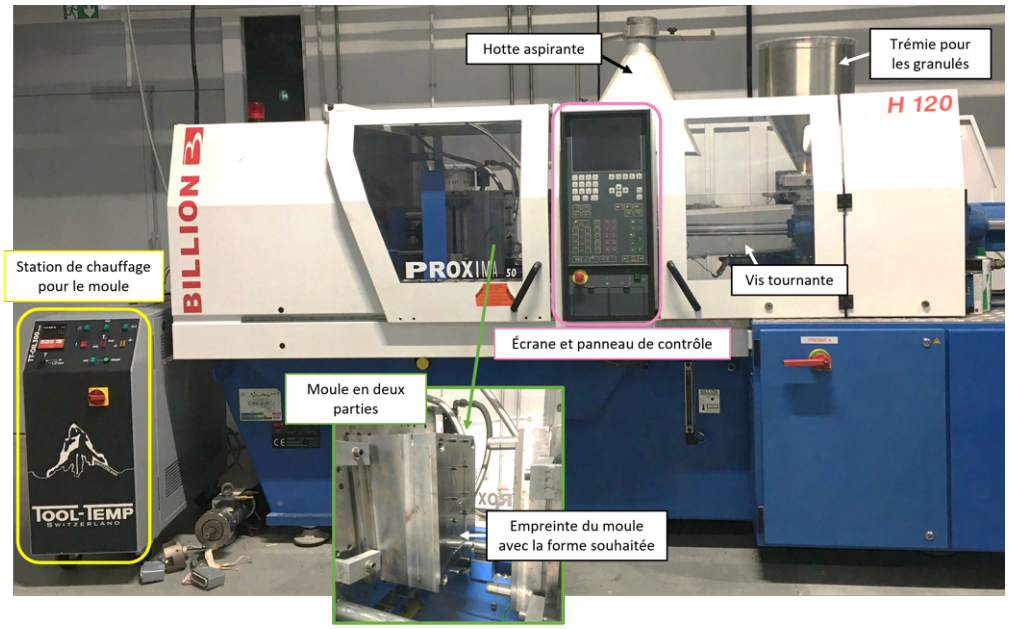

Figure 2: Machine de moulage par injection utilisée pour l'injection de plaques PEKK.

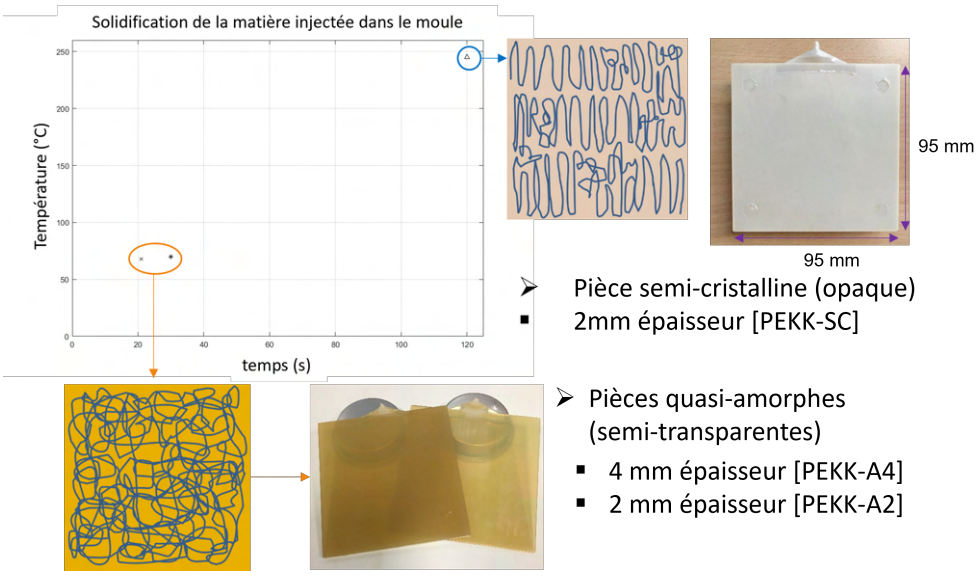

Figure 3: Temps et température de refroidissement utilisés pour la solidification de la matière PEKK dans le moule.

Après la fabrication des échantillons, il était important de les caractériser pour valider leur compatibilité avec le procédé de soudage. Tout d'abord, les transitions thermiques des matériaux ont été caractérisées par calorimétrie différentielle à balayage (DSC) à l'aide d'un système DSC 1 Stare de Mettler Toledo. Des échantillons de 6 ± 3 mg sont extraits des plaques PEKK et placés dans des moules en aluminium hermétiques. En utilisant des rampes de 10 K/min, les échantillons sont chauffés de 100°C à 390°C, refroidis de 390°C à 100°C, puis chauffés à nouveau de 100°C à 390°C sous un flux d'azote de 50 mL/min. Au début de chaque essai, les échantillons sont stabilisés à 100°C pendant 5 minutes, et il n'y a pas de pause entre les cycles de chauffage et de refroidissement.

La Figure 4a montre le thermogramme DSC obtenu pour les échantillons de PEKK-A. Ce thermogramme nous permet de déduire les transitions thermiques du matériau et leur degré de cristallinité. La caractérisation des transitions thermiques du matériau fournit des informations importantes concernant les températures à atteindre lors du soudage pour obtenir la fusion et la cristallisation à l'interface. Pour le soudage au laser, il est important de faire fondre les deux échantillons à l'interface afin que leurs molécules puissent interdiffuser entre elles. Ainsi, la température de fusion du polymère obtenue par cette caractérisation indique la température à atteindre lors de l'irradiation du matériau (318°C). Ensuite, lors du refroidissement, les polymères se solidifient, ce qui permet de créer le joint de soudure. Au cours du procédé de refroidissement, le matériau peut également cristalliser. Pour obtenir la cristallisation du joint de soudure, il est important de connaître les températures de cristallisation du matériau. Les températures de cristallisation à froid (Tcc) et à chaud (Tc) obtenues par DSC étaient respectivement de 205°C et 295°C. Ces températures indiquent la possibilité pour le matériau de cristalliser à partir de la forme amorphe (ou à faible cristallinité) et à partir de l'état fondu, respectivement. Par exemple, pour obtenir la cristallisation d'un joint de soudure in situ, il est important de maintenir la température du joint à la Tc pendant un

certain temps (en fonction de la cinétique de cristallisation du matériau). Il serait également possible de cristalliser le joint après le soudage par recuit à Tcc.

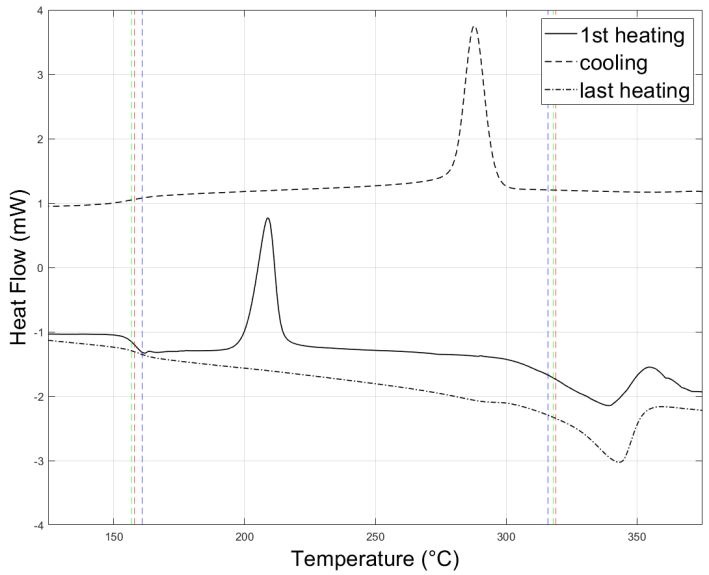

(a)

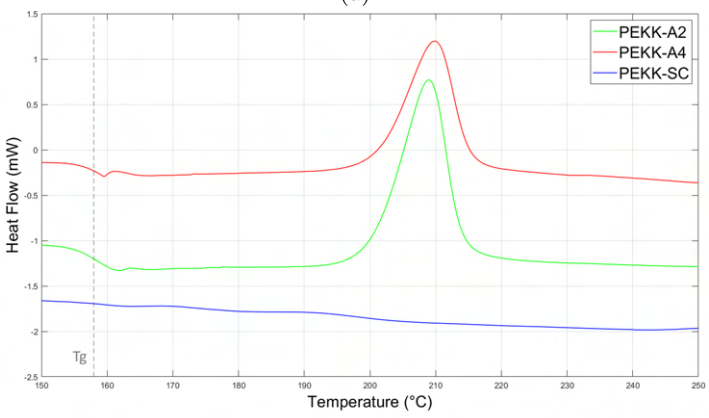

(b)

Figure 4: (a) Thermogramme typique DSC des plaques injectées en PEKK 7002, (b) pics de cristallisation froide.

La Figure 4b montre les pics de cristallisation froide des échantillons lors du prermier chauffage. Comme il est observable, les échantillons amorphes (PEKK-A2 et PEKK-A4) montrent un pic exothermique autour de 205 °C. Cela indique que le matériau a cristallisé avec l'augmentation de la température depuis l'état solide, montrant que la matière avait un degré de cristallinité faible, et pouvant être considérés comme amorphes. D'un autre côté, le pic exothérmique n'apparaît pas sur la courbe du PEKK-SC, indiquant que son degré de cristallinité était déjà assez élevé dans son état initial, pouvant être considéré semi-cristallin.

Les tests DSC ont également permis de caractériser les degrés de cristallinité (Xc) des échantillons analysés. Ces valeurs ont confirmé la différence de cristallinité entre les trois échantillons injectés. Les échantillons PEKK-A ont montré un faible Xc inférieur à 6 %, alors que les échantillons PEKK-SC ont montré un Xc élevé de 24 %. Les résultats obtenus concernant les transitions thermiques et la caractérisation du degré de cristallinité des plaques injectées de PEKK 7002 sont résumés dans le Tableau 1.

Plaque	**Tg (°C)**	**Tm (°C)**	**Tcc (°C)**	**Tc (°C)**	**Xc (%)**
PEKK-A2	151	337	204	293	5 ± 1
PEKK-A4	152	336	205	293	6 ± 2
PEKK-SC	160	338	-	293	24 ± 2

Table 1: Transitions thermiques et degrés de cristallinité des plaques injectées en PEKK 7002

Pour réaliser un soudage par LTW, la partie supérieure doit être aussi transparente que possible à la longueur d'onde du laser (dans notre cas, 975 nm) afin que le laser puisse irradier l'interface. En outre, la partie inférieure doit absorber l'énergie du laser à l'interface. Les propriétés optiques des échantillons injectés ont été caractérisées pour vérifier s'ils étaient adéquats en tant que parties transparentes et absorbantes.

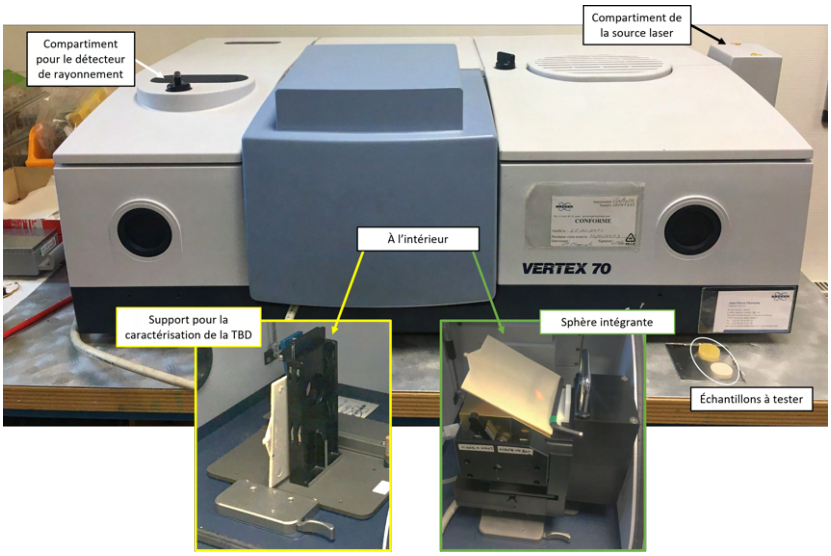

Figure 5: Spectophotomètre utilisé pour la caractérisation optique des échantillons PEKK.

Un spectrophotomètre Vertex 70 (Figure 5) a été utilisé pour obtenir les spectres de transmission et de réflexion des échantillons (Figure 6). À partir de là, les facteurs de transmission, de réflexion et d'absorption ont été déterminés à la longueur d'onde d'intérêt (correspondant à la machine à souder au laser utilisée ici pour le soudage : 975 nm). Les échantillons de PEKK-A ont montré un facteur de transmission supérieur à 60 %, validant leur aptitude à servir de pièces semi-transparentes. Les échantillons de PEKK-SC ont montré un faible

facteur de transmission de 20 % avec un facteur d'absorption plus élevé de 32 %, validant leur aptitude à être utilisés comme pièces absorbantes. Le résumé de ces valeurs est présenté dans le Tableau 2. Par conséquent, les pièces en PEKK peuvent être soudées par LTW dans une configuration de chevauchement où l'échantillon amorphe de PEKK est placé au-dessus de l'échantillon semi-cristallin de PEKK. Cette configuration d'assemblage sera désormais appelée *PEKK-A/SC*.

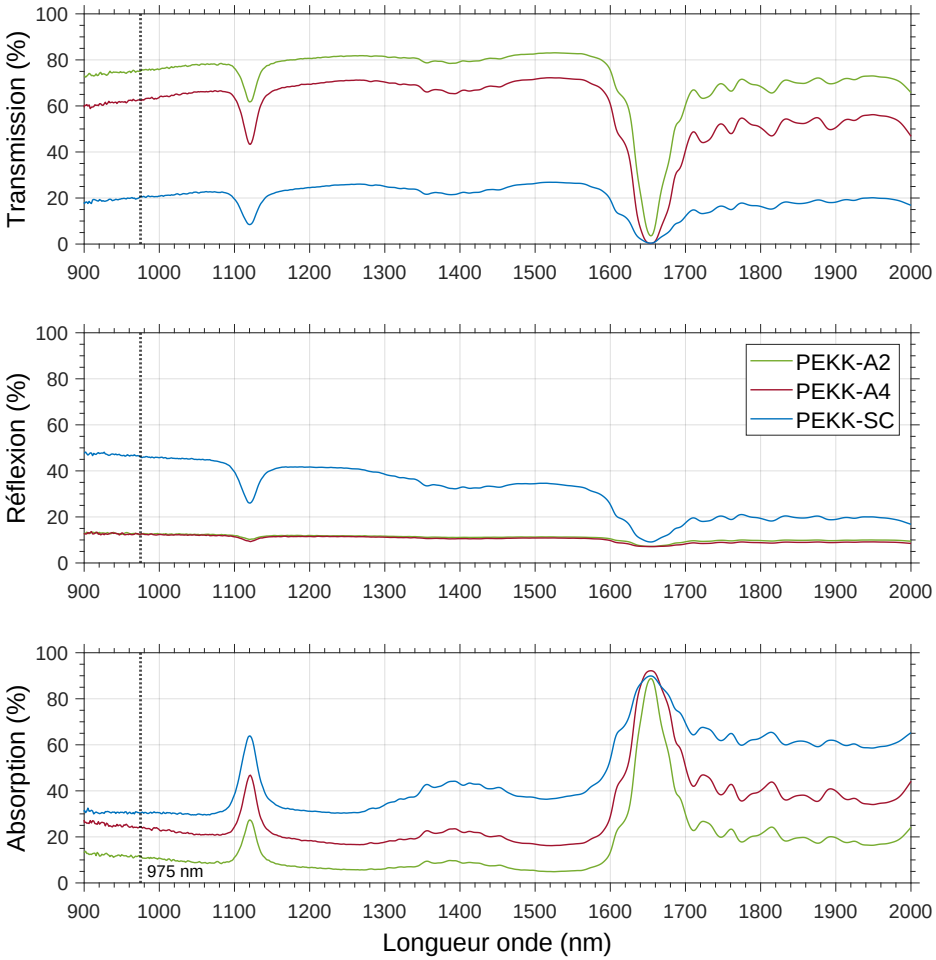

Figure 6: Spectres de transmission, réflexion et absorption hemisphériques des plaques injectées en PEKK 7002.

Plaque	T (%)	R (%)	A (%)
PEKK-A2	75 ± 1,5	13 ± 0,1	12 ± 1,5
PEKK-A4	62 ± 0,7	13 ± 0,1	25 ± 0,7
PEKK-SC	20 ± 0,02	48 ± 1,7	32 ± 1,7

Table 2: Facteurs de transmission, réflexion et absorption des plaques injectées en PEKK 7002

Une première caractérisation des propriétés thermiques du matériau a également été effectuée. La conductivité thermique k [W/m·K] de chaque échantillon a été caractérisée à l'aide d'un analyseur à disque chaud (TPS2500 hot disk analyzer de Hotdisk Instrument). Comme prévu pour un polymère, les échantillons ont montré une faible conductivité thermique, inférieure à 0,25 W/m · K. Ce qui n'était pas prévu, c'est que les plaques semi-cristallines ont montré une conductivité plus faible que les plaques amorphes, contrairement à la littérature [Klein, 2012, Villar et al., 2018].

La capacité calorifique Cp [J/kg·K] est caractérisé par mesures en DSC sur une TA Instrument Q200. Des échantillons avec un poids de 10 ± 1,5 mg sont testés avec une rampe de 5 °C/min. La densité ρ [kg/m^3] de la matière a été extrait de la fiche technique du fournisseur [Arkema, 2021].

Les propriétés thermiques des échantillons sont indiquées dans le Tableau 3. Les propriétés thermiques du matériau sont importantes pour développer la simulation numérique du procédé de soudage.

Plaque	k [W/m·K]	Cp [J/kg·K]	ρ [kg/m^3]
PEKK-A2 et A4	0,246	973	1290
PEKK-SC	0,211	1138	1290

Table 3: Propriétés thermiques des plaques injectées en PEKK 7002

Soudage laser par transmission de pièces PEKK

La machine de soudage laser ES Laser, Bordeaux, France, est utilisée pour le projet (Figure 7). C'est une machine à laser diode avec longueur d'onde de 975 nm et une puissance laser qui peut aller jusqu'à 222 Watts. La machine a été acquise par le laboratoire LGP au début de la thèse, financée par la région Occitanie dans le cadre d'un CPER, arrivant au laboratoire en décembre 2021.

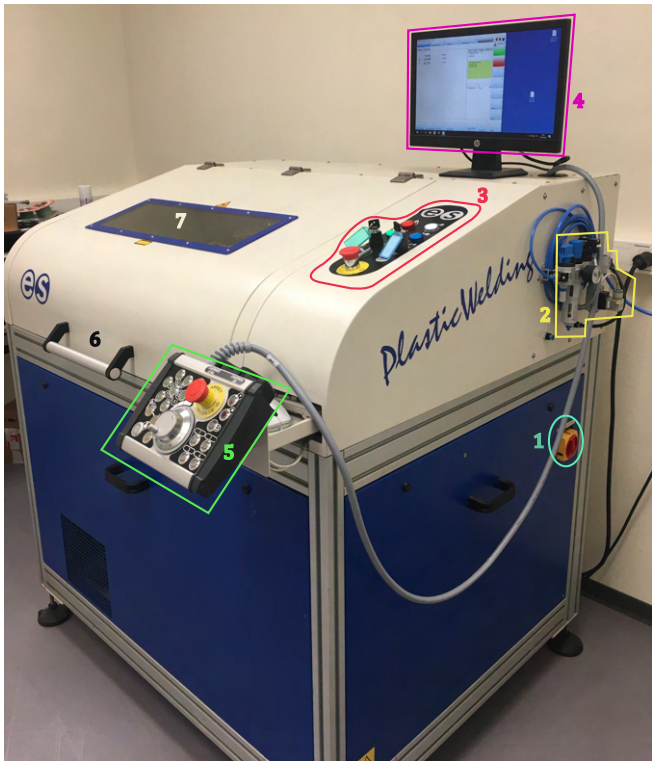

Figure 7: Machine à soudage laser ES Weld 200, visualisation extérieure avec les composants indiqués par les numéros (1) sectionneur général, (2) pompe à air comprimé, (3) panneau de clés d'activation du laser, (4) écran, (5) pupitre commande numérique, (6) porte de protection et (7) vitre d'observation.

Avant de commencer les essais de soudage, il était important de tester la réponse des échantillons au faisceau laser. Des tests d'irradiation ont été effectués sur les échantillons pour vérifier l'interaction entre le faisceau laser et le matériau. Différents paramètres du procédé ont été testés : la focalisation du faisceau laser, la puissance et le temps d'irradiation. Les tests ont été réalisés dans des conditions statiques et dynamiques. Pour la condition statique, l'irradiation a été effectuée pendant un temps fixe sans mouvement. Dans les conditions dynamiques, le faisceau laser s'est déplacé de sa position initiale à la longueur indiquée à une vitesse fixe. L'objectif était de chauffer suffisamment la zone irradiée pour permettre la fusion de l'échantillon sans le brûler. Les essais d'irradiation ont d'abord été effectués sur des échantillons semi-cristallins, puis transposés à la configuration de l'assemblage A/SC.

Pour la configuration de chevauchement de l'A/SC, la surface irradiée était l'interface de l'assemblage. Il était important de prendre en compte le facteur de transmission obtenu par la caractérisation optique pour obtenir la puissance d'irradiation de l'interface. À la fin de la campagne d'interaction L-M, la première combinaison procédé-paramètres permettant la fusion dans la zone irradiée sans brûlure a été déterminée pour l'échantillon SC et la configuration d'assemblage A/SC.

Pour réaliser la soudure des échantillons par LTW, dix paramètres différents ont été définis, dont huit sont fixes et deux sont variables. Les deux paramètres variables sont la puissance du laser à l'interface et l'épaisseur de la partie supérieure semi-transparente. Ce sont les paramètres choisis pour être étudiés pour le procédé de soudage laser par transmission sur les échantillons PEKK.

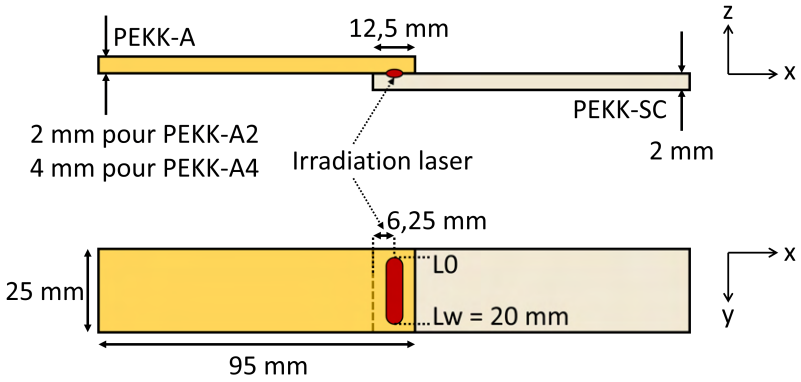

Figure 8: Représentation graphique de la configuration du joint de recouvrement utilisé pour le soudage en LTW du PEKK-A/SC (pas à l'échelle).

Les échantillons utilisés pour le soudage ont été découpés à partir des plaques injectées afin d'obtenir un assemblage à chevauchement, comme le montre la Figure 8. Cette configuration permet de tester mécaniquement l'assemblage en utilisant un essai de cisaillement à recouvrement simple (Single Lap Shear test), conformément à la norme ISO 4587:2003. Le premier paramètre modifié est l'épaisseur de l'échantillon amorphe supérieur, qui est de 2 et 4 mm. A partir de là, deux types d'assemblages ont été obtenus : A2/SC et A4/SC. Ensuite, l'autre paramètre variable est l'intensité de la puissance pour irradier l'interface. Quatre puissances différentes ont été utilisées entre 75 et 95 Watts. Lors du soudage, neuf assemblages ont été créés pour chaque puissance et pour chaque type d'assemblage. La configuration de l'assemblage pour le soudage en LTW du PEKK-A/SC est illustrée à la Figure 9.

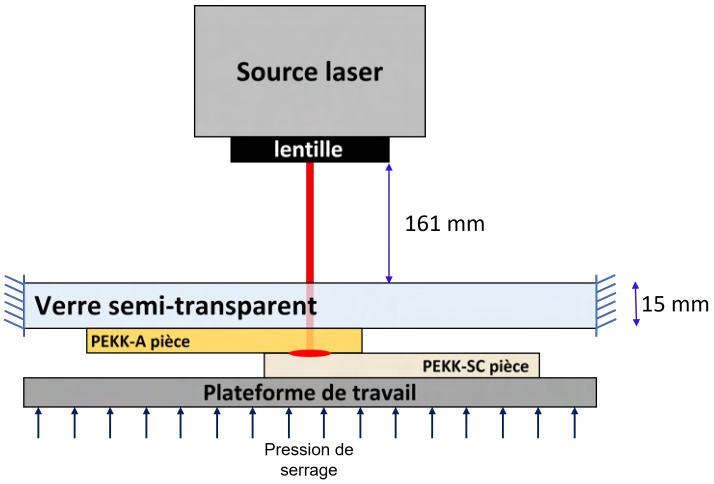

Figure 9: Configuration de soudage à l'intérieur de la machine (représentation graphique, pas à l'échelle).

Propriétés mécaniques des joints soudés

Des essais de cisaillement dans le plan (in-plan shear tests) ont été utilisés pour tester la résistance mécanique des assemblages, comme le montre la Figure 10. Les assemblages soudés ont été soumis à un essai de cisaillement à recouvrement simple (SLS en anglais) à l'aide d'une machine de traction INSTRON 550R. Une cellule de charge de 5 kN et une vitesse de charge transversale de 2800 N/min ont été utilisées. Huit assemblages ont été testés pour chaque configuration d'assemblage. Les essais SLS ont été choisis pour caractériser la résistance mécanique du joint soudé avec une valeur quantitative qui pourrait être comparée à la littérature et aux exigences de l'industrie, notamment l'industrie aérospatiale.

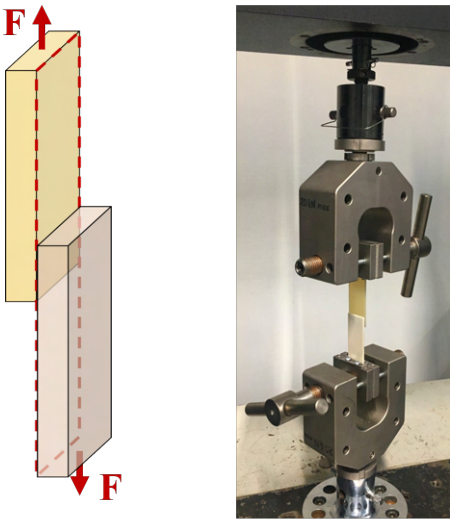

Figure 10: Représentation graphique et banc expérimental de l'essai mécanique de cisaillement à recouvrement simple.

Avec les tests SLS, la résistance de la soudure peut être quantifiée si l'assemblage est séparé au niveau de la zone de chevauchement. Cependant, les assemblages testés présentaient deux types de rupture, l'une au niveau de la pièce principale et l'autre au niveau de l'interface à l'intérieur du joint. Lorsque les assemblages se sont rompus au niveau de la pièce brute, on a conclu que le joint était plus résistant que l'échantillon d'origine. Pour le second type de rupture, la contrainte de cisaillement par recouvrement (LSS) a été calculée pour donner une valeur numérique à la résistance mécanique du joint soudé. Une bonne résistance mécanique a été trouvée pour ces assemblages, comme le montre la Figure 11, entre 40 et 60 MPa. Les valeurs de résistance obtenues sont supérieures aux exigences de l'industrie. Elles sont également supérieures aux valeurs trouvées dans la littérature pour des assemblages similaires [Potente et al., 2001, Amanat et al., 2011, Liu et al., 2022].

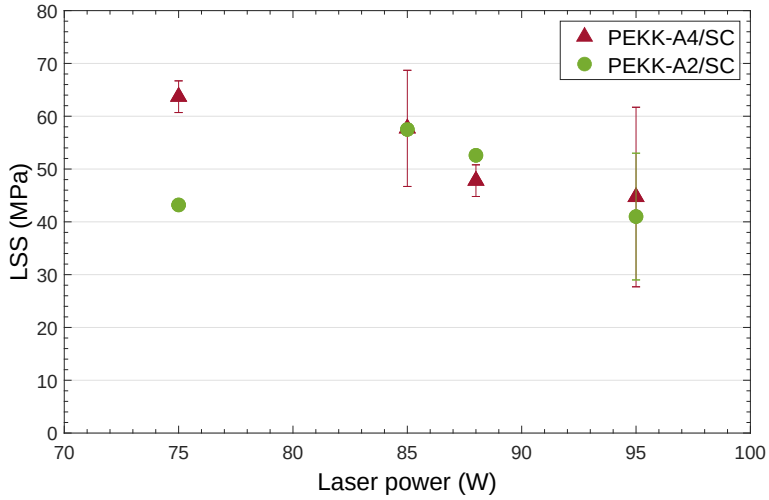

Figure 11: Valeurs de résistance au cisaillement par recouvrement (LSS) obtenues pour les assemblages soudés PEKK-A/SC qui se sont rompus à l'interface et à l'intérieur du joint.

Morphologie des joints soudés

Les assemblages soudés ont également été caractérisés morphologiquement par des observations au microscope optique. L'objectif était de caractériser le joint de soudure créé au niveau de la zone irradiée. Deux caractérisations ont été effectuées. La première caractérisation a porté sur la zone affectée thermiquement (ZAT) des assemblages qui s'est rompue à l'interface lors des essais mécaniques. Les dimensions de la zone irradiée ont été obtenues : longueur, largeur et surface. Les surfaces obtenues à partir de ces zones ont été utilisées pour calculer la valeur LSS de chaque assemblage.

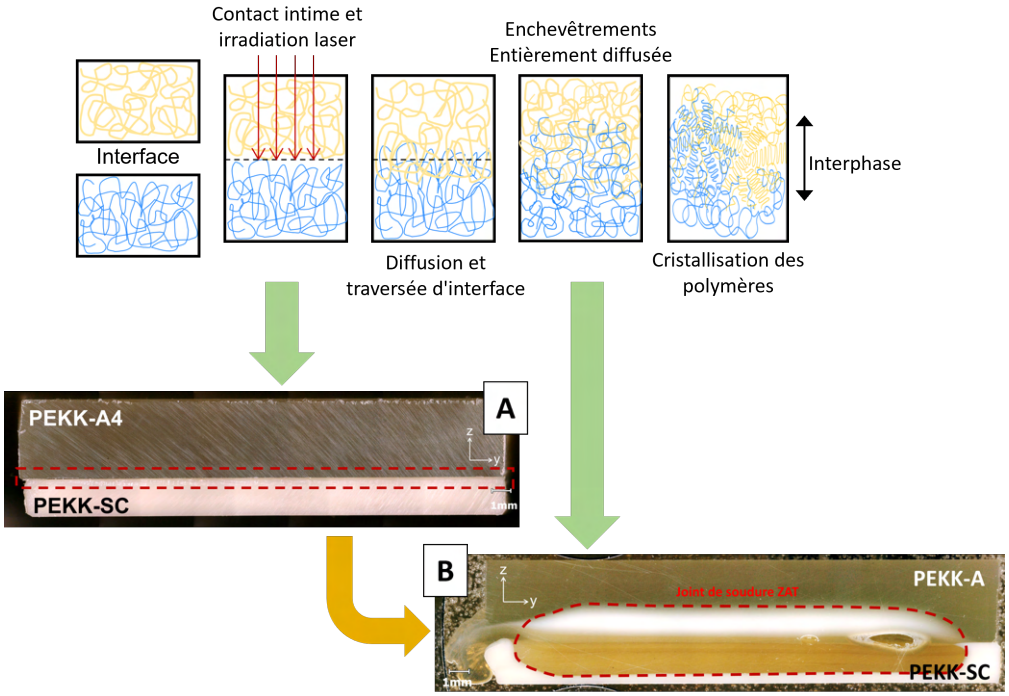

Figure 12: Coupe transversale du joint de soudure le long du chemin de soudage de l'assemblage PEKK-A4/SC A) avant et B) après le soudage.

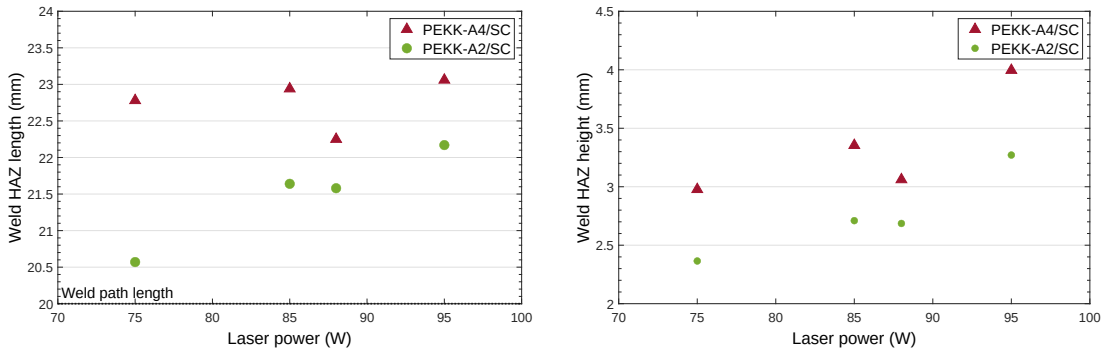

(a) (b)

Figure 13: Dimensions de la ZAT du joint de soudure en corrélation avec la puissance du laser utilisé pour effectuer le soudage: (a) longueur et (b) hauteur.

La deuxième caractérisation a permis d'étudier la section transversale du joint de soudure le long de la trajectoire de soudage. Les joints de soudure ont été coupés et enrobés pour être visualisés au microscope optique. Une micrographie de la section transversale de la soudure est présentée dans la Figure 12. Le premier fait intéressant observé est la couleur de la ZAT du joint de soudure. Un gradient de couleur allant du jaune au blanc a été trouvé à l'intérieur. Ces couleurs nous ont permis d'identifier qualitativement le degré de cristallinité de la ZAT.

Ensuite, les dimensions du joint de soudure (largeur et longueur) ont été mesurées le long de la trajectoire de la soudure. Ces dimensions ont été corrélées à la puissance du laser et à la résistance de la soudure, comme le montre la Figure 13. Ces visualisations nous ont permis de valider la capacité du procédé de soudage et des paramètres définis à générer un bon joint de soudure.

Recuit des assemblages soudés

Dans cette étude, pendant le soudage des échantillons thermoplastiques PEKK-A/SC, des modifications de la structure cristalline des échantillons ont été observées. L'irradiation laser a permis de faire fondre le matériau à l'interface, ce qui a permis de souder les échantillons. Cependant, le joint de soudure s'est développé dans une morphologie plus complexe en raison des réponses différentes de chaque échantillon à l'irradiation laser. L'échantillon absorbant PEKK-SC a fondu et est resté amorphe après le soudage et le refroidissement. En revanche, l'échantillon semi-transparent PEKK-A a cristallisé à froid, près de l'interface, pendant l'irradiation. Ces modifications de la structure cristalline du matériau soulèvent des questions sur les interactions entre les paramètres du laser et la réponse des pièces en PEKK pendant le LTW. Cependant, des travaux supplémentaires sont nécessaires pour améliorer la cristallinité et la résistance des joints de soudure.

Afin d'améliorer la qualité de la soudure sur les assemblages PEKK-A/SC, augmenter la cristallisation du joint est une des possibilités. Cela permettra de rendre plus homogène la ZAT et d'améliorer les propriétés morphologiques et mécaniques des assemblages. Pour y parvenir, il s'avère nécessaire d'effectuer un traitement thermique post-soudage sur les assemblages. Le traitement thermique qui permet de cristalliser la matière est le recuit. Le recuit se réalise sur les assemblages dans un four hermétique à température et temps fixe.

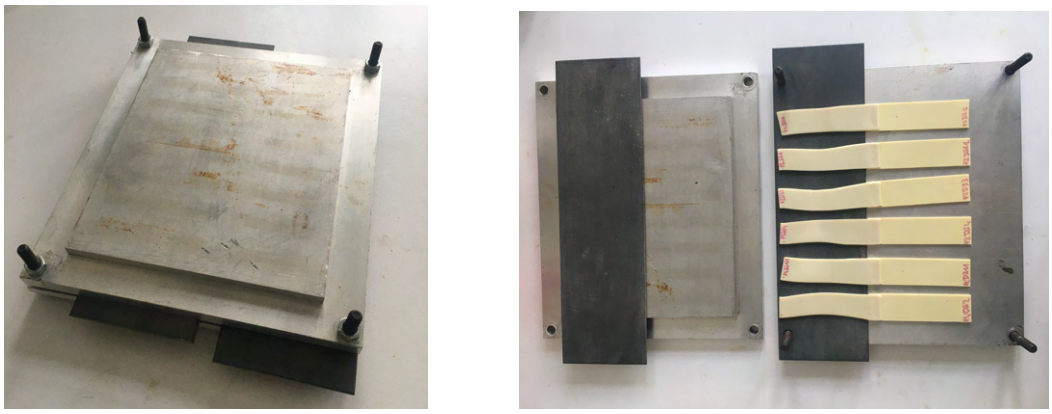

(a) (b)

Figure 14: Moule fabriqué pour le recuit des assemblages soudés : a) fermé et b) ouvert avec les assemblages recuits.

Les tests préliminaires de recuit ont été effectués sur des assemblages PEKK-A/SC pour trouver la température et le temps requis pour réussir une cristallisation élevée au niveau du

joint. Un moule a été aussi conçu (Figure 14) pour assurer le recuit homogène des assemblages, tout en évitant la déformation des pièces assemblées. À partir de ces tests préliminaires de recuit, la température et le temps de recuit ont été sélectionnés : un recuit de 3 h à 190 °C pour huit assemblages dans le moule.

Des nouveaux assemblages en PEKK-A/SC ont été réalisés comme pour la première campagne de soudage. Pour cette nouvelle campagne, seulement deux puissances ont été étudiées : P2 et P4. Ces valeurs de puissance ont été sélectionnées à partir de résultats de la première campagne : P2 étant la valeur de puissance qui a donné la résistance en LSS la plus importante, tandis que P4 a donné la résistance en LSS la plus faible, comme cela peut être observé sur la Figure 11. Les deux épaisseurs de 2 et 4 mm de la pièce PEKK-A (semi-transparent) restent identiques pour l'étude. Quatre assemblages ont été réalisés par puissance et épaisseur, pour obtenir un total de 16 assemblages pour l'étude. Les soudures ont été effectuées de la même manière que pour la première étude. Après soudage, tous les assemblages ont été recuits dans le moule à l'intérieur du four à 190 °C pour 3 h. Après recuit, les assemblages ont été caractérisés mécaniquement et morphologiquement en utilisant les mêmes méthodes que pour les soudures non recuites. Les assemblages soudés qui ont subi un recuit après le soudage sont appelés « PEKK-Ac/SC » pour les distinguer des assemblages non recuits (PEKK-A/SC).

La Figure 15 montre la section transversale d'un assemblage recuit, comparé avec les sections transversales avant et après soudage. La ZAT du joint recuit présente une coloration plus homogène que celle du joint obtenu après soudage (Figure 12). En effet, la section transversale complète de l'assemblage cristallisé ne présente qu'une seule coloration, qui est beige. La présence de cette couleur sur les échantillons de PEKK 70/30 indique que le matériau a une forte cristallinité. On peut donc en déduire que le joint de soudure obtenu après recuit est homogène en termes de cristallinité.

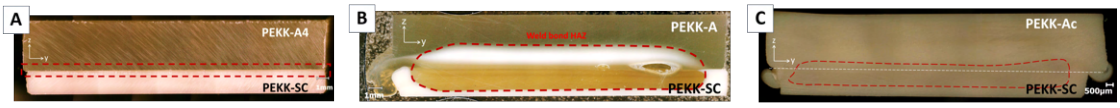

Figure 15: Coupe transversale du joint de soudure le long du chemin de soudage de l'assemblage PEKK-A4/SC A) avant, B) après le soudage et C) après recuit post-soudage.

Les valeurs de résistance au cisaillement (LSS) des assemblages recuits sont présentées dans la Figure 16 et comparées à celles obtenues pour les assemblages PEKK-A/SC NC. La résistance de la soudure diminue avec la puissance pour chaque combinaison d'assemblage. Néanmoins, des valeurs de résistance plus élevées sont obtenues pour les assemblages cristallisés. La résistance des assemblages augmente de plus de 10 % lorsqu'ils sont cristallisés.

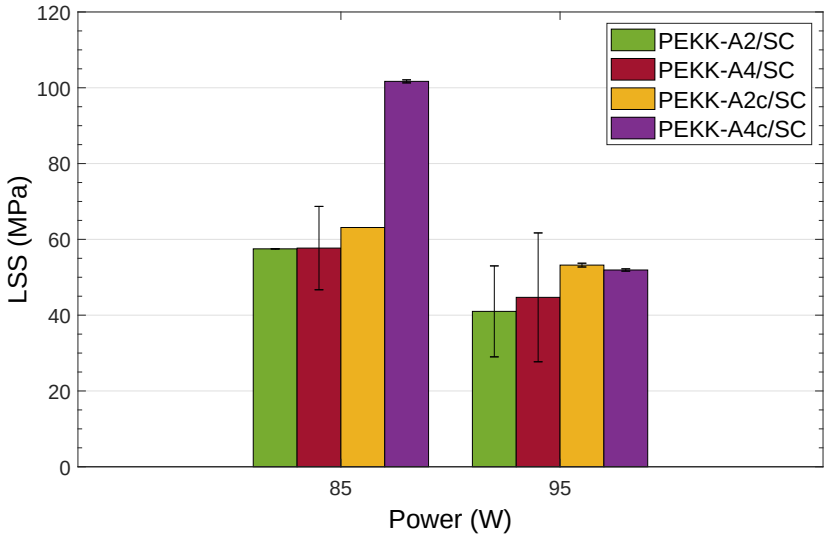

Figure 16: Résistance au cisaillement (LSS) des assemblages PEKK recuits (PEKK-Ac/SC) comparés aux assemblages PEKK non recuits (PEKK-A/SC).

Modélisation du soudage laser par transmission des pièces PEKK

Les questions générées par les modifications de la structure cristalline du matériau observées au cours du procédé LTW des pièces en PEKK sont censées trouver une réponse ici. Les méthodes expérimentales ne sont pas bien adaptées pour répondre à ces questions. La surveillance de la température à l'interface de la soudure et la mesure de la cristallinité du joint de soudure développée en raison des gradients thermiques sont difficiles à caractériser. Pour surmonter ces difficultés, la modélisation du procédé LTW est devenue un outil fonctionnel.

Des modèles de calcul pour simuler le procédé de LTW des thermoplastiques ont été utilisés et étudiés depuis le début des années 2000 [Becker and Potente, 2002]. Les modèles numériques et les simulations ont été utilisés pour fournir des informations qu'il est difficile d'obtenir par les seules méthodes expérimentales. En outre, les modèles peuvent être utilisés pour prédire l'influence de divers paramètres sur les propriétés de la soudure et peuvent aider à optimiser le procédé pour différents matériaux et géométries [Hu et al., 2023].

Les simulations numériques constituent un outil et un domaine de choix pour l'étude du procédé et des paramètres de LTW. Lorsqu'il s'agit de déterminer les paramètres du procédé de soudage, les simulations numériques peuvent fournir une approche plus systématique et plus efficace que les méthodes conventionnelles d'essai et d'erreur. En outre, les simulations numériques peuvent aider à comprendre les mécanismes de soudage en analysant l'impact des propriétés des matériaux et des paramètres du procédé sur la distribution de la température, la concentration des contraintes ou les dimensions du joint de soudure. Cela peut conduire à l'optimisation du procédé de soudage et à l'amélioration de la qualité du joint soudé. L'utilisation d'une approche de simulation numérique fournit une base théorique solide pour anticiper les conditions idéales et optimiser les opérations de LTW.

Dans le cas de cette étude, la modélisation numérique est employée pour mieux comprendre les mécanismes complexes de cristallisation observés dans les expériences de soudage laser transmission de pièces en PEKK-A/SC. Le procédé de soudage par transmission laser est simulé à l'aide du logiciel MatLab en résolvant les différents modèles par la méthode des différences finies.

Les modélisations du procédé de soudage laser par transmission ont été réalisées sur MatLab en appliquant la méthode des différences finies. Ces modélisations consistent à résoudre l'équation de transfert de la chaleur à chaque pas de temps, tout en incluant une source de chaleur qui est générée par le laser. Et de faire évoluer la cristallinité de la matière avec l'évolution de la température due à l'irradiation laser.

La géométrie du modèle est montrée sur la Figure 17a. Cette géométrie représente la section chevauchée des assemblages dans l'espace 3D pour le domaine. Comme dans les conditions expérimentales, le PEKK-A est placé sur le PEKK-SC. Les propriétés matériau caractérisées au préalable expérimentalement ont été utilisés pour alimenter le modèle et le rendre plus proche de la réalité.

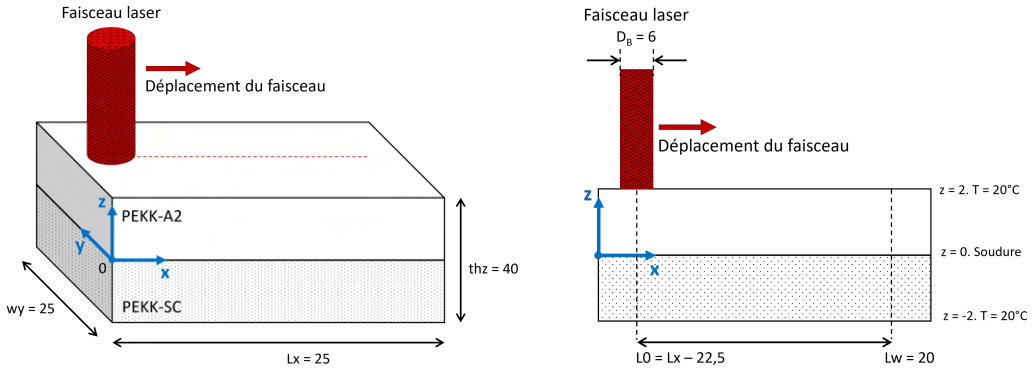

(a) (b)

Figure 17: Représentation schématique de (a) la géométrie du modèle et (b) ses conditions limites.

Hypothèses prises en compte pour la modélisation :

- Un contact parfait est supposé à l'interface entre les deux pièces, cela pour simuler la pression de serrage appliqué sur les conditions expérimentales.
- Densité et conductivité thermique de la matière sont supposé constantes.
- Les conditions limites sont spécifiés dans les surfaces supérieure et inférieure de l'assemblage, avec une température ambient de 20 °C (Figure 17b).

Dans la simulation, comme dans les essais expérimentaux, le laser irradie l'interface de la zone chevauchée dans son centre. Cette irradiation est appliquée dans la surface supérieure de la pièce PEKK-A pour la modélisation. L'irradiation est modélisée avec l'équation d'un laser à profile Gaussien qui est en mouvement dans l'axe X pour chaque pas de temps t [s] à une vitesse v [mm/min] et avec une puissance initiale égale à P_{top} [W], montrée ci-dessous :

$$I(x,y,t) = \frac{P_{top}}{2\pi.\sigma^2} exp\left[\frac{-(x - v\cdot t - 0,0025)^2 + (y - \frac{wy}{2})^2}{2\sigma^2}\right]$$

Avec P_{top} = P_o× 0,83 et v = 60 mm/min. P_o étant la puissance du laser qui arrive à la surface supérieure de la pièce PEKK-A.

Ensuite, les modèles utilisés pour la simulation sont présentés dans le Tableau 4. Avec les propriétés matériau déjà mentionnées et caractérisées dans la partie *Matériau d'étude*. Et avec $0 \leq X_c \leq X_\infty$, $X_\infty = 0,27$, $w_1 = 0,78$ et $w_2 = 1 - w_1$.

Modèle	**Équation**
Transfert de la chaleur	$\rho C_p \frac{\partial T}{\partial t} = k \cdot \nabla^2 T + Q(x,y,z,t)$
Source de chaleur	$Q(x,y,z,t) = \alpha(X_c) \cdot [1 - R_i] \cdot I(x,y,t) \cdot exp[-\alpha(X_c) \cdot z]$
Propriétés d'absorption	$\alpha(X_c) = 2124 \cdot X_c - 32$
Cinétique de cristallisation	$X_c = [w_1 \cdot X_1(t) + w_2 \cdot X_2(t)] \times X_\infty$

Table 4: Modèles employés pour simuler le soudage laser par transmission des pièces PEKK-A/SC

Ces modélisations ont permis d'observer l'évolution des différentes variables étudies au niveau du joint : la température, la zone affectée thermiquement et la cristallinité du joint.

La Figure 18 montre le champ de température obtenu pour le premier et dernier second d'irradiation du laser. Ce champ est montré dans la section transversal de l'assemblage au long du chemin parcouru par le laser. La figure montre que le champ de température n'est pas homogène entre les parties supérieure et inférieure. Il s'étend au fur et à mesure que le laser se déplace. Cela indique que les deux échantillons ont fondu dans leur volume lors du processus d'irradiation, mais dans une épaisseur différente, comme cela a été observé expérimentalement.

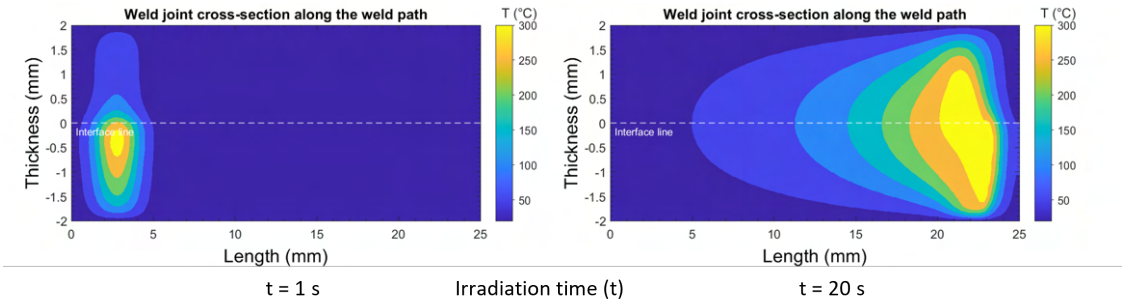

Figure 18: Champ de température pendant l'irradiation du laser.

La Figure 19 montre le champ de cristallinité à la section transversale du joint de soudure. Comme nous pouvons le constater, deux zones identifiables sont obtenues comme dans les conditions expérimentales. Une zone amorphe 1 couvrant les deux échantillons, et une zone cristallisée à froid 2 se développant sur la zone 1.

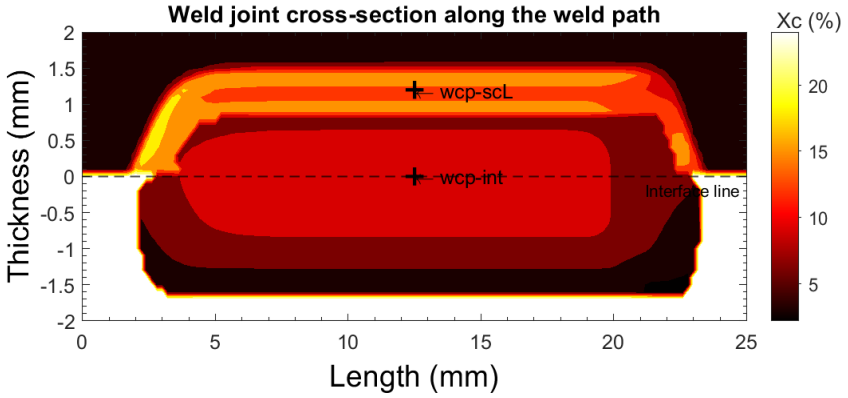

Figure 19: Champ de cristallinité obtenu après soudage.

Si l'on observe les courbes de température et de cristallinité (Figure 20), on peut établir une corrélation entre la vitesse de chauffage élevée du processus de soudage et les phénomènes de fusion. Et la vitesse de refroidissement élevée avec la difficulté du PEKK-SC à recristalliser après la fusion, et avec la cristallisation froide acquise sur l'échantillon de PEKK-A au-dessus de la couche fondue.

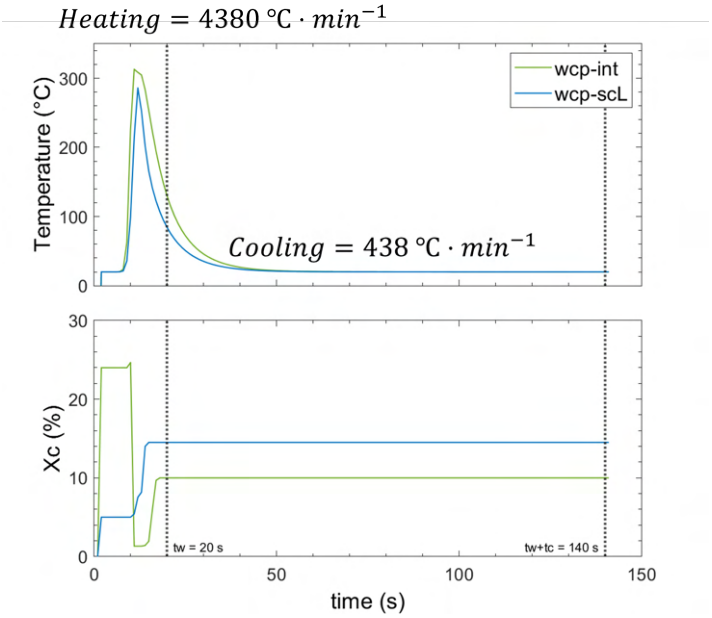

Figure 20: Évolution de la température (T) et de la cristallinité (Xc) du joint pendant le soudage.

Les simulations ont également été exécutées pour quatre différentes puissances de laser et comparées aux résultats expérimentaux, comme montré dans la Figure 21. La morphologie du joint de soudure prédite par la modélisation numérique est conforme et comparable aux résultats expérimentaux obtenus lors de la soudure au laser de PEKK-A2/SC.

Comme on peut le remarquer, la forme de la ZAT du joint de soudure simulé est similaire à la forme expérimentale : une forme ovale avec un gradient de cristallinité, d'un Xc faible à un Xc élevé, avec une transition du bas vers le haut. Ainsi, les deux zones définies à l'intérieur du joint de soudure sont détectables dans les quatre assemblages simulés. De plus, les dimensions peuvent être mesurées. Et ces zones changent de profondeur avec la valeur de la puissance, avec des profondeurs similaires à celles observées expérimentalement.

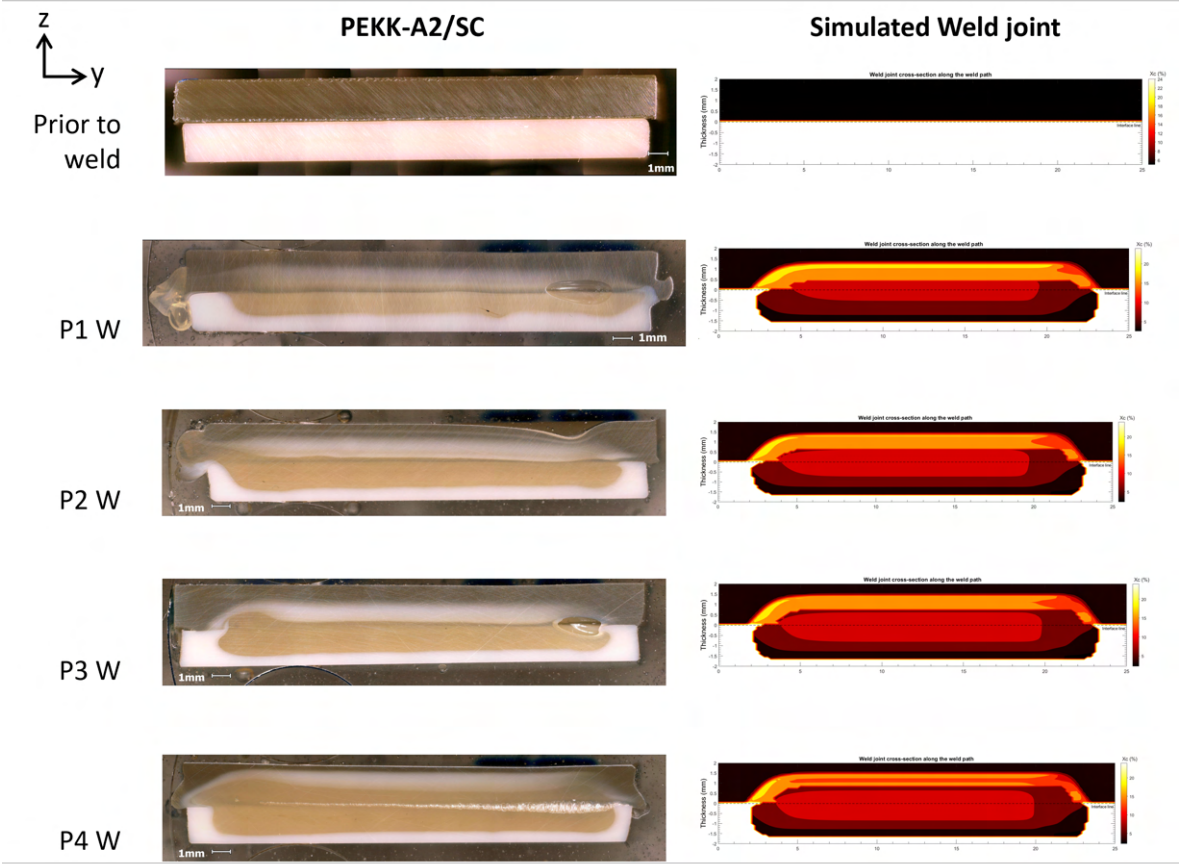

Figure 21: Morphologie du joint soudé. Résultats expérimentaux et numériques.

Soudage laser par transmission du PEKK composite

Jusqu'à présent, aucune étude n'a été trouvée dans la littérature sur le soudage d'échantillons de PEKK chargé de fibres courtes de carbone par LTW. Cependant, certaines études ont été réalisées sur le soudage par LTW d'échantillons de PEEK et fibres de carbone, un thermoplastique semi-cristallin de la même famille que le PEKK. *Vacogne et Wise*, 2011 ont soudé des films amorphes de PEEK de 300 microns à du PEEK avec de tapes de fibres de carbone de 175 microns [Vacogne and Wise, 2011]. *Liu et al.*, 2022 a étudié le procédé LTW entre la résine PEEK et le PEEK renforcé par des fibres de carbone unidirectionnelles en utilisant des films de 0,2 mm d'épaisseur pour les deux échantillons [Liu et al., 2022]. *Korycki et al.*, 2022 ont soudé du polyetherimide (PEI) de 1,2 et 4 mm d'épaisseur à du PEEK à fibres de carbone de 1 mm d'épaisseur [Korycki et al., 2022]. Dans toutes ces études, les échantillons de PEEK en fibre de carbone ont été utilisés comme partie absorbante inférieure pour le procédé de soudage par transmission laser. Par conséquent, pour réaliser le soudage laser transmission d'échantillons composites en fibre de carbone, ceux-ci doivent être soudés avec un échantillon thermoplastique amorphe ou semi-transparent sur la partie supérieure. Ainsi, dans la présente étude, les échantillons PEKK-CF sont soudés aux échantillons PEKK-A dans une configuration de chevauchement où le PEKK-A est placé sur le PEKK-CF, comme montré dans la Figure 22. Cette configuration d'assemblage est appelée *PEKK-A/CF* pour l'étude.

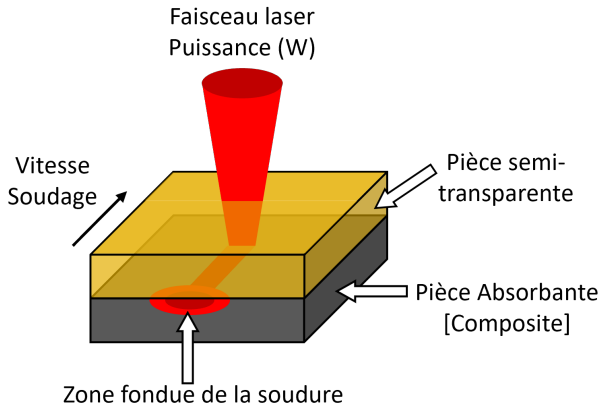

Figure 22: Schéma représentant la configuration d'assemblage PEKK-A/CF.

Le PEKK-CF a été fournie par la société Arkema, France. Ces sont des plaques injectées en PEKK 8010 chargées de fibres de carbone courtes à 30 % en masse (PEKK-CF) en 2 mm d'épaisseur. Les plaques injectées en PEKK-A ont été fabriquées pour l'étude en 2 et 4 mm d'épaisseur, appelées PEKK-A2 et PEKK-A4, respectivement. Par conséquent, deux configurations d'assemblage sont étudiées : PEKK-A2/CF et PEKK-A4/CF.

Avant soudage, une campagne d'interaction laser- matière (LMI) est menée sur la configuration de chevauchement PEKK-A/CF. Les tests LMI ont permis de définir la fenêtre de soudabilité pour le soudage laser par transmission du PEKK-A/CF pour un laser diode à 975 nm comme longueur d'onde. Cette fenêtre de soudabilité es montré dans le diagramme de la

Figure 23. Ensuite, les paramètres de soudage de l'étude concernant la vitesse de balayage et la puissance du laser sont délimités à partir du test LMI et de la fenêtre de soudabilité définie. Trois puissances de laser différentes ont été étudiées pour irradier l'interface des assemblages : P1 (12 W), P2 (18 W) et P3 (24 W). La soudure a été réalisée à une vitesse constante de 10 mm/s avec un diamètre de faisceau de 5 mm.

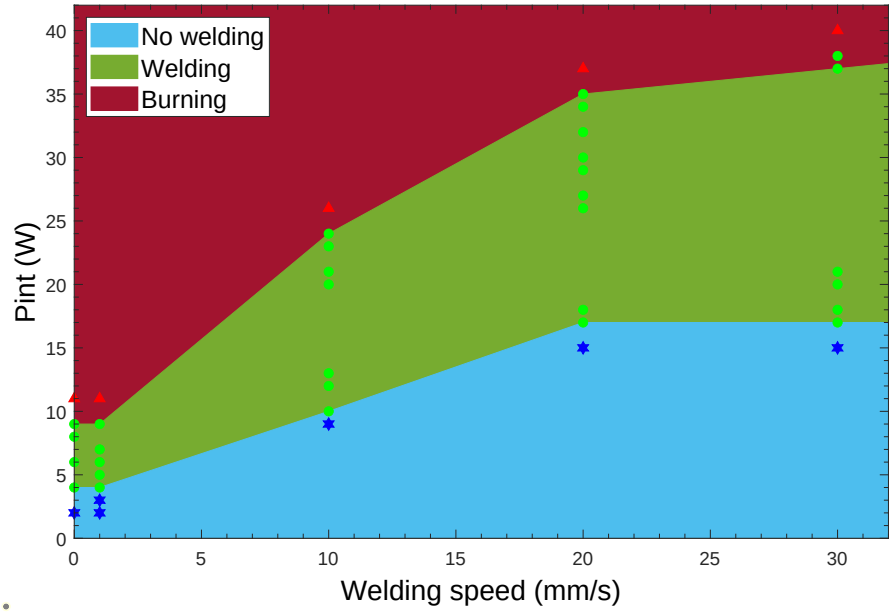

Figure 23: Fenêtre de soudabilité des pièces PEKK-A/CF.

Cinq soudures ont été réalisées par configuration d'assemblage et par puissance. Les joints de soudure des assemblages post-soudés ont été observés au microscope à travers l'échantillon PEKK-A afin de caractériser leur forme et leurs dimensions. Ensuite, tous les assemblages ont été testés mécaniquement par un essai de cisaillement à recouvrement unique (SLS en anglais). La plupart des assemblages se sont rompus au niveau de la pièce PEKK-CF, à proximité du joint de soudure. Ce type de rupture est appelé *substrat près du joint* (SNJ en anglais). Les assemblages PEKK-A2/CF soudés avec P3 ont subi une rupture interfaciale (sur ces assemblages, la zone irradiée a brûlé lors du soudage). Les assemblages SNJ après rupture ont été étudiés au microscope sur sa section transversale au long du trajet soudé.

La Figure 24 montre des micrographies représentatives des joints de soudure développés sur les assemblages PEKK-A/CF pour chaque niveau de puissance employée. Dans les micrographies on peut observer la ZAT des joints de soudure à l'interface de l'assemblage. Les observations ont été effectués à partir de l'échantillon supérieur PEKK-A qui, étant semi-transparent, nous permets de visualiser l'interface du joint. Comme il est observable dans la Figure 24 à gauche, les ZAT développées dans les assemblages PEKK-A2/CF ont une forme de commette avec une largeur qui augmente avec la longueur. Dans les assemblages PEKK-A4/CF (Figure 24 à droite), les ZAT sont plus constantes en largeur dans sa longueur. Les ZAT observés pour les puissances de 12 et 18 W montrent une surface à coloration noire et homogène. Sur les joints de soudure obtenus avec la P3 (24 W), la ZAT montre une coloration

non homogène, entre noir et jaune. Ici on peut déduire que des vides ou zones brulés sont présents dans la ZAT, ce qui génère un manque de cohésion dans la zone irradiée, donc une soudure moins performante. Il faut donc faire attention avec la puissance maximale employé pour éviter des zones sans cohésion dans la zone irradiée.

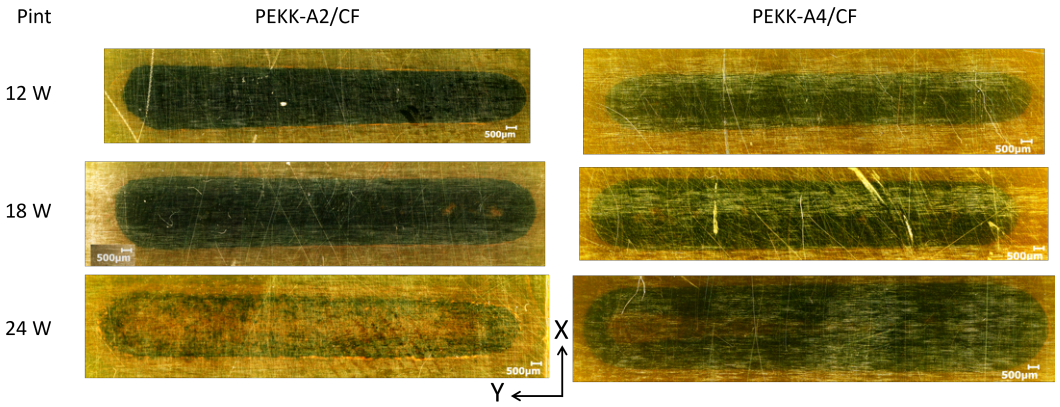

Figure 24: Micrographies des joints de soudure des assemblages PEKK-A/CF.

Figure 25 montre les dimensions des ZAT dans les joints de soudure obtenus pour chaque puissance et configuration d'assemblage. La longueur (Lw) est mesurée dans l'axe Y, correspondant à la longueur maximale de la ZAT. Tandis que la largeur (Wc) est mesurée dans l'axe X au centre de la longueur obtenue de la ZAT. Dans l'ensemble, ses dimensions augmentent avec la puissance utilisée pour souder l'assemblage. À l'exception des assemblages PEKK-A2/CF soudés avec P3, qui montrent une chute après P2. Cette diminution dans les dimensions de la ZAT à la puissance maximal peut être liée à que la zone irradiée a été brulé, ce qui a empêché la diffusion de la chaleur, contraignant aussi la génération d'une zone fondue et soudé plus ample.

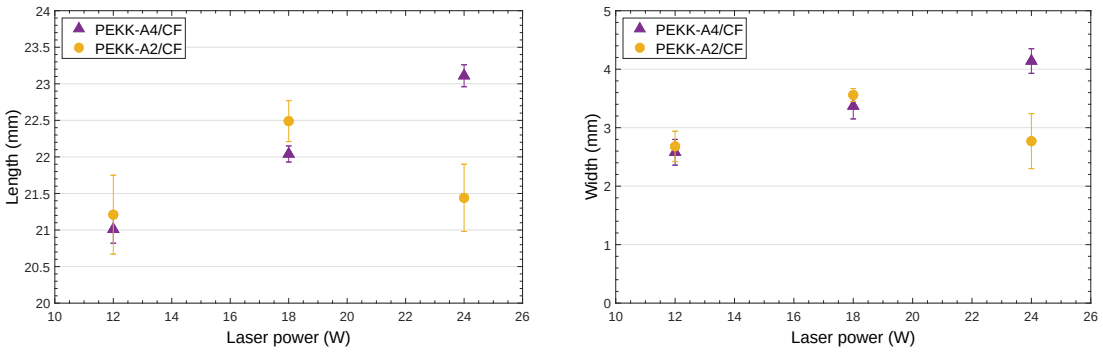

(a) (b)

Figure 25: (a) Longueur et (b) largeur des ZAT des joints de soudure des assemblages PEKK-A/CF.

Dans la Figure 26 on peut observer la résistance mécanique des assemblages (LSS) pour chaque puissance de soudage et configuration d'assemblage employées. La résistance des assemblages augmente en augmentant la puissance de P1 à P2. Après, de P2 à P3, cette résistance diminue, cela dû à l'apparition de vides et/ou zones brulés à l'intérieur du joint. Cette diminution est plus marquée dans les assemblages PEKK-A2/CF indiquant une faible, ou nulle, cohésion au niveau du joint. Ainsi, comme indiqué auparavant dans les morphologies des ZAT, la puissance maximale à utiliser doit être optimisé pour éviter de surchauffer la zone irradié et obtenir une meilleure soudure.

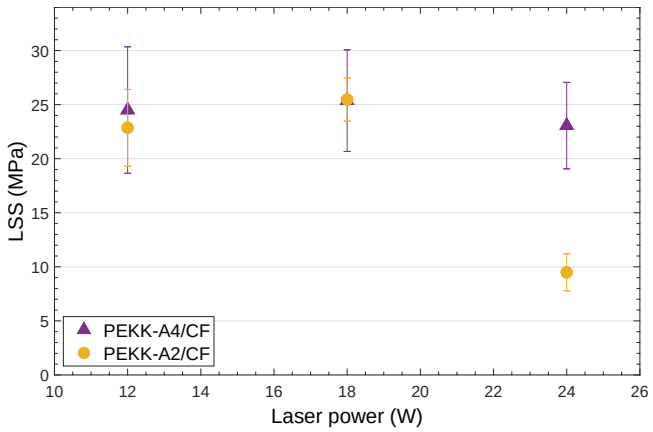

Figure 26: Resistance mécanique (LSS) des assemblages PEKK-A/CF.

Appendix A

Drying protocol for PEKK 7002 pellets

---

1. Samples preparation: a quantity (30.6 g) of pelleted polymer was distributed in three glass containers.
2. Samples initial mass: the initial mass of each sample was measured with a digital scale with 0.01 mg of precision. This initial mass will be considered the 100% value of the mass for each sample.
3. Oven: the oven was programmed at 120°C. Then, the three samples were put into the oven to begin the drying process.
4. Mass tracking: the mass of each sample was check at each drying hour from 7 hours. Then they were checked after 22, 24 and 30 hours of drying.
5. Final mass lost: the final mass lost was identified after the last check for each sample.
6. Results tracking and visualization: the mass was tracked in a table for each sample at each hour indicated. Then, the mass lost evolution was traced in a graph, using the mass percentage.

Appendix B

Mass lost tracking when drying PEKK 7002 pellets samples

Drying time (hr)	**mass B1 (g)**	**mass B1 (%)**	**mass B2 (g)**	**mass B2 (%)**	**mass B3 (g)**	**mass B3 (%)**	**Average (%)**
0	10.21618	100.00%	10.25618	100.00%	10.21543	100.00%	100.000%
1	10.20652	99.91%	10.24222	99.86%	10.20027	99.85%	99.874%
2	10.19939	99.84%	10.23707	99.81%	10.19629	99.81%	99.821%
3	10.19897	99.83%	10.23648	99.81%	10.19503	99.80%	99.813%
4	10.19870	99.83%	10.23538	99.80%	10.1948	99.80%	99.808%
5	10.19819	99.82%	10.23539	99.80%	10.19454	99.80%	99.806%
6	10.19782	99.82%	10.23477	99.79%	10.19433	99.79%	99.802%
7	10.19715	99.81%	10.23469	99.79%	10.19383	99.79%	99.798%
22	10.19602	99.80%	10.23333	99.78%	10.19305	99.78%	99.787%
24	10.19625	99.80%	10.23326	99.78%	10.19283	99.78%	99.787%
30	10.19640	99.81%	10.23334	99.78%	10.19277	99.78%	99.787%
Total Lost	0.01978	0.19%	0.02284	0.22%	0.02266	0.22%	0.21%

Table 5: Mass of the PEKK pellets samples (in grams and in percentage) for each time monitored.

Drying time (hr)	Mass lost (%)	Moisture content lost (%)
0	0.00	0
1	0.13	59
2	0.18	84
3	0.19	88
4	0.19	90
5	0.19	91
6	0.20	93
7	0.20	95
22	0.21	100
24	0.21	100
30	0.21	100

Table 6: Mass lost and moisture content lost in % per drying time. Average values.

Bibliography

[Abed et al., 2001] Abed, S., Laurens, P., Carrétéro, C., Deschamps, J. R., and Duval, C. (2001). Diode laser welding of polymers: Microstructures of the welded zones for polypropylene. In *International Congress on Applications of Lasers & Electro-Optics*, pages 1499–1507, Jacksonville, Florida, USA. Laser Institute of America.

[Acherjee, 2019] Acherjee, B. (2019). 3-d fe heat transfer simulation of quasi-simultaneous laser transmission welding of thermoplastics. *Journal of the Brazilian Society of Mechanical Sciences and Engineering*, 41(10):466.

[Acherjee, 2020] Acherjee, B. (2020). Laser transmission welding of polymers – A review on process fundamentals, material attributes, weldability, and welding techniques. *Journal of Manufacturing Processes*, 60:227–246.

[Acherjee, 2021a] Acherjee, B. (2021a). Laser transmission welding of polymers–a review on welding parameters, quality attributes, process monitoring, and applications. *Journal of Manufacturing Processes*, 64:421–443.

[Acherjee, 2021b] Acherjee, B. (2021b). State-of-art review of laser irradiation strategies applied to laser transmission welding of polymers. *Optics & Laser Technology*, 137:106737.

[Acherjee et al., 2010] Acherjee, B., Kuar, A., Mitra, S., and Misra, D. (2010). Selection of process parameters for optimizing the weld strength in laser transmission welding of acrylics. *Proceedings of the Institution of Mechanical Engineers, Part B: Journal of Engineering Manufacture*, 224(10):1529–1536.

[Acherjee et al., 2011] Acherjee, B., Kuar, A. S., Mitra, S., and Misra, D. (2011). Modeling and analysis of simultaneous laser transmission welding of polycarbonates using an fem and rsm combined approach. *Optics & Laser Technology*, 44(4):995–1006.

[Acherjee et al., 2012] Acherjee, B., Kuar, A. S., Mitra, S., and Misra, D. (2012). Modeling of laser transmission contour welding process using fea and doe. *Optics & Laser Technology*, 44(5):1281–1289.

[Acherjee et al., 2013] Acherjee, B., Kuar, A. S., Mitra, S., and Misra, D. (2013). Finite element simulation of laser transmission thermoplastic welding of circular contour using a moving heat source. *International Journal of Mechatronics and Manufacturing Systems*, 6(5-6):437–454.

[Aden et al., 2013] Aden, M., Liviany, F., and Olowinsky, A. (2013). Joint strength for laser transmission welding of thermoplastics: a simulation approach. *International Polymer Processing*, 28(1):79–83.

[Ageorges et al., 2001] Ageorges, C., Ye, L., and Hou, M. (2001). Advances in fusion bonding techniques for joining thermoplastic matrix composites: a review. *Composites Part A: Applied Science and Manufacturing*, 32(6):839–857.

[Akué Asséko et al., 2015] Akué Asséko, A. C., Cosson, B., Deleglise, M., Schmidt, F., Le Maoult, Y., and Lafranche, E. (2015). Analytical and numerical modeling of light scattering in composite transmission laser welding process. *International Journal of Material Forming*, 8:127–135.

[Alqurashi et al., 2021] Alqurashi, H., Khurshid, Z., Syed, A. U. Y., Habib, S. R., Rokaya, D., and Zafar, M. S. (2021). Polyetherketoneketone (pekk): An emerging biomaterial for oral implants and dental prostheses. *Journal of Advanced Research*, 28:87–95.

[Amanat et al., 2011] Amanat, N., Chaminade, C., Grace, J., James, N. L., and McKenzie, D. R. (2011). Optimal process parameters for thermoplastic polyetheretherketone joints fabricated using transmission laser welding and lumogen® ir absorptive pigment. *Journal of Laser Applications*, 23(1).

[Amanat et al., 2010] Amanat, N., James, N. L., and McKenzie, D. R. (2010). Welding methods for joining thermoplastic polymers for the hermetic enclosure of medical devices. *Medical Engineering & Physics*, 32(7):690–699.

[Arkema, 2021] Arkema (2021). *Technical Data. Kepstan 7000 series.*

[Arkema, 2023] Arkema (2023). *Technical Data. Kepstan 8010C30.*

[Arkema, 2024] Arkema, I. (2024). kepstan pekk polymer range.

[Asseko and Cosson, 2023] Asseko, A. C. A. and Cosson, B. (2023). Soudage laser par transmission de composites. *Techniques de l'ingénieur.*

[Asseko et al., 2016] Asseko, A. C. A., Cosson, B., Lafranche, É., Schmidt, F., and Le Maoult, Y. (2016). Effect of the developed temperature field on the molecular interdiffusion at the interface in infrared welding of polycarbonate composites. *Composites Part B: Engineering*, 97:53–61.

[Asséko et al., 2015] Asséko, A. C. A., Cosson, B., Schmidt, F., Le Maoult, Y., Gilblas, R., and Lafranche, E. (2015). Laser transmission welding of composites–part b: Experimental validation of numerical model. *Infrared Physics & Technology*, 73:304–311.

[Atanasov, 1995] Atanasov, P. A. (1995). Laser welding of plastics: theory and experiments. *Optical Engineering*, 34(10):2976.

[Avakian et al., 1990] Avakian, P., Gardner, K., and Matheson Jr, R. (1990). A comment on crystallization in pekk and peek resins. *Journal of Polymer Science Part C: Polymer Letters*, 28(8):243–246.

[Avenet, 2021] Avenet, J. (2021). *Assemblage par fusion de composites à matrice thermoplastique : Caractérisation expérimentale et modélisation de la cinétique d'auto-adhésion hors équilibre.* PhD thesis, Université de Nantes, France.

[Avrami, 1939] Avrami, M. (1939). Kinetics of Phase Change. I General Theory. *The Journal of Chemical Physics*, 7(12):1103–1112. Publisher: American Institute of Physics.

[Bachmann and Russek, 2002] Bachmann, F. G. and Russek, U. A. (2002). Laser welding of polymers using high-power diode lasers. In *Photon Processing in Microelectronics and Photonics*, volume 4637, pages 505–518. SPIE.

[Bachmann et al., 2000] Bachmann, F. G., Takahashi, R., and Fujishima, S. (2000). Micro materials processing with high-power diode lasers. pages 220–223, Omiya, Saitama, Japan.

[Balkan et al., 2008] Balkan, O., Demirer, H., Ezdeşir, A., and Yıldırım, H. (2008). Effects of welding procedures on mechanical and morphological properties of hot gas butt welded PE, PP, and PVC sheets. *Polymer Engineering & Science*, 48(4):732–746. _eprint: https://onlinelibrary.wiley.com/doi/pdf/10.1002/pen.21014.

[Becker and Potente, 2002] Becker, F. and Potente, H. (2002). A step towards understanding the heating phase of laser transmission welding in polymers. *Polymer Engineering & Science*, 42(2):365–374.

[Berger et al., 2015] Berger, S., Oefele, F., and Schmidt, M. (2015). Laser transmission welding of carbon fiber reinforced thermoplastic using filler material—a fundamental study. *Journal of laser Applications*, 27(S2).

[Blundell and Osborn, 1983] Blundell, D. J. and Osborn, B. N. (1983). The morphology of poly(aryl-ether-ether-ketone). *Polymer*, 24(8):953–958.

[Bölle et al., 2022] Bölle, S., Alms, J., Weihermüller, M., Robisch, M., Wipperfürth, J., Hopmann, C., and Dahlmann, R. (2022). Modelling of the melting point shift in semi-crystalline thermoplastics dependent on prior cooling rate and heating rate. *Polymer*, 254:125100.

[Brandt et al., 1993] Brandt, J., Drechsler, K., and Richter, H. (1993). The use of high-performance thermoplastic composites for structural aerospace applications-status and outlook. *ICCM/9. Composites: Properties and Applications.*, 6:143–150.

[Carrega, 2009] Carrega, M. (2009). *Aide-mémoire - Matières plastiques*. Dunod edition.

[Casalino and Ghorbel, 2008] Casalino, G. and Ghorbel, E. (2008). Numerical model of CO2 laser welding of thermoplastic polymers. *Journal of Materials Processing Technology*, 207(1):63–71.

[Chabert et al., 2020] Chabert, F., Garnier, C., Sangleboeuf, J., Asseko, A. C. A., and Cosson, B. (2020). Transmission laser welding of polyamides: Effect of process parameter and material properties on the weld strength. *Procedia Manufacturing*, 47:962–968.

[Chang, 1988] Chang, I. (1988). Pekk as a new thermoplastic matrix for high-performance composites. *SAMPE Q.;(United States)*, 19(4).

[Chelaghma, 2018] Chelaghma, S. A. (2018). *Fonctionnalisation de composites C/PEKK pour application aérospatiale: caractérisation, modélisation et influence sur les propriétés du composite*. PhD thesis, Université Paul Sabatier-Toulouse III, France.

[Cheng et al., 1996] Cheng, S. Z. D., Ho, R.-M., Hsiao, B. S., and Gardner, K. H. (1996). Polymorphism and crystal structure identification in poly(aryl ether ketone ketone)s. *Macromolecular Chemistry and Physics*, 197(1):185–213. _eprint: https://onlinelibrary.wiley.com/doi/pdf/10.1002/macp.1996.021970115.

[Choupin, 2017] Choupin, T. (2017). *Mechanical performances of PEKK thermoplastic composites linked to their processing parameters*. PhD thesis, ENSAM, Paris, France.

[Choupin et al., 2018] Choupin, T., Fayolle, B., Régnier, G., Paris, C., Cinquin, J., and Brulé, B. (2018). A more reliable dsc-based methodology to study crystallization kinetics: Application to poly (ether ketone ketone)(pekk) copolymers. *Polymer*, 155:109–115.

[Choupin et al., 2017] Choupin, T., Fayolle, B., Régnier, G., Paris, C., Cinquin, J., and Brulé, B. (2017). Isothermal crystallization kinetic modeling of poly(etherketoneketone) (PEKK) copolymer. *Polymer*, 111:73–82.

[Coelho et al., 2003] Coelho, J. M. P., Abreu, M., and Rodrigues, F. C. (2003). Thermal modeling co2 laser radiation transmission welding of superposed thermoplastic films. *Optical Engineering*, 42:3365–3373.

[Coelho et al., 2000] Coelho, J. P., Abreu, M. A., and Pires, M. C. (2000). High-speed laser welding of plastic "lms. *Optics and Lasers in Engineering*.

[Cosson et al., 2009] Cosson, B., Schmidt, F., and Maoult, Y. L. (2009). Numerical infrared heating of semi transparent thermoplastic using ray tracing method. *International Journal of Material Forming*, 2:267–270.

[Costa et al., 2012] Costa, A. P. d., Botelho, E. C., Costa, M. L., Narita, N. E., and Tarpani, J. R. (2012). A review of welding technologies for thermoplastic composites in aerospace applications. *Journal of Aerospace Technology and Management*, 4(3):255–266.

[Dave et al., 2021] Dave, F., Ali, M. M., Sherlock, R., Kandasami, A., and Tormey, D. (2021). Laser transmission welding of semi-crystalline polymers and their composites: A critical review. *Polymers*, 13(5):675.

[Devrient et al., 2011] Devrient, M., Frick, T., and Schmidt, M. (2011). Laser transmission welding of optical transparent thermoplastics. *Physics Procedia*, 12:157–165.

[Doumeng et al., 2021] Doumeng, M., Makhlouf, L., Berthet, F., Marsan, O., Delbé, K., Denape, J., and Chabert, F. (2021). A comparative study of the crystallinity of polyetheretherketone by using density, dsc, xrd, and raman spectroscopy techniques. *Polymer Testing*, 93:106878.

[Dowden, 2001] Dowden, J. M. (2001). *The mathematics of thermal modeling: an introduction to the theory of laser material processing*. Chapman and Hall/CRC.

[ES Laser, 2024] ES Laser, I. (2024). Machine de soudure laser.

[Fink, 2014] Fink, J. K. (2014). Chapter 6 - poly(aryl ether ketone)s. In Fink, J. K., editor, *High Performance Polymers (Second Edition)*, Plastics Design Library, pages 153–175. William Andrew Publishing, second edition edition.

[Friedrich et al., 1995] Friedrich, K., Lu, Z., and Hager, A. (1995). Recent advances in polymer composites' tribology. *Wear*, 190(2):139–144.

[Gardner et al., 1994] Gardner, K. H., Hsiao, B. S., and Faron, K. L. (1994). Polymorphism in poly (aryl ether ketone) s. *Polymer*, 35(11):2290–2295.

[Gardner et al., 1992] Gardner, K. H., Hsiao, B. S., Matheson, R. R., and Wood, B. A. (1992). Structure, crystallization and morphology of poly (aryl ether ketone ketone). *Polymer*, 33(12):2483–2495.

[Geiger et al., 2009] Geiger, M., Frick, T., and Schmidt, M. (2009). Optical properties of plastics and their role for the modelling of the laser transmission welding process. *Production Engineering*, 3:49–55.

[Ghorbel et al., 2009] Ghorbel, E., Casalino, G., and Abed, S. (2009). Laser diode transmission welding of polypropylene: Geometrical and microstructure characterisation of weld. *Materials & Design*, 30(7):2745–2751.

[Gillner et al., 2000] Gillner, A., Bosse, L., Kramer, T., Olowinsky, A. M., and Wild, M. (2000). Laser joining of microcomponents with fiber lasers and diode lasers. In *First International Symposium on Laser Precision Microfabrication*, volume 4088, pages 260–263. SPIE.

[Gonçalves et al., 2021] Gonçalves, L. F. F. F., Duarte, F. M., Martins, C. I., and Paiva, M. C. (2021). Laser welding of thermoplastics: An overview on lasers, materials, processes and quality. *Infrared Physics & Technology*, 119:103931.

[Goyal and Kant, 2023] Goyal, D. K. and Kant, R. (2023). Mechanism of bonding during laser transmission welding using EIP absorber. *Materials and Manufacturing Processes*, 38(4):485–493.

[Goyal et al., 2022] Goyal, D. K., Yadav, R., and Kant, R. (2022). An integrated hybrid methodology for estimation of absorptivity and interface temperature in laser transmission welding. *The International Journal of Advanced Manufacturing Technology*, 121(5):3771–3786.

[Hillier, 1965] Hillier, I. H. (1965). Modified avrami equation for the bulk crystallization kinetics of spherulitic polymers. *Journal of Polymer Science Part A: General Papers*, 3(9):3067–3078. _eprint: https://onlinelibrary.wiley.com/doi/pdf/10.1002/pol.1965.100030902.

[Ho et al., 1995] Ho, R., Cheng, S. Z. D., Hsiao, B. S., and Gardner, K. H. (1995). Crystal morphology and phase identification in poly(aryl ether ketone)s and their copolymers. 3. polymorphism in a polymer containing alternated terephthalic acid and isophthalic acid isomers. *Macromolecules*, 28:1938–1945.

[Ho et al., 1994] Ho, R.-M., Cheng, S. Z., Hsiao, B. S., and Gardner, K. H. (1994). Crystal morphology and phase identifications in poly (aryl ether ketone) s and their copolymers. 1. polymorphism in pekk. *Macromolecules*, 27(8):2136–2140.

[Hsiao et al., 1991a] Hsiao, B. S., Chang, I. Y., and Sauer, B. B. (1991a). Isothermal crystallization kinetics of poly (ether ketone ketone) and its carbon-fibre-reinforced composites. *Polymer*, 32(15):2799–2805.

[Hsiao et al., 1991b] Hsiao, B. S., Chang, I. Y., and Sauer, B. B. (1991b). Isothermal crystallization kinetics of poly(ether ketone ketone) and its carbon-fibre-reinforced composites. *Polymer*, 32(15):2799–2805.

[Hsiao et al., 1994] Hsiao, B. S., Gardner, K. H., and Cheng, S. Z. (1994). Crystallization of poly (aryl ether ketone ketone) copolymers containing terephthalate/isophthalate moieties. *Journal of Polymer Science Part B: Polymer Physics*, 32(16):2585–2594.

[Hu et al., 2023] Hu, S., Li, F., and Zuo, P. (2023). Numerical simulation of laser transmission welding—a review on temperature field, stress field, melt flow field, and thermal degradation. *Polymers*, 15(9):2125.

[Inc., 2018] Inc., A. (2018). Kepstan® pekk general brochure. Available on the website of Arkema https://hpp.arkema.com/en/product-families/kepstan-pekk-polymer-range/literature/, 900 First Avenue King of Prussia, PA 19406. This is the general brochure of Kepstan PEKK material conculted in 2021.

[Jankus and Bendikiene, 2022] Jankus, S. M. and Bendikiene, R. (2022). Effect of the melt-down on thermoplastic joint produced by quasi-simultaneous laser transmission welding. *CIRP Journal of Manufacturing Science and Technology*, 39:104–114.

[Jones, 2002] Jones, I. A. (2002). Laser welding for plastic components. *Assembly Automation*, 22:129–135.

[Juhl et al., 2013a] Juhl, T. B., Christiansen, J. d., and Jensen, E. A. (2013a). Investigation on high strength laser welds of polypropylene and high-density polyethylene. *Journal of Applied Polymer Science*, 129(5):2679–2685.

[Juhl et al., 2013b] Juhl, T. B., de Claville Christiansen, J., and Jensen, E. A. (2013b). Mechanical testing of polystyrene/polystyrene laser welds. *Polymer testing*, 32(3):475–481.

[Kagan and Bray, 2001] Kagan, V. and Bray, R. G. (2001). Advantages and limitations of laser welding technology for semi-crystalline reinforced plastics. In *International Congress on Applications of Lasers & Electro-Optics*, pages 1218–1227, Jacksonville, Florida, USA. Laser Institute of America.

[Kagan et al., 2002] Kagan, V. A., Bray, R. G., and Kuhn, W. P. (2002). Laser Transmission Welding of Semi-Crystalline Thermoplastics—Part I: Optical Characterization of Nylon Based Plastics. *Journal of Reinforced Plastics and Composites*, 21(12):1101–1122.

[Ke and Wu, 1998] Ke, Y.-C. and Wu, Z. (1998). The absorption behavior and crystallization of poly (aryl ether ketone) films. *Journal of applied polymer science*, 67(12):2065–2075.

[Klein, 2012] Klein, R. (2012). *Laser welding of plastics: materials, processes and industrial applications*. John Wiley & Sons.

[Korycki et al., 2022] Korycki, A., Garnier, C., Bonmatin, M., Laurent, E., and Chabert, F. (2022). Assembling of carbon fibre/peek composites: Comparison of ultrasonic, induction, and transmission laser welding. *Materials*, 15(18):6365.

[Kumar and Bandyopadhyay, 2021] Kumar, N. and Bandyopadhyay, A. (2021). A state-of-the-art review of laser welding of polymers—part ii: Weld-quality studies. *Welding Journal*, 100:249–258.

[Liu et al., 2022] Liu, Y., Zhang, W., Liu, J., Guan, Y., and Ding, X. (2022). Study on microstructures and mechanical performance of laser transmission welding of poly-ether-ether-ketone (peek) and carbon fiber reinforced peek (cfr-peek). *Journal of Laser Applications*, 34(4).

[Maloo et al., 2022] Maloo, L. M., Toshniwal, S. H., Reche, A., Paul, P., and Wanjari, M. B. (2022). A sneak peek toward polyaryletherketone (paek) polymer: a review. *Cureus*, 14(11).

[Mamuschkin et al., 2014] Mamuschkin, V., Olowinsky, A., Britten, S. W., and Engelmann, C. (2014). Investigations on laser transmission welding of absorber-free thermoplastics. In *Laser-based Micro-and Nanoprocessing VIII*, volume 8968, pages 224–232. SPIE.

[Martineau et al., 2019] Martineau, L., Chabert, F., Boniface, B., and Bernhart, G. (2019). Effect of interfacial crystalline growth on autohesion of peek. *International Journal of Adhesion and Adhesives*, 89:82–87.

[Matus-Aguirre et al., 2024] Matus-Aguirre, M., Cosson, B., Garnier, C., Schmidt, F., Akué-Asséko, A. C., and Chabert, F. (2024). Characterization and modeling of laser transmission welded polyetherketoneketone (pekk) joints: influence of process parameters and annealing on weld properties. *Journal of Advanced Joining Processes*, page 100252.

[Matus Aguirre et al., 2023] Matus Aguirre, M., Garnier, C., Gilblas, R., Benoit, C., Asseko, A. C. A., Schmidt, F., and Chabert, F. (2023). Laser transmission welding of PEKK: Influence of material properties and process parameters on the weld strength. In *Materials Research Proceedings*, volume 28, pages 1829–1840. Materials Research Forum LLC.

[Mingareev et al., 2012] Mingareev, I., Weirauch, F., Olowinsky, A., Shah, L., Kadwani, P., and Richardson, M. (2012). Welding of polymers using a 2m thulium fiber laser. *Optics & Laser Technology*, 44(7):2095–2099.

[Nakamata, 1987] Nakamata, H. (1987). Process for joining different kinds of synthetic resins. Patent Number: 4 636 609, United States Patent.

[Nakhaei et al., 2013] Nakhaei, M. R., Mostafa Arab, N. B., and Naderi, G. (2013). Application of response surface methodology for weld strength prediction in laser welding of polypropylene/clay nanocomposite. *Iranian Polymer Journal*, 22(5):351–360.

[Namazi, 2017] Namazi, H. (2017). Polymers in our daily life. *BioImpacts: BI*, 7(2):73.

[Nguyen and Ishida, 1987] Nguyen, H. X. and Ishida, H. (1987). Poly (aryl-ether-ether-ketone) and its advanced composites: A review. *Polymer composites*, 8(2):57–73.

[Nonhof, 1994] Nonhof, C. (1994). Laser welding of polymers. *Polymer Engineering & Science*, 34(20):1547–1549.

[Özişik et al., 2017] Özişik, M. N., Orlande, H. R., Colaço, M. J., and Cotta, R. M. (2017). *Finite difference methods in heat transfer*. CRC press.

[Parlevliet and Weimer, 2011] Parlevliet, P. and Weimer, C. (2011). Thermoplastic high performance composites: environmental requirements on future helicopter airframes. *ICCM-18*, pages 21–26.

[Patel and Spruiell, 1991] Patel, R. M. and Spruiell, J. E. (1991). Crystallization kinetics during polymer processing—analysis of available approaches for process modeling. *Polymer Engineering & Science*, 31(10):730–738.

[Pérez-Martín et al., 2022] Pérez-Martín, H., Mackenzie, P., Baidak, A., Brádaigh, C. M. Ó., and Ray, D. (2022). Crystallisation behaviour and morphological studies of pekk and carbon fibre/pekk composites. *Composites Part A: Applied Science and Manufacturing*, 159:106992.

[Potente and Becker, 1999] Potente, H. and Becker, F. (1999). Weld strength behavior of laser butt welds. In *SPE/Antec*, volume 99, pages 1402–1405.

[Potente et al., 2001] Potente, H., Becker, F., Fiegler, G., and Korte, J. (2001). Investigations towards application of a new technique on laser transmission welding. *Welding in the World*, 45(5-6):15–20.

[Potente et al., 1999] Potente, H., Korte, J., and Becker, F. (1999). Laser Transmission Welding of Thermoplastics: Analysis of the Heating Phase. *Journal of Reinforced Plastics and Composites*, 18(10):914–920. Publisher: SAGE Publications Ltd STM.

[Potente et al., 2009] Potente, H., Schöppner, V., Bonefeld, D., Wilke, L., and Hage, C. (2009). Experiments regarding the influence of pressure profiling on laser-transmission welding. *Welding in the World*, 53:R246–R252.

[Pravin et al., 2022] Pravin, K. S., Prasanna, B., Chatterjee, U., Sinha, N., Mandal, N., and Roy, S. K. (2022). Application of peek: A future revolution in prosthodontics. *Dental journal of Indira Gandhi Institute of Medical Sciences*, 1(1):56–63.

[Pritchard, 1994] Pritchard, G. (1994). *Anti-corrosion polymers: PEEK, PEKK and other polyaryls*, volume 80. iSmithers Rapra Publishing.

[Quiroga Cortés et al., 2016] Quiroga Cortés, L., Caussé, N., Dantras, E., Lonjon, A., and Lacabanne, C. (2016). Morphology and dynamical mechanical properties of poly ether ketone ketone (PEKK) with meta phenyl links. *Journal of Applied Polymer Science*, 133(19). _eprint: https://onlinelibrary.wiley.com/doi/pdf/10.1002/app.43396.

[Rezvani Ghomi et al., 2021] Rezvani Ghomi, E., Eshkalak, S. K., Singh, S., Chinnappan, A., Ramakrishna, S., and Narayan, R. (2021). Fused filament printing of specialized biomedical devices: a state-of-the art review of technological feasibilities with peek. *Rapid Prototyping Journal*, 27(3):592–616.

[Rhew et al., 2003] Rhew, M., Mokhtarzadeh, A., and Benatar, A. (2003). Diode laser chracterization and measurement of optical properties of polycarbonate and high-density polyethylene. In *ANTEC 2003 Conference Proceedings*, volume 1, pages 1056–1060.

[Russek, 2001] Russek, U.-A. (2001). Laser beam welding of polymers with high power diode lasers joining innovation for micro and macro technologies. *International Congress on Applications of Lasers & Electro-Optics*, 2001(1):483–491. Publisher: Laser Institute of America.

[Russek et al., 2003] Russek, U. A., Palmen, A., Staub, H., Poehler, J., Wenzlau, C., Otto, G., Poggel, M., Koeppe, A., and Kind, H. (2003). Laser beam welding of thermoplastics. In *Photon Processing in Microelectronics and Photonics II*, volume 4977, pages 458–472, San Jose, CA. SPIE.

[Seferis, 1986] Seferis, J. C. (1986). Polyetheretherketone (peek): Processing-structure and properties studies for a matrix in high performance composites. *Polymer composites*, 7(3):158–169.

[Segovia et al., 2017] Segovia, J., Lozano-Martín, D., Martín, M., Chamorro, C., Villamañán, M., Pérez, E., Izquierdo, C. G., and del Campo, D. (2017). Updated determination of the molar gas constant r by acoustic measurements in argon at uva-cem. *Metrologia*, 54(5):663.

[Silvus Jr and Wachtell, 1970] Silvus Jr, H. J. and Wachtell, S. (1970). Perforating, welding, and cutting plastic films with a continuous CO2 laser. *PA State University, Engineering Proceedings*, pages 88–97.

[Stokes, 1989] Stokes, V. K. (1989). Joining methods for plastics and plastic composites: An overview. *Polymer Engineering & Science*, 29(19):1310–1324. _eprint: https://onlinelibrary.wiley.com/doi/pdf/10.1002/pen.760291903.

[Su et al., 2020] Su, J., Tan, C., Wu, Z., Wu, L., Gong, X., Chen, B., Song, X., and Feng, J. (2020). Influence of defocus distance on laser joining of cfrp to titanium alloy. *Optics & Laser Technology*, 124:106006.

[Ussing et al., 2007] Ussing, T., Petersen, L. V., Nielsen, C. B., Helbo, B., and Højslet, L. (2007). Micro laser welding of polymer microstructures using low power laser diodes. *The International Journal of Advanced Manufacturing Technology*, 33(1):198–205.

[Vacogne and Wise, 2011] Vacogne, C. and Wise, R. (2011). Joining of high performance carbon fibre/peek composites. *Science and Technology of Welding and Joining*, 16(4):369–376.

[Veazey et al., 2017] Veazey, D., Hsu, T., and Gomez, E. D. (2017). Next generation high-performance carbon fiber thermoplastic composites based on polyaryletherketones. *Journal of applied polymer science*, 134(6).

[Velisaris and Seferis, 1986] Velisaris, C. N. and Seferis, J. C. (1986). Crystallization kinetics of polyetheretherketone (peek) matrices. *Polymer Engineering & Science*, 26(22):1574–1581. _eprint: https://onlinelibrary.wiley.com/doi/pdf/10.1002/pen.760262208.

[Villar et al., 2016] Villar, M., Chabert, F., Garnier, C., Nassiet, V., Diez, J. C., Sotelo, A., Madre, M. A., Duchesne, C., and Cussac, P. (2016). Laser transmission welding as an assembling process for high temperature electronic packaging. In *2016 International Conference on Electrical Systems for Aircraft, Railway, Ship Propulsion and Road Vehicles & International Transportation Electrification Conference (ESARS-ITEC)*, pages 1–5. IEEE.

[Villar et al., 2018] Villar, M., Garnier, C., Chabert, F., Nassiet, V., Samélor, D., Diez, J. C., Sotelo, A., and Madre, M. A. (2018). In-situ infrared thermography measurements to master transmission laser welding process parameters of PEKK. *Optics and Lasers in Engineering*, 106:94–104.

[Vodicka, 1996] Vodicka, R. (1996). Thermoplastics for airframe applications: a review of the properties and repair methods for thermoplastic composites. *DSTO Aeronautical and Maritime Research Laboratory*.

[Wang et al., 2010] Wang, C., Bates, P., and Zak, G. (2010). Optical Properties Characterization of Thermoplastics Used in Laser Transmission Welding: Scattering and Absorbance. *Advanced Materials Research*, 97-101:3836–3841.

[Wang et al., 2016] Wang, X., Guo, D., Chen, G., Jiang, H., Meng, D., Yan, Z., and Liu, H. (2016). Thermal degradation of pa66 during laser transmission welding. *Optics & Laser Technology*, 83:35–42.

[Wippo et al., 2016] Wippo, V., Winter, Y., Jaeschke, P., Suttmann, O., and Overmeyer, L. (2016). The influence of laser welding processes on the weld seam quality of thermoplastic composites with high moisture content. *Physics Procedia*, 83:1064–1072.

[Wu et al., 2021] Wu, J., Lu, S., Wang, H.-J., Wang, Y., and Xia, F.-B. (2021). A review on laser transmission welding of thermoplastics. *The International Journal of Advanced Manufacturing Technology*, 116:2093–2109.

[Xu et al., 2015a] Xu, X. F., Bates, P. J., and Zak, G. (2015a). Effect of glass fiber and crystallinity on light transmission during laser transmission welding of thermoplastics. *Optics & Laser Technology*, 69:133–139.

[Xu et al., 2015b] Xu, X. F., Parkinson, A., Bates, P. J., and Zak, G. (2015b). Effect of part thickness, glass fiber and crystallinity on light scattering during laser transmission welding of thermoplastics. *Optics & Laser Technology*, 75:123–131.

[Yousefpour et al., 2004] Yousefpour, A., Hojjati, M., and Immarigeon, J.-P. (2004). Fusion Bonding/Welding of Thermoplastic Composites. *Journal of Thermoplastic Composite Materials*, 17(4):303–341.

[Zeyrek et al., 2022] Zeyrek, B., Aydogan, B., Dilekcan, E., and Ozturk, F. (2022). Review of thermoplastic composites in aerospace industry. *Int. J. Eng. Tech. Inf*, 3:1–6.

[Zol et al., 2023] Zol, S. M., Alauddin, M. S., Said, Z., Mohd Ghazali, M. I., Hao-Ern, L., Mohd Farid, D. A., Zahari, N. A. H., Al-Khadim, A. H. A., and Abdul Aziz, A. H. (2023). Description of poly (aryl-ether-ketone) materials (paeks), polyetheretherketone (peek) and polyetherketoneketone (pekk) for application as a dental material: a materials science review. *Polymers*, 15(9):2170.

RÉPUBLIQUE FRANÇAISE
Liberté
Égalité
Fraternité

Université de Toulouse

Titre : Soudage laser par transmission de thermoplastique semi-cristallin PEKK : prédiction de la cristallinité du joint de soudure et de la résistance mécanique des assemblages

Mots clés : Soudage laser, Soudage de polymères, Cristallisation, Composites, Simulation numérique, polyéthercétonecétone

Résumé : Les matériaux thermoplastiques gagnent en popularité dans l'industrie aérospatiale en tant qu'alternatives aux métaux et aux thermodurcissables, offrant des avantages tels que la rapidité de fabrication, la réparabilité et la recyclabilité. Leur capacité à ramollir et à fondre sous l'effet de la chaleur leur permet d'être soudés sans avoir besoin d'incorporer de composants. De plus, certains thermoplastiques présentent une résistance aux environnements extrêmes, tels que des températures élevées et divers produits chimiques, ce qui les rend idéaux pour des applications exigeantes. Ces caractéristiques font des thermoplastiques des matériaux adaptés aux applications où la réduction du poids, les performances et la durabilité sont des critères essentiels.

Dans ce contexte, le soudage par transmission laser (LTW) se révèle être une technique efficace pour le soudage des thermoplastiques en raison de sa simplicité, de sa précision et de sa capacité à produire des joints de haute qualité. Dans cette technique, un faisceau laser traverse une partie supérieure semi-transparente et est absorbé par une pièce inférieure absorbante, ce qui génère de la chaleur à l'interface pour faire fondre et fusionner les pièces. Le procédé LTW repose sur les propriétés thermochimiques et optiques des matériaux à souder. Le soudage laser de thermoplastiques semi-cristallins, tels que les polyaryléthercétone (PAEK), nécessite une attention particulière. Le polyéthercétonecétone (PEKK) a reçu moins d'attention que le PEEK en soudage laser. Cependant, le PEKK est un matériau encore plus prometteur pour le soudage laser par transmission en raison de sa cinétique de cristallisation modifiable par rapport au PEEK.

Cette thèse doctorale étudie le procédé de soudage laser par transmission du PEKK, en se concentrant sur l'influence des propriétés du matériau et des paramètres de soudage sur la morphologie et les propriétés mécaniques du joint de soudure. La configuration d'assemblage consiste en un échantillon de PEKK quasi-amorphe sur une pièce de PEKK fortement cristallisée (PEKK-A/SC). Les propriétés thermophysiques et optiques des matériaux sont caractérisées afin de s'assurer qu'ils sont adaptés au LTW. Ensuite, les paramètres du procédé, tels que la puissance du laser et l'épaisseur de la pièce semi-transparente, sont systématiquement étudiés pour comprendre leur impact sur les propriétés du joint. Certains assemblages sont recuits à la température de cristallisation à froid du PEKK pour améliorer la qualité des joints soudés. La qualité des assemblages soudés et recuits est évaluée à l'aide d'essais mécaniques de cisaillement à simple recouvrement et de la microscopie.

Le procédé LTW est modélisé à l'aide de la méthode des différences finies sous environnement MatLab, en incorporant le transfert de chaleur et la cinétique de cristallisation du PEKK. Cette modélisation a permis de comprendre l'histoire thermique des échantillons pendant le soudage et de prédire l'évolution de la cristallinité du joint de soudure en fonction des paramètres de soudage.

Après avoir étudié et validé le procédé LTW pour le PEKK, la thèse étend l'étude LTW aux composites PEKK renforcés par des fibres courtes de carbone (PEKK-CF). Pour permettre le LTW des échantillons PEKK-CF, le PEKK quasi-amorphe est utilisé comme pièce supérieure pour l'assemblage. Cela représente un nouveau domaine de recherche, car aucune étude antérieure n'a été trouvée sur le soudage laser par transmission des composites PEKK-CF. Le soudage des échantillons de PEKK-CF est optimisé par des essais expérimentaux, et la qualité du joint de soudure est évaluée en faisant varier l'intensité de laser.

Les résultats de cette thèse contribuent à une meilleure compréhension du procédé de soudage laser par transmission du PEKK et de ses composites, et fournissent des lignes directrices pour optimiser les paramètres de soudage et améliorer la résistance des joints dans les applications industrielles.

Title: Laser transmission welding (LTW) of semi-crystalline thermoplastic PEKK: prediction of the weld joint crystallinity and mechanical strength of assemblies

Key words: Laser welding, Polymers welding, Crystallization, Composites, Numerical simulation, polyetherketoneketone

Abstract: Thermoplastic materials are gaining popularity in the aerospace industry as alternatives to metals and thermosets, providing benefits such as fast manufacturing, repairability, and recyclability. Their ability to soften and melt allows them to be welded without needing to incorporate external components. Additionally, high-performance thermoplastics exhibit resistance to harsh environments, such as high temperatures and various chemicals, making them ideal for high-demanding applications. These features make thermoplastics suitable for applications in which weight reduction, performance, and durability are essential.

Laser transmission welding (LTW) has emerged as an effective technique for welding thermoplastics due to its simplicity, precision, and ability to produce high-quality joints. In LTW, a laser beam passes through a semi-transparent upper part and is absorbed by a lower absorbent sample, generating heat at the interface to assemble the parts. The LTW process relies on the thermo-chemical and optical properties of the materials to be welded. Careful consideration is needed when laser welding semi-crystalline thermoplastics, like polyaryletherketones (PAEK). Polyetherketoneketone (PEKK) has received less attention than PEEK in laser welding. However, PEKK is a more promising material for LTW due to its unique crystallization properties compared to PEEK. The crystallization kinetics of PEKK can be modified, which provides better control of its crystallinity by manipulating processing parameters.

This PhD thesis investigates the laser transmission welding process of PEKK, focusing on the influence of material properties and process parameters on the weld joint morphology and mechanical properties. The overlapping configuration consists of a quasi-amorphous semi-transparent PEKK sample over a highly crystallized opaque PEKK one (PEKK-A/SC). Thermo-physical and optical properties of the PEKK samples are characterized to ensure their suitability for LTW. Then, process parameters for LTW, such as laser power and thickness of the upper part, are systematically studied to understand their impact on weld joint properties. After welding, some assemblies are annealed at the cold crystallization temperature of PEKK to enhance joint quality. The quality of the weld joints is assessed by mechanical tests and microscopic observations. Single lap-shear tests are employed to identify the failure type and mechanical strength of assemblies. Microscopy is used to analyze failure zones and the weld joint morphology on the cross-section along the welding path.

A numerical simulation of the LTW process of PEKK parts was developed in MatLab using the finite differences method, incorporating heat transfer and the crystallization kinetics of PEKK. This model provided insights into the thermal history of the samples during welding and predicted the evolution of weld joint crystallinity as a function of welding parameters. The developed simulations offer insights into the complex thermal and crystallization behaviors observed during LTW of PEKK parts.

Furthermore, after studying and validating the LTW process for PEKK polymer, this thesis extends the LTW study to PEKK composites reinforced with short carbon fibers (PEKK-CF). To enable LTW of PEKK-CF samples, the quasi-amorphous PEKK is used as the upper part for the overlapping configuration. That represents a novel area of research, with no prior studies found on LTW of PEKK-CF composites. The welding of PEKK-CF samples is optimized through experimental trials, and the weld joint quality is evaluated under varying laser intensities and the thickness of the upper part.

The findings from this thesis contribute to a deeper understanding of the LTW process for PEKK and its composites, providing valuable guidelines for optimizing welding parameters and improving joint strength in industrial applications.

RÉPUBLIQUE FRANÇAISE
Liberté Égalité Fraternité

Université de Toulouse

Titre : Soudage laser par transmission de thermoplastique semi-cristallin PEKK : prédiction de la cristallinité du joint de soudure et de la résistance mécanique des assemblages

Mots clés : Soudage laser, Soudage de polymères, Cristallisation, Composites, Simulation numérique, Polyéthercétonecétone

Résumé : Les matériaux thermoplastiques gagnent en popularité dans l'industrie aérospatiale en tant qu'alternatives aux métaux et aux thermodurcissables, offrant des avantages tels que la rapidité de fabrication, la réparabilité et la recyclabilité. Leur capacité à ramollir et à fondre sous l'effet de la chaleur leur permet d'être soudés sans avoir besoin d'incorporer de composants. De plus, certains thermoplastiques présentent une résistance aux environnements extrêmes, tels que des températures élevées et divers produits chimiques, ce qui les rend idéaux pour des applications exigeantes. Ces caractéristiques font des thermoplastiques des matériaux adaptés aux applications où la réduction du poids, les performances et la durabilité sont des critères essentiels.
Dans ce contexte, le soudage par transmission laser (LTW) se révèle être une technique efficace pour le soudage des thermoplastiques en raison de sa simplicité, de sa précision et de sa capacité à produire des joints de haute qualité. Dans cette technique, un faisceau laser traverse une partie supérieure semi-transparente et est absorbé par une pièce inférieure absorbante, ce qui génère de la chaleur à l'interface pour faire fondre et fusionner les pièces. Le procédé LTW repose sur les propriétés thermochimiques et optiques des matériaux à souder. Le soudage laser de thermoplastiques semi-cristallins, tels que les polyaryléthercétone (PAEK), nécessite une attention particulière. Le polyéthercétonecétone (PEKK) a reçu moins d'attention que le PEEK en soudage laser. Cependant, le PEKK est un matériau encore plus prometteur pour le soudage laser par transmission en raison de sa cinétique de cristallisation modifiable par rapport au PEEK.
Cette thèse doctorale étudie le procédé de soudage laser par transmission du PEKK, en se concentrant sur l'influence des propriétés du matériau et des paramètres de soudage sur la morphologie et les propriétés mécaniques du joint de soudure. La configuration d'assemblage consiste en un échantillon de PEKK quasi-amorphe sur une pièce de PEKK fortement cristallisée (PEKK-A/SC). Les propriétés thermophysiques et optiques des matériaux sont caractérisées afin de s'assurer qu'ils sont adaptés au LTW. Ensuite, les paramètres du procédé, tels que la puissance du laser et l'épaisseur de la pièce semi-transparente, sont systématiquement étudiés pour comprendre leur impact sur les propriétés du joint. Certains assemblages sont recuits à la température de cristallisation à froid du PEKK pour améliorer la qualité des joints soudés. La qualité des assemblages soudés et recuits est évaluée à l'aide d'essais mécaniques de cisaillement à simple recouvrement et de la microscopie.
Le procédé LTW est modélisé à l'aide de la méthode des différences finies sous environnement MatLab, en incorporant le transfert de chaleur et la cinétique de cristallisation du PEKK. Cette modélisation a permis de comprendre l'histoire thermique des échantillons pendant le soudage et de prédire l'évolution de la cristallinité du joint de soudure en fonction des paramètres de soudage.
Après avoir étudié et validé le procédé LTW pour le PEKK, la thèse étend l'étude LTW aux composites PEKK renforcés par des fibres courtes de carbone (PEKK-CF). Pour permettre le LTW des échantillons PEKK-CF, le PEKK quasi-amorphe est utilisé comme pièce supérieure pour l'assemblage. Cela représente un nouveau domaine de recherche, car aucune étude antérieure n'a été trouvée sur le soudage laser par transmission des composites PEKK-CF. Le soudage des échantillons de PEKK-CF est optimisé par des essais expérimentaux, et la qualité du joint de soudure est évaluée en faisant varier l'intensité de laser.
Les résultats de cette thèse contribuent à une meilleure compréhension du procédé de soudage laser par transmission du PEKK et de ses composites, et fournissent des lignes directrices pour optimiser les paramètres de soudage et améliorer la résistance des joints dans les applications industrielles.

Title: Laser transmission welding (LTW) of semi-crystalline thermoplastic PEKK: prediction of the weld joint crystallinity and mechanical strength of assemblies

Key words: Laser welding, Polymers welding, Crystallization, Composites, Numerical simulation, Polyetherketoneketone

Abstract: Thermoplastic materials are gaining popularity in the aerospace industry as alternatives to metals and thermosets, providing benefits such as fast manufacturing, repairability, and recyclability. Their ability to soften and melt allows them to be welded without needing to incorporate external components. Additionally, high-performance thermoplastics exhibit resistance to harsh environments, such as high temperatures and various chemicals, making them ideal for high-demanding applications. These features make thermoplastics suitable for applications in which weight reduction, performance, and durability are essential.
Laser transmission welding (LTW) has emerged as an effective technique for welding thermoplastics due to its simplicity, precision, and ability to produce high-quality joints. In LTW, a laser beam passes through a semi-transparent upper part and is absorbed by a lower absorbent sample, generating heat at the interface to assemble the parts. The LTW process relies on the thermo-chemical and optical properties of the materials to be welded. Careful consideration is needed when laser welding semi-crystalline thermoplastics, like polyaryletherketones (PAEK). Polyetherketoneketone (PEKK) has received less attention than PEEK in laser welding. However, PEKK is a more promising material for LTW due to its unique crystallization properties compared to PEEK. The crystallization kinetics of PEKK can be modified, which provides better control of its crystallinity by manipulating processing parameters.
This PhD thesis investigates the laser transmission welding process of PEKK, focusing on the influence of material properties and process parameters on the weld joint morphology and mechanical properties. The overlapping configuration consists of a quasi-amorphous semi-transparent PEKK sample over a highly crystallized opaque PEKK one (PEKK-A/SC). Thermo-physical and optical properties of the PEKK samples are characterized to ensure their suitability for LTW. Then, process parameters for LTW, such as laser power and thickness of the upper part, are systematically studied to understand their impact on weld joint properties. After welding, some assemblies are annealed at the cold crystallization temperature of PEKK to enhance joint quality. The quality of the weld joints is assessed by mechanical tests and microscopic observations. Single lap-shear tests are employed to identify the failure type and mechanical strength of assemblies. Microscopy is used to analyze failure zones and the weld joint morphology on the cross-section along the welding path.
A numerical simulation of the LTW process of PEKK parts was developed in MatLab using the finite differences method, incorporating heat transfer and the crystallization kinetics of PEKK. This model provided insights into the thermal history of the samples during welding and predicted the evolution of weld joint crystallinity as a function of welding parameters. The developed simulations offer insights into the complex thermal and crystallization behaviors observed during LTW of PEKK parts.
Furthermore, after studying and validating the LTW process for PEKK polymer, this thesis extends the LTW study to PEKK composites reinforced with short carbon fibers (PEKK-CF). To enable LTW of PEKK-CF samples, the quasi-amorphous PEKK is used as the upper part for the overlapping configuration. That represents a novel area of research, with no prior studies found on LTW of PEKK-CF composites. The welding of PEKK-CF samples is optimized through experimental trials, and the weld joint quality is evaluated under varying laser intensities and the thickness of the upper part.
The findings from this thesis contribute to a deeper understanding of the LTW process for PEKK and its composites, providing valuable guidelines for optimizing welding parameters and improving joint strength in industrial applications.